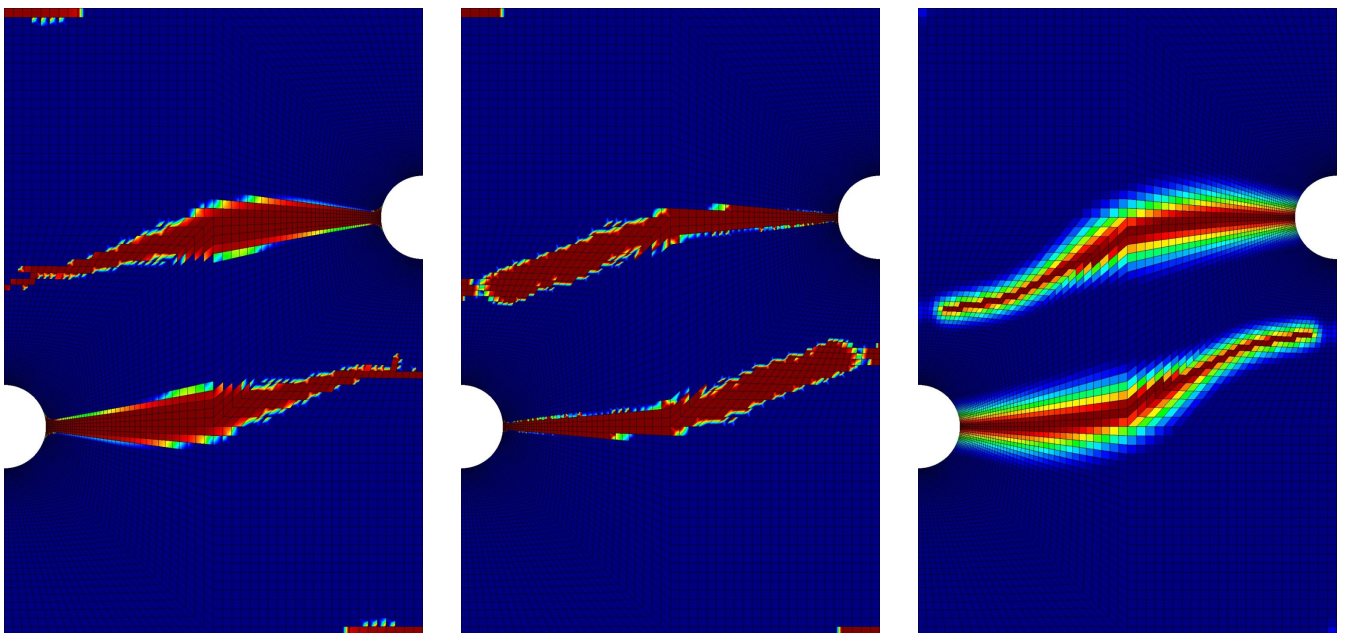


Efficient Approaches for Regularized Damage Models: Variational Modeling and Numerical Treatment

Stephan Schwarz



RUHR-UNIVERSITÄT BOCHUM
Institut für Mechanik

**Efficient Approaches for Regularized Damage Models:
Variational Modeling and Numerical Treatment**

Dissertation zur Erlangung des Grades

Doktor-Ingenieur

der Fakultät für Maschinenbau
der Ruhr-Universität Bochum

von

Stephan Schwarz

aus Neumünster

Bochum 2019

Mitteilungen aus dem Institut für Mechanik Nr. 182

Herausgeber (Publisher):
Institut für Mechanik
— Schriftenreihe —
Ruhr-Universität Bochum
D-44780 Bochum

ISBN 978-3-935892-60-5

This material is presented to ensure timely dissemination of scholarly and technical work. Copyright and all rights therein are retained by the copyright holders. All persons copying this information are expected to adhere to the terms and constraints invoked by the author's copyright. These works or parts of it may not be used to repost reprint/republish or for creating new collective works for resale or redistribution to servers or lists without the explicit permission of the copyright holder.

Dieses Werk ist urheberrechtlich geschützt. Die dadurch begründeten Rechte, insbesondere die der Übersetzung, des Nachdrucks, des Vortrags, der Entnahme von Abbildungen und Tabellen, der Funksendung, der Mikroverfilmung oder der Vervielfältigung auf anderen Wegen und der Speicherung in Datenverarbeitungsanlagen, bleiben, auch bei nur auszugsweiser Verwertung, vorbehalten. Eine Vervielfältigung dieses Werkes oder von Teilen dieses Werkes ist zulässig. Sie ist grundsätzlich vergütungspflichtig. Zuwiderhandlungen unterliegen den Strafbestimmungen des Urheberrechtsgesetzes.

©2019 Stephan Schwarz, Institut für Mechanik, Ruhr-Universität Bochum

Printed in Germany

Einreichung der Dissertation (thesis submission): 06.06.2019

Tag der mündlichen Prüfung (thesis defense): 18.07.2019

Erster Referent (first referee):

PD Dr.-Ing. Philipp Junker

Zweiter Referent (second referee):

Prof. Dr. rer. nat. Klaus Hackl

Vorsitzender (committee chair):

Prof. Dr.-Ing. Cemal Esen

Vorwort

Die vorliegende Dissertation ist das Ergebnis meiner Arbeit als wissenschaftlicher Mitarbeiter am Lehrstuhl für Mechanik – Materialtheorie an der Ruhr-Universität Bochum. Dabei haben mich verschiedene Personen unterstützt, wofür ich an dieser Stelle Danke sagen möchte.

Zunächst danke ich der Promotionskommission, bestehend aus dem Vorsitzenden Prof. Dr.-Ing. Cemal Esen, dem Erstgutachter PD Dr.-Ing. Philipp Junker sowie dem Zweitgutachter Prof. Dr. rer. nat. Klaus Hackl. Herr Esen, vielen Dank für die unkomplizierte und sympathische Übernahme des Vorsitzes. Philipp, ich danke Dir für die intensive Betreuung und Unterstützung, sowie für den kollegialen aber auch freundschaftlichen Umgang in den letzten Jahren. Ich konnte aus dieser Zeit viel für mich mitnehmen und habe eine Menge dazu gelernt. Herr Hackl, Ihnen danke ich zum einen für die Möglichkeit, an Ihrem Lehrstuhl arbeiten und promovieren zu dürfen, zum anderen aber auch für die gute Zusammenarbeit und Unterstützung.

Ebenfalls danke ich meinen Kollegen am Lehrstuhl, die mich in den letzten Jahren begleitet haben. Als erstes möchte ich Frau Dr.-Ing. Johanna Waimann danken, mit der ich über fünf Jahre ein Büro und sehr viel Kaffee geteilt habe. Johanna, wir haben nicht nur ausgezeichnet zusammengearbeitet, interessante Gespräche sowie hitzige Diskussionen geführt, sondern auch eine echte Freundschaft aufgebaut. Einen besonderen Dank möchte ich auch Herrn Dr.-Ing. Ulrich Hoppe aussprechen. Ulrich, Du bist eine große Unterstützung für den gesamten Lehrstuhl, sorgst beruflich und privat stets für eine gute Atmosphäre und warst in vielen Dingen mein erster Ansprechpartner. Ich möchte auch Dustin Jantos und Christopher Riedel danken. Insbesondere in der letzten Phase der Arbeit habt Ihr mich motiviert und mit schokoladehaltigen Keksen bei Laune gehalten, zudem konnten wir auch fachlich viele interessante und hilfreiche Gespräche führen. Natürlich danke ich auch den anderen und ehemaligen Kollegen des Lehrstuhls. Außerdem nicht unerwähnt lassen möchte ich Herrn Prof. Sanjay Govindjee von der University of California, Berkeley. Vielen Dank für die Betreuung meiner Masterarbeit an Ihrem Lehrstuhl sowie für die erneute Einladung nach Berkeley während meiner Promotionszeit.

Ganz besonders möchte ich meinen Freunden und meiner Familie danken. Meinen besten Freunden Marcel und Julian danke ich dafür, dass ich immer auf Eure Freundschaft zählen kann und dass Ihr mich auch in schwierigen Phasen motiviert und aufgeheitert habt. Meinen Eltern danke ich für die andauernde Unterstützung in allen Lebensbereichen, für die Ermöglichung diesen Weg zu gehen und dass Ihr in jeglicher Hinsicht immer für mich da seid. Auch meiner Schwester Katharina danke ich für ihre Unterstützung und Freundschaft, ich bin froh, dass es Dich gibt. Abschließend möchte ich meiner Lebensgefährtin danken. Sandra, Du hast mir stets den Rücken freigehalten, mich aufgemuntert, mir Kraft gegeben und immer an mich geglaubt. Ich danke Dir dafür und für alles andere.

Recklinghausen, 2019

Stephan Schwarz

Summary

The modeling of damage enables failure predictions, which is why it has become an important tool for academic research and industrial applications. Thereby, characteristic softening and localization effects lead to ill-posed boundary value problems due to non-convex and non-coercive energies. Consequently, numerical instabilities and mesh-dependent finite element results occur, which do not allow for physically correct failure predictions. In order to solve the aforementioned problems, regularization strategies are applied. However, regularization is usually accompanied by a high numerical effort leading to longer computation times in the end. Subject of current research is the development of novel approaches that regularize damage models with less disadvantages. Exactly this research describes the main topic of the present work. Consequently, three novel approaches are introduced, which are based on different strategies. The first model is based on energy relaxation along with a non-linear homogenization of two phases. The second model uses a limitation of the rate in connection with an emulated representative volume element. The third model has a gradient-enhanced formulation and efficiently evaluates the Laplace operator. After calibrating the parameters for all models, numerical calculations for three different boundary value problems were performed. These include the double-notched beam, the plate with a centered hole, and the cracked plate. The results are compared with respect to damage distributions as well as to global structural responses. By this and other aspects, such as computation times and implementation, the different novel models are contrasted with each other and assessed.

Kurzfassung

Die Modellierung von Schädigung ermöglicht Versagensvorhersagen, wodurch sie zu einem wichtigen Mittel für wissenschaftliche Forschung und industrielle Anwendung geworden ist. Dabei führen charakteristische Entfestigungs- und Lokalisierungseffekte aufgrund von nicht konvexen und nicht koerziven Energien zu schlecht gestellten Randwertproblemen. Folglich treten numerische Instabilitäten und netzabhängige Finite-Elemente-Ergebnisse auf, welche keine physikalisch korrekten Versagensvorhersagen ermöglichen. Um die genannten Probleme zu lösen, werden Regularisierungsstrategien angewendet. Allerdings geht die Regularisierung normalerweise mit einem hohen numerischen Aufwand einher, welcher letztlich zu längeren Berechnungszeiten führt. Gegenstand aktueller Forschung ist die Entwicklung neuartiger Ansätze, welche Schädigungsmodelle mit weniger Nachteilen regularisieren. Genau diese Forschung beschreibt das zentrale Thema der vorliegenden Arbeit. Folglich werden drei neuartige Ansätze vorgestellt, welche auf unterschiedlichen Strategien basieren. Das erste Modell basiert auf Energierelaxierung zusammen mit einer nicht linearen Homogenisierung zweier Phasen. Das zweite Modell verwendet eine Limitierung der Rate im Zusammenhang mit einem emulierten repräsentativen Volumenelement. Das dritte Modell hat eine Gradienten-erweiterte Formulierung und wertet den Laplace Operator sehr effizient aus. Nach einer Kalibrierung der Parameter aller Modelle werden numerische Berechnungen anhand von drei verschiedenen Randwertproblemen vorgenommen. Dabei enthalten sind der doppelt gekerbte Balken, die zentral gelochte Platte und die vorgekerbte Platte. Die Ergebnisse werden hinsichtlich der Schädigungsverteilung sowie der globalen Strukturantwort verglichen. Mit diesen und anderen Aspekten, zum Beispiel Berechnungszeiten und Implementierung, werden die unterschiedlichen neuartigen Modelle einander gegenübergestellt und bewertet.

Contents

Nomenclature	xi
1 Introduction	1
1.1 Motivation and Objectives	1
1.2 Outline	2
2 Fundamentals	3
2.1 Mathematical Notation	3
2.1.1 Tensor Notation	3
2.1.2 Tensor Products	4
2.1.3 Tensor Analysis	4
2.1.4 Voigt Notation	5
2.2 Calculus of Variations	5
2.3 Legendre-Fenchel Transformation	7
2.4 Laws of Thermodynamics	8
2.4.1 First Law of Thermodynamics: Balance of Energy	8
2.4.2 Second Law of Thermodynamics: Imbalance of Entropy	9
2.5 Free Energy and Constitutive Equations	10
2.6 Hamilton's Principle	12
2.6.1 Conservative Materials	12
2.6.2 Non-Conservative Materials	13
2.6.3 General Usage of Hamilton's Principle	14
2.6.4 Principle of the Minimum of the Dissipation Potential	14
2.7 Numerical Treatment of Evolution Equations	15
2.8 Finite Element Method	18
2.8.1 Discretization	18
2.8.2 Shape Functions and Interpolation	18
2.8.3 Operator Matrix and Strains	20
2.8.4 Gauß Quadrature	21
2.8.5 Residual and Tangent Matrix	22
2.9 Determination of Stresses and Material Tangent	23
2.9.1 Linear Material Behavior	23
2.9.2 Non-Linear Material Behavior	23
3 Damage Modeling and Regularization Strategies	27
3.1 Different Perspectives on Damage	27
3.2 Failure Criteria	29
3.3 Micromechanical Damage Models	30
3.4 Continuum Damage Models	31
3.5 Necessity of Regularization	32
3.6 Viscous Regularization	34
3.7 Integral-Type Regularization	35

3.8	Gradient-Enhanced Regularization	36
3.9	Selected Regularization Strategies for Investigation	38
4	Novel Approaches to Regularized Damage Models	41
4.1	Fundamentals of Damage Modeling	41
4.2	Model I: Relaxation Based Regularization with Two-Phases	42
4.2.1	Two-phase Damage Modeling by Relaxation	42
4.2.2	Non-Linear Homogenization between Reuß and Voigt	49
4.2.3	Additional Consideration of Viscosity for Mesh-Independence	53
4.2.4	Determination of Stresses and Material Tangent	53
4.2.5	Algorithm on Finite Element Level	54
4.3	Model II: Relaxation Based Regularization with the Emulated RVE	55
4.3.1	Variational Damage Modeling	55
4.3.2	Condensed Energy without Coercivity	56
4.3.3	Coercivity by Rate-Limitation	58
4.3.4	Quasiconvexity by Relaxation	60
4.3.5	The Emulated Representative Volume Element	61
4.3.6	Elimination of Rate-Dependence	63
4.3.7	Determination of Stresses and Material Tangent	64
4.3.8	Algorithm on Material Point and Finite Element Level	65
4.3.9	Numerical Results on Material Point Level	67
4.4	Model III: Gradient-Enhanced Regularization with Efficient Laplacian	70
4.4.1	Variational Damage Modeling	70
4.4.2	Numerical Treatment of the Displacement Field	73
4.4.3	Numerical Treatment of the Damage Function for One-Dimensionality	74
4.4.4	Numerical Treatment of the Damage Function for Structured Meshes	76
4.4.5	Numerical Treatment of the Damage Function for Unstructured Meshes	78
4.4.6	Allocation of the Neighborhood Relations	80
4.4.7	Algorithm on Finite Element Level	82
5	Preparatory Work for Finite Element Results	83
5.1	Boundary Value Problems for Investigations	83
5.1.1	Double-Notched Plate	84
5.1.2	Plate with a Centered Hole	84
5.1.3	Cracked Plate	85
5.2	Parameter Identification for Model I	86
5.2.1	Investigation of Rate-Dependence	86
5.2.2	Investigation of Homogenization	87
5.2.3	Investigation of Regularizing Viscosity	90
5.2.4	Selected Parameter Set	91
5.3	Parameter Identification for Model II	92
5.3.1	Investigation of Rate-Dependence	92
5.3.2	Investigation of Regularizing Subdomains	94
5.3.3	Investigation of Regularizing Rate-Limitation	97
5.3.4	Selected Parameter Set	98
5.4	Parameter Identification for Model III	99
5.4.1	Investigation of Rate-Dependence	99
5.4.2	Investigation of Regularization Parameter	101
5.4.3	Selected Parameter Set	102

6	Model Comparison with Finite Element Results	105
6.1	Damage Modeling without Regularization	105
6.1.1	Damage Distributions for the Double-Notched Plate (Stru. Mesh) . . .	106
6.1.2	Damage Distributions for the Double-Notched Plate (Unstru. Mesh) . .	107
6.1.3	Force-Displacement Diagrams for the Double-Notched Plate	108
6.1.4	Damage Distributions for the Plate with a Centered Hole (Stru. Mesh) .	109
6.1.5	Damage Distributions for the Plate with a Centered Hole (Unstru. Mesh)	110
6.1.6	Force-Displacement Diagrams for the Plate with a Centered Hole . . .	111
6.1.7	Damage Distributions for the Cracked Plate (Stru. Mesh)	112
6.1.8	Damage Distributions for the Cracked Plate (Unstru. Mesh)	113
6.1.9	Force-Displacement Diagrams for the Cracked Plate	114
6.2	Localized Damage Characteristics	115
6.2.1	Damage Distributions for the Double-Notched Plate (Stru. Mesh) . . .	117
6.2.2	Damage Distributions for the Double-Notched Plate (Unstru. Mesh) . .	118
6.2.3	Force-Displacement Diagrams for the Double-Notched Plate	119
6.2.4	Damage Distributions for the Plate with a Centered Hole (Stru. Mesh) .	120
6.2.5	Damage Distributions for the Plate with a Centered Hole (Unstru. Mesh)	121
6.2.6	Force-Displacement Diagrams for the Plate with a Centered Hole . . .	122
6.2.7	Damage Distributions for the Cracked Plate (Stru. Mesh)	123
6.2.8	Damage Distributions for the Cracked Plate (Unstru. Mesh)	124
6.2.9	Force-Displacement Diagrams for the Cracked Plate	125
6.3	Diffusive Damage Characteristics	126
6.3.1	Damage Distributions for the Double-Notched Plate (Stru. Mesh) . . .	128
6.3.2	Damage Distributions for the Double-Notched Plate (Unstru. Mesh) . .	129
6.3.3	Force-Displacement Diagrams for the Double-Notched Plate	130
6.3.4	Damage Distributions for the Plate with a Centered Hole (Stru. Mesh) .	131
6.3.5	Damage Distributions for the Plate with a Centered Hole (Unstru. Mesh)	132
6.3.6	Force-Displacement Diagrams for the Plate with a Centered Hole . . .	133
6.3.7	Damage Distributions for the Cracked Plate (Stru. Mesh)	134
6.3.8	Damage Distributions for the Cracked Plate (Unstru. Mesh)	135
6.3.9	Force-Displacement Diagrams for the Cracked Plate	136
6.4	Investigation of Computation Times	137
7	Discussion of Models and Comparison	139
7.1	Discussion of Model I	139
7.2	Discussion of Model II	139
7.3	Discussion of Model III	140
7.4	Comparative Discussion and Final Remarks	140
8	Conclusions	143
8.1	Summary	143
8.2	Additional and Future Research	144
A	Appendix - Additional Derivations to Model I	147
	References	151
	Reference to Pre-Publications	163
	Curriculum Vitae	164

Nomenclature

Latin notations

a	General tensor of zeroth order
\mathbf{a}	General tensor of first order
A	Surface
\mathbf{A}	General tensor of second order
b	General tensor of zeroth order
\mathbf{b}	General tensor of first order
\mathbf{B}	General tensor of second order in Section 2.1
\mathbf{B}	Strain operator matrix
\mathbf{B}^{∇^2}	Coefficient matrix of relevant inverted spatial increments
c	General tensor of zeroth order
\mathbf{c}	General tensor of first order
C	Constant as energy limit
\mathbf{C}	General tensor of second order
d, d^*	Damage variable
\mathbf{D}	Coefficient matrix of spatial increments
e	Counter for elements
$\mathbf{e}_1, \mathbf{e}_2, \mathbf{e}_3$	Cartesian basis
$\mathbf{e}_i, \mathbf{e}_j, \mathbf{e}_k, \mathbf{e}_l$	General Cartesian basis
E	Young's modulus
f	General function in Chapter 2
f	Damage function
\mathbf{f}	Volume forces
\mathbf{f}^*	Resulting forces
F	Force
g	Counter for Gauß points
G	Total stored energy
\dot{G}	Energy release rate
h	Heat source
i	Counter for subdomains of Model II [ERVE]
i	Central or neighboring element of Model III [LAP]
j	General counter
\mathbf{J}	Jacobian matrix
k	Fixed amount of evolving damage
l	Length of first order
m	Sampling points
n	Counter for nodes
n	Subdomains of Model II [ERVE]
\mathbf{n}	Normal vector
N_e	Number of elements
N_{GP}	Number of Gauß points

N_n	Number of nodes
\mathbf{N}	Shape functions
o	Polynomial degree
p	Driving force
\hat{p}	Dissipative force
q	Value of a function
\mathbf{q}	Heat flux
r	Value of a function
r_1	Dissipation parameter
r_2	Viscosity parameter
\mathbf{R}_u	Residual of displacement field
s	Specific entropy
t	Time
\mathbf{t}	Traction forces
u	Displacement
\mathbf{u}	Displacements
\mathbf{u}^*	Prescribed displacements
\mathbf{v}	Velocity
V	Volume
w	Weight factor
x	Argument of a function
x_i	Physical coordinates
\mathbf{x}	Physical coordinates
y	General function
\mathbf{y}	General variable of first order
z	General function

Greek notations and other symbols

α	Regularization parameter
α^*	Non-local weight function
β	Regularization parameter
γ, γ^*	Karush-Kuhn-Tucker parameter
$\Delta\mathcal{D}$	Dissipation distance
$\Delta\rho$	Consistency parameter
ε	Strain
$\boldsymbol{\varepsilon}$	Strain tensor
ζ	Coordinate for non-local range
θ	Temperature
κ	Numerical factor for damaged phase
λ	Internal variable
Λ	Vector of Laplace operator
ν	Poisson's ratio
ξ_i	Natural coordinates
$\boldsymbol{\xi}$	Natural coordinates
Π_{ext}	External potential
Π_{int}	Internal potential

ρ	Density
$\boldsymbol{\sigma}$	Stress tensor
τ	Ratio describing point on secant
φ	Non-local field function
Φ	Yield function
Ψ	Helmholtz free energy
Ψ_0	Helmholtz free energy for undamaged material
ω	Length
Ω	Volume of body
Ω_e	Volume of element
Ω_i	Volume of central or neighboring element of Model III [LAP]
Ω_{rep}	Volume of representative volume element
$\partial\Omega$	Boundary of body
\mathbb{A}	General tensor of fourth order
\mathbb{B}	General tensor of fourth order
\mathbb{C}	General tensor of fourth order
\mathbb{E}	Stiffness tensor
\mathbb{E}_0	Stiffness tensor for undamaged material
\mathcal{A}	Integration constant
\mathcal{C}	Constrain
$\mathcal{D}, \check{\mathcal{D}}$	Dissipation function
\mathcal{E}	Internal energy
\mathcal{F}	General functional
\mathcal{G}	Gibbs energy
\mathcal{H}	Absolute entropy production
\mathcal{K}	Kinetic energy
\mathcal{L}	Lagrangian
\mathcal{Q}	Thermal power
\mathcal{S}	Entropy production
\mathcal{V}	Dissipative forces
\mathcal{W}	Mechanical power
ℓ_{ext}	Power of external forces
∞	Infinity

Abbreviations

cond	Condensed
ERVE	Emulated representative volume element
GP	Gauß point
LAP	Laplace
PMDP	Principle of the minimum of the dissipation potential
RD	Rate-dependent
REL	Relaxation/relaxed
RI	Rate-independent
RVE	Representative volume element

Mathematical operators

$\arg \min(\cdot)$	Argument of the minimum
$\operatorname{div}(\cdot)$	Divergence
$\operatorname{grad}(\cdot)$	Gradient
$\inf(\cdot)$	Infimum
$\lim(\cdot)$	Limit of a function
$\min(\cdot)$	Minimum
$\operatorname{sgn}(\cdot)$	Signum function
$\sup(\cdot)$	Supremum
$D(\cdot)$	Derivative with respect to a function and direction
$L(\cdot)$	Linearization with respect to a function and direction
$Q(\cdot)$	Quasiconvex envelope
$\delta(\cdot)$	Variation
$\partial(\cdot)$	Partial derivative
$\Delta(\cdot)$	Increment
$\nabla(\cdot)$	Nabla operator
$d(\cdot)/dt = (\dot{\cdot})$	Time derivative / rate
$d(\cdot)/dx$	Total derivative with respect to x
$\partial(\cdot)/\partial x$	Partial derivative with respect to x
$(\bar{\cdot})$	New origin for coordinate transformation in Section 2.2
(\cdot)	Non-local value in Section 3.7
(\cdot)	Effective value in Section 4.3
(\cdot)	Averaged value in Section 4.4
(\cdot)	Voigt notation
$(\hat{\cdot})$	Reference to physical nodal coordinate
$(\cdot)^*$	Legendre-Fenchel transformation
$[\cdot]_+$	Permits only positive values
$(\cdot)^I$	Reference to natural nodal coordinate
$(\cdot)_{GP}$	Reference to Gauß points
$(\cdot)_{\text{eff}}$	Effective value
$(\cdot)^k$	Reference to last iteration step
$(\cdot)^{k+1}$	Reference to current iteration step
$(\cdot)^m$	Reference to last time step
$(\cdot)^{m+1}$	Reference to current time step
$(\cdot)'$	First derivative
$(\cdot)''$	Second derivative
$(\cdot)^{-1}$	Inverted
$(\cdot)^T$	Transposed
$ (\cdot) $	Absolute value / vector norm
$\langle(\cdot)\rangle$	Microscopic field

1 Introduction

1.1 Motivation and Objectives

The modeling of damage enables to capture the degradation of material strength or material resistance as a result of microscopic defects. Consequently, such material models play an important role for both academic research as well as for industrial applications: it allows for failure predictions and describes the resulting behavior of completely or partially damaged materials. An accurate prediction of failure is essential for respective stages of component development with regard to material selection and design concept. Therefore, components can be constructed that resist loads to be expected within defined tolerances. Damage modeling can also be applied for the examination of suitability of existing components with respect to changed conditions, for example.

In light of past experience, it is well-known that damage modeling is accompanied by softening and localization effects. Due to the underlying non-convex and non-coercive energies, ill-posed boundary value problems occur. In context of finite element calculations, this leads to numerical instabilities and mesh-dependent results. Thus, numerical calculations no longer allow for physically correct interpretations regarding failure prediction and material behavior.

Consequently, regularization strategies have to be applied in order to solve the aforementioned numerical instability problems and particularly to achieve mesh-independent finite element results. In the last decades, different regularization techniques have been developed and are now frequently used. The most common strategies thereby are gradient-enhanced, integral-type, and viscous regularization. However, regularized damage models usually suffer from a high numerical effort that leads in turn to high computation times. This particularly applies for the gradient-enhancement and the use of integral terms. Additionally, the regularization usually has a huge impact on the damage distribution and therefore on the final results. This impact is even depending on the applied loading rate in case of viscous regularization, which is limited to specific materials only due to its formulation. Although the literature provides a large amount of well-established regularized damage models and innovative ideas, further improvements are an object of current research. Hereby, the main focus is on the improvement of model efficiency providing shorter computation times. The core functions of mesh-independent and physically expectable numerical results remain important, of course. This also includes reasonable impacts on the damage distribution in order to remain typical crack characteristics, which can be distinguished in brittle or ductile damage. Besides that, the models are expected to be numerically stable, mathematically conform and preferably easy to implement.

The objectives of this thesis are directly derived from the aforementioned desired improvements demanding for novel procedures of regularization. In recent years, during my research at the Institute of Mechanics of Materials at the Ruhr-Universität Bochum, I have been working on different regularization approaches for damage models that have been inspired by established procedures from the literature interacting with completely new ideas. Consequently, several novel approaches have been developed, each of which exhibit interesting features and new ideas

to be mentioned. Three of these novel regularized damage models are considered in this work. Herein, the model derivations and descriptions are presented in the same order as they have been derived during my research. Finally, the main task of this thesis is the comparison of the novel regularized damage models by contrasting the different approaches and numerical results with each other with a focus on efficiency and mesh-independence.

1.2 Outline

This thesis is structured as follows: after this introductory part contained in Chapter 1, the fundamentals are introduced in Chapter 2 providing the mathematical and methodical foundations for this work. Additionally, a detailed insight into both the damage modeling by considering different descriptions as well as different kinds of regularization strategies is given in Chapter 3. Based on that, the three newly derived regularized damage models are presented in Chapter 4. The first model is based on energy relaxation in connection with a two-phase damage approach involving an undamaged and a damaged state. The second one combines a rate-limitation with a novel interpretation of an underlying microstructure, which is represented by the new emulated representative volume element. The third model is enhanced with a gradient formulation, in which the Laplace operator is evaluated very efficiently and suitable operator splits are applied. Afterwards in Chapter 5, the aforementioned investigations are initially prepared by providing the applied boundary value problems including a double-notched beam, a plate with a centered hole, and a cracked plate. Furthermore, the respective set of parameters are identified and calibrated. Representative simulation examples are subsequently performed by means of the finite element method in Chapter 6. The three considered damage models are compared with respect to different damage characteristics and stated boundary value problems. A detailed discussion of the numerical results is object of Chapter 7. In conclusion, the key aspects, findings and results as well as additional and possible future research are summarized in Chapter 8.

2 Fundamentals

This chapter provides relevant fundamentals in regards to this thesis. In Section 2.1 the mathematical notation is clarified. Section 2.2 introduces the calculus of variations. The Legendre-Fenchel transformation is presented in Section 2.3. Afterwards, the laws of thermodynamics are provided in Section 2.4. Based on that, Section 2.5 applies the free energy in context of constitutive equations. In Section 2.6 the Hamilton's principle is derived. Section 2.7 describes the numerical treatment of the evolution equations. The finite element method is established in Section 2.8. Hereto, the stresses and the material tangent are given in Section 2.9. Corresponding literature is respectively indicated.

2.1 Mathematical Notation

The notation and mathematical principles, which are applied throughout this thesis, are presented in this section. Initially, the tensor notation is given in Subsection 2.1.1, afterwards tensor products are introduced in Subsection 2.1.2, then Subsection 2.1.3 briefly describes the tensor analysis and finally the Voigt notation is given in Subsection 2.1.4. The provided information is mainly based on the works of Altenbach and Altenbach (1994) and Holzapfel (2000).

2.1.1 Tensor Notation

In general, tensors are categorized by their order. With regard to an exemplary Cartesian basis e_i with $i = 1, 2, 3$ the tensor of zeroth order corresponds to a scalar denoted as a, b, c, \dots , whereas the tensor of first order corresponds to a vector denoted as $\mathbf{a}, \mathbf{b}, \mathbf{c}, \dots$ with

$$\mathbf{a} = \begin{pmatrix} a_1 \\ a_2 \\ a_3 \end{pmatrix}, \quad (2.1)$$

additionally the tensor of second order corresponds to a dyadic denoted as $\mathbf{A}, \mathbf{B}, \mathbf{C}, \dots$ with

$$\mathbf{A} = \begin{pmatrix} A_{11} & A_{12} & A_{13} \\ A_{21} & A_{22} & A_{23} \\ A_{31} & A_{32} & A_{33} \end{pmatrix}, \quad (2.2)$$

and there are also tensors of higher order, for example fourth order is denoted as $\mathbb{A}, \mathbb{B}, \mathbb{C}, \dots$

Even though the symbolic notation is illustrative, the index notation more precisely describes mathematical operations and is therefore used here. By doing this, the vector \mathbf{a} becomes

$$\mathbf{a} = a_1 \mathbf{e}_1 + a_2 \mathbf{e}_2 + a_3 \mathbf{e}_3, \quad (2.3)$$

considering Einstein's summation convention for two identical indices leads to

$$\mathbf{a} = a_i \mathbf{e}_i := \sum_i a_i \mathbf{e}_i . \quad (2.4)$$

Additionally, the tensor of second order \mathbf{A} can be formulated as

$$\mathbf{A} = A_{ij} \mathbf{e}_i \otimes \mathbf{e}_j , \quad (2.5)$$

and the tensor of fourth order \mathbb{A} respectively

$$\mathbb{A} = A_{ijkl} \mathbf{e}_i \otimes \mathbf{e}_j \otimes \mathbf{e}_k \otimes \mathbf{e}_l . \quad (2.6)$$

2.1.2 Tensor Products

The dot product or scalar product of two vectors \mathbf{a} and \mathbf{b}

$$\mathbf{a} \cdot \mathbf{b} = a_i b_i = c \quad (2.7)$$

provides a scalar quantity c , the dot product of a tensor of second order \mathbf{A} and a vector \mathbf{b}

$$\mathbf{A} \cdot \mathbf{b} = A_{ij} b_j \mathbf{e}_i = \mathbf{c} \quad (2.8)$$

provides a vectorial quantity \mathbf{c} , and the dot product of two tensors of second order \mathbf{A} and \mathbf{B}

$$\mathbf{A} \cdot \mathbf{B} = A_{ij} B_{jl} \mathbf{e}_i \otimes \mathbf{e}_l = \mathbf{C} \quad (2.9)$$

provides a tensor of second order \mathbf{C} . Furthermore, the double dot product of a tensor of fourth order \mathbb{A} and a tensor of second order \mathbf{B} is described by a double contraction

$$\mathbb{A} : \mathbf{B} = A_{ijkl} B_{kl} \mathbf{e}_i \otimes \mathbf{e}_j = \mathbf{C} \quad (2.10)$$

providing a tensor of second order \mathbf{C} again. Besides that, the dyadic product or tensor product for also exemplarily two vectors \mathbf{a} and \mathbf{b}

$$\mathbf{a} \otimes \mathbf{b} = a_i b_j \mathbf{e}_i \otimes \mathbf{e}_j = \mathbf{C} \quad (2.11)$$

provides a tensor of second order \mathbf{C} and have already been used before.

2.1.3 Tensor Analysis

The Nabla operator ∇ is a fundamental tool and basis for other operations. Generally, the Nabla operator is a vector containing partial derivatives with respect to the basis \mathbf{e}_i , therefore

$$\nabla := \frac{\partial}{\partial x_i} \mathbf{e}_i . \quad (2.12)$$

In regard to a function $f(\mathbf{x})$, the dyadic product of ∇ and f is the gradient of f

$$\text{grad}f = \nabla f = \frac{\partial f}{\partial x_i} \mathbf{e}_i, \quad (2.13)$$

In regard to a vector $\mathbf{a}(\mathbf{x})$, the dot product of ∇ and \mathbf{a} is the divergence of \mathbf{a}

$$\text{div}\mathbf{a} = \nabla \cdot \mathbf{a} = \frac{\partial a_i}{\partial x_i}. \quad (2.14)$$

2.1.4 Voigt Notation

The relation between strains $\boldsymbol{\varepsilon}$ and stresses $\boldsymbol{\sigma}$ is described by the Hooke's law as follows

$$\boldsymbol{\sigma} = \mathbb{E} : \boldsymbol{\varepsilon}. \quad (2.15)$$

Hereby, the three-dimensional stiffness tensor \mathbb{E} , a tensor of fourth order, is of size $3 \times 3 \times 3 \times 3$ with consequently 81 entries whereas the stress tensor $\boldsymbol{\sigma}$ as well as the strain tensor $\boldsymbol{\varepsilon}$ are of size 3×3 with consequently 9 entries presented as follows

$$\boldsymbol{\sigma} = \begin{pmatrix} \sigma_{11} & \sigma_{12} & \sigma_{13} \\ \sigma_{21} & \sigma_{22} & \sigma_{23} \\ \sigma_{31} & \sigma_{32} & \sigma_{33} \end{pmatrix}, \quad \boldsymbol{\varepsilon} = \begin{pmatrix} \varepsilon_{11} & \varepsilon_{12} & \varepsilon_{13} \\ \varepsilon_{21} & \varepsilon_{22} & \varepsilon_{23} \\ \varepsilon_{31} & \varepsilon_{32} & \varepsilon_{33} \end{pmatrix}. \quad (2.16)$$

In order to simplify the notation and implementation as well as to save data, the Voigt notation introduced by Voigt (1910) and denoted by $(\tilde{\cdot})$ is considered, thus

$$\tilde{\boldsymbol{\sigma}} = \tilde{\mathbb{E}} \cdot \tilde{\boldsymbol{\varepsilon}}. \quad (2.17)$$

The Voigt notation takes advantage of redundant information due to symmetry and reduces the stress and strain tensors to vectors of length 6 and reduces the stiffness tensor to the second order possessing a size of 6×6 with consequently 36 entries, the following applies

$$\begin{pmatrix} \sigma_{11} \\ \sigma_{22} \\ \sigma_{33} \\ \sigma_{23} \\ \sigma_{13} \\ \sigma_{12} \end{pmatrix} = \begin{pmatrix} \mathbb{E}_{1111} & \mathbb{E}_{1122} & \mathbb{E}_{1133} & \mathbb{E}_{1123} & \mathbb{E}_{1113} & \mathbb{E}_{1112} \\ \mathbb{E}_{2211} & \mathbb{E}_{2222} & \mathbb{E}_{2233} & \mathbb{E}_{2223} & \mathbb{E}_{2213} & \mathbb{E}_{2212} \\ \mathbb{E}_{3311} & \mathbb{E}_{3322} & \mathbb{E}_{3333} & \mathbb{E}_{3323} & \mathbb{E}_{3313} & \mathbb{E}_{3312} \\ \mathbb{E}_{2311} & \mathbb{E}_{2322} & \mathbb{E}_{2333} & \mathbb{E}_{2323} & \mathbb{E}_{2313} & \mathbb{E}_{2312} \\ \mathbb{E}_{1311} & \mathbb{E}_{1322} & \mathbb{E}_{1333} & \mathbb{E}_{1323} & \mathbb{E}_{1313} & \mathbb{E}_{1312} \\ \mathbb{E}_{1211} & \mathbb{E}_{1222} & \mathbb{E}_{1233} & \mathbb{E}_{1223} & \mathbb{E}_{1213} & \mathbb{E}_{1212} \end{pmatrix} \cdot \begin{pmatrix} \varepsilon_{11} \\ \varepsilon_{22} \\ \varepsilon_{33} \\ 2\varepsilon_{23} \\ 2\varepsilon_{13} \\ 2\varepsilon_{12} \end{pmatrix}. \quad (2.18)$$

The stiffness tensor \mathbb{E} is often denoted by \mathbb{E}_0 in this thesis relating to undamaged material.

2.2 Calculus of Variations

This section introduces functionals on the basis of classical examples. The Gâteaux derivative as well as the stationarity point are considered with help of linearization. The subsequent is based on the works of Lanczos (1970), Dacorogna (1989), Simo and Hughes (2000), Gelfand and Fomin (2000), and Kielhöfer (2010) with a focus on Elsgolc (1961) and Junker (2016).

Initially, a function f relates a variable x , serving as the argument, to a value q . The expression $f(x) = q$ is consequently used. Moreover, this function $f(x)$ itself can basically constitute as an argument as well, this is realized by a functional \mathcal{F} that relates $f(x)$ to a value r , in this case the expression $\mathcal{F}[f(x)] = r$ is used.

The application of functionals can be illustrated by the classical examples of calculating the length of a curve or the size of a surface area. The length l of a curve $y(x)$ is thereby given by

$$l := \mathcal{F}[y(x)] = \int_{x_0}^{x_1} \sqrt{1 + (y'(x))^2} dx, \quad (2.19)$$

while the area A of a surface $z(x, y)$ can be determined in consideration of the boundary $\partial\Omega$ by

$$A := \mathcal{F}[z(x, y)] = \int_{\partial\Omega} \sqrt{1 + \left(\frac{\partial z}{\partial x}\right)^2 + \left(\frac{\partial z}{\partial y}\right)^2} dA. \quad (2.20)$$

In context of functions, the variations are preferably termed as the increment Δx of the argument x of a function $f(x)$ while the increment is the difference of two values $\Delta x = x - x_0$. A function $f(x)$ is thereby called continuous if small variations of the argument x lead to small variations of the function $f(x)$. Analogously in the context of functionals, the increment or preferably termed the variation δf of the argument $f(x)$ of a functional $\mathcal{F}[f(x)]$ is described by the difference of two functions $\delta f = f(x) - f_0(x)$. Thereby, the functional is called continuous if small variations of the argument $f(x)$ lead to small variations of the functional $\mathcal{F}[f(x)]$.

Continuous functions and functionals can be differentiated in order to determine extrema. At this point, the differentiation of functionals, also referred to as the calculus of variations, is regarded. For this purpose, the linear approximation as a necessary tool is first introduced for functions and then transferred to functionals. Initially, the function $f(x)$ will undergo a coordinate transformation with the new origin \bar{x} , direction δx and length ω in direction δx , thus

$$f(x) \rightarrow f(\bar{x} + \omega\delta x). \quad (2.21)$$

The related derivative around \bar{x} is given by

$$\left. \frac{d}{d\omega} f(\bar{x} + \omega\delta x) \right|_{\omega=0} = \lim_{\omega \rightarrow 0} \frac{f(\bar{x} + \omega\delta x) - f(\bar{x})}{\omega} = f'(\bar{x})\delta x =: \mathbf{D}f(\bar{x})(\delta x). \quad (2.22)$$

According to this, the derivative of $f(x)$ around \bar{x} in direction of δx is described by the operator \mathbf{D} . Finally, building on this, the linearization for $f(x)$ around \bar{x} in direction of δx is described by the operator \mathbf{L} as follows

$$\mathbf{L}f(\bar{x})(\delta x) = f(\bar{x}) + \mathbf{D}f(\bar{x})(\delta x). \quad (2.23)$$

The transformation for functionals reads

$$\mathcal{F}[f] \rightarrow \mathcal{F}[\bar{f} + \omega\delta f], \quad (2.24)$$

the related derivative, known as the Gâteaux derivative, is given by

$$\left. \frac{d}{d\omega} \mathcal{F}[\bar{f} + \omega\delta f] \right|_{\omega=0} = \lim_{\omega \rightarrow 0} \frac{\mathcal{F}[\bar{f} + \omega\delta f] - \mathcal{F}[\bar{f}]}{\omega} = \mathcal{F}'[\bar{f}]\delta f =: \mathbf{D}\mathcal{F}[\bar{f}](\delta f), \quad (2.25)$$

and the linearization of the functional is achieved by

$$\mathcal{L}\mathcal{F}[\bar{f}](\delta f) = \mathcal{F}[\bar{f}] + \mathcal{D}\mathcal{F}[\bar{f}](\delta f) . \quad (2.26)$$

Finally, extrema of functionals are determined by the stationarity condition as follows

$$\mathcal{D}\mathcal{F}[\bar{f}](\delta f) = 0 \quad \forall \delta f , \quad (2.27)$$

consequently, \bar{f} is the stationarity point of \mathcal{F} if the derivatives in all directions δf are equal to zero. In this thesis, the shorter notation for the Gâteaux derivative is used

$$\mathcal{D}\mathcal{F}[\bar{f}](\delta f) =: \delta\mathcal{F} . \quad (2.28)$$

2.3 Legendre-Fenchel Transformation

The Legendre-Fenchel transformation is introduced in this section and an illustration with the aid of a simple example is provided afterwards. Literature on the Legendre-Fenchel transformation is given by Dacorogna (1989), Šilhavý (1997), Gelfand and Fomin (2000), and Kielhöfer (2010) which are taken into account here. However, the subsequent is mainly based on the works of Lanczos (1970) and Rockafellar and Wets (1998).

The Legendre-Fenchel transformation, mentioned in the framework of dualization, transforms a function f with a set of variables x_i into a new function f^* with a new set of variables y_i , which corresponds to the partial derivatives of the original function f . In case of convex functions, a further transformation of the new function f^* results in the original function $f^{**} \equiv f$, thus both systems, f and f^* , are considered to be equivalent. This transformation is also called dual transformation. The main idea is to transform a function and particularly its variables into an equivalent function with different variables which can more easily be handled. The general formulation of the Legendre-Fenchel transformation, which is also valid for non-convex functions, as well as the partial derivative of f are given by

$$f^*(\mathbf{y}) := \sup_{\mathbf{x}} \{ \mathbf{x} \cdot \mathbf{y} - f(\mathbf{x}) \} , \quad (2.29)$$

$$\mathbf{y}(\mathbf{x}) = \frac{\partial f(\mathbf{x})}{\partial \mathbf{x}} . \quad (2.30)$$

The transformation backwards in case of convexity and the respective partial derivative read

$$f = f^{**}(\mathbf{x}) := \sup_{\mathbf{y}} \{ \mathbf{y} \cdot \mathbf{x} - f^*(\mathbf{y}) \} , \quad (2.31)$$

$$\mathbf{x}(\mathbf{y}) = \frac{\partial f(\mathbf{y})}{\partial \mathbf{y}} . \quad (2.32)$$

The application of the supremum allows to consider non-convex and non-continuous functions, as well. However, the duality gets lost due to possible identical gradients and not uniquely differentiable functions. Thus, convexity and continuity are required for duality, see Dacorogna (1989) and Šilhavý (1997).

2.4 Laws of Thermodynamics

The first law is characterized by the balance of energy given in Subsection 2.4.1 and the second law by the imbalance of entropy given in Subsection 2.4.2. Both are the foundation for Hamilton's principle allowing for a thermodynamically consistent derivation of the presented material models. The subsequent is based on works of Šilhavý (1997), Holzapfel (2000), and Demtröder (2017) and especially on Gurtin et al. (2010), Müller (2016), and Holm (2018).

2.4.1 First Law of Thermodynamics: Balance of Energy

The first law of thermodynamics deals with the balance of energy in a closed system considering the rate of the internal energy $\dot{\mathcal{E}}$ and kinetic energy $\dot{\mathcal{K}}$ as well as the mechanical \mathcal{W} and thermal power \mathcal{Q} . The global form is given by

$$\dot{\mathcal{E}} + \dot{\mathcal{K}} = \mathcal{W} + \mathcal{Q}. \quad (2.33)$$

Hereby, the internal energy \mathcal{E} corresponds to

$$\mathcal{E} = \int_{\Omega} \Psi \, dV + \int_{\Omega} \theta s \, dV, \quad (2.34)$$

including the Helmholtz free energy Ψ , the absolute temperature θ , and the specific entropy s . The volume of the considered body is denoted by Ω . Moreover, the kinetic energy \mathcal{K} reads

$$\mathcal{K} = \int_{\Omega} \frac{1}{2} \rho |\mathbf{v}|^2 \, dV, \quad (2.35)$$

taking the density ρ and the velocity \mathbf{v} into account. The mechanical power \mathcal{W} is defined as

$$\mathcal{W} = \int_{\Omega} \mathbf{f} \cdot \mathbf{v} \, dV + \int_{\partial\Omega} \mathbf{t} \cdot \mathbf{v} \, dA \quad (2.36)$$

$$= \int_{\Omega} \left(\frac{d}{dt} \frac{1}{2} \rho |\mathbf{v}|^2 + \boldsymbol{\sigma} : \dot{\boldsymbol{\varepsilon}} \right) dV, \quad (2.37)$$

with the volume forces \mathbf{f} and externally acting traction forces \mathbf{t} . Hereby, the application of Cauchy's theorem $\mathbf{t} = \boldsymbol{\sigma} \cdot \mathbf{n}$ and the balance of linear momentum $\nabla \cdot \boldsymbol{\sigma} + \mathbf{f} = \rho \dot{\mathbf{v}}$ to the first equation results in the second equation. Finally, the thermal power \mathcal{Q} is presented by

$$\mathcal{Q} = \int_{\Omega} h \, dV - \int_{\partial\Omega} \mathbf{q} \cdot \mathbf{n} \, dA \quad (2.38)$$

$$= \int_{\Omega} (h - \nabla \cdot \mathbf{q}) \, dV, \quad (2.39)$$

containing the internal heat source h and the heat flux \mathbf{q} which flows perpendicularly across the boundary $\partial\Omega$ as described by the normal vector \mathbf{n} . The second equation is obtained by applying the Gauß theorem to the first one. Altogether, the balance of energy can be assembled as follows

$$\int_{\Omega} \left(\dot{\Psi} + (\dot{\theta}s) + \frac{d}{dt} \frac{1}{2} \rho |\mathbf{v}|^2 \right) dV = \int_{\Omega} \left(\frac{d}{dt} \frac{1}{2} \rho |\mathbf{v}|^2 + \boldsymbol{\sigma} : \dot{\boldsymbol{\varepsilon}} + h - \nabla \cdot \mathbf{q} \right) dV. \quad (2.40)$$

Eliminating the identical integrals transfers the balance of energy into its local form and additionally reducing the redundant kinetic term provides

$$\dot{\Psi} + \dot{\theta}s + \theta\dot{s} = \boldsymbol{\sigma} : \dot{\boldsymbol{\epsilon}} + h - \nabla \cdot \mathbf{q} . \quad (2.41)$$

2.4.2 Second Law of Thermodynamics: Imbalance of Entropy

The second law of thermodynamics is characterized by the imbalance of entropy dealing with the direction and irreversibility of processes and follows the first law from the last Subsection 2.4.1. Hereby, entropy is defined differently in the literature, Holm (2018) for instance describes the entropy as a measure of energy amount that irreversibly transforms from a state of for mechanical work usable into unusable energy or alternatively from an ordered into less ordered state. Heating a system thereby corresponds to transforming usable into unusable energy by dissipation that is consequently accompanied by an increase of entropy. Only in case of equilibrium, the entropy can stay constant. Both the increase as well as the constant state of entropy are basically the main statements of the imbalance of entropy for irreversible processes in closed systems.

In this context the entropy is denoted as the absolute entropy production \mathcal{H} and corresponds to the following formulation

$$\mathcal{H} = \int_{\Omega} \left(\dot{s} + \nabla \cdot \frac{\mathbf{q}}{\theta} - \frac{h}{\theta} \right) dV , \quad (2.42)$$

which for the mentioned reasons exhibits non-negativity regarding closed systems, thus

$$\mathcal{H} \geq 0 . \quad (2.43)$$

The volume-weighted quantity of the absolute entropy production \mathcal{H} is the entropy production \mathcal{S} defined as

$$\mathcal{H} = \int_{\Omega} \mathcal{S} dV \quad (2.44)$$

Again, the elimination of identical integrals provides the local form of the second law of thermodynamics in Equation (2.45) and additionally applying the quotient rule transforms this formulation into the second Equation (2.46), consequently

$$\mathcal{S} = \dot{s} + \nabla \cdot \frac{\mathbf{q}}{\theta} - \frac{h}{\theta} \quad (2.45)$$

$$= \dot{s} + \frac{1}{\theta} \nabla \cdot \mathbf{q} - \frac{1}{\theta^2} \mathbf{q} \cdot \nabla \theta - \frac{h}{\theta} . \quad (2.46)$$

Naturally, the non-negativity also applies for the entropy production \mathcal{S} , thus

$$\mathcal{S} \geq 0 . \quad (2.47)$$

The local form of the first law can be solved for the internal heat source h as follows

$$h = \dot{\Psi} + \dot{\theta}s + \theta\dot{s} - \boldsymbol{\sigma} : \dot{\boldsymbol{\epsilon}} + \nabla \cdot \mathbf{q} . \quad (2.48)$$

Multiplying the local form of the second law of thermodynamics in Equation (2.46) with the absolute temperature θ provides the first subsequent equation. Taking into account h from Equation (2.48) leads to the second one

$$\theta \mathcal{S} = \theta \dot{s} + \nabla \cdot \mathbf{q} - \frac{1}{\theta} \mathbf{q} \cdot \nabla \theta - h \quad (2.49)$$

$$= \theta \dot{s} + \nabla \cdot \mathbf{q} - \frac{1}{\theta} \mathbf{q} \cdot \nabla \theta - \dot{\Psi} - \dot{\theta} s - \theta \dot{s} + \boldsymbol{\sigma} : \dot{\boldsymbol{\varepsilon}} - \nabla \cdot \mathbf{q} . \quad (2.50)$$

After some simplifications the reduced form of the second law of thermodynamics is resulting

$$\theta \mathcal{S} = -\dot{\Psi} - \frac{1}{\theta} \mathbf{q} \cdot \nabla \theta - \dot{\theta} s + \boldsymbol{\sigma} : \dot{\boldsymbol{\varepsilon}} \geq 0 , \quad (2.51)$$

which contains the dissipation $\theta \mathcal{S}$ on the left-hand side and the Clausius-Duhem inequality on the right-hand side.

2.5 Free Energy and Constitutive Equations

This section basically results from the laws of thermodynamics presented in the previous Section 2.4 and introduces constitutive equations on the basis of the Clausius-Duhem inequality (Equation 2.51), by means of the Coleman-Noll procedure (see Coleman and Noll (1963) and Coleman and Gurtin (1967)) and by considering the Helmholtz free energy. These constitutive equations are the foundation for the Hamilton's principle in Section 2.6. The subsequent is based on works from Šilhavý (1997), Holzapfel (2000), Gurtin et al. (2010), and Holm (2018).

The subsequent general formulation of the constitutive equations connects the process quantities that include the strain $\boldsymbol{\varepsilon}$, the temperature θ , the gradient of temperature $\nabla \theta$, and the internal variable λ (assumed to be scalar in line with most of the used material models in this thesis and also typical for the applied isotropic considerations) with the response or constitutive functions that includes the Helmholtz free energy Ψ , stress $\boldsymbol{\sigma}$, entropy s , and heat flux \mathbf{q} . Therefore

$$\begin{aligned} \Psi &= \Psi(\boldsymbol{\varepsilon}, \theta, \nabla \theta, \lambda) , & \boldsymbol{\sigma} &= \boldsymbol{\sigma}(\boldsymbol{\varepsilon}, \theta, \nabla \theta, \lambda) , \\ s &= s(\boldsymbol{\varepsilon}, \theta, \nabla \theta, \lambda) , & \mathbf{q} &= \mathbf{q}(\boldsymbol{\varepsilon}, \theta, \nabla \theta, \lambda) . \end{aligned} \quad (2.52)$$

Hereby, the underlying Helmholtz free energy Ψ is in a general form and can be customized in order to describe a desired material behavior. The corresponding rate of the general Helmholtz free energy is achieved by applying the chain rule as follows

$$\dot{\Psi} = \frac{\partial \Psi}{\partial \boldsymbol{\varepsilon}} : \dot{\boldsymbol{\varepsilon}} + \frac{\partial \Psi}{\partial \theta} \dot{\theta} + \frac{\partial \Psi}{\partial (\nabla \theta)} \cdot (\dot{\nabla} \theta) + \frac{\partial \Psi}{\partial \lambda} \dot{\lambda} . \quad (2.53)$$

The first subsequent equation can be derived by inserting $\dot{\Psi}$ into the Clausius-Duhem inequality in Equation 2.51. Rearranging then provides the second one

$$\theta \mathcal{S} = -\frac{\partial \Psi}{\partial \boldsymbol{\varepsilon}} : \dot{\boldsymbol{\varepsilon}} - \frac{\partial \Psi}{\partial \theta} \dot{\theta} - \frac{\partial \Psi}{\partial (\nabla \theta)} \cdot (\dot{\nabla} \theta) - \frac{\partial \Psi}{\partial \lambda} \dot{\lambda} - \frac{1}{\theta} \mathbf{q} \cdot \nabla \theta - \dot{\theta} s + \boldsymbol{\sigma} : \dot{\boldsymbol{\varepsilon}} \quad (2.54)$$

$$= \left(\boldsymbol{\sigma} - \frac{\partial \Psi}{\partial \boldsymbol{\varepsilon}} \right) : \dot{\boldsymbol{\varepsilon}} - \left(s + \frac{\partial \Psi}{\partial \theta} \right) \dot{\theta} - \frac{\partial \Psi}{\partial (\nabla \theta)} \cdot (\dot{\nabla} \theta) - \frac{\partial \Psi}{\partial \lambda} \dot{\lambda} - \frac{1}{\theta} \mathbf{q} \cdot \nabla \theta \geq 0 . \quad (2.55)$$

At this point, the Coleman-Noll procedure (Coleman and Noll (1963) and Coleman and Gurtin (1967)) allows an interpretation of the second Equation (2.55) by considering all terms separately resulting in the wanted constitutive equations.

Equation (2.55) has to be valid for all materials or processes and therefore for all extreme cases. Initially, a pure elastic deformation without any internal variables under constant temperature in time and homogenous temperature in space is assumed, which consequently only results in a change of strains ε . This allows to calculate the stresses σ in accordance with

$$\sigma - \frac{\partial \Psi}{\partial \varepsilon} = \mathbf{0} \quad (2.56)$$

$$\Leftrightarrow \sigma = \frac{\partial \Psi}{\partial \varepsilon} . \quad (2.57)$$

Afterwards, a pure cooling or heating without any internal variables under constant strain and homogenous temperature in space is assumed, which thus only results in a change of temperature θ in time. Herewith, the entropy s is given by

$$s + \frac{\partial \Psi}{\partial \theta} = 0 \quad (2.58)$$

$$\Leftrightarrow s = -\frac{\partial \Psi}{\partial \theta} . \quad (2.59)$$

As for example mentioned in the works of Bargmann and Steinmann (2005) or Gurtin et al. (2010), the Helmholtz free energy Ψ as well as the temperature θ are independent from the gradient of the temperature $\nabla \theta$, therefore

$$\frac{\partial \Psi}{\partial (\nabla \theta)} = \mathbf{0} \quad (2.60)$$

$$\Rightarrow \Psi = \Psi(\varepsilon, \theta, \lambda) . \quad (2.61)$$

Now, analogously to the stresses and entropy, the term including the internal variable λ can be considered separately as well. The subsequent expression allows to define the thermodynamic driving force p that also provides information about the evolution direction of the internal variable. The following applies

$$-\frac{\partial \Psi}{\partial \lambda} \dot{\lambda} \geq 0 \quad (2.62)$$

$$\Rightarrow -\frac{\partial \Psi}{\partial \lambda} =: p . \quad (2.63)$$

The aforementioned case regarding the internal variable can be assigned to mechanical dissipation whereas the following to thermal dissipation, respectively. Hereby, the heat flux \mathbf{q} causes an opposite directed temperature gradient $\nabla \theta$ in order to fulfill the heat conduction inequality in line with works of Holzapfel (2000), Gurtin et al. (2010), or Demtröder (2017) for example.

$$-\frac{1}{\theta} \mathbf{q} \cdot \nabla \theta \geq 0 \quad (2.64)$$

$$\Rightarrow \mathbf{q} \sim -\nabla \theta . \quad (2.65)$$

With the derived relations of the constitutive equations necessary foundations for the Hamilton's principle in Section 2.6 have been achieved.

2.6 Hamilton's Principle

Continuous materials with conservative and non-conservative behavior are considered in Section 2.6.1 and 2.6.2. The Gibbs energy for non-conservative materials includes a general and a special case. The general case in Section 2.6.3 is addressed to materials including a gradient of the internal variable. The special case in Section 2.6.4 does not include this gradient and results in the well-known principle of the minimum of the dissipation potential (PMDP). The subsequent is mainly based on the work of Junker (2016). Additionally, the derivation of the Hamilton's principle is based on and inspired by works of Hamilton (1834), Hamilton (1835), and Bedford (1985) while Bailey (2002) presented a different view on this topic. The PMDP originates from works of Onsager (1931), Ortiz and Repetto (1999), Ortiz and Stainier (1999), Carstensen et al. (2001), and Hackl and Fischer (2008) and for non-isothermal processes from work of Hackl et al. (2011) and Junker et al. (2014).

2.6.1 Conservative Materials

Continuous materials are assumed and therefore the Gibbs energy can be formulated by considering the internal and external potential, Π_{int} and Π_{ext} , according to

$$\mathcal{G} := \Pi_{\text{int}} + \Pi_{\text{ext}} . \quad (2.66)$$

Π_{int} includes the Helmholtz free energy Ψ based on the strains $\boldsymbol{\varepsilon}$ and an internal variable λ , thus

$$\Pi_{\text{int}} := \int_{\Omega} \Psi(\boldsymbol{\varepsilon}, \lambda) \, dV , \quad (2.67)$$

and Π_{ext} considers the volume forces \mathbf{f} and the tractions \mathbf{t} as follows

$$\Pi_{\text{ext}} := - \int_{\Omega} \mathbf{f} \cdot \mathbf{u} \, dV - \int_{\partial\Omega} \mathbf{t} \cdot \mathbf{u} \, dA . \quad (2.68)$$

The Gibbs energy can then be composed to

$$\mathcal{G} := \int_{\Omega} \Psi(\boldsymbol{\varepsilon}, \lambda) \, dV - \int_{\Omega} \mathbf{f} \cdot \mathbf{u} \, dV - \int_{\partial\Omega} \mathbf{t} \cdot \mathbf{u} \, dA . \quad (2.69)$$

Initially, conservative materials are considered that naturally do not take into account dissipative processes and consequently only involve the kinetic energy that is defined by

$$\mathcal{K} := \int_{\Omega} \frac{1}{2} \rho |\dot{\mathbf{u}}|^2 \, dV . \quad (2.70)$$

Thus, the Hamilton's principle for continuous and conservative materials reads

$$\int_{t_0}^{t_1} (\delta\mathcal{K} - \delta\mathcal{G}) \, dt = 0 , \quad (2.71)$$

the static case simplifies the Hamilton's principle by neglecting the kinetic energy, hence

$$\delta\mathcal{G} = 0 . \quad (2.72)$$

2.6.2 Non-Conservative Materials

In contrast to conservative materials, non-conservative materials take into account dissipative processes. The dissipative character of microstructural evolution can be taken into account by means of a so-called dissipative force \hat{p} (not equal to driving force p), which is assumed to be derivable from a dissipation potential \mathcal{D} as

$$\hat{p} := - \frac{\partial \mathcal{D}}{\partial \dot{\lambda}} . \quad (2.73)$$

At this point the aforementioned dissipation function \mathcal{D} is introduced in more detail. It describes the amount of energy that is converted from elastic or kinetic to dissipative energy. This process is irreversible and is characterized by the production of heat. Several approaches for the dissipation function are generally possible, the most common ones are presented subsequently.

A standard approach for rate-independent material models of elastoplastic-type is

$$\mathcal{D} := r_1 |\dot{\lambda}| , \quad (2.74)$$

with the dissipation parameter r_1 serving as an energetic threshold. Rate-dependent material models of viscoelastic-type can be described by

$$\mathcal{D} := \frac{r_2}{2} \dot{\lambda}^2 , \quad (2.75)$$

whereby the parameter r_2 describes the viscosity of the material. Both approaches can be merged to an elasto-viscoplastic-type as follows

$$\mathcal{D} := r_1 |\dot{\lambda}| + \frac{r_2}{2} \dot{\lambda}^2 . \quad (2.76)$$

Finally, the Hamilton's principle for continuous and non-conservative materials is defined by

$$\int_{t_0}^{t_1} (\delta \mathcal{K} - \delta \mathcal{G} + \delta \mathcal{V}) dt = 0 . \quad (2.77)$$

Analogously to Equation (2.71), the kinetic energy is neglected again and an additional term related to the dissipative work is considered. This results in a simplified Hamilton's principle as

$$\delta \mathcal{G} - \delta \mathcal{V} = 0 . \quad (2.78)$$

Thereby, $\delta \mathcal{V}$ is referred to as virtual work of the dissipative forces \mathcal{V} and is given by

$$\delta \mathcal{V} = \int_{\Omega} \hat{p} \delta \lambda dV . \quad (2.79)$$

Altogether, Hamilton's principle for continuous and non-conservative material under static conditions is provided by

$$\delta \mathcal{G} + \int_{\Omega} \frac{\partial \mathcal{D}}{\partial \dot{\lambda}} \delta \lambda dV = 0 . \quad (2.80)$$

Depending on the Gibbs energy, different cases are available that are presented hereinafter.

2.6.3 General Usage of Hamilton's Principle

The most general case of the Hamilton's principle assumes a Gibbs energy that is depending on the displacement field \mathbf{u} (and strains $\boldsymbol{\varepsilon}$), the internal variable λ , and its gradient $\nabla\lambda$, thus

$$\mathcal{G} = \mathcal{G}(\mathbf{u}, \lambda, \nabla\lambda) . \quad (2.81)$$

As a result, the Hamilton's principle becomes

$$\delta\mathcal{G} + \int_{\Omega} \frac{\partial\mathcal{D}}{\partial\dot{\lambda}} \delta\lambda \, dV = \delta_{\mathbf{u}}\mathcal{G} + \delta_{\lambda}\mathcal{G} + \int_{\Omega} \frac{\partial\mathcal{D}}{\partial\dot{\lambda}} \delta\lambda \, dV = 0 \quad \forall \delta\mathbf{u}, \delta\lambda , \quad (2.82)$$

whereat the displacement field \mathbf{u} and the internal variable λ are considered separately by $\delta_{\mathbf{u}}\mathcal{G}$ and $\delta_{\lambda}\mathcal{G}$ yielding the two independent stationarity conditions

$$\int_{\Omega} \frac{\partial\Psi}{\partial\boldsymbol{\varepsilon}} : \delta\boldsymbol{\varepsilon} \, dV - \int_{\Omega} \mathbf{f} \cdot \delta\mathbf{u} \, dV - \int_{\partial\Omega} \mathbf{t} \cdot \delta\mathbf{u} \, dA = 0 \quad \forall \delta\mathbf{u} , \quad (2.83)$$

$$\int_{\Omega} \frac{\partial\Psi}{\partial\lambda} \delta\lambda \, dV + \int_{\Omega} \frac{\partial\Psi}{\partial\nabla\lambda} \cdot \delta\nabla\lambda \, dV + \int_{\Omega} \frac{\partial\mathcal{D}}{\partial\dot{\lambda}} \delta\lambda \, dV = 0 \quad \forall \delta\lambda . \quad (2.84)$$

Integration by parts of the first stationarity condition regarding the displacement field \mathbf{u} and with $\boldsymbol{\sigma} = \partial\Psi/\partial\boldsymbol{\varepsilon}$ according to Equation (2.56) provides

$$\nabla \cdot \boldsymbol{\sigma} + \mathbf{f} = \mathbf{0} \quad \forall \mathbf{x} \in \Omega , \quad (2.85)$$

$$\boldsymbol{\sigma} \cdot \mathbf{n} = \mathbf{t} \quad \forall \mathbf{x} \in \partial\Omega , \quad (2.86)$$

whereby the first equation is assigned to Cauchy's equation of equilibrium and the second one to Cauchy's theorem, see works of Altenbach and Altenbach (1994), Holzapfel (2000), and Willner (2003) for instance. Moreover, integration by parts of the second stationarity condition with respect to the internal variable λ in Equation (2.84) provides

$$\frac{\partial\Psi}{\partial\lambda} - \nabla \cdot \left(\frac{\partial\Psi}{\partial\nabla\lambda} \right) + \frac{\partial\mathcal{D}}{\partial\dot{\lambda}} = 0 \quad \forall \mathbf{x} \in \Omega , \quad (2.87)$$

$$\left(\frac{\partial\Psi}{\partial\nabla\lambda} \right) \cdot \mathbf{n} = 0 \quad \forall \mathbf{x} \in \partial\Omega , \quad (2.88)$$

at which the first equation is referred to as the Helmholtz equation and the second one is the Neumann boundary condition, see for example works of Achenbach (1975), Schäfer (1999), and Riley et al. (2006). Application of this general case is presented for damage modeling by Junker et al. (2018) or for topology optimization by Junker and Hackl (2016), for instance.

2.6.4 Principle of the Minimum of the Dissipation Potential

The principle of the minimum of the dissipation potential (PMDP) assumes a Gibbs energy that is no longer depending on the gradient of the internal variable $\nabla\lambda$. Only the displacement field \mathbf{u} (and consequently on the strains $\boldsymbol{\varepsilon}$ again) and the internal variable λ are considered, thus

$$\mathcal{G} = \mathcal{G}(\mathbf{u}, \lambda) . \quad (2.89)$$

The two independent stationarity conditions of Hamilton's principle simplify to

$$\int_{\Omega} \frac{\partial \Psi}{\partial \boldsymbol{\varepsilon}} : \delta \boldsymbol{\varepsilon} \, dV - \int_{\Omega} \mathbf{f} \cdot \delta \mathbf{u} \, dV - \int_{\partial \Omega} \mathbf{t} \cdot \delta \mathbf{u} \, dA = 0 \quad \forall \delta \mathbf{u}, \quad (2.90)$$

$$\int_{\Omega} \frac{\partial \Psi}{\partial \lambda} \delta \lambda \, dV + \int_{\Omega} \frac{\partial \mathcal{D}}{\partial \dot{\lambda}} \delta \dot{\lambda} \, dV = 0 \quad \forall \delta \lambda, \quad (2.91)$$

Integration by parts provides the strong form of the balance of linear momentum (see Equations (2.85) and (2.86)), but the second stationarity condition can be transformed into the following simple expression

$$\frac{\partial \Psi}{\partial \lambda} + \frac{\partial \mathcal{D}}{\partial \dot{\lambda}} = 0, \quad (2.92)$$

which is known as Biot's equation, see work of Biot (1962). Integration then with respect to the rate of the internal variable $\dot{\lambda}$ provides

$$\frac{\partial \Psi}{\partial \lambda} \dot{\lambda} + \mathcal{D} + \mathcal{A} \rightarrow \min_{\dot{\lambda}}, \quad (2.93)$$

which has to be minimized with respect to $\dot{\lambda}$ and involves an integration constant \mathcal{A} that is arbitrary and can be defined as

$$\mathcal{A} := \frac{\partial \Psi}{\partial \boldsymbol{\varepsilon}} : \dot{\boldsymbol{\varepsilon}}. \quad (2.94)$$

Finally, the Lagrangian can be formulated by

$$\mathcal{L} := \dot{\Psi} + \mathcal{D} \rightarrow \min_{\dot{\lambda}}, \quad (2.95)$$

where the first term $\dot{\Psi}$ collects the derivatives of Ψ with respect to both included quantities: the stresses $\boldsymbol{\varepsilon}$ and the internal variable λ . This Lagrangian actually represents the PMDP. It is a mathematical potential that allows to consider constraints by appropriate penalty terms.

The PMDP as a special case of Hamilton's principle for continuous and non-conservative materials underlying a restricted Gibbs energy without consideration of gradients of the internal variable is now been derived as well. It is also firmly established in the literature for example in the area of damage modeling represented by works of Dimitrijevic and Hackl (2008) and Schwarz et al. (2018b), but also in other research areas like for instance topology optimization in the work of Junker and Hackl (2015) or the modeling of shape memory alloys that is extensively presented by investigations of Waimann (2018).

A similar approach is the principle of the maximum dissipation that can be found in works of Hackl and Fischer (2008), Hackl et al. (2011), and Junker (2011) for example.

2.7 Numerical Treatment of Evolution Equations

The numerical treatment of evolution equations is presented in this section taking up the evolution equations from the previous Section 2.6 and preparing their numerical application. Therefore, the works of Schäfer (1999) and Simo and Hughes (2000) served as a basis.

In general, the material behavior with respect to an internal variable λ depends on the applied dissipation function which are introduced in Subsection 2.6.2. Thereby, the rate-independent (“RI”) material behavior is related to a dissipation function of elastoplastic-type given by $\mathcal{D}_{\text{RI}} := r_1 |\dot{\lambda}|$ in Equation (2.74). In return, the rate-dependent (“RD”) material behavior is related to a dissipation function of elasto-viscoplastic-type given by $\mathcal{D}_{\text{RD}} := r_1 |\dot{\lambda}| + \frac{r_2}{2} \dot{\lambda}^2$ in Equation (2.76). Provided that r_1 is the dissipation parameter and r_2 the viscosity parameter.

Application of Hamilton’s principle from Subsection 2.6.3 or of the PMDP from Subsection 2.6.4 provides the evolution equation for the internal variable λ . In accordance with the underlying material behavior, the evolution equation has the following form

$$\dot{\lambda}_{\text{RI}} = \frac{|\dot{\lambda}|}{r_1} p_{\text{RI}} = \Delta \rho p_{\text{RI}}, \quad (2.96)$$

$$\dot{\lambda}_{\text{RD}} = \frac{1}{r_2} [|p_{\text{RD}}| - r_1]_+, \quad (2.97)$$

where $|\dot{\lambda}|/r_1$ can be identified as the consistency parameter $\Delta \rho \geq 0$, p is the driving force of the internal variable λ and $[x]_+ := (x + |x|)/2$ only permits positive values. In the rate-independent case, the mentioned consistency parameter $\Delta \rho$ has to be determined. Hereto, the Legendre transformation according to Section 2.3 is performed as follows

$$\mathcal{D}_{\text{RI}}^* = \sup_{\dot{\lambda}} \{ p_{\text{RI}} \dot{\lambda} - \mathcal{D}_{\text{RI}} \} = \sup_{\dot{\lambda}} \{ |\dot{\lambda}| (p_{\text{RI}} \operatorname{sgn} \dot{\lambda} - r_1) \} = \sup_{\dot{\lambda}} \left\{ \frac{|\dot{\lambda}|}{r_1} (p_{\text{RI}}^2 - r_1^2) \right\}. \quad (2.98)$$

Consequently, a yield function Φ is obtained by

$$\Phi := p_{\text{RI}}^2 - r_1^2 \leq 0, \quad (2.99)$$

which carries the same information as

$$\Phi := |p_{\text{RI}}| - r_1 \leq 0. \quad (2.100)$$

Finally, the consistency parameter $\Delta \rho$ can be computed from the condition $\Phi = 0$. Thus, the Karush-Kuhn-Tucker conditions read

$$\Delta \rho \geq 0, \quad \Phi \leq 0, \quad \Delta \rho \Phi = 0. \quad (2.101)$$

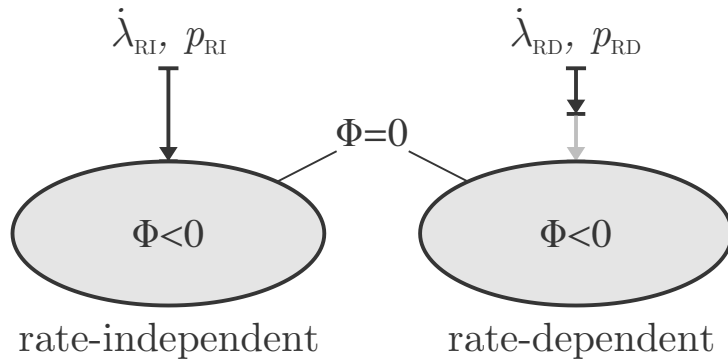


Figure 2.1: Schematic illustration of the rate-independent and rate-dependent (left/right) evolution of the internal variable λ with respect to the yield function Φ . Image inspired by Simo and Hughes (2000).

Both, the rate-independent and rate-dependent evolution of the internal variable λ , are presented in Figure 2.1. This evolution is defined by the direction and amount. The direction is always given by the respective driving force p whereas the amount depends on the respective formulation. In the rate-independent case, the determination of the consistency parameter $\Delta\rho$ leads to an amount of evolution which exactly fulfills the yield function Φ . In turn, the rate-dependent evolution of λ is limited by the viscosity parameter r_2 and by the subsequently introduced time increment Δt . Therefore, the damage variable evolves in a direction normal to the yield surface. However, in the viscous case no microstructural state granting $\Phi = 0$ is (necessarily) reached. For the evolution equations different time discretizations are used in this thesis: the explicit method, the implicit method and, in some cases, different time discretizations are applied to the strains and internal variable resulting in an operator split.

The explicit time discretization, also referred to as forward Euler method, is related to the previous time step m by means of $\lambda^{m+1} = \lambda^{m+1}(\boldsymbol{\varepsilon}^m, \lambda^m)$, thus

$$\lambda_{\text{RI}}^{m+1} = \lambda^m + \begin{cases} \Delta\rho p_{\text{RI}}(\boldsymbol{\varepsilon}^m, \lambda^m) & \text{for } |p_{\text{RI}}| > r_1 \\ 0 & \text{else} \end{cases}, \quad (2.102)$$

$$\lambda_{\text{RD}}^{m+1} = \lambda^m + \begin{cases} \frac{\Delta t}{r_2} (|p_{\text{RD}}(\boldsymbol{\varepsilon}^m, \lambda^m)| - r_1) & \text{for } |p_{\text{RD}}| > r_1 \\ 0 & \text{else} \end{cases}. \quad (2.103)$$

The implicit time discretization, also referred to as backward Euler method, is related to the current time step $m + 1$ by means of $\lambda^{m+1} = \lambda^{m+1}(\boldsymbol{\varepsilon}^{m+1}, \lambda^{m+1})$, thus

$$\lambda_{\text{RI}}^{m+1} = \lambda^m + \begin{cases} \Delta\rho p_{\text{RI}}(\boldsymbol{\varepsilon}^{m+1}, \lambda^{m+1}) & \text{for } |p_{\text{RI}}| > r_1 \\ 0 & \text{else} \end{cases}, \quad (2.104)$$

$$\lambda_{\text{RD}}^{m+1} = \lambda^m + \begin{cases} \frac{\Delta t}{r_2} (|p_{\text{RD}}(\boldsymbol{\varepsilon}^{m+1}, \lambda^{m+1})| - r_1) & \text{for } |p_{\text{RD}}| > r_1 \\ 0 & \text{else} \end{cases}. \quad (2.105)$$

The combined time discretization applies different methods to the strains and internal variable resulting in an operator split. The strains from the previous time step m can be combined with the internal variable of the current time step $m + 1$ by means of $\lambda^{m+1} = \lambda^{m+1}(\boldsymbol{\varepsilon}^m, \lambda^{m+1})$, thus

$$\lambda_{\text{RI}}^{m+1} = \lambda^m + \begin{cases} \Delta\rho p_{\text{RI}}(\boldsymbol{\varepsilon}^m, \lambda^{m+1}) & \text{for } |p_{\text{RI}}| > r_1 \\ 0 & \text{else} \end{cases}, \quad (2.106)$$

$$\lambda_{\text{RD}}^{m+1} = \lambda^m + \begin{cases} \frac{\Delta t}{r_2} (|p_{\text{RD}}(\boldsymbol{\varepsilon}^m, \lambda^{m+1})| - r_1) & \text{for } |p_{\text{RD}}| > r_1 \\ 0 & \text{else} \end{cases}. \quad (2.107)$$

Otherwise, the internal variable from the previous time step m can be combined with the strains of the current time step $m + 1$ by means of $\lambda^{m+1} = \lambda^{m+1}(\boldsymbol{\varepsilon}^{m+1}, \lambda^m)$, thus

$$\lambda_{\text{RI}}^{m+1} = \lambda^m + \begin{cases} \Delta\rho p_{\text{RI}}(\boldsymbol{\varepsilon}^{m+1}, \lambda^m) & \text{for } |p_{\text{RI}}| > r_1 \\ 0 & \text{else} \end{cases}, \quad (2.108)$$

$$\lambda_{\text{RD}}^{m+1} = \lambda^m + \begin{cases} \frac{\Delta t}{r_2} (|p_{\text{RD}}(\boldsymbol{\varepsilon}^{m+1}, \lambda^m)| - r_1) & \text{for } |p_{\text{RD}}| > r_1 \\ 0 & \text{else} \end{cases}. \quad (2.109)$$

2.8 Finite Element Method

The finite element method is introduced in this section. The discretization is given in Subsection 2.8.1 and the shape functions and interpolation in Subsection 2.8.2. Then the operator matrix and strains are presented in Subsection 2.8.3. In Subsection 2.8.4 the Gauß quadrature is introduced and finally the formulation and treatment of the residual is given in Subsection 2.8.5. The following is mainly based on the works of Schäfer (1999), Zienkiewicz et al. (2005), Fish and Belytschko (2007), and Taylor (2017a) but also on Wriggers (2001), Bathe (2002), Zienkiewicz and Taylor (2005), Hermann (2011), and Taylor (2017b).

2.8.1 Discretization

The basic concept of the finite element method is the discretization transforming continuous problems with infinite computing effort into discrete and resolvable problems, see Zienkiewicz et al. (2005). For an accurate solution, the number of discrete elements can be high. The starting point for the discretization is the division of the considered body with the total volume Ω into a finite number N_e of the already mentioned elements with the volume Ω_e , thus

$$\Omega = \sum_{e=1}^{N_e} \Omega_e, \quad (2.110)$$

whereby these elements are also referred to as finite elements. This discretization can then be transferred to the integrals of variational equations in accordance with

$$\int_{\Omega} (\cdot) dV = \sum_{e=1}^{N_e} \int_{\Omega_e} (\cdot) dV. \quad (2.111)$$

A similar procedure can also be applied to the boundaries of the considered body. The mentioned elements are built up by a specific number N_n of nodes n (eight for cubic-like or so-called hexahedral elements), whereby these nodes are described by physical coordinates \boldsymbol{x} denoted as

$$\boldsymbol{x} = (x_1 \quad x_2 \quad x_3)^T. \quad (2.112)$$

2.8.2 Shape Functions and Interpolation

The discretization of the body usually does not provide regular cubes of equal length due to the given boundary value problem, thus the elements are differently and arbitrarily shaped hexahedrons. For that reason, the coordinates as well as the displacements are consistently mapped to a reference element with cubical shape, which represents the simplest case and allows for a straightforward application of the Gauß quadrature introduced later in Subsection 2.8.4. The nodes of the reference element are described by so-called natural coordinates $\boldsymbol{\xi}$ denoted as

$$\boldsymbol{\xi} = (\xi_1 \quad \xi_2 \quad \xi_3)^T. \quad (2.113)$$

Both an arbitrarily shaped element related to the physical coordinates as well as the mentioned reference element related to the natural coordinates are illustrated by Figure 2.2.

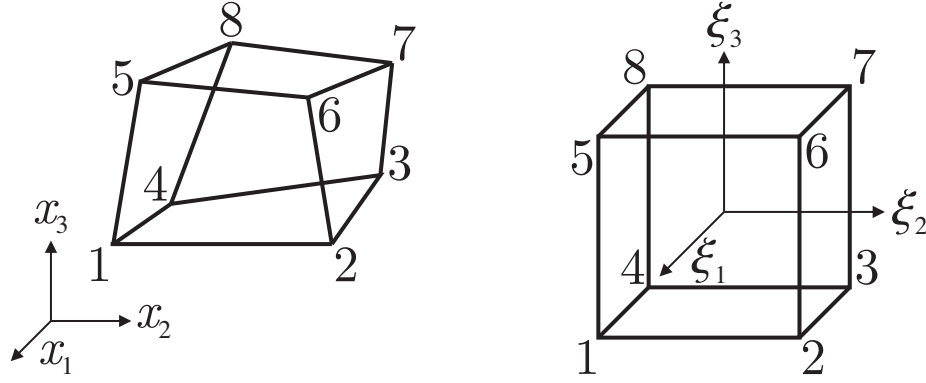


Figure 2.2: Arbitrary/reference element in physical/natural coordinates (left/right).

Hereby, the mapping from the physical coordinate system to the natural one requires an interpolation that is introduced by the shape functions N . These shape functions are identically applied to the nodal coordinates \hat{x} as well as to the nodal displacements \hat{u} , both related to the corner points of the physical coordinate system, in accordance with the isoparametric concept and furthermore the same shape functions are also applied to the variation of the nodal displacements $\delta\hat{u}$ according to the Galerkin (or Bubnov-Galerkin) method. The following applies

$$\mathbf{x} = \mathbf{N} \cdot \hat{\mathbf{x}}, \quad \mathbf{u} = \mathbf{N} \cdot \hat{\mathbf{u}}, \quad \delta\mathbf{u} = \mathbf{N} \cdot \delta\hat{\mathbf{u}}. \quad (2.114)$$

As mentioned before, the elements in the physical coordinate system have different and arbitrary shapes, therefore the applied trilinear shape functions for hexahedral elements are only related to the consistent natural coordinate system by means of

$$N^I(\boldsymbol{\xi}) = \frac{1}{8}(1 + \xi_1^I \xi_1)(1 + \xi_2^I \xi_2)(1 + \xi_3^I \xi_3), \quad (2.115)$$

provided that $\boldsymbol{\xi}^I = (\xi_1^I \ \xi_2^I \ \xi_3^I)^T$ with $\xi_j^I \in \{-1, 1\}$ are the nodal coordinates (corner points) of the natural coordinate system with $I \in \{1, 2, 3, 4, 5, 6, 7, 8\}$ resulting in eight shape functions N^I . It is also provided that the origin of the natural coordinate system is located in the center of the cube and that the edges of the cube have a length of two. The eight shape functions originating from Equation (2.115) are then assembled to a matrix, accordingly

$$\mathbf{N} = \mathbf{N}(\boldsymbol{\xi}) = \begin{pmatrix} N^1(\boldsymbol{\xi}) & 0 & 0 & N^2(\boldsymbol{\xi}) & 0 & 0 & \dots & N^8(\boldsymbol{\xi}) & 0 & 0 \\ 0 & N^1(\boldsymbol{\xi}) & 0 & 0 & N^2(\boldsymbol{\xi}) & 0 & \dots & 0 & N^8(\boldsymbol{\xi}) & 0 \\ 0 & 0 & N^1(\boldsymbol{\xi}) & 0 & 0 & N^2(\boldsymbol{\xi}) & \dots & 0 & 0 & N^8(\boldsymbol{\xi}) \end{pmatrix}, \quad (2.116)$$

whereas the nodal coordinates $\hat{\mathbf{x}}$ and nodal displacements $\hat{\mathbf{u}}$ of the physical coordinate system are related to a specific element e and assembled to the vectors

$$\hat{\mathbf{x}} = \hat{\mathbf{x}}_e = (\hat{x}_1^1 \ \hat{x}_2^1 \ \hat{x}_3^1 \ \hat{x}_1^2 \ \hat{x}_2^2 \ \hat{x}_3^2 \ \dots \ \hat{x}_1^8 \ \hat{x}_2^8 \ \hat{x}_3^8)^T, \quad (2.117)$$

$$\hat{\mathbf{u}} = \hat{\mathbf{u}}_e = (\hat{u}_1^1 \ \hat{u}_2^1 \ \hat{u}_3^1 \ \hat{u}_1^2 \ \hat{u}_2^2 \ \hat{u}_3^2 \ \dots \ \hat{u}_1^8 \ \hat{u}_2^8 \ \hat{u}_3^8)^T, \quad (2.118)$$

so that the interpolated coordinates \mathbf{x} and displacements \mathbf{u} are depending on the natural coordinate system according to $\mathbf{x} = \mathbf{x}(\boldsymbol{\xi})$ and $\mathbf{u} = \mathbf{u}(\boldsymbol{\xi})$ respectively. The transfer between the physical and natural systems is enabled by the Jacobian matrix \mathbf{J} introduced hereinafter.

2.8.3 Operator Matrix and Strains

The strain ε is determined under the assumption of small deformations by

$$\varepsilon = \frac{1}{2} (\nabla \mathbf{u} + \mathbf{u} \nabla) . \quad (2.119)$$

This strain-displacement relation can also be formulated by the strain operator matrix $\tilde{\mathbf{B}}$ containing the corresponding derivatives under consideration of the Voigt notation, therefore

$$\tilde{\varepsilon} = \tilde{\mathbf{B}} \cdot \mathbf{u} , \quad (2.120)$$

with

$$\tilde{\mathbf{B}} = \begin{pmatrix} \frac{\partial}{\partial x_1} & 0 & 0 \\ 0 & \frac{\partial}{\partial x_2} & 0 \\ 0 & 0 & \frac{\partial}{\partial x_3} \\ 0 & \frac{\partial}{\partial x_3} & \frac{\partial}{\partial x_2} \\ \frac{\partial}{\partial x_3} & 0 & \frac{\partial}{\partial x_1} \\ \frac{\partial}{\partial x_2} & \frac{\partial}{\partial x_1} & 0 \end{pmatrix} . \quad (2.121)$$

Taking into account the shape functions from Equation (2.114) allows to substitute as follows

$$\tilde{\varepsilon} = \tilde{\mathbf{B}} \cdot \mathbf{N} \cdot \hat{\mathbf{u}} = \mathbf{B} \cdot \hat{\mathbf{u}} , \quad (2.122)$$

corresponding to a derivative of the natural coordinates ξ in \mathbf{N} with respect to the physical coordinates x in $\tilde{\mathbf{B}}$. This derivative is denoted by the operator matrix $\mathbf{B} = \tilde{\mathbf{B}} \cdot \mathbf{N}$. The components of \mathbf{B} can be determined by considering $\partial \mathbf{N}(\xi) / \partial x$ using the chain rule, thus

$$\frac{\partial \mathbf{N}(\xi)}{\partial x_1} = \frac{\partial \mathbf{N}(\xi)}{\partial \xi_1} \frac{\partial \xi_1}{\partial x_1} + \frac{\partial \mathbf{N}(\xi)}{\partial \xi_2} \frac{\partial \xi_2}{\partial x_1} + \frac{\partial \mathbf{N}(\xi)}{\partial \xi_3} \frac{\partial \xi_3}{\partial x_1} , \quad (2.123)$$

$$\frac{\partial \mathbf{N}(\xi)}{\partial x_2} = \frac{\partial \mathbf{N}(\xi)}{\partial \xi_1} \frac{\partial \xi_1}{\partial x_2} + \frac{\partial \mathbf{N}(\xi)}{\partial \xi_2} \frac{\partial \xi_2}{\partial x_2} + \frac{\partial \mathbf{N}(\xi)}{\partial \xi_3} \frac{\partial \xi_3}{\partial x_2} , \quad (2.124)$$

$$\frac{\partial \mathbf{N}(\xi)}{\partial x_3} = \frac{\partial \mathbf{N}(\xi)}{\partial \xi_1} \frac{\partial \xi_1}{\partial x_3} + \frac{\partial \mathbf{N}(\xi)}{\partial \xi_2} \frac{\partial \xi_2}{\partial x_3} + \frac{\partial \mathbf{N}(\xi)}{\partial \xi_3} \frac{\partial \xi_3}{\partial x_3} . \quad (2.125)$$

This set of equations can be reformulated as follows

$$\begin{pmatrix} \frac{\partial \mathbf{N}(\xi)}{\partial x_1} \\ \frac{\partial \mathbf{N}(\xi)}{\partial x_2} \\ \frac{\partial \mathbf{N}(\xi)}{\partial x_3} \end{pmatrix} = \begin{pmatrix} \frac{\partial \xi_1}{\partial x_1} & \frac{\partial \xi_2}{\partial x_1} & \frac{\partial \xi_3}{\partial x_1} \\ \frac{\partial \xi_1}{\partial x_2} & \frac{\partial \xi_2}{\partial x_2} & \frac{\partial \xi_3}{\partial x_2} \\ \frac{\partial \xi_1}{\partial x_3} & \frac{\partial \xi_2}{\partial x_3} & \frac{\partial \xi_3}{\partial x_3} \end{pmatrix} \cdot \begin{pmatrix} \frac{\partial \mathbf{N}(\xi)}{\partial \xi_1} \\ \frac{\partial \mathbf{N}(\xi)}{\partial \xi_2} \\ \frac{\partial \mathbf{N}(\xi)}{\partial \xi_3} \end{pmatrix} , \quad (2.126)$$

or alternatively shorter in accordance with

$$\frac{\partial \mathbf{N}(\boldsymbol{\xi})}{\partial \mathbf{x}} = \mathbf{J}^{-1} \cdot \frac{\partial \mathbf{N}(\boldsymbol{\xi})}{\partial \boldsymbol{\xi}}, \quad (2.127)$$

including the inverted well-known Jacobian matrix \mathbf{J}^{-1} . Then, inverting this equation yields

$$\frac{\partial \mathbf{N}(\boldsymbol{\xi})}{\partial \boldsymbol{\xi}} = \mathbf{J} \cdot \frac{\partial \mathbf{N}(\boldsymbol{\xi})}{\partial \mathbf{x}}. \quad (2.128)$$

Generally, the Jacobian \mathbf{J} is defined as follows

$$\mathbf{J} = \frac{\partial \mathbf{x}}{\partial \boldsymbol{\xi}} = \frac{\partial (\mathbf{N} \cdot \hat{\mathbf{x}})}{\partial \boldsymbol{\xi}} = \frac{\partial \mathbf{N}}{\partial \boldsymbol{\xi}} \cdot \hat{\mathbf{x}}. \quad (2.129)$$

This Jacobian can easily be calculated element-wise just by considering the given shape functions \mathbf{N} and the respective geometry $\hat{\mathbf{x}}$. Then, Equation (2.127) allows to calculate all required derivatives for the operator matrix \mathbf{B} , which have to be allocated appropriately.

2.8.4 Gauß Quadrature

At this point the Gauß quadrature is taken into account, see Zienkiewicz et al. (2005), Fish and Belytschko (2007), and Hermann (2011) for example. The objective is to avoid integrating over the element volumes and to take advantage of the numerical integration instead, thus

$$\int_{-1}^1 f(x) dx \approx \sum_{j=1}^m w(x_j) f(x_j). \quad (2.130)$$

This is exact for polynomial degrees o premising $o \leq 2m - 1$ with m sampling points under the assumption of an appropriate choice of the weights $w(x_j)$ and coordinates x_j and for the specified boundaries. For the given application, the integral is extended to the three-dimensional consideration and adjusted according to the integrals of the natural elements. In context of finite elements the Gauß points are denoted by N_{GP} . Therefore

$$\int_{-1}^1 \int_{-1}^1 \int_{-1}^1 f(\boldsymbol{\xi}) \det \mathbf{J}(\boldsymbol{\xi}) d\xi_1 d\xi_2 d\xi_3 = \sum_{g=1}^{N_{GP}} w_{GP} f(\boldsymbol{\xi}_{GP}^g) \det \mathbf{J}(\boldsymbol{\xi}_{GP}^g). \quad (2.131)$$

Exact integration is provided because of two sampling points $m = 2$ in each spatial direction, which always fulfills the condition $o < 4 - 1$ in the present case. The determinant of the Jacobian $\det \mathbf{J}$ is considered as a result of the coordinate transformation. Furthermore, the weights are constant and prescribed by $w_{GP} = 1$ and the prescribed coordinates of the Gauß points denoted by the subscript $(\cdot)_{GP}$ and of number $N_{GP} = m^3 = 8$ are given by

$$\begin{aligned} \boldsymbol{\xi}_{GP}^1 &= (+1/\sqrt{3} \quad -1/\sqrt{3} \quad -1/\sqrt{3}), & \boldsymbol{\xi}_{GP}^2 &= (+1/\sqrt{3} \quad +1/\sqrt{3} \quad -1/\sqrt{3}), \\ \boldsymbol{\xi}_{GP}^3 &= (-1/\sqrt{3} \quad +1/\sqrt{3} \quad -1/\sqrt{3}), & \boldsymbol{\xi}_{GP}^4 &= (-1/\sqrt{3} \quad -1/\sqrt{3} \quad -1/\sqrt{3}), \\ \boldsymbol{\xi}_{GP}^5 &= (+1/\sqrt{3} \quad -1/\sqrt{3} \quad +1/\sqrt{3}), & \boldsymbol{\xi}_{GP}^6 &= (+1/\sqrt{3} \quad +1/\sqrt{3} \quad +1/\sqrt{3}), \\ \boldsymbol{\xi}_{GP}^7 &= (-1/\sqrt{3} \quad +1/\sqrt{3} \quad +1/\sqrt{3}), & \boldsymbol{\xi}_{GP}^8 &= (-1/\sqrt{3} \quad -1/\sqrt{3} \quad +1/\sqrt{3}). \end{aligned} \quad (2.132)$$

2.8.5 Residual and Tangent Matrix

The Gibbs energy according to Equation (2.69) is the starting point, therefore

$$\mathcal{G} := \int_{\Omega} \Psi(\boldsymbol{\varepsilon}, \lambda) \, dV - \int_{\Omega} \mathbf{f} \cdot \mathbf{u} \, dV - \int_{\partial\Omega} \mathbf{t} \cdot \mathbf{u} \, dA. \quad (2.133)$$

Analogously to Equation (2.83), the stationarity condition for the Gibbs energy with respect to the underlying primary variable \mathbf{u} corresponding to the displacement field can be derived as

$$\delta\mathcal{G} = \int_{\Omega} \boldsymbol{\sigma} : \delta\boldsymbol{\varepsilon} \, dV - \int_{\Omega} \mathbf{f} \cdot \delta\mathbf{u} \, dV - \int_{\partial\Omega} \mathbf{t} \cdot \delta\mathbf{u} \, dA = 0 \quad \forall \delta\mathbf{u}, \quad (2.134)$$

with stresses $\boldsymbol{\sigma} = \partial\Psi/\partial\boldsymbol{\varepsilon}$ according to Equation (2.56), which have to be determined as presented in Section 2.9. Finally, the derived shape functions \mathbf{N} as well as the operator matrix \mathbf{B} can be inserted into the variation of the Gibbs energy in Equation (2.134) providing the residual \mathbf{R}_u of the displacement field. After eliminating the superfluous $\delta\hat{\mathbf{u}}$, the following results

$$\mathbf{R}_u = \int_{\Omega} \mathbf{B}^T \cdot \tilde{\boldsymbol{\sigma}} \, dV - \int_{\Omega} \mathbf{N}^T \cdot \mathbf{f} \, dV - \int_{\partial\Omega} \mathbf{N}^T \cdot \mathbf{t} \, dA \stackrel{!}{=} \mathbf{0}. \quad (2.135)$$

These integrals over the total volume of the considered body can now be discretized by the subdivision into element-wise integrals according to Equation (2.111), therefore

$$\mathbf{R}_u = \sum_{e=1}^{N_e} \int_{\Omega_e} \mathbf{B}^T \cdot \tilde{\boldsymbol{\sigma}} \, dV - \sum_{e=1}^{N_e} \int_{\Omega_e} \mathbf{N}^T \cdot \mathbf{f} \, dV - \sum_{e=1}^{N_e} \int_{\partial\Omega_e} \mathbf{N}^T \cdot \mathbf{t} \, dA \stackrel{!}{=} \mathbf{0}. \quad (2.136)$$

Finally, the derived element-wise residual \mathbf{R}_u from Equation (2.136) under consideration of the Gauss quadrature in Equation (2.131) has to become zero. Hereto, the Newton-Raphson method, see works of Schäfer (1999), Zienkiewicz et al. (2005), Fish and Belytschko (2007), and Hermann (2011) for example, is applied as follows

$$\mathbf{R}_u^{k+1} = \mathbf{R}_u^k + \frac{d\mathbf{R}_u^k}{d\mathbf{u}^k} \cdot \Delta\mathbf{u}^{k+1} \stackrel{!}{=} \mathbf{0}, \quad (2.137)$$

with the iteration number k and the displacement increment $\Delta\mathbf{u}$ by means of

$$\Delta\mathbf{u}^{k+1} = - \left[\frac{d\mathbf{R}_u^k}{d\mathbf{u}^k} \right]^{-1} \cdot \mathbf{R}_u^k, \quad (2.138)$$

so that the displacements can be updated by

$$\mathbf{u}^{k+1} = \mathbf{u}^k + \Delta\mathbf{u}^{k+1}. \quad (2.139)$$

Within the residual \mathbf{R}_u^k the stresses $\tilde{\boldsymbol{\sigma}}$ are included and have to be determined as done in the Section 2.9 hereinafter. Moreover, the derivative of the residuum with respect to the displacements $d\mathbf{R}_u^k/d\mathbf{u}$, which is denoted as the tangent matrix, has to be calculated, therefore

$$\frac{d\mathbf{R}_u^k}{d\mathbf{u}} = \sum_{e=1}^{N_e} \sum_{g=1}^{N_{GP}} \mathbf{B}^T \cdot \frac{d\tilde{\boldsymbol{\sigma}}}{d\mathbf{u}} \det \mathbf{J} = \sum_{e=1}^{N_e} \sum_{g=1}^{N_{GP}} \mathbf{B}^T \cdot \frac{d\tilde{\boldsymbol{\sigma}}}{d\tilde{\boldsymbol{\varepsilon}}} \cdot \mathbf{B} \det \mathbf{J}, \quad (2.140)$$

where the notation of the Jacobian, which is depending on the element and each Gauß point, was shortened for clarity. The newly occurred derivative $d\tilde{\sigma}/d\tilde{\epsilon}$ is denoted as the material tangent and is also determined in the following section. The material tangent describes the linear or non-linear slope of the stress-strain curve of the material.

2.9 Determination of Stresses and Material Tangent

As described in the previous Subsection 2.8.5, the determination of the stresses as well as the material tangent is necessary in order to calculate the residual as well as the tangent matrix from Equations (2.136) and (2.140). In this section the Voigt notation is used.

2.9.1 Linear Material Behavior

For materials with a linear stress-strain relation according to the pure elastic case, the stresses $\tilde{\sigma}$ are only depending on the strains $\tilde{\epsilon}$ as described by Hooke's law as

$$\tilde{\sigma} = \tilde{\sigma}(\tilde{\epsilon}) = \tilde{\mathbb{E}}_0 \cdot \tilde{\epsilon} . \quad (2.141)$$

Then, the material tangent can trivially be determined by

$$\frac{d\tilde{\sigma}}{d\tilde{\epsilon}} = \tilde{\mathbb{E}}_0 , \quad (2.142)$$

where the material tangent is exactly corresponding to the stiffness matrix $\tilde{\mathbb{E}}_0$. For the present linear elastic behavior, the material tangent is obviously constant and thus the tangent matrix as well. Consequently, the Newton-Raphson method converges in one step or is not required at all and the displacements could analytically be solved.

2.9.2 Non-Linear Material Behavior

It should be mentioned that the non-linearity is limited to the stress-strain relation as a result of microstructural changes, for example. Geometrical non-linearity is not considered here. For the non-linear stress-strain relation, the stresses $\tilde{\sigma}$ are no longer only depending on the strains $\tilde{\epsilon}$ but also on the internal variable λ , which in turn can also depend on $\tilde{\epsilon}$ according to the respective evolution equations. Hence, the stresses, which are described here in a generally applicable formulation, are formulated as

$$\tilde{\sigma} = \tilde{\sigma}(\tilde{\epsilon}, \lambda) . \quad (2.143)$$

At this point a linear approximation of the stresses by use of the Taylor's theorem, see work of Hermann (2011) for example, is done resulting in

$$\tilde{\sigma}^{m+1} = \tilde{\sigma}^m + \left. \frac{\partial \tilde{\sigma}}{\partial \tilde{\epsilon}} \right|^m \cdot \Delta \tilde{\epsilon} + \left. \frac{\partial \tilde{\sigma}}{\partial \lambda} \right|^m \Delta \lambda , \quad (2.144)$$

including the increment of the strains $\Delta\tilde{\boldsymbol{\varepsilon}} = \tilde{\boldsymbol{\varepsilon}}^{m+1} - \tilde{\boldsymbol{\varepsilon}}^m$, the increment of the internal variable $\Delta\lambda = \lambda^{m+1} - \lambda^m$ and the stresses from the previous time-step $\boldsymbol{\sigma}^m$. Based on that, the material tangent can be derived by

$$\left. \frac{d\tilde{\boldsymbol{\sigma}}}{d\tilde{\boldsymbol{\varepsilon}}} \right|^{m+1} = \left. \frac{\partial\tilde{\boldsymbol{\sigma}}}{\partial\tilde{\boldsymbol{\varepsilon}}} \right|^m + \left. \frac{\partial\tilde{\boldsymbol{\sigma}}}{\partial\lambda} \right|^m \otimes \left. \frac{\partial\lambda}{\partial\tilde{\boldsymbol{\varepsilon}}} \right|^{m+1}, \quad (2.145)$$

whereat the first two terms on the right-hand side can straightforwardly be calculated and can also be used for the determination of the stresses. The third one, the derivative of the internal variable $(\partial\lambda/\partial\tilde{\boldsymbol{\varepsilon}})|^{m+1}$, has to be investigated in more detail. Hereby, the rate-independent and the rate-dependent case have to be distinguished as subsequently presented.

Rate-Independent Material Behavior

The evolution equation for rate-independent behavior according to Section 2.7 might appear as

$$\lambda^{m+1} = \lambda^m + \Delta\rho p(\tilde{\boldsymbol{\varepsilon}}^{m+1}, \lambda^m), \quad (2.146)$$

with the consistency parameter $\Delta\rho$ depending on the current strains

$$\Delta\rho = \Delta\rho(\tilde{\boldsymbol{\varepsilon}}^{m+1}). \quad (2.147)$$

The wanted derivative of the internal variable $(\partial\lambda/\partial\tilde{\boldsymbol{\varepsilon}})|^{m+1}$ can be derived as

$$\left. \frac{\partial\lambda}{\partial\tilde{\boldsymbol{\varepsilon}}} \right|^{m+1} = \Delta\rho \frac{\partial p(\tilde{\boldsymbol{\varepsilon}}^{m+1}, \lambda^m)}{\partial\tilde{\boldsymbol{\varepsilon}}^{m+1}} + \frac{\partial\Delta\rho}{\partial\tilde{\boldsymbol{\varepsilon}}^{m+1}} p(\tilde{\boldsymbol{\varepsilon}}^{m+1}, \lambda^m). \quad (2.148)$$

Here, the first term can be calculated directly whereas the second one, the derivative of the consistency parameter $\Delta\rho$, has to involve the yield function Φ introduced in Section 2.7, therefore

$$\Phi = \Phi(\tilde{\boldsymbol{\varepsilon}}^{m+1}, \lambda^{m+1}) \quad (2.149)$$

$$= |p(\tilde{\boldsymbol{\varepsilon}}^{m+1}, \lambda^{m+1})| - r_1 \stackrel{!}{=} 0 \quad (2.150)$$

$$= |p(\tilde{\boldsymbol{\varepsilon}}^{m+1}, \lambda^m + \Delta\rho p(\tilde{\boldsymbol{\varepsilon}}^{m+1}, \lambda^m))| - r_1 \stackrel{!}{=} 0 \quad (2.151)$$

This derivative of $\Delta\rho$ can be achieved by taking the derivative of the yield function

$$\frac{d\Phi}{d\tilde{\boldsymbol{\varepsilon}}^{m+1}} = \frac{\partial\Phi}{\partial\tilde{\boldsymbol{\varepsilon}}^{m+1}} + \frac{\partial\Phi}{\partial\Delta\rho} \frac{\partial\Delta\rho}{\partial\tilde{\boldsymbol{\varepsilon}}^{m+1}} \stackrel{!}{=} 0 \quad (2.152)$$

and subsequently by rearranging as follows

$$\frac{\partial\Delta\rho}{\partial\tilde{\boldsymbol{\varepsilon}}^{m+1}} = - \left(\frac{\partial\Phi}{\partial\Delta\rho} \right)^{-1} \frac{\partial\Phi}{\partial\tilde{\boldsymbol{\varepsilon}}^{m+1}}. \quad (2.153)$$

The both appearing terms can again be calculated straightforwardly. Finally, the wanted derivative of the internal variable is derived by

$$\left. \frac{\partial\lambda}{\partial\tilde{\boldsymbol{\varepsilon}}} \right|^{m+1} = \Delta\rho \frac{\partial p(\tilde{\boldsymbol{\varepsilon}}^{m+1}, \lambda^m)}{\partial\tilde{\boldsymbol{\varepsilon}}^{m+1}} - \left(\frac{\partial\Phi}{\partial\Delta\rho} \right)^{-1} \frac{\partial\Phi}{\partial\tilde{\boldsymbol{\varepsilon}}^{m+1}} p(\tilde{\boldsymbol{\varepsilon}}^{m+1}, \lambda^m). \quad (2.154)$$

Rate-Dependent Material Behavior

In the other case of rate-dependent material behavior, see Section 2.7, the evolution equation no longer has a consistency parameter but is described by viscous quantities as follows

$$\lambda^{m+1} = \lambda^m + \frac{\Delta t}{r_2} p(\tilde{\epsilon}^{m+1}, \lambda^m). \quad (2.155)$$

In contrast to the previous case, the wanted derivative of the internal variable $(\partial\lambda/\partial\tilde{\epsilon})|^{m+1}$ can easily be achieved by

$$\left. \frac{\partial\lambda}{\partial\tilde{\epsilon}} \right|^{m+1} = \frac{\Delta t}{r_2} \frac{\partial p(\tilde{\epsilon}^{m+1}, \lambda^m)}{\partial\tilde{\epsilon}^{m+1}}. \quad (2.156)$$

3 Damage Modeling and Regularization Strategies

This section introduces damage modeling initially with Section 3.1 providing different perspectives on damage in general. Afterwards, these perspectives are further discussed starting with Section 3.2 in which failure criteria are presented. This is followed by Section 3.3 introducing micromechanical damage models. Finally, in Section 3.4 continuum damage models are presented. Building on that, several regularization strategies are discussed. First, the necessity of regularization strategies is justified in Section 3.5. Then, Section 3.6 introduces the viscous regularization, followed by integral-type regularization in Section 3.7. Finally, gradient-enhanced regularization is presented in Section 3.8. The provided information is based on the literature given by Krajcinovic (1996) and Hornbogen et al. (2008) with a focus on the works of Skrzypek and Ganczarski (1999) and Gross and Seelig (2011). Further literature is respectively stated

3.1 Different Perspectives on Damage

Damage characterizes the degradation of material strength or material resistance resulting as a macroscopic effect of causing microscopic defects. Hereby, material damage in general describes the mere existence of voids, cavities and tiny cracks (microcracks) on the microstructural level, which are also already contained in the initial state of all materials up to a certain level. Notwithstanding the previous description, the damage evolution results from processes of void nucleation, growth and coalescence as well as from processes of microcrack initiation and propagation leading to macroscopic damage in the end, see Figure 3.1. The mentioned damage evolution is basically what damage modeling in this theses is about. Thereby, damage is not to be confused with fracture mechanics as described by Hertzberg et al. (2013), Anderson (2005), and Gross and Seelig (2011) for example, which basically describes the behavior of a specific crack in contrast to the present damage description that rather constitutes a smeared quantity of the material's state. However, the evolving damage can also be interpreted as a crack in the case of thin damage zones approaching zero stiffness for example.



Figure 3.1: Failure by brittle damage of a bike's pedal arm. Image taken from Lokilech (2007).

In the mentioned context, different scales of consideration can be distinguished for damage modeling as shown in Figure 3.2, starting with the usually unconsidered atomic scale that takes into account molecular dynamics and the configuration and breaks of atomic bonds. On the next level, the already introduced microscopic scale includes the previously mentioned defects and processes on which many damage formulations are based on. And finally, the most widely used macroscopic scale is described by the continuum mechanics and can be related to the microscopic scale. As a result, several techniques of transition, averaging or simplification were developed across the different scales.

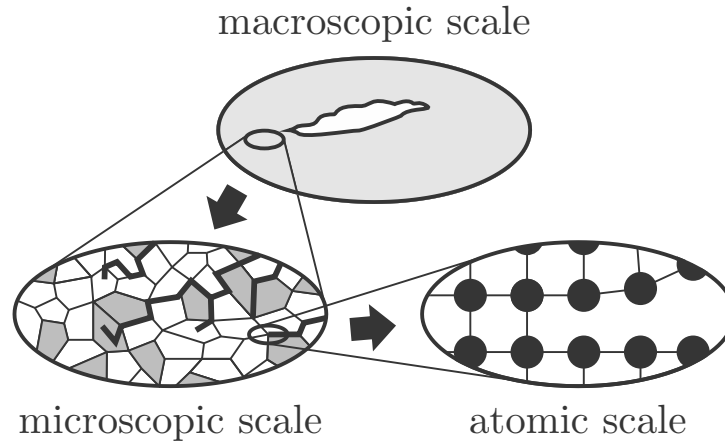


Figure 3.2: Schematic illustration of damage on different scales: macroscopic scale (top), microscopic scale (left) and atomic scale (right). Image inspired by Skrzypek and Ganczarski (1999).

Generally, damage models can not only be distinguished by the scale of consideration, but also by their global response during damage, which can be categorized by a brittle or ductile behavior, see Figure 3.3. Brittle damage is usually related to the initiation and propagation of microcracks whereat the resulting macroscopic crack, which arises as a consequence of unstable material deterioration and which develops suddenly and dominating compared to other cracks, usually has a preferred direction. This brittle behavior leads to a sudden drop of the otherwise linear global material response and to a very fine crack propagation. A typical example for brittle behaving materials are for example glasses.

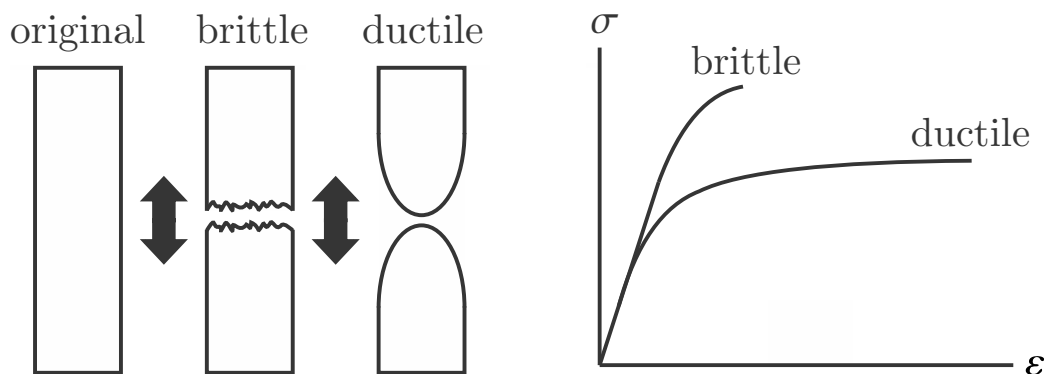


Figure 3.3: Schematic illustration of damage characteristics: tensile specimen in original and damaged/failed state with brittle/ductile damage and related stress-strain diagram (from left to right). Image inspired by Gross and Seelig (2011).

In contrast, ductile damage is usually related to the nucleation, growth and coalescence of voids and occurs in the context of plasticity. Ductile cracks usually develop slowly compared to the brittle case, which is physically induced by a plastic zone propagating in front of the crack tip and decreasing stresses. Since a lot of energy conversion is involved in these plastic deformations, ductile materials are usually more resistant against crack propagation. The global material response of this ductile materials is usually characterized by plastic behavior and a smooth drop while the crack propagation is accompanied by plastic zones and therefore more distributed. A typical example for ductile behaving materials are sorts of metals. It should be considered that the behavior of materials related to brittleness or ductility is temperature-dependent in most cases.

The presented models in this thesis do not consider plasticity at all. Even though according enhancements to plasticity are partly existing, for example in the work of Schwarz et al. (2018b) and Hoormazdi et al. (2019), they are not part of this investigation. Since no plastic deformations are included, the models cannot directly be related to ductile behavior. However, the manner how damage is occurring and propagating and the related impact on the global material response can certainly be classified as being rather brittle or being rather ductile. For this purpose, the intensity of the drop of the material's global response as well as the thickness of the cracks are accordingly assigned. The objective hereby is to investigate and evaluate how the respective damage models are able to constitute rather brittle or rather ductile behavior or something inbetween. In this context, the models behavior is described as being brittle-like with localized damage or on the contrary as being ductile-like with diffusive damage without disclaiming the actual physical meaning.

3.2 Failure Criteria

The simplest method of damage modeling is just to completely disregard any conditions or processes on lower scales by defining a failure criterion based on stress or strain states. This is also one of the oldest procedures to characterize material failure. In this context, damage distinguishes only two states namely completely intact and completely failed material. Hereto, the failure criterion somehow represents a yield limit whose exceeding separates the two mentioned states. This can exemplarily be illustrated by the following equation

$$\sigma \leq \sigma_{\text{fail}} , \quad (3.1)$$

inducing the state of failure when exceeding σ_{fail} . This corresponds to a maximum damage state d_{max} with for example $d_{\text{max}} = 1$ in case of a damage function $f = 1 - d$. The respective evolution of damage d for the current time step $m + 1$ could be described as follows

$$d^{m+1} = d_{\text{max}} . \quad (3.2)$$

In general, failure criteria do not affect the material description or behavior. Therefore, failed material in context of finite element calculations for example can be implemented by deleting according elements or by zero stress assumptions which can result from the above mentioned maximum damage state.

In this context, the following well-known failure criteria can be mentioned for example: Taking into account the maximum normal stresses as a failure criterion goes back to Rankine

(1857), whereas Saint-Venant (1856) therefore concerned the maximum normal strains and Tresca (1864) the maximum shear stresses. A combination of both, the maximum shear stresses as well as the maximum normal stresses, were considered by the Coulomb-Mohr criterion based on the works of Coulomb (1776) and Mohr (1906). The implementation of damage models based on the idea of failure criteria was for example shown in connection with eigenfracture schemes by Schmidt et al. (2009) and Pandolfi and Ortiz (2012) in which the erosion of elements is described by a jump from elastic to failed material.

3.3 Micromechanical Damage Models

Micromechanical damage models take into account microstructural processes. Hereto, the information of void nucleation, growth and coalescence is transferred to the macroscopic scale by simplification or homogenization. On the macroscopic scale this information is captured by a therefore smeared or sort of effective damage variable describing the microstructure usually by the volume fraction of voids. These volume fractions can be determined in different ways. The aforementioned simplification is related to an appropriate mathematical formulation describing microstructural effects, for example by modeling dislocations and inclusions or using equivalent descriptions for general inhomogeneities. Homogenization is usually related to the involvement of a representative volume element (RVE) gathering the microstructural processes as accurately as possible and averaging this description to a macroscopic quantity, see Figure 3.4.

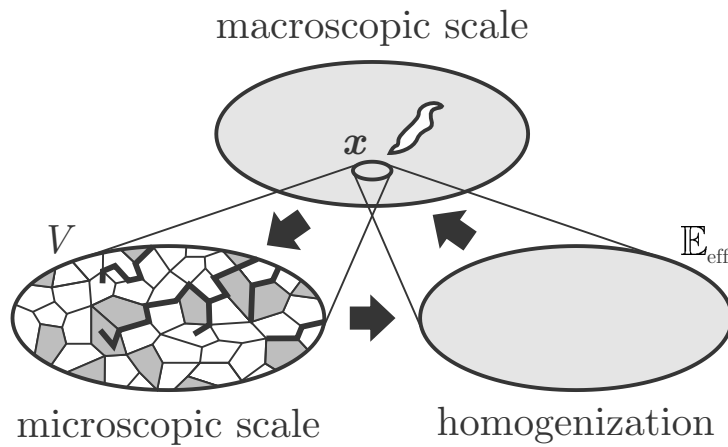


Figure 3.4: Schematic illustration of homogenization (right) by mapping the microscopic scale (left) by the effective stiffness tensor \mathbb{E}_{eff} to the macroscopic scale (top). Image inspired by Gross and Seelig (2011).

This averaging procedure relates the stresses and strains of a specific material point of the macroscopic scale \boldsymbol{x} to a specific volume area V of the microscopic scale where the stresses and strains arise as fluctuation fields. Averaging these microscopic fields is denoted by $\langle \cdot \rangle$ and provides the macroscopic quantities given by

$$\langle \boldsymbol{\sigma} \rangle = \frac{1}{V} \int_V \boldsymbol{\sigma}(\boldsymbol{x}) dV, \quad (3.3)$$

$$\langle \boldsymbol{\varepsilon} \rangle = \frac{1}{V} \int_V \boldsymbol{\varepsilon}(\boldsymbol{x}) dV. \quad (3.4)$$

This allows to define an effective stiffness tensor \mathbb{E}_{eff} as follows

$$\langle \boldsymbol{\sigma} \rangle = \mathbb{E}_{\text{eff}} : \langle \boldsymbol{\varepsilon} \rangle . \quad (3.5)$$

A well-known and often quoted example for describing the void volume fraction as an internal variable is done in the work of Gurson (1977) in which the void nucleation and growth was related to local plastic flow for porous ductile materials. Based on that, Tvergaard (1981) improved the formulation of Gurson by adjustable parameters and a further modification in the work of Tvergaard and Needleman (1984) is widespread in the literature until today. The use of representative volume elements (RVE) is popular in many applications as is also for the description of the microstructure in context of damage, which is described in the works of Krajcinovic (1996), Skrzypek and Ganczarski (1999), and Gross and Seelig (2011) for example.

3.4 Continuum Damage Models

In contrast to the previous, continuum damage models are rather a phenomenologically motivated approach for damage modeling and not directly related to microstructural processes. These models are formulated in a more pragmatic way in context of effective stresses or strains for example. Incidentally, an investigation regarding these effective quantities is given by Simo and Ju (1987) and Simo and Ju (1989). The material softening for continuum damage models is also described by an internal damage variable with smeared or averaging character whose specific physical meaning is related to its respective application.

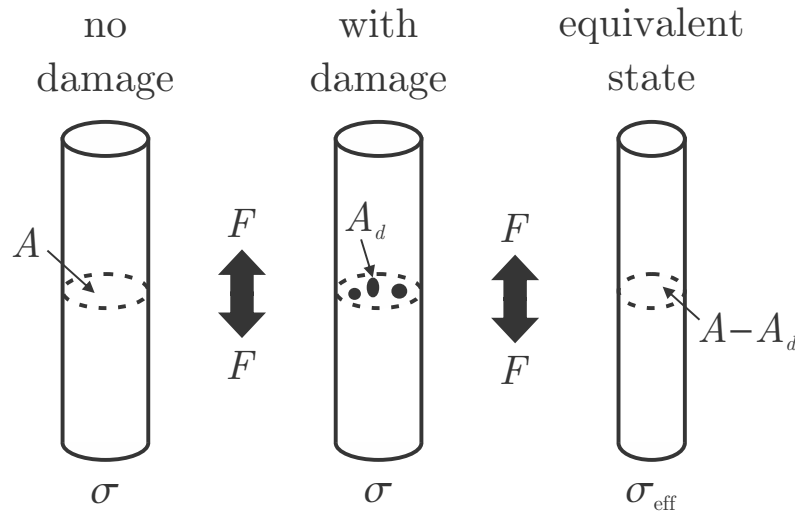


Figure 3.5: One-dimensional schematic illustration of the effective stress concept providing a state with no damage and a cross-section area A (left), a state with damaged cross-section area A_d (center) and an equivalent state with effective stresses based on the remaining undamaged cross-section area $A - A_d$ (right). Image inspired by Skrzypek and Ganczarski (1999).

The phenomenological description of damage models originates from the work of Kachanov (1958) and Kachanov (1999) in which a scalar damage variable is applied in context of effective stresses. A more physical interpretation was introduced by Rabotnov (1959) who related the reduction of the cross section area due to defects with the damage variable. This for continuum

damage models underlying concept is illustrated in Figure 3.5. The effective stresses shown there are based on the remaining undamaged cross section area $A - A_d$, consequently

$$\sigma_{\text{eff}} = \frac{F}{A - A_d} = \frac{\sigma}{1 - d}, \quad (3.6)$$

with the applied forces F and the damage d . Besides a scalar formulation of the damage variable, also vectorial damage variables or second-, fourth- or even eighth-order damage tensors can be found in the literature. The scalar formulation is usually related to isotropic damage, for example in the works of Lemaitre (1971) and Wriggers and Moftah (2006), and higher-order tensors on the contrary for anisotropic damage, in the work of Chaboche (1981), Matzenmiller et al. (1995) and Menzel et al. (2005) for instance. Another approach of continuum damage models is given by two-state models that were introduced by Francfort and Marigo (1993), developed by Francfort and Garroni (2006) and are related to Allaire and Kohn (1993) and Allaire and Lods (1999). Hereby, two phases, an undamaged and damaged one, are considered and the current damage state is described by a mixture of both phases by the use of relaxation.

3.5 Necessity of Regularization

Damage models are characterized by softening effects and localization corresponding to discontinuous deformation states in the limit case, described by Simo et al. (1993) for example. It is well-known that these models share ill-posed boundary value problems which results from non-convex and non-coercive energies as investigated for instance by Ball (1977), Dacorogna (1982a), Dacorogna (1982b), Ciarlet (1988) and Francfort and Mielke (2006). These energies prevent finding a unique global stationarity point for the numerical calculations. At this point, coercivity and convexity are generally introduced with respect to a function f on the basis of Rockafellar and Wets (1998).

A function $f(x)$ is called coercive if it has a superlinear growth, consequently

$$\lim_{|x| \rightarrow \infty} \frac{f(x)}{|x|} = \infty. \quad (3.7)$$

This is illustrated in the diagram on the left-hand side of Figure 3.6 in which f_1 represents a coercive and f_2 a non-coercive function. Both are separated by the limit case of a linear function illustrated by the dashed line. In regard to damage modeling, the requirement of zero stresses $\sigma = \partial\Psi/\partial\varepsilon$ after failure, as shown on the left-hand side of Figure 3.7, leads to an energy Ψ possessing a slope which is equal to zero. Therefore, this energy is no longer growing and accordingly non-coercive. Finding a stationarity point for a non-coercive energy that becomes constant after some limit strain is of course problematic.

Moreover, a function $f(x)$ is called convex if any point, described by $\tau \in (0, 1)$, on an arbitrary secant of the two points at x_0 and x_1 is always above the function, consequently

$$f((1 - \tau)x_0 + \tau x_1) \leq (1 - \tau)f(x_0) + \tau f(x_1) \quad \forall \tau \in (0, 1). \quad (3.8)$$

An illustration is again provided, the diagram on the right-hand side of Figure 3.6 presents a convex function. In regard to damage modeling, the decrease of the material stiffness is accompanied by a non-convex energy Ψ , as shown on the right-hand side of Figure 3.7. The depicted

secant is obviously located below the energy curve. Non-convex energies are also problematic for finding a stationarity point, since the local minimum does not necessarily correspond to the global one. This is why convexity can also be interpreted as the stability of the function regarding superimposed fluctuations of the argument of the function.

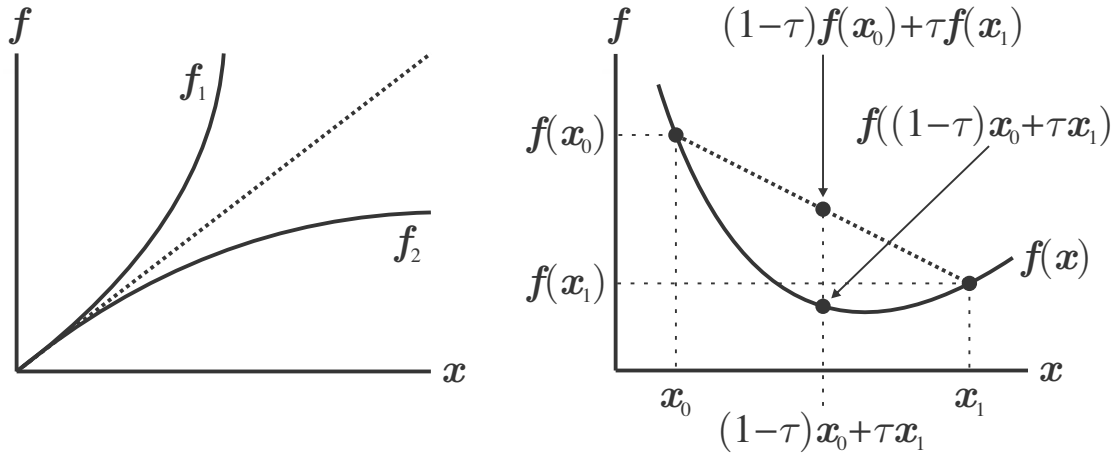


Figure 3.6: Schematic illustration of coercivity (left) and convexity (right) with respect to a function f . Inspired by Rockafellar and Wets (1998)

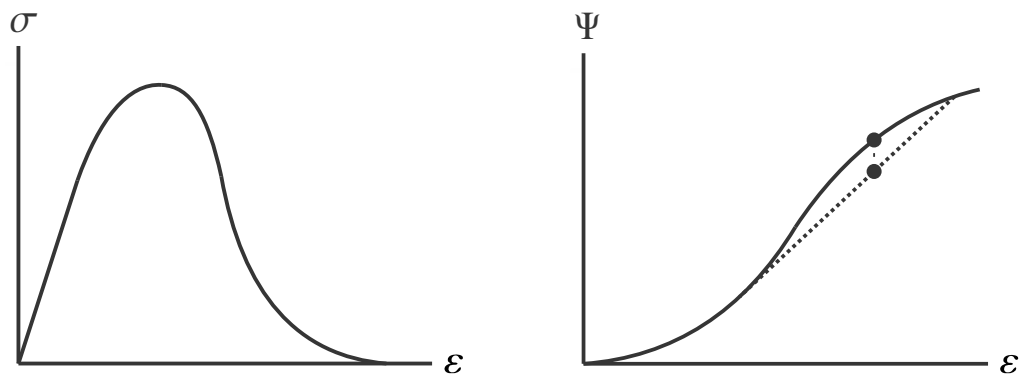


Figure 3.7: Schematic illustration of a non-coercive energy resulting in not-rising stresses for infinite strains (left) and a non-convex energy in context of damage modeling (right).

Those critical energies lead to numerical instabilities and mesh-dependent finite element results. For that reason, strategies that somehow take into account the non-local behavior of the damage have to be considered in order to achieve well-posedness and therefore stability and mesh-independence. This is also often described by the incorporation of an internal length scale. In general, those strategies are called regularization, which can be distinguished in several categories depending on their respective operating principle. The most common regularization strategies are gradient-enhanced regularization, integral-type regularization and viscous regularization. Hereto, an overview is given by Forest and Lorentz (2004) and a comparison of non-local and gradient-enhanced formulations by Peerlings et al. (2001). Of course, there are further strategies for regularization and some models can not clearly be assigned to a specific category, for example the work of Yang and Misra (2012) who distance themselves from other regularization strategies and at the same time describe the model as a development of the gradient theory. Subsequently, the three mentioned most common regularization strategies are presented in more detail.

3.6 Viscous Regularization

The main idea of viscous regularization is to limit and thus slow down the evolution of damage in a specific element. For a standard formulation of the energy Ψ by means of

$$\Psi = \frac{1}{2} \varepsilon : f(d) \mathbb{E}_0 : \varepsilon , \quad (3.9)$$

with a to be selected damage function $f(d)$ according to Section 4.1, the viscous regularization can exemplarily be described by the evolution equation in Equation (2.97) which results from an elasto-viscoplastic dissipation function. The evolution of the damage d for the current time-step $m + 1$ corresponds to

$$d^{m+1} = d^m + \frac{\Delta t}{r_2} [|p(\varepsilon^{m+1}, d^m)| - r_1]_+ \quad (3.10)$$

with the driving force $p(\varepsilon^{m+1}, d^m)$ and the threshold r_1 . The aforementioned limitation is given by the viscosity parameter r_2 and the time-increment Δt . The latter is based on the combined time discretization from Equation (2.109). The consequent missing amount of dissipated energy due to the limited evolution is then counterbalanced by surrounding elements evolving damage in order to maintain at least the same total energy dissipation compared to the case of no regularization. As a result, propagating damage zones in finite element calculations are no longer limited to individual or rows of elements but smooth transitions between damaged and undamaged zones are occurring. Viscously regularized damage models do not possess a direct spatial internal length scale but there is rather a conforming length scale in time that corresponds to the same regularizing effects. Therefore, stable and mesh-independent finite element results are achieved. Furthermore, viscous effects can easily be implemented and the numerical effort is low compared to other regularization strategies. However, it should be considered that the calculations are strongly depending on the loading velocity in return and this rate-dependence is a remarkable drawback since the corresponding viscous parameters are hardly or difficultly applicable to materials like metals or concrete.

The first who introduced viscous regularization to localization problems was Needleman (1988) by presenting a rate-dependent formulation that implicitly introduces a length scale eliminating the pathological mesh sensitivity associated with localization problems for quasi-static as well as dynamic problems. Moreover, numerical instability problems for approaching the rate-independent limit were investigated. Some time later, Sluys and De Borst (1992) applied the viscous regularization for localization problems of cracked medium in relation to wave propagation and reflections on the cracked zone. It was also stated that the width of the localization zone is depending on the length scale parameter as well as the loading rate and limit cases were investigated as well. In another example, the relation between the material length scale and the width of shear bands in context of viscoplastic regularization is examined by Wang et al. (1996). In the work of Dube et al. (1996), a damage model with a rate-independent formulation was converted into a rate-dependent one with the objective of capturing more effects regarding the loading rate of concrete. This procedure was based on the Perzyna viscoplasticity, considering some modifications, and it was possible to achieve well-posedness as well as mesh objectivity of the numerical results also in relation to wave propagation. Furthermore, the mentioned Perzyna viscoplasticity was instrument for regularization in the work of Faria et al. (1998) in which a new constitutive model was introduced capturing tensile-compression asymmetry by two scalar damage variables and applied to massive concrete structures. An interesting

investigation on the rate-dependence of viscous damage models was done by Chaboche et al. (2001) who applied interface debonding models, resulting in a new kind of viscous regularization with a limited dependence on the loading rate. Departing from viscous regularization, a similar approach is presented in the work of Suffis et al. (2003) in which the delay effect is used analogously to viscosity in order to slow down the damage evolution and therefore to achieve mesh objectivity. Thereby, the characteristic damage length was investigated by a comparison of numerical and analytical studies. Another damage model by Allix (2012) investigates some limitations of the rate-dependencies by bounding the rate of the internal variables, described as the bounded rate concept. This has certain similarities to the damage Model II [ERVE] presented in Section 4.3 in this thesis. A further model based on viscoplasticity by Niazi et al. (2013) takes up viscous regularization in order to critically investigate and evaluate the reason for existence of this regularization strategy in comparison to gradient-enhancement or integral-type. Deeper studies yield that there are many restrictions but for rate-dependent materials, for high temperature or for high deformation rates the viscous regularization can provide physical results. A development of the viscous regularized damage Model I [REL], presented in Section 4.2, is given by Langenfeld et al. (2018).

3.7 Integral-Type Regularization

None of the presented damage models in this thesis are related to integral-type regularization which seems to have become less important over time at least for damage modeling. In contrast, a similar procedure is quite popular in context of topology optimization by applying density filters with integral terms, see for example works of Bourdin (2001) and Hägg and Wadbro (2017). However, the concept of integral-type regularization for damage modeling is obvious and there is a lot of literature on that topic. The main idea for integral-type formulations is to no longer relate the governing equations to a specific point but to instead replace this relation by an integral term, which functions as an weighted spatial average over the defined surroundings of the considered point. Exemplary for the integral-type regularization in general, this is illustrated by the following formulation based on the works of Bažant and Pijaudier-Cabot (1988) and Jirásek (1998), which are further discussed later. The underlying energy Ψ is based on the non-local damage variable $\bar{d}(\mathbf{x})$ at position \mathbf{x} as described by

$$\Psi = \frac{1}{2} \boldsymbol{\varepsilon} : (1 - \bar{d}(\mathbf{x})) \mathbb{E}_0 : \boldsymbol{\varepsilon} . \quad (3.11)$$

This non-local quantity arises from the integral over the neighborhood by means of

$$\bar{d}(\mathbf{x}) = \int_{\Omega} \alpha^*(\mathbf{x}, \boldsymbol{\zeta}) d(\boldsymbol{\zeta}) d\boldsymbol{\zeta} , \quad (3.12)$$

with the volume of the entire body Ω and a to be selected non-local weight function $\alpha^*(\mathbf{x}, \boldsymbol{\zeta})$ taking effect in the range of the points $\boldsymbol{\zeta}$ and \mathbf{x} . The evolution of the damage $d \in [0, 1]$ for the current time-step $m + 1$ is given by

$$d^{m+1} = 1 - (1 + \alpha(p(\boldsymbol{\varepsilon}^{m+1}) - r_1))^{-\beta} , \quad (3.13)$$

with the energy release rate $p(\boldsymbol{\varepsilon}^{m+1})$ analogously to the driving force, the local damage threshold r_1 and the material parameters α and β . Due to the defined surroundings an internal length scale is introduced and directly described by an adjustable parameter. This finally leads to stable

and mesh-independent finite element results, which, depending on the respective implementation, can be numerically expensive.

The first practically applied and in this context frequently quoted damage model with integral-type regularization was presented by Pijaudier-Cabot and Bažant (1987). In this work, previous approaches were improved by basically limiting the non-local treatment only to variables that control strain softening and to consider elastic parts of the strain as local. In this early stage of development, a usually typical weighting function was initially not included in the model but mentioned. Shortly thereafter, this weighting function was then implemented by Bažant and Pijaudier-Cabot (1988) besides some other improvements and investigations. Almost at the same time Bažant and Lin (1988) additionally introduced a smeared cracking with rotating orientation depending on the maximum principal strain in order to achieve more physical numerical results that are closer to experimental data. In the work of Jirásek (1998) a comparison of several integral-type approaches is provided under consideration of numerical as well as analytical solutions. An integral-based strategy can also be found in the work of Liu et al. (1999) in context of multiple-scale mesh-free methods as an alternative to commonly applied numerical methods for example the finite element method. Comi (2001) proposed a damage model with two isotropic damage variables and two internal length scales in order to capture tensile-compression asymmetry for rock-like materials. A further very detailed comparison of integral-type approaches is given by Bažant and Jirásek (2002) who additionally take into account plasticity. They discuss the progress of integral-type regularization models and their physical explanations, advantages, and applications. Also Lorentz and Andrieux (2003) considered several non-local approaches and extensively analyzed them in regards to thermodynamic consistency and discussed the dilemma between formulations providing effective regularization and fulfilling the thermodynamics. A coupled damage-plasticity model based on the non-local integral-type regularization is presented by Nguyen et al. (2015). This model is addressed to ductile materials and is able to consider the pre-cracking hardening as well as the post-cracking softening and further focuses on the determination of model parameters related to experimental data with a novel calibration method.

3.8 Gradient-Enhanced Regularization

The probably most common regularization technique is the gradient-enhancement. The main idea is to directly or indirectly apply a gradient to the internal variable, or more precisely the damage variable in the present case. This gradient is then penalized which corresponds to penalizing the differences or transitions between completely damaged and completely undamaged zones. In context of finite element calculations for example, this results in transforming individual or series of individual damaged elements into smooth transitions between these damaged and undamaged parts of the considered geometry. For this purpose, several strategies for applying the gradient to the model are available, whereat a non-local quantity can only be considered of course. First formulations hereby applied the gradient on the strains, for example in the work of Pijaudier-Cabot et al. (1988) as described hereinafter, and these formulations are related to so-called micromorphic models which are still used today. However, the today probably most common approach is to introduce a field function that is coupled to the local damage variable. Exemplary for the gradient-enhanced regularization in general, this approach is illustrated with a specific energetic formulation which is based on the work of Dimitrijevic and Hackl (2008),

which is again mentioned later. This energy Ψ is provided by the following equation

$$\Psi = \frac{1}{2} \boldsymbol{\varepsilon} : f(d) \mathbb{E}_0 : \boldsymbol{\varepsilon} + \frac{\alpha}{2} (\varphi - d)^2 + \frac{\beta}{2} |\nabla \varphi|^2, \quad (3.14)$$

with the damage variable d , a to be selected damage function $f(d)$ according to Section 4.1, the regularization parameters α and β , the field function φ and the gradient of the field function $\nabla \varphi$. The first term of the equation is related to a standard damage model. The mentioned coupling between the damage variable and the field function is done by the second term which penalizes the differences between both quantities depending on α . Hereto, the field function has to be calculated with the help of the additional stationarity condition

$$\int_{\Omega} \alpha (\varphi - d) \delta \varphi \, dV + \int_{\Omega} \beta \nabla \varphi \cdot \nabla \delta \varphi \, dV = 0 \quad \forall \delta \varphi. \quad (3.15)$$

The actual regularization is then enabled by penalizing the gradient of the field function in the third term which can be adjusted by β . The evolution of the damage d for the current time-step $m + 1$ is described by

$$d^{m+1} = d^m + \Delta \rho p(\boldsymbol{\varepsilon}^{m+1}, d^{m+1}, \varphi^{m+1}), \quad (3.16)$$

with the driving force $p(\boldsymbol{\varepsilon}^{m+1}, d^{m+1}, \varphi^{m+1})$. This implicit and rate-independent formulation is based on Equation (2.104) and can be solved with the yield function $\Phi = |p(\boldsymbol{\varepsilon}^{m+1}, d^{m+1}, \varphi^{m+1})| - r_1$ considering the threshold value r_1 . The described procedure introduced an internal length scale that corresponds, roughly said, to the range of the gradient which is adjustable with β or a corresponding prefixed parameter in other damage models. In general, this strategy of gradient-enhancement leads to mesh-independent finite element results in the end. However, the field function in the mentioned approach increases the number of unknowns at the nodes and therefore drastically also the numerical effort.

The first gradient-enhanced damage models were applied to the strains and these formulations are referred to as micromorphic models as mentioned before. They are originating from integral-type damage models which can be transformed by use of the Taylor series, incidentally this procedure does not apply for all gradient-enhanced formulations in general. Pijaudier-Cabot et al. (1988) dealt with this topic by comparing several approaches and by describing the transfer from integral-type to gradient-enhancement. However, in that work some physical explanations were not yet clarified and the gradient-enhancement was still presented as a special case of the integral formulations. A more general investigation of gradient formulations, which is related to localization in regards to fracture but also to the formation and propagation of deformation bands describing plastic flow, is given by Aifantis (1992). A consistent implementation into the finite element scheme is for example given by Peerlings et al. (1995) for a gradient-enhanced damage model considering quasi-brittle failure mechanisms. As already mentioned before, the gradient was initially applied directly to the strains but further research provided formulations that are affecting the internal variables instead, as for example done by De Borst and Mühlhaus (1992) in regard to plasticity who also presented the corresponding numerical treatment. This procedure was later adopted to damage modeling as for example shown in the work of Lorentz and Andrieux (1999) in which a variational framework for models with gradients of internal variables was generally derived and then, amongst others, applied to an already existing damage model based on homogenization. Based on that, Lorentz and Benallal (2005) discussed several numerical aspects with a focus on the numerical integration of the gradient constitutive equations providing a specific algorithm. Another very interesting work

is presented by Abu Al-Rub and Voyiadjis (2005) who formulated a new algorithmic implementation for gradient-enhanced damage models in order to circumvent large modifications of existing finite element codes for the computation of the higher-order gradient terms. The idea is close to the presented damage Model III [LAP] in Section 4.4 of this thesis, however the implicit scheme is solved globally, which is expensive, and the model is limited to regular meshes only. Finally, the at the beginning mentioned gradient-enhanced formulation with use of the coupled field function, which probably can be considered as the most common approach for gradient-enhanced regularization today, is introduced by Dimitrijevic and Hackl (2008). The procedure has already been explained before, the model was also extended to the framework of plasticity by Dimitrijevic and Hackl (2011) and was applied in context of fragmentation of nano-structured nodes for batteries by Dimitrijevic et al. (2012). Furthermore, phase-field models can also be interpreted as gradient-enhanced models. For example Miehe et al. (2010a) presented a thermodynamically consistent approach based on variational principles and multi-field finite element implementations and an alternative including a more robust algorithm based on operator splits is also given by Miehe et al. (2010b). Another example for phase-field models is given by Strobl and Seelig (2015), who has taken the orientation of cracks into account in order to satisfy crack boundary conditions. This work was continued also by Strobl and Seelig (2016) in which the focus was on the choice of the constitutive assumptions in regard to achieve more flexible formulations. Brepols et al. (2017) presented a gradient-enhanced model, which is a current example for micromorphic damage models, including a two-surface formulation for the distinct but coupled treatment of damage and plasticity. An example related to the extended finite element method (XFEM) is given by Peters and Hackl (2005) in which different numerical aspects were investigated. Moreover, XFEM was also subject of investigation in the work of Pezeshki et al. (2018). Therein, crack propagation under dynamic loading is modeled with a continuous-discrete approach in context of gradient-enhanced damage.

3.9 Selected Regularization Strategies for Investigation

The previous Sections 3.7 to 3.8 have introduced different strategies for the regularization of damage models, some of which have been used for the three novel approaches referred to as Model I [REL], Model II [ERVE], and Model III [LAP] presented in Chapter 4. In addition, all of these approaches can be assigned to an underlying damage model according to the previous Sections 3.2 to 3.4.

All of the damage models presented in this theses belong to the group of continuum damage models. Hereby, Model I [REL] is based on two-state models. These models only consider an undamaged and damaged phase and allow for mixtures in order to represent different damage states. Model II [ERVE] indeed emulates a microstructure for numerical reasons but the damage is still phenomenologically formulated. The latter also applies for Model III [LAP].

Even though the novel approaches belong to the same group of damage models, the regularization strategies are different. Model I [REL] and Model II [ERVE] are related to different kinds of viscous regularization whereas Model III [LAP] is related to the gradient-enhanced regularization. Integral-type regularization has not been considered for investigation since, from our point of view, this strategy has become less popular in context of damage modeling and is furthermore too expensive.

The viscous regularization in case of Model I [REL] interacts with the non-linear homogenization of the energy. Nevertheless, the regularization of the model is fundamentally based on the involvement of viscous effects. A completely different kind of viscous regularization is applied in case of Model II [ERVE]. This regularization combines a rate-limitation of the evolving damage variable with an numerical interpretation of the microstructure by use of an newly introduced emulated representative volume element (ERVE). A special feature is the elimination of rate-dependence. The gradient-enhancement of Model III [LAP] is highly improved by a very efficient evaluation of the Laplace operator as well as a skilled selection of operator splits. All applied regularization strategies are expected to improve existing and common approaches. More details on the models are presented hereinafter followed by the respective investigations.

4 Novel Approaches to Regularized Damage Models

In this chapter three underlying regularized damage models are presented. Initially, fundamentals of damage modeling relating to different damage functions are introduced in Section 4.1. Afterwards in Section 4.2, Model I [REL] is presented which is based on two phases and energy relaxation. Subsequently, Section 4.3 introduces Model II [ERVE] using an emulated representative volume element (ERVE). Finally, Model III [LAP] that efficiently evaluates a Laplacian for gradient-enhancement is presented in Section 4.4.

4.1 Fundamentals of Damage Modeling

Typical damage functions are introduced as most damage models are based on their application like the present models in this thesis. Only Model I [REL] has an alternative formulation that is based on the mixture of the underlying phases. Nevertheless, a general interpretation as a mixture of phases can basically be done for all presented damage models. The Helmholtz free energy Ψ of a material suffering from damage is formulated as follows

$$\Psi = f(d) \Psi_0 , \quad (4.1)$$

with the energy Ψ_0 related to the undamaged material described by

$$\Psi_0 = \frac{1}{2} \boldsymbol{\varepsilon} : \mathbb{E}_0 : \boldsymbol{\varepsilon} , \quad (4.2)$$

and with the damage function $f(d)$ that is based on the damage variable d . This damage variable d increases from 0, representing the undamaged state, to a specific value or towards infinity. Accordingly, the damage function $f(d)$ describes the reduction of material stiffness and decreases from 1 to 0, thus from a completely undamaged to a completely damaged state. For that reason, the behavior of the damage variable and function have to be coordinated and furthermore, the damage function has to meet several requirements based on the formulation of the respective damage models. Usually, the damage function has to be at least twice differentiable in order to ensure damage depending driving forces for example. A typical choice is

$$f(d) = e^{-d} , \quad (4.3)$$

with $d \in [0, \infty[$ and $d = 0$ representing the undamaged material whereas the damaged material is striving towards infinity. This exponential function has the advantage, that the damage variable is not bounded, the derivatives can easily be achieved as often as required and furthermore these derivatives are corresponding to the negative initial function, thus $f'(d) = -f(d)$. It is applied in the works of Dimitrijevic and Hackl (2008) and Dimitrijevic and Hackl (2011) for example. Moreover, a more popular choice for a damage function is

$$f(d) = (1 - d)^2 , \quad (4.4)$$

with $d \in [0, 1]$ and again $d = 0$ for the undamaged material that is striving due to evolving damage against $d = 1$ for the completely damaged state. This damage function is often used in the literature, for example in work of Miehe et al. (2010b) and Brepols et al. (2017). A further common and basic damage function is given by

$$f(d) = 1 - d, \quad (4.5)$$

with basically the same properties as before but with a slightly different behavior. However, the main difference is that this linear damage function results in thermodynamic driving forces that are independent from the damage variable d . This function is actually the first formulated one and can for example be found in the works of Kachanov (1958), Lemaitre (1985), Kachanov (1999), and Wriggers and Moftah (2006).

4.2 Model I: Relaxation Based Regularization with Two-Phases

In this chapter a regularized damage model based on relaxation with use of two phases is presented. The model is directly based on the works of Junker et al. (2016) and Schwarz et al. (2016) and was also enhanced with plasticity in the works of Schwarz et al. (2017) and Schwarz et al. (2018b). The model is denoted as Model I [REL] in this thesis.

Subsequently, Subsection 4.2.1 first introduces two-phase damage models by relaxation, afterwards the non-linear homogenization between the Reuß and Voigt energy is presented in Subsection 4.2.2, then in Subsection 4.2.3 viscosity is additionally considered for mesh-independence. The stresses and material tangent is determined in Subsection 4.2.4 and finally Subsection 4.2.5 provides the respective algorithm on the material point level.

4.2.1 Two-phase Damage Modeling by Relaxation

The underlying idea of the two-phase model is to distinguish an undamaged and a damaged phase and to allow intermediate states by (volume) fractions that are described by the damage variable d . But first, the two phases are introduced by respective Helmholtz free energies

$$\Psi_0(\boldsymbol{\varepsilon}) := \frac{1}{2} \boldsymbol{\varepsilon} : \mathbb{E}_0 : \boldsymbol{\varepsilon}, \quad (4.6)$$

$$\Psi_1(\boldsymbol{\varepsilon}) := \frac{1}{2} \boldsymbol{\varepsilon} : \kappa \mathbb{E}_0 : \boldsymbol{\varepsilon}, \quad (4.7)$$

whereby the subscripts refer to the undamaged (0) and damaged (1) material and the numerical factor $\kappa \ll 1$ describes the reduction of the damaged phase in relation to the undamaged phase. The two energies are illustrated by Figure 4.1 in the condensed space. The color green is related to the undamaged and red is related to the damaged phase. For the consideration in the condensed space, dissipative processes and therefore the dissipation function \mathcal{D} is taken into account. The condensed energy state Ψ^{cond} is defined as

$$\Psi^{\text{cond}} := \Psi + \int \mathcal{D}(\dot{d}) dt, \quad (4.8)$$

with the rate of the damage parameter denoted by \dot{d} . As already mentioned before, the damage variable $d \in [0, 1]$ allows to describe the prescribed damage states as well as the intermediate states and serves as a volume fraction: $d = 0$ is related to the completely undamaged state, $d = 1$ is related to the completely damaged state, and all values inbetween are related to intermediate states that describe the increase of the damage from 0 to 1. Hereto, a mixture of the energy states Ψ_0 and Ψ_1 has to be realized that can be done by several homogenization methods.

The opposite ends hereby are the Voigt and the Reuß bounds: while the Reuß energy describes a linear transition from Ψ_0 to Ψ_1 leading to a convex energy that is associated with mesh-independent numerical results, the Voigt energy on the contrary describes an instantaneous jump from Ψ_0 to Ψ_1 at the intersection point leading to a non-convex energy that is associated with mesh-dependent numerical results.

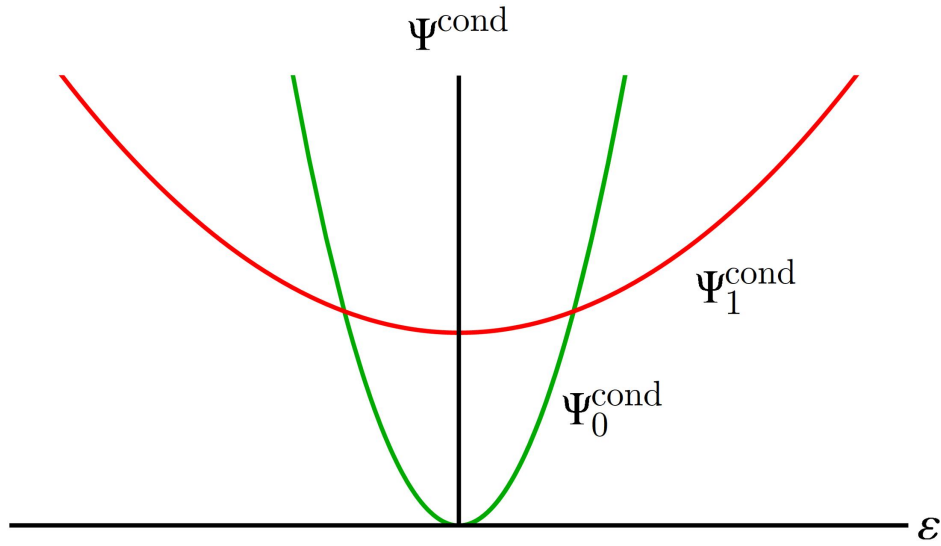


Figure 4.1: Model I [REL]: Undamaged and damaged energy in the condensed space.

The relaxed Reuß energy $\Psi^{\text{rel}} = \Psi_{\text{Reuß}}$ as well as the Voigt energy Ψ_{Voigt} are defined by

$$\Psi_{\text{Reuß}} = \inf_{\varepsilon_i} \{ (1-d) \Psi_0(\varepsilon_0) + d \Psi_1(\varepsilon_1) \mid (1-d) \varepsilon_0 + d \varepsilon_1 = \varepsilon \}, \quad (4.9)$$

$$\Psi_{\text{Voigt}} = \inf \{ \Psi_0, \Psi_1 \}, \quad (4.10)$$

accordingly these expressions results in

$$\Psi_{\text{Reuß}} = \frac{1}{2} \varepsilon : \mathbb{E}_{\text{Reuß}} : \varepsilon, \quad (4.11)$$

$$\Psi_{\text{Voigt}} = \frac{1}{2} \varepsilon : \mathbb{E}_{\text{Voigt}} : \varepsilon, \quad (4.12)$$

with the related elastic tensors

$$\mathbb{E}_{\text{Reuß}} = \left[(1-d) \mathbb{E}_0^{-1} + d \frac{1}{\kappa} \mathbb{E}_0^{-1} \right]^{-1} = f_{\text{Reuß}}(d) \mathbb{E}_0, \quad (4.13)$$

$$\mathbb{E}_{\text{Voigt}} = \begin{cases} \mathbb{E}_0 & : \Psi_0 < \Psi_1 \\ \kappa \mathbb{E}_0 & : \text{else} \end{cases}, \quad (4.14)$$

and respective damage function

$$f_{\text{Reuß}}(d) = \left[1 - d + d \frac{1}{\kappa} \right]^{-1} . \quad (4.15)$$

Finally, the stresses can be achieved by the derivative of the total energy, thus

$$\boldsymbol{\sigma}_{\text{Reuß}} = \frac{\partial \Psi_{\text{Reuß}}}{\partial \boldsymbol{\varepsilon}} = \mathbb{E}_{\text{Reuß}} : \boldsymbol{\varepsilon} , \quad (4.16)$$

$$\boldsymbol{\sigma}_{\text{Voigt}} = \frac{\partial \Psi_{\text{Voigt}}}{\partial \boldsymbol{\varepsilon}} = \mathbb{E}_{\text{Voigt}} : \boldsymbol{\varepsilon} . \quad (4.17)$$

Both homogenization energies and related stresses are illustrated by Figures 4.2 to 4.5: the green curves correspond to the undamaged states, the red curves to the damaged states as before, and additionally, the blue curves to the homogenized intermediate states. Figures 4.2 and 4.3 present the Reuß bound and Figures 4.4 and 4.5 the Voigt bound.

Although the Reuß energy seems to be the more appropriate choice because of the convexity and the associated mesh-independent results, the stress behavior is unexpected from a physical point of view: there is absolutely no drop of the stresses but a plateau instead. Usually, one would expect a significant drop of stresses for damage problems. Therefore, the Reuß bound requires more investigation, but first the plots for the Voigt bound are presented.

Whereas the Voigt energy provides a very significant drop of stresses, which complies with the characteristic of damage problems, unfortunately it comes along with a non-convex energy that is associated with mesh-dependent results by default. Therefore, this energy cannot be an appropriate choice for a regularized damage model. For the mentioned reasons, the Reuß bound is generally preferable since mesh-independent results are in the focus of interest at this point, therefore further investigation are continued considering the Reuß bound.

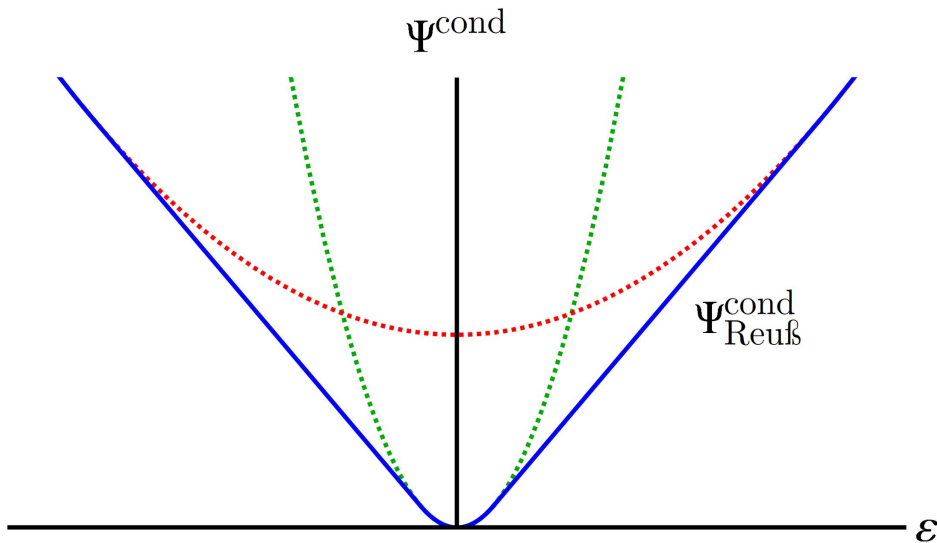


Figure 4.2: Model I [REL]: Energies in condensed space for the Reuß bound.

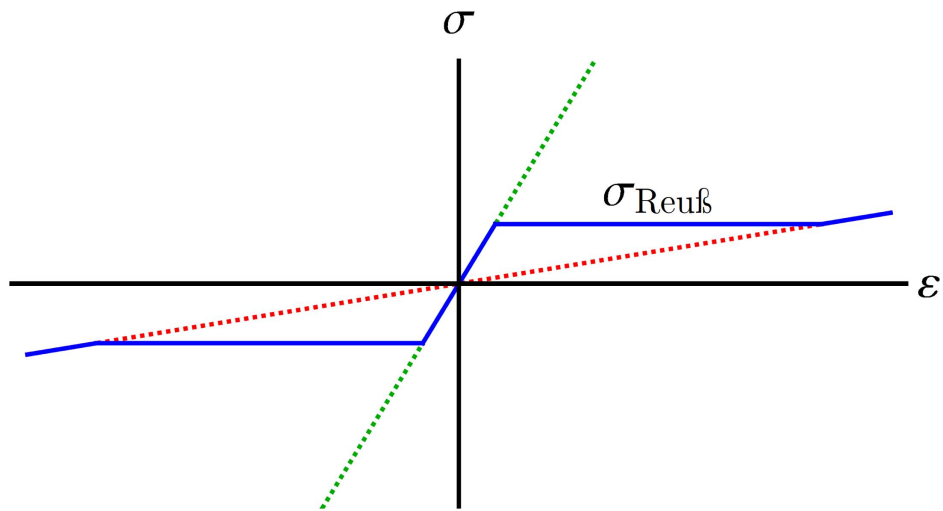


Figure 4.3: Model I [REL]: Stresses for the Reuß bound.

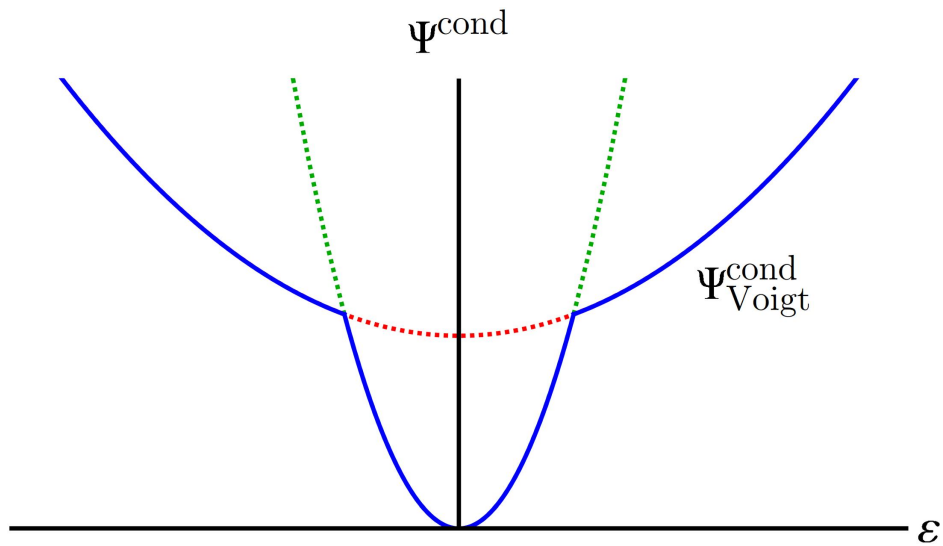


Figure 4.4: Model I [REL]: Energies in condensed space for the Voigt bound.

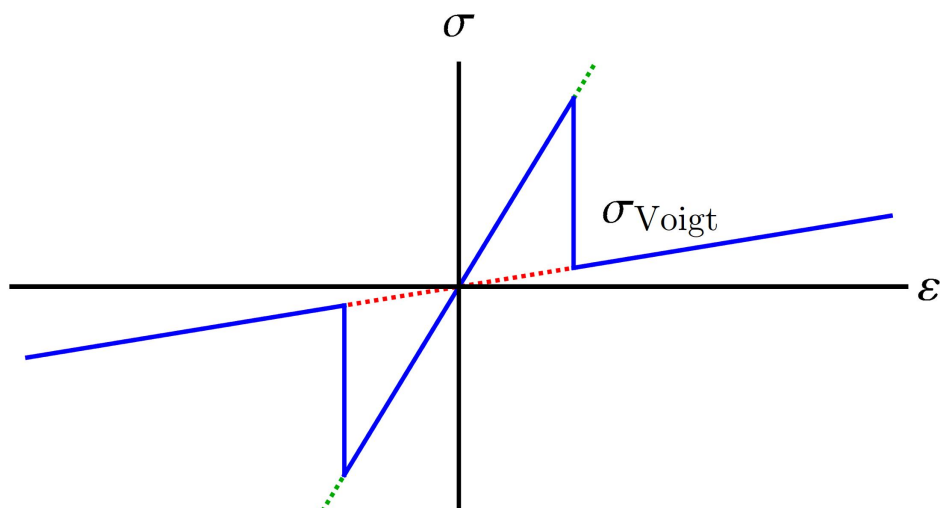


Figure 4.5: Model I [REL]: Stresses for the Voigt bound.

In order to achieve the evolution equation for the damage variable d the Hamilton principle based on Section 2.6 is applied

$$\delta\mathcal{G} + \int_{\Omega} \frac{\partial\mathcal{D}}{\partial\dot{d}} \delta d \, dV = 0, \quad (4.18)$$

which can be transformed into the principle of the minimum of the dissipation potential (PMDP) according to Subsection 2.6.4, since there is no dependence on the gradient of d . The Lagrangian \mathcal{L} , which has to be minimized with respect to the rate of the internal variable d , reads

$$\mathcal{L} := \dot{\Psi}_{\text{Reu}\beta} + \mathcal{D} + \mathcal{C} \rightarrow \min_d. \quad (4.19)$$

Hereby, the Lagrangian \mathcal{L} consists of three parts: the time-derivative of the Helmholtz free energy $\dot{\Psi}_{\text{Reu}\beta}$, the dissipation function \mathcal{D} and the constraints \mathcal{C} that have to be taken into account. The time-derivative of the Helmholtz free energy $\dot{\Psi}_{\text{Reu}\beta}$ is derived by the chain rule, thus

$$\dot{\Psi}_{\text{Reu}\beta} = \frac{\partial\Psi_{\text{Reu}\beta}}{\partial\boldsymbol{\varepsilon}} : \dot{\boldsymbol{\varepsilon}} + \frac{\partial\Psi_{\text{Reu}\beta}}{\partial d} \dot{d}. \quad (4.20)$$

The dissipation function is first chosen to be rate-independent (RI), therefore an elasto-plastic approach of order one is used as given by

$$\mathcal{D}_{\text{RI}} = r_1 |\dot{d}|, \quad (4.21)$$

where the dissipation parameter r_1 functions as an energetic threshold for the damage evolution. Since the damage variable d can only increase and only until $d = 1$ for physical reasons, the damage evolution is constrained by the Karush-Kuhn-Tucker parameter γ as follows

$$\gamma = \begin{cases} -\gamma^* & : \dot{d} < 0 \\ \gamma^* & : \dot{d} > 0 \wedge d = 1 \\ 0 & : \text{else} . \end{cases} \quad (4.22)$$

Collecting all parts of the Lagrangian \mathcal{L} provides the underlying equation for the PMDP

$$\mathcal{L} := \frac{\partial\Psi_{\text{Reu}\beta}}{\partial\boldsymbol{\varepsilon}} : \dot{\boldsymbol{\varepsilon}} + \frac{\partial\Psi_{\text{Reu}\beta}}{\partial d} \dot{d} + r_1 |\dot{d}| + \gamma \dot{d} \rightarrow \min_d. \quad (4.23)$$

The minimization condition for the Lagrangian \mathcal{L} reads

$$\frac{\partial\mathcal{L}}{\partial\dot{d}} = \frac{\partial\Psi_{\text{Reu}\beta}}{\partial d} + r_1 \frac{\dot{d}}{|\dot{d}|} + \gamma \ni 0. \quad (4.24)$$

After introducing the driving force

$$p = -\frac{\partial\Psi_{\text{Reu}\beta}}{\partial d} = -\frac{1}{2} f'_{\text{Reu}\beta}(d) \boldsymbol{\varepsilon} : \mathbb{E}_0 : \boldsymbol{\varepsilon}, \quad (4.25)$$

where

$$f'_{\text{Reu}\beta}(d) = \left(1 - \frac{1}{\kappa}\right) \left(1 - d + d\frac{1}{\kappa}\right)^{-2}, \quad (4.26)$$

the rate-independent (“RI”) evolution equation of the damage variable d can finally be derived solving Equation (4.24) for the rate of the internal variable considering an active-set for the Karush-Kuhn-Tucker parameter γ and introducing the consistency parameter $\Delta\rho$, thus

$$\dot{d}_{\text{RI}} := \dot{d} = \Delta\rho p = \frac{|\dot{d}|}{r_1} p. \quad (4.27)$$

Performing the Legendre transformation for \mathcal{D} provides

$$\mathcal{D}^* = \sup_{\dot{d}} \left\{ p\dot{d} - \mathcal{D} \right\} = \sup_{\dot{d}} \left\{ |\dot{d}|(p \operatorname{sgn} \dot{d} - r_1) \right\}, \quad (4.28)$$

which allows to determine the consistency parameter $\Delta\rho$ by the obtained yield function

$$\Phi := |p| - r_1. \quad (4.29)$$

A rate- and mesh-independent damage model with a convex energy has been derived.

The proceeding numerical treatment in regard to finite element calculations is postponed to Appendix A since this model variant is not the final one. The stresses are analogous to Equation (4.52) and read as follows

$$\tilde{\boldsymbol{\sigma}}^{m+1} = f_{\text{Reu}\beta}(d^m) \tilde{\mathbb{E}}_0 \cdot \tilde{\boldsymbol{\varepsilon}}^{m+1} + f'_{\text{Reu}\beta}(d^m) \tilde{\mathbb{E}}_0 \cdot \tilde{\boldsymbol{\varepsilon}}^m \Delta d. \quad (4.30)$$

The material tangent, analogous to Equation (A.17), corresponds to

$$\begin{aligned} \left. \frac{d\tilde{\boldsymbol{\sigma}}}{d\tilde{\boldsymbol{\varepsilon}}} \right|^{m+1} &= f_{\text{Reu}\beta}(d^m) \tilde{\mathbb{E}}_0 - \left(\tilde{\mathbb{E}}_0 \cdot \tilde{\boldsymbol{\varepsilon}}^m \right) \otimes \left(\tilde{\mathbb{E}}_0 \cdot \tilde{\boldsymbol{\varepsilon}}^{m+1} \right) \times \left(\Delta\rho f'_{\text{Reu}\beta}(d^m)^2 \right. \\ &\quad \left. - f'_{\text{Reu}\beta}(d^m) \frac{-f'_{\text{Reu}\beta}(d^{m+1}) + \frac{1}{2} f''_{\text{Reu}\beta}(d^{m+1}) \tilde{\boldsymbol{\varepsilon}}^{m+1} \cdot \tilde{\mathbb{E}}_0 \cdot \tilde{\boldsymbol{\varepsilon}}^{m+1} \Delta\rho f'_{\text{Reu}\beta}(d^m)}{\frac{1}{2} f''_{\text{Reu}\beta}(d^{m+1}) \tilde{\boldsymbol{\varepsilon}}^{m+1} \cdot \tilde{\mathbb{E}}_0 \cdot \tilde{\boldsymbol{\varepsilon}}^{m+1}} \right) \end{aligned} \quad (4.31)$$

and, according to Equation (A.18), in case of no evolving damage the tangent simplifies to

$$\left. \frac{d\tilde{\boldsymbol{\sigma}}}{d\tilde{\boldsymbol{\varepsilon}}} \right|^{m+1} = f_{\text{Reu}\beta}(d^m) \tilde{\mathbb{E}}_0. \quad (4.32)$$

The overall finite element procedure is additionally provided by Algorithm 5. In order to investigate the behavior of the model in more detail, finite element calculations for a double-notched plate (geometry given in Section 5.1 and parameters in Subsection 5.2.4) have been performed and the results are provided subsequently: the global structural response is presented in Figure 4.6 and the related damage distribution is presented by Figure 4.7.

Although the damage distribution in the coarse mesh at first glance slightly differs from the other meshes in Figure 4.7 by having a thicker damage zone, the total amount of damage seems to be comparable to the coinciding middle and fine meshes since the value of the damage function is smaller. The difference in the damage distribution can be a result of a too coarse mesh or distorted elements for example, however, the global response by means of the

force-displacement curves in Figure 4.6 confirm the expected mesh-independent behavior of the convex damage model for all three meshes.

The obvious disadvantage of the convex damage model is the missing drop in the force-displacements diagram in Figure 4.6 as already assumed by the mathematical derivation of stresses providing the plateau in Figure 4.3. This missing drop also has an impact on the damage distribution since the results differ from other results that are presented later. The plateau behavior contradicts the physical expectations and thus further modifications are necessary. Hereto, the following Subsection 4.2.2 deals with a modification of the homogenization method.

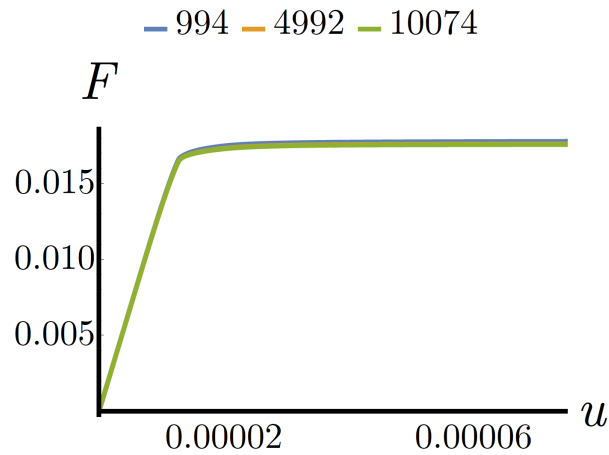


Figure 4.6: Model I [REL] rate-independent: Comparing different numbers of elements (as stated) by double-notched plate for structures meshes.

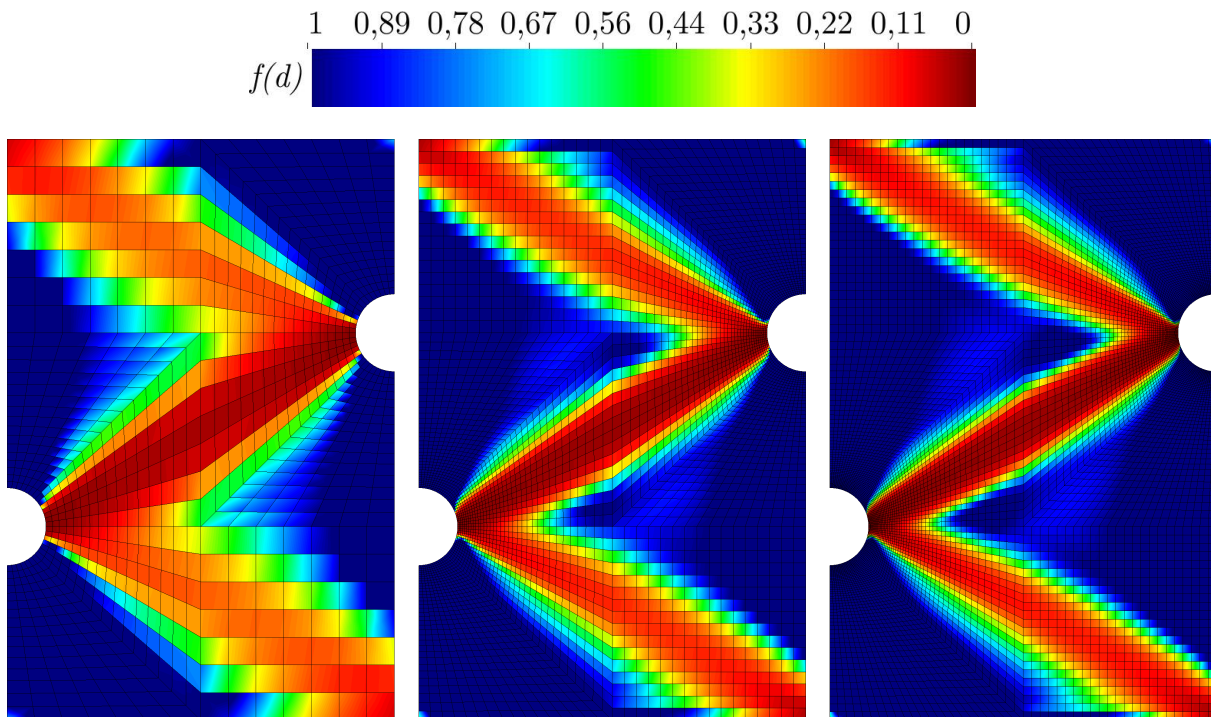


Figure 4.7: Model I [REL] rate-independent: Distribution of $f(d)$ for the double-notched plate with 994, 4992, and 10074 structured elements (left to right).

4.2.2 Non-Linear Homogenization between Reuß and Voigt

The previous Subsection 4.2.1 presented a convex damage model based on the Reuß bound. The model provided mesh-independent results but at the expense of unphysical stress-strain/force-displacement curves: the expected drop of stresses/forces was missing. For that reason, the homogenization method has to be modified in order to achieve an energy that provides mesh-independent results as well as a typical physical behavior including decreasing stresses/forces.

The fundamental idea is to find a compromise between the Reuß and Voigt bound and thus between a completely convex and non-convex energy. While the Reuß bound provides a linear transition between the damage states, the Voigt bound directly jumps from one state to the other. The new energy will be considered inbetween and thus provide a non-linear behavior. This non-linear homogenization of the damage states is supposed to ensure the dropping stresses/forces. At the same time, the energy has to be close enough to the Reuß bound in order to ensure mesh-independent results. The introduction of a parameter β allows for the mentioned non-linear homogenization and a switch between the Reuß and the Voigt energy or naturally something in between. Thus, the energy Ψ_β is introduced by

$$\Psi_\beta := \inf_{\varepsilon_i} \left\{ (1 - \alpha d - d^\beta) \Psi_0(\varepsilon_0) + (\alpha d + d^\beta) \Psi_1(\varepsilon_1) \mid (1 - \alpha d - d^\beta) \varepsilon_0 + (\alpha d + d^\beta) \varepsilon_1 = \varepsilon \right\}, \quad (4.33)$$

with the very small parameter $1 \gg \alpha > 0$, which ensures non-zero driving forces in Equations (4.38) and (4.39) in case of $\varepsilon \neq \mathbf{0}$ and $d = 0$, and the parameter $\beta > 1$ of course, which controls the non-linear homogenization. This modified expression finally results in

$$\Psi_\beta = \frac{1}{2} \varepsilon : \mathbb{E}_\beta : \varepsilon, \quad (4.34)$$

with the related elastic tensor

$$\mathbb{E}_\beta = \left[(1 - \alpha d - d^\beta) \mathbb{E}_0^{-1} + (\alpha d + d^\beta) \frac{1}{\kappa} \mathbb{E}_0^{-1} \right]^{-1} = f_\beta(d) \mathbb{E}_0, \quad (4.35)$$

and the respective damage function

$$f_\beta(d) = \left[1 + (\alpha d + d^\beta) \left(\frac{1}{\kappa} - 1 \right) \right]^{-1}. \quad (4.36)$$

As in the previous section, the stresses can be calculated by taking the derivative of the energy

$$\boldsymbol{\sigma} = \frac{\partial \Psi_\beta}{\partial \boldsymbol{\varepsilon}} = f_\beta(d) \mathbb{E}_0 : \boldsymbol{\varepsilon}. \quad (4.37)$$

The modified energy is illustrated by Figures 4.8 and 4.9. Again, the green and red curves are related to the undamaged and damaged states and the blue curves to the homogenized states. The blue dashed curves remind of the convex Reuß energy whereas the blue solid curves represent the new non-linear homogenization. Finally, decreasing stresses are achieved due to the modification. This is due to the non-linearity of the energy whose derivative is no longer constant but linearly decreasing. The intensity of the drop of stresses is naturally depending on the curvature of the energy and therefore on the chosen homogenization parameter β , which in this context acts as the regularization parameter. Further investigations are following hereinafter.

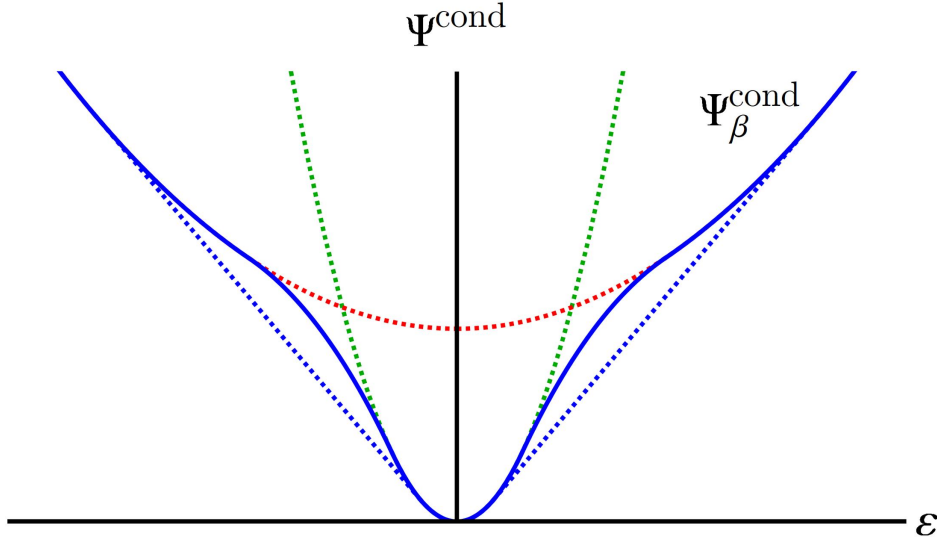


Figure 4.8: Model I [REL]: Energies in condensed space for the non-linear homogenization.

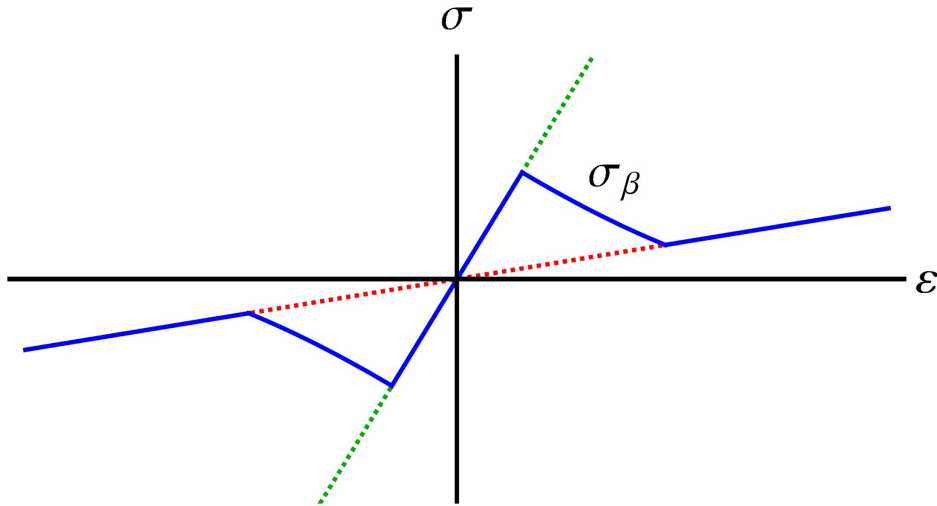


Figure 4.9: Model I [REL]: Stresses for the non-linear homogenization.

Analogously to the last Section 4.2.1, the evolution equation for the damage variable d has to be derived with the PMDP, see Subsection 2.6.4. Identical steps are skipped. The driving force

$$p_\beta := -\frac{\partial \Psi_\beta}{\partial d} = -\frac{1}{2} f'_\beta(d) \varepsilon : \mathbb{E}_0 : \varepsilon \quad (4.38)$$

for the modified energy is derived including

$$f'_\beta(d) = (\alpha + \beta d^{\beta-1}) \left(\frac{1}{\kappa} - 1 \right) \left(1 + (\alpha d + d^\beta) \left(\frac{1}{\kappa} - 1 \right) \right)^{-2}. \quad (4.39)$$

Herewith a modified, rate-independent damage model with an “almost” convex energy which is capable of dropping stresses/forces has been derived. The numerical parameter α as well as the regularization parameter β allow to control the homogenization that includes the opposite ends of convexity: a distinction into three cases is possible: a parameter set of $\alpha = 0$ and $\beta = 1$ leads to the completely convex energy characterized by the Reuß bound, a parameter set of $\alpha = 0$ and $\beta \rightarrow \infty$ leads to the completely non-convex energy characterized by the Voigt bound, and a

mixture between both opposite cases is realized by a parameter set of $\alpha \neq 0$ and $\beta > 1$ leading to the desired modified energy. The numerical treatment in regard to finite element calculations is analogous to the last section, the stresses are based on Equation (4.52) resulting in

$$\tilde{\sigma}^{m+1} = f_\beta(d^m) \tilde{\mathbb{E}}_0 \cdot \tilde{\epsilon}^{m+1} + f'_\beta(d^m) \tilde{\mathbb{E}}_0 \cdot \tilde{\epsilon}^m \Delta d, \quad (4.40)$$

the material tangent is based on Equation (A.17), therefore

$$\left. \frac{d\tilde{\sigma}}{d\tilde{\epsilon}} \right|^{m+1} = f_\beta(d^m) \tilde{\mathbb{E}}_0 - \left(\tilde{\mathbb{E}}_0 \cdot \tilde{\epsilon}^m \right) \otimes \left(\tilde{\mathbb{E}}_0 \cdot \tilde{\epsilon}^{m+1} \right) \times \left(\Delta \rho f'_\beta(d^m)^2 - f'_\beta(d^m) \frac{-f'_\beta(d^{m+1}) + \frac{1}{2} f''_\beta(d^{m+1}) \tilde{\epsilon}^{m+1} \cdot \tilde{\mathbb{E}}_0 \cdot \tilde{\epsilon}^{m+1} \Delta \rho f'_\beta(d^m)}{\frac{1}{2} f''_\beta(d^{m+1}) \tilde{\epsilon}^{m+1} \cdot \tilde{\mathbb{E}}_0 \cdot \tilde{\epsilon}^{m+1}} \right), \quad (4.41)$$

and for no evolving damage it is based on Equation (A.18), consequently

$$\left. \frac{d\tilde{\sigma}}{d\tilde{\epsilon}} \right|^{m+1} = f_\beta(d^m) \tilde{\mathbb{E}}_0. \quad (4.42)$$

Based on that, numerical results are presented for different regularization parameters β . In regard to the results for the double-notched plate, it is focused on the global responses presented in Figure 4.11 in order to evaluate the behavior of the modified energies. Nevertheless, the related damage distribution for different meshes presenting the strongest force-decreasing case at $\beta = 1.3$ is provided in Figure 4.10 for illustrations.

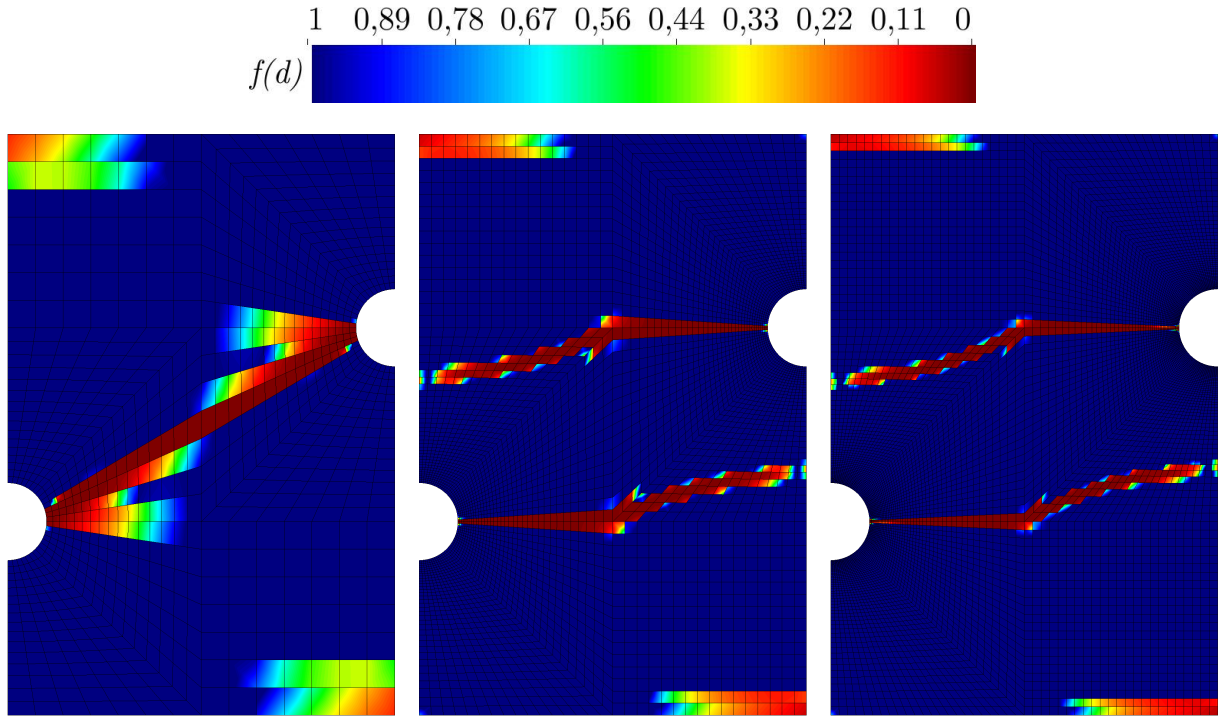


Figure 4.10: Model I [REL] rate-independent and non-linear: Distribution of $f(d)$ for finite element calculations with 994, 4992 and 10074 structured elements (left to right) for the double-notched plate considering the regularization parameter $\beta = 1.3$.

Concluding the global responses in Figure 4.11, the modification of the damage model by means of applying a non-linear homogenization method allows for a more physical behavior due to the dropping stresses/forces, but unfortunately even for small values of the regularization parameter β and therefore slight drops of stresses/forces this modification leads to mesh-dependent finite element results. Adjusting the regularization parameter β to a smaller value in order to move the non-linear energy even closer to the Reuß bound improves the mesh-independence but at the expense of the physical meaningfulness: the drop of stresses/forces disappears and finally the improvement of the modification disappears as well. There is no acceptable compromise between a more convex energy providing mesh-independent results and a less convex energy providing physical behavior.

For illustration purposes, the most physical case with the strongest drop, which is still not sufficient, is presented in Figure 4.10. The regularization parameter for this case is $\beta = 1.3$ and the mentioned mesh-dependence can clearly be seen by the different and localized cracks.

For the stated reasons, a less convex energy with physical correct behavior providing dropping stresses/forces has to be chosen and the consequent mesh-dependence has to be removed by considering some viscosity as presented in the subsequent Subsection 4.2.3.

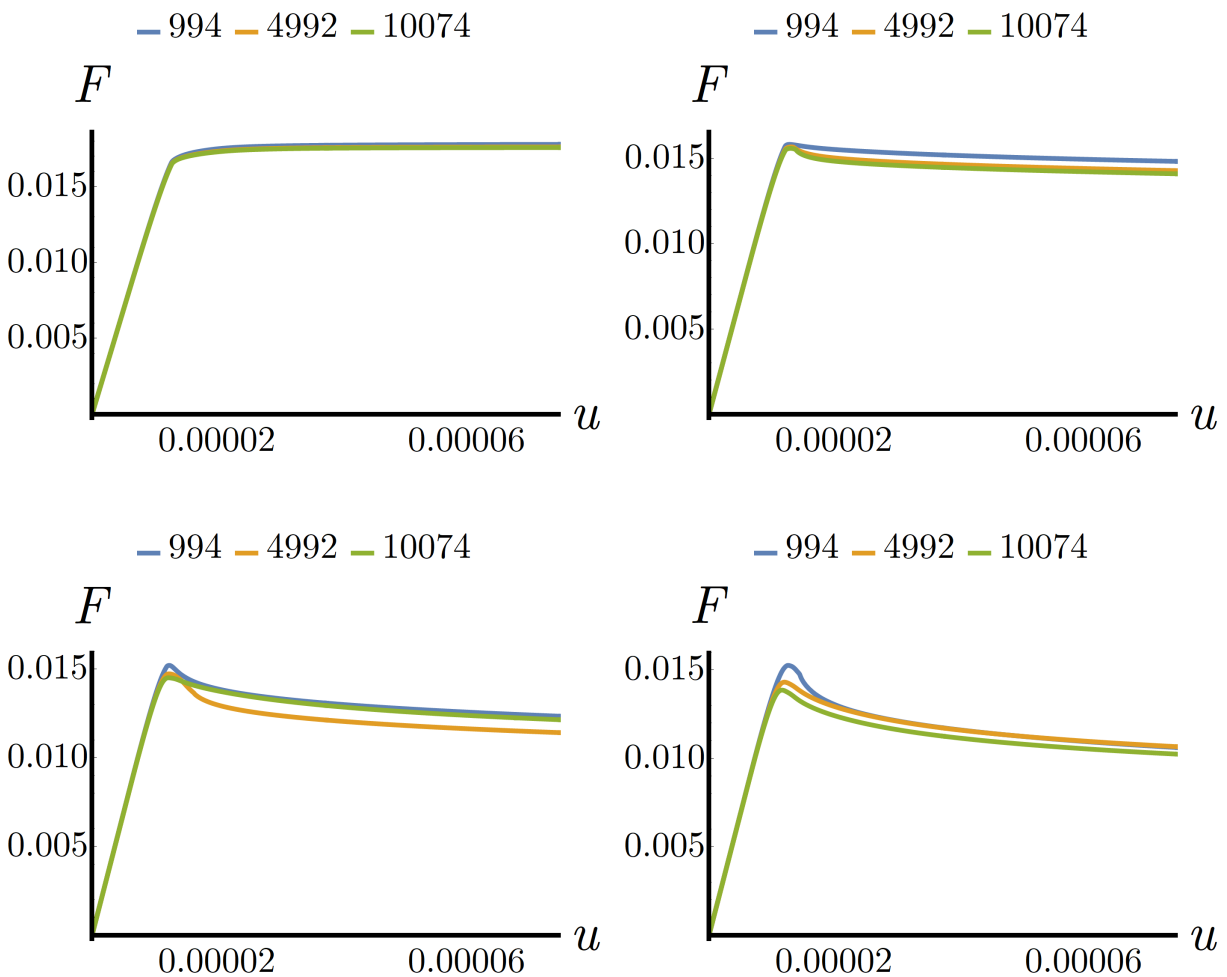


Figure 4.11: Model I [REL] rate-independent and non-linear: Study on regularization parameters $\beta = \{1.0, 1.1, 1.2, 1.3\}$ (top left to bottom right) with different numbers of elements (as stated) by double-notched plate for structured meshes.

4.2.3 Additional Consideration of Viscosity for Mesh-Independence

A damage model considering a non-linear homogenization method providing physical correct drops of stresses/forces but also mesh-depending results is presented in the previous Subsection 4.2.2. After choosing physical meaningful regularization parameters, which ensure a sufficient drop of stresses/forces, the resulting mesh-dependence has to be removed by adding viscous effects to the model. Therefore, the model becomes rate-dependent.

The desired viscosity is considered by choosing a rate-dependent (“RD”) dissipation function \mathcal{D} by means of an elasto-viscoplastic approach of order two as follows

$$\mathcal{D}_{\text{RD}} = r_1 |\dot{d}| + \frac{r_2}{2} \dot{d}^2 . \quad (4.43)$$

At this point the procedure is again analogous to Subsection 4.2.1 and also based on the non-linear homogenized model from the last Subsection 4.2.2. Identical steps are skipped again. The modification of the dissipation function \mathcal{D} results in changes of the Lagrangian \mathcal{L} , thus

$$\mathcal{L} := \frac{\partial \Psi_\beta}{\partial \boldsymbol{\varepsilon}} : \dot{\boldsymbol{\varepsilon}} + \frac{\partial \Psi_\beta}{\partial d} \dot{d} + r_1 |\dot{d}| + \frac{r_2}{2} \dot{d}^2 + \gamma \dot{d} \rightarrow \min_d , \quad (4.44)$$

while the minimization condition for the Lagrangian \mathcal{L} turns into

$$\frac{\partial \mathcal{L}}{\partial \dot{d}} = \frac{\partial \Psi_\beta}{\partial d} + r_1 \frac{\dot{d}}{|\dot{d}|} + r_2 \dot{d} + \gamma . \quad (4.45)$$

The driving force p_β conforms to the last Subsection 4.2.2. The rate-dependent evolution equation of the damage variable d is derived by solving Equation (4.45) for the rate of the internal variable considering, again, an active-set for the Karush-Kuhn-Tucker parameter γ , therefore

$$\dot{d}_{\text{RD}} = \frac{1}{r_2} [|p_\beta| - r_1]_+ , \quad (4.46)$$

whereas $[x]_+ := (x + |x|)/2$, permitting only positive values. Finally, a physical meaningful and mesh-independent damage model is achieved including a non-linear homogenization method as well as viscous effects resulting in a rate-depending behavior. The numerical treatment is presented in Algorithm 1 provided in Subsection 4.2.5 and this model is selected for the main finite element calculations and results in the corresponding Chapters 5 and 6.

4.2.4 Determination of Stresses and Material Tangent

The determination of stresses and the material tangent for the rate-dependent case presented in the previous Subsection 4.2.3 is based on Section 2.9. The stresses are given by

$$\tilde{\boldsymbol{\sigma}} = \tilde{\boldsymbol{\sigma}}(\tilde{\boldsymbol{\varepsilon}}, d) = f(d) \tilde{\mathbb{E}}_0 \cdot \tilde{\boldsymbol{\varepsilon}} , \quad (4.47)$$

and a linear approximation by means of the Taylor’s theorem results in

$$\tilde{\boldsymbol{\sigma}}^{m+1} = \tilde{\boldsymbol{\sigma}}^m + \left. \frac{\partial \tilde{\boldsymbol{\sigma}}}{\partial \tilde{\boldsymbol{\varepsilon}}} \right|^m \cdot \Delta \tilde{\boldsymbol{\varepsilon}} + \left. \frac{\partial \tilde{\boldsymbol{\sigma}}}{\partial d} \right|^m \Delta d , \quad (4.48)$$

with the increment of the strains $\Delta \tilde{\boldsymbol{\varepsilon}} = \tilde{\boldsymbol{\varepsilon}}^{m+1} - \tilde{\boldsymbol{\varepsilon}}^m$ and the increment of the internal variable or rather damage variable $\Delta d = d^{m+1} - d^m$. The stresses $\tilde{\boldsymbol{\sigma}}^m$ from the last time-step as well as both appearing derivatives can straightforwardly be calculated by

$$\tilde{\boldsymbol{\sigma}}^m = f(d^m) \tilde{\mathbb{E}}_0 \cdot \tilde{\boldsymbol{\varepsilon}}^m, \quad (4.49)$$

$$\left. \frac{\partial \tilde{\boldsymbol{\sigma}}}{\partial \tilde{\boldsymbol{\varepsilon}}} \right|^m = f(d^m) \tilde{\mathbb{E}}_0, \quad (4.50)$$

$$\left. \frac{\partial \tilde{\boldsymbol{\sigma}}}{\partial d} \right|^m = f'(d^m) \tilde{\mathbb{E}}_0 \cdot \tilde{\boldsymbol{\varepsilon}}^m, \quad (4.51)$$

resulting in the following formulation for the stresses

$$\tilde{\boldsymbol{\sigma}}^{m+1} = f(d^m) \tilde{\mathbb{E}}_0 \cdot \tilde{\boldsymbol{\varepsilon}}^{m+1} + f'(d^m) \tilde{\mathbb{E}}_0 \cdot \tilde{\boldsymbol{\varepsilon}}^m \Delta d. \quad (4.52)$$

Now, the tangent can be derived by

$$\left. \frac{d\tilde{\boldsymbol{\sigma}}}{d\tilde{\boldsymbol{\varepsilon}}} \right|^{m+1} = \left. \frac{\partial \tilde{\boldsymbol{\sigma}}}{\partial \tilde{\boldsymbol{\varepsilon}}} \right|^m + \left. \frac{\partial \tilde{\boldsymbol{\sigma}}}{\partial d} \right|^m \otimes \left. \frac{\partial d}{\partial \tilde{\boldsymbol{\varepsilon}}} \right|^{m+1}, \quad (4.53)$$

including the two already determined derivatives as well as the derivative of the damage variable $(\partial d / \partial \tilde{\boldsymbol{\varepsilon}}) |^{m+1}$. For the latter, the evolution equation has to be taken into account, thus

$$d^{m+1} = d^m + \frac{\Delta t}{r_2} (p(\tilde{\boldsymbol{\varepsilon}}^{m+1}, d^m) - r_1). \quad (4.54)$$

The according derivative of the damage variable is given by

$$\left. \frac{\partial d}{\partial \tilde{\boldsymbol{\varepsilon}}} \right|^{m+1} = \frac{\Delta t}{r_2} \frac{\partial p(\tilde{\boldsymbol{\varepsilon}}^{m+1}, d^m)}{\partial \tilde{\boldsymbol{\varepsilon}}^{m+1}}, \quad (4.55)$$

with the same derivative of the driving force as in the previous case

$$\frac{\partial p(\tilde{\boldsymbol{\varepsilon}}^{m+1}, d^m)}{\partial \tilde{\boldsymbol{\varepsilon}}^{m+1}} = -f'(d^m) \tilde{\mathbb{E}}_0 \cdot \tilde{\boldsymbol{\varepsilon}}^{m+1}. \quad (4.56)$$

This can simply be inserted into the material tangent derived in Equation (4.53), therefore

$$\left. \frac{d\tilde{\boldsymbol{\sigma}}}{d\tilde{\boldsymbol{\varepsilon}}} \right|^{m+1} = f(d^m) \tilde{\mathbb{E}}_0 - \frac{\Delta t}{r_2} f'(d^m)^2 (\tilde{\mathbb{E}}_0 \cdot \tilde{\boldsymbol{\varepsilon}}^m) \otimes (\tilde{\mathbb{E}}_0 \cdot \tilde{\boldsymbol{\varepsilon}}^{m+1}). \quad (4.57)$$

Again, in case of no damage evolution, the material tangent becomes

$$\left. \frac{d\tilde{\boldsymbol{\sigma}}}{d\tilde{\boldsymbol{\varepsilon}}} \right|^{m+1} = f(d^m) \tilde{\mathbb{E}}_0. \quad (4.58)$$

4.2.5 Algorithm on Finite Element Level

The subsequent presented Algorithm 1 provides an overview of the implementation of Model I [REL] presented in Section 4.2, whereby it is related to the rate-dependent model variant in

Subsection 4.2.3. The algorithm for the rate-independent model variants of Subsections 4.2.1 and 4.2.2 is postponed to the Appendix A and presented by Algorithm 5.

Algorithm 1: Model I [REL]: Rate-dependent finite element algorithm.

input: $\tilde{\varepsilon}^m, \tilde{\varepsilon}^{m+1}, d^m$

calc: $p^{m+1} = p(\tilde{\varepsilon}^{m+1}, d^m)$

calc: $\Phi^{m+1} = \Phi(p(\tilde{\varepsilon}^{m+1}, d^m))$

if $\Phi^{m+1} > 0$ **then**

$$\left| \begin{array}{l} d^{m+1} = d^m + \frac{\Delta t}{r_2} (p^{m+1} - r_1) \end{array} \right.$$

else

$$\left| \begin{array}{l} d^{m+1} = d^m \end{array} \right.$$

calc: $\tilde{\sigma}^{m+1} = \tilde{\sigma}(\tilde{\varepsilon}^m, \tilde{\varepsilon}^{m+1}, d^m, d^{m+1})$

calc: $\frac{d\tilde{\sigma}^{m+1}}{d\tilde{\varepsilon}^{m+1}} = \frac{d\tilde{\sigma}}{d\tilde{\varepsilon}}(\tilde{\varepsilon}^m, \tilde{\varepsilon}^{m+1}, d^m, d^{m+1})$

4.3 Model II: Relaxation Based Regularization with the Emulated RVE

This chapter presents a regularized damage model based on variational modeling and the emulated representative volume element (ERVE). The model, which is denoted as Model II [ERVE] in this thesis, is directly based on the work of Schwarz et al. (2018a) and Schwarz et al. (2019b).

In Subsection 4.3.1 a basic variational damage model is introduced. Afterwards, in Subsection 4.3.2 the time-incremental setting is considered. The problem of non-coercivity is solved due to rate-limitation of the damage evolution in Subsection 4.3.3. Then in Subsection 4.3.4, quasi-convexity is achieved by relaxation. In Subsection 4.3.5, the stated ERVE is introduced. A rate-independent formulation of the model is provided in Subsection 4.3.6. Subsequently in Subsection 4.3.7, the stresses and the tangent operator are calculated and finally algorithms for the material point as well as for the finite element level are presented in Subsection 4.3.8.

4.3.1 Variational Damage Modeling

The model is based on the Helmholtz free-energy function Ψ with isotropic damage, thus

$$\Psi = f(d) \Psi_0, \quad (4.59)$$

considering the damage function $f(d)$, see more details in Section 4.1, and

$$\Psi_0 = \frac{1}{2} \varepsilon : \mathbb{E}_0 : \varepsilon. \quad (4.60)$$

For the present model, the damage function $f(d) = e^{-d}$ with $d \in [0, \infty[$ is used for material point simulations and $f(d) = (1 - d)^2$ with $d \in [0, 1]$ is used for finite element simulations.

Applying the principle of the minimum of the dissipation potential (PMDP), according to Subsection 2.6.4, allows to obtain the evolution equation for d as

$$\dot{d} = \arg \min \left\{ \dot{\Psi}(\boldsymbol{\varepsilon}, d) + \mathcal{D}(\dot{d}) \mid \dot{d} \right\}. \quad (4.61)$$

Therein, $\mathcal{D}(\dot{d})$ is the dissipation function that can be defined according to the assumed material behavior. The rate-independent formulation

$$\mathcal{D}(\dot{d}) = \begin{cases} r_1 \dot{d} & \text{for } \dot{d} \geq 0 \\ \infty & \text{for } \dot{d} < 0 \end{cases}, \quad (4.62)$$

is applied to the present model, in which the parameter r_1 equals the yield limit for the initiation of damage and it is already considered that the damage can only increase but not decrease.

4.3.2 Condensed Energy without Coercivity

Initially, investigations of energies without the coercivity are taken into account. The time-incremental setting is hereto considered in order to allow for a better understanding of problems regarding the ill-posedness. Thus, the so-called dissipation distance $\Delta\mathcal{D}$ is introduced by

$$\Delta\mathcal{D}(d_0, d_1) = \min \left\{ \int_{t_0}^{t_1} \mathcal{D}(\dot{d}) dt \mid \dot{d}; d(t_0) = d_0, d(t_1) = d_1 \right\}, \quad (4.63)$$

with $\Delta t = t_1 - t_0$. The dissipation distance describes the dissipated energy from the damage state d_0 to d_1 within Δt . Therefore, the dissipation distance for the aforementioned dissipation function in Equation (4.62) becomes

$$\Delta\mathcal{D}(d_0, d_1) = \begin{cases} r_1(d_1 - d_0) & \text{for } d_1 \geq d_0 \\ \infty & \text{for } d_1 < d_0 \end{cases}. \quad (4.64)$$

The Gibbs energy according to Equation (2.69) is written in the form

$$\mathcal{G} = \int_{\Omega} \Psi dV + \int_{\Omega} \Delta\mathcal{D}(d_0, d_1) dV - \int_{\Omega} \mathbf{f} \cdot \mathbf{u} dV - \int_{\partial\Omega} \mathbf{t} \cdot \mathbf{u} dA \quad (4.65)$$

and the related minimization problem reads

$$\{\mathbf{u}, d_1\} = \arg \min \{ \mathcal{G} \mid \mathbf{u}, d_1 \}. \quad (4.66)$$

The minimization with respect to d_1 results in a time-incremental version of the evolution equation presented in Equation (4.61), yielding

$$d_1 = \arg \min \{ \Psi(\boldsymbol{\varepsilon}, d_1) + \Delta\mathcal{D}(d_0, d_1) \mid d_1 \}, \quad (4.67)$$

and this minimization is a point-wise operation inducing the condensed energy

$$\Psi_{d_0}^{\text{cond}}(\boldsymbol{\varepsilon}) = \min \left\{ f(d_1) \Psi_0(\boldsymbol{\varepsilon}) + \Delta \mathcal{D}(d_0, d_1) \mid d_1 \right\}. \quad (4.68)$$

The minimization with respect to \mathbf{u} leads to the elastic equilibrium analogously to Equation (2.83). Hereby, a purely elastic problem as to be solved, it follows

$$\mathbf{u} = \arg \min \left\{ \int_{\Omega} \Psi_{d_0}^{\text{cond}} \, dV - \int_{\Omega} \mathbf{f} \cdot \mathbf{u} \, dV - \int_{\partial\Omega} \mathbf{t} \cdot \mathbf{u} \, dA \mid \mathbf{u} \right\}. \quad (4.69)$$

By means of this purely elastic problem the well-posedness of the time-incremental formulation can be investigated since these kinds of problems are well understood, see for example the work of Ball (1977). The existence of a solution is ensured by coercivity and quasiconvexity, see Section 3.5 for more information. Initially, the coercivity is investigated which describes the superlinear growth of energy as a function of strains. Hereto, the stress of the completely damaged ($d = d_{\max}$) material

$$\boldsymbol{\sigma} = f(d_{\max}) \frac{\partial \Psi_0}{\partial \boldsymbol{\varepsilon}} = \frac{\partial \Psi_{d_0}^{\text{cond}}}{\partial \boldsymbol{\varepsilon}} = f(d_{\max}) \mathbb{E}_0 : \boldsymbol{\varepsilon} \quad (4.70)$$

has to be able to describe the complete material deterioration for large strains as illustrated on the left-hand side of Figure 4.12, therefore

$$\lim_{\|\boldsymbol{\varepsilon}\| \rightarrow \infty} \boldsymbol{\sigma} = \lim_{\|\boldsymbol{\varepsilon}\| \rightarrow \infty} f(d_{\max}) \mathbb{E}_0 : \boldsymbol{\varepsilon} = \mathbf{0}, \quad (4.71)$$

whereat this is also an additional condition for $f(d_1)$. Thereby, the stationarity condition

$$f'(d_1) \Psi_0 + r_1 = 0 \quad \text{for } d_1 \geq d_0 \quad (4.72)$$

relates d_1 and $\boldsymbol{\varepsilon}$ with each other. Taking into account Equations (4.71) and (4.72) leads to

$$\lim_{\|\boldsymbol{\varepsilon}\| \rightarrow \infty} \Psi_{d_0}^{\text{cond}}(\boldsymbol{\varepsilon}) \leq C, \quad (4.73)$$

with $C > 0$ depending on d_0 and \mathbb{E}_0 only. This constant C ensures zero stresses and therefore fulfills the condition in (4.71). However, the sublinear growth of the energy violates the coercivity conditions as illustrated on the right-hand side of Figure 4.12. Moreover, Figure 3.6 illustrates the limit case of coercivity.

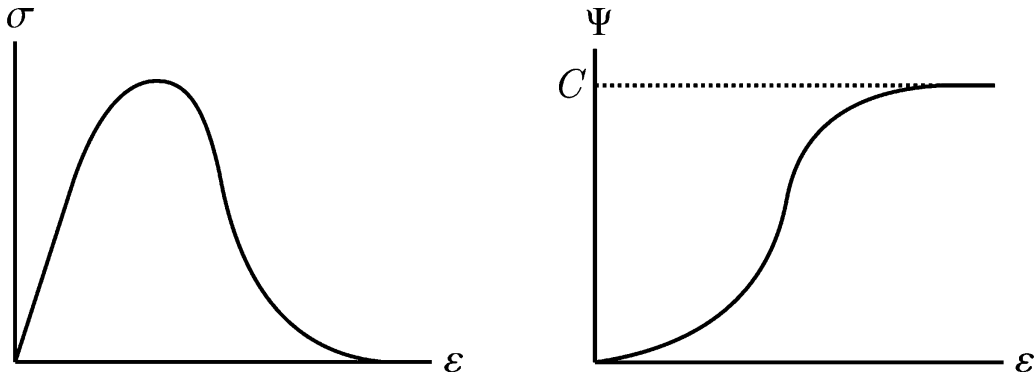


Figure 4.12: Schematic illustration of the non-coercivity by zero stresses for infinite strains (left) and resulting constant energy (right) limited by C .

4.3.3 Coercivity by Rate-Limitation

Coercivity of the condensed energy can be achieved by rate-limitation of the evolution of damage. Hereto, the dissipation function has to be modified such that

$$\mathcal{D}(\dot{d}_1) = \begin{cases} r_1 \dot{d}_1 & \text{for } 0 \leq \dot{d}_1 \leq k \\ \infty & \text{else} \end{cases}, \quad (4.74)$$

with the positive parameter k limiting the amount of evolving damage. Thus, $\Delta\mathcal{D}$ becomes

$$\Delta\mathcal{D}(d_0, d_1, \Delta t) = \begin{cases} r_1(d_1 - d_0) & \text{for } 0 \leq d_1 - d_0 \leq k\Delta t \\ \infty & \text{else} \end{cases}, \quad (4.75)$$

which explicitly is depending on Δt . Therefore, the model is henceforward rate-dependent. In contrast to other two-state models for example in the works of Allaire and Kohn (1993), Francfort and Marigo (1993), Allaire and Lods (1999), and Francfort and Garroni (2006), the restriction to only two damage states is not asserted in a global sense but, in the present case, it is applied to individual time-increments. Consequently, stresses are able to decrease in contrast to usual two-state models and therefore Equation (4.71) is not violated. Assuming that $f'(d_1) \Psi_0 + r_1 = 0$ provides the unique solution $d_1^*(\Psi_0/r_1)$ which allows to pose the condensed energy as

$$\Psi_{d_0}^{\text{cond}}(\varepsilon) = \begin{cases} f(d_0) \Psi_0 & \text{for } d_1^*(\Psi_0/r_1) < d_0 \\ f(d_1^*(\Psi_0/r_1)) \Psi_0 + r_1(d_1^*(\Psi_0/r_1) - d_0) & \text{for } d_0 \leq d_1^*(\Psi_0/r_1) < d_0 + k\Delta t \\ f(d_0 + k\Delta t) \Psi_0 + r_1 k\Delta t & \text{for } d_1^*(\Psi_0/r_1) > d_0 + k\Delta t \end{cases}. \quad (4.76)$$

The condensed energy $\Psi_{d_0}^{\text{cond}}$ consists of three parts: two convex parts represented by the first (marked green) and third (marked red) term describe different damage states and a linear part (marked blue) represented by the second term describes a mixture state. The effective energy over all time-steps results in a concave development due to the material deterioration.

All mentioned parts are also illustrated in Figures 4.13 and 4.14, where solid lines are always assigned to the current time-step and dashed lines to the previous time-steps: the green lines (first term in Equation (4.76)) arise from the energy landscape of the previous time-steps, the red lines (third term in Equation (4.76)) correspond to the energy landscape of the current time-step, and the blue relaxation curve (second term in Equation (4.76)) is the mixture energy that is always tangential to the mentioned green and red lines. While damage is evolving during loading, see Figure 4.13, the stiffness correspondingly reduces and therefore the slope of the energies (green and red lines) decreases as well. As a result, the mixture energy (blue curve) evolves in time providing an effective energy over all time-steps that is presented by the black line in Figure 4.14. This effective energy arises as follows: the damage microstructure realized in the material is based on the discretized current load (indicated by the external strain $\varepsilon(t)$) as well as on the (fixed) damage state of the previous time-step, whereby the damage increment is limited by the exact amount of $k\Delta t$ and therefore the energy of the current time-step is directly given. Consequently, $\Psi_{d_0}^{\text{cond}}$ can directly be computed and complies with the set of relaxed energy states over all discretized time-steps. Even though the condensed energy has achieved the property of coercivity, due to the resulting concave development in Figure 4.14 based on Equation (4.76), the energy is still not quasiconvex and therefore still ill-posed.

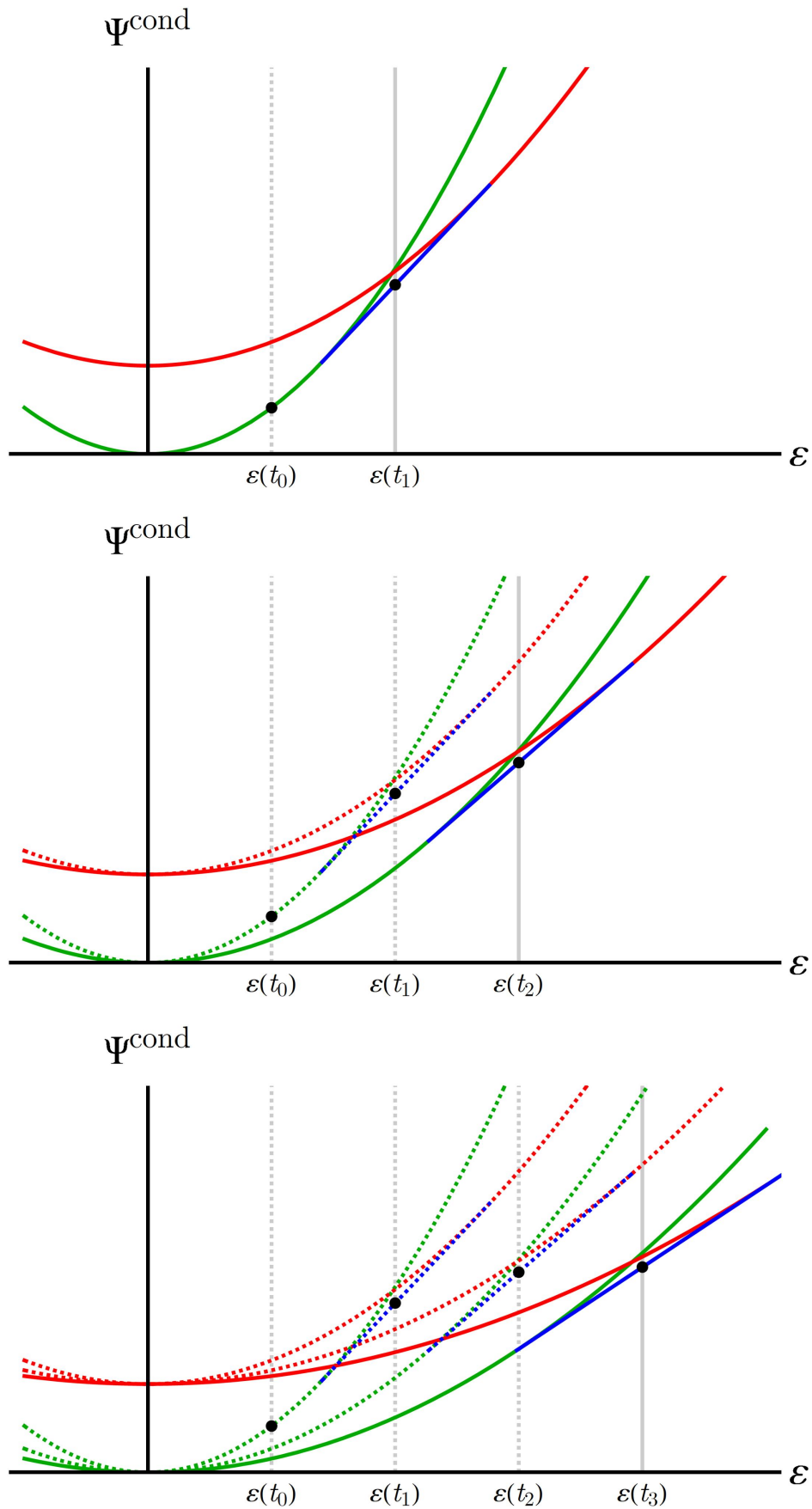


Figure 4.13: Model II [ERVE]: Time-incremental energies of evolving damage for time steps t_1 to t_3 (from top to bottom).

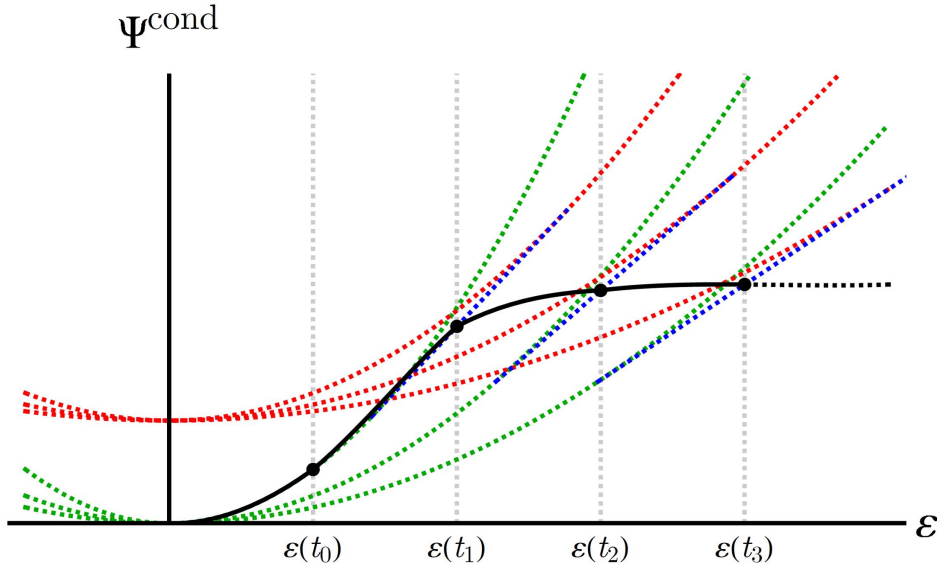


Figure 4.14: Model II [ERVE]: Time-incremental energies for effective energy over all time steps of evolving damage (black curve).

4.3.4 Quasiconvexity by Relaxation

After considering coercivity, at this point quasiconvexity is additionally taken into account. Quasiconvexity describes the stability of energy in the context of superimposed fluctuations of the displacement field, see Section 3.5 for more information. Hereto, calculating the quasiconvex envelope of the potential leads to the desired property of quasiconvexity, thus

$$\mathbb{Q}\Psi_{d_0}^{\text{cond}}(\boldsymbol{\varepsilon}) = \inf \left\{ \int_{\Omega_{\text{rep}}} \Psi_{d_0}^{\text{cond}}(\boldsymbol{\varepsilon} + \nabla \mathbf{u}(\mathbf{x})) dV \mid \mathbf{u}; \mathbf{u} \text{ periodic on } \partial\Omega_{\text{rep}} \right\}, \quad (4.77)$$

whereby $\mathbf{u} = \mathbf{u}(\mathbf{x})$ describes a superimposed fluctuation field that is considered for finding the optimal fluctuation by minimization defined on a representative volume element Ω_{rep} , which has a unit volume. See for example work of Dacorogna (1982a). In this context, the strain field as well as the damage variable are wanted quantities. Solving is quite challenging particularly because there are not only two global damage states like in several other works for example by Allaire and Kohn (1993), Allaire and Lods (1999), and Francfort and Garroni (2006), but there are many damage states evolving due the time-incremental setting by means of the rate-limitation, see Figure 4.14 for illustration.

Therefore, the rate-limited damage within a time-increment becomes a field $d_0 = d_0(\mathbf{x})$ as well, which is build on the stationarity condition in Equation (4.72). This distributed damage field arises from a distributed strain field $\boldsymbol{\varepsilon} = \boldsymbol{\varepsilon}(\mathbf{x})$ in Ω_{rep} and functions as the initial condition of the next time-increment. This practice leads to the following quasiconvex energy with a fixed damage distribution

$$\mathbb{Q}\Psi(\boldsymbol{\varepsilon}, d_1) = \inf \left\{ \int_{\Omega_{\text{rep}}} \Psi(\boldsymbol{\varepsilon} + \nabla \mathbf{u}(\mathbf{x}), d_1(\mathbf{x})) dV \mid \mathbf{u}; \mathbf{u} \text{ periodic on } \partial\Omega_{\text{rep}} \right\}. \quad (4.78)$$

An appropriate dissipation functional considering $\dot{d}_1 = \dot{d}_1(\mathbf{x})$ is given by

$$\check{\mathcal{D}}(\dot{d}_1) = \int_{\Omega_{\text{rep}}} \mathcal{D}(\dot{d}_1(\mathbf{x})) dV, \quad (4.79)$$

whereas the evolution of the damage variable d is described by

$$\dot{d}_1 = \arg \min \left\{ \mathbf{Q}\dot{\Psi}(\boldsymbol{\varepsilon}, d_1) + \check{\mathcal{D}}(\dot{d}_1) \mid \dot{d}_1 \right\}. \quad (4.80)$$

Since it is numerically expensive to calculate $\mathbf{Q}\dot{\Psi}$, which involves solving a high dimensional global optimization problem, this approach (Equation (4.80)) is unsuitable for modeling damage evolution. Consequently, the compatibility of the fluctuation field is no longer regarded but therefore the quasiconvex envelope is calculated, which ensures a well-posed damage model.

Furthermore, the damage distribution inside Ω_{rep} is not directly calculated, but in contrast, it can be interpreted as a microstructured damage variable that is modeled by assuming a specific number of subdomains. This approach is called the emulated representative volume element (ERVE), adopted from Schwarz et al. (2019b).

4.3.5 The Emulated Representative Volume Element

The emulated representative volume element (ERVE) covers the description of damage distribution inside Ω_{rep} by a specific number of subdomains. This idea originates from the interpretation as a microstructured damage variable as presented by the systematic development in Figure 4.15: Initially, a mixture between a completely undamaged state and a damaged state occurs that is represented by two subdomains, see $n = 2$, whereby the damage increase is prescribed by $k\Delta t = 0.1$. Then, these subdomains are again subdivided in the next time-step of evolving damage, see $n = 4$. Afterwards, this process reiterates, see $n = 8$, and with every time-step the number of subdomains increases exponentially, see $n = 2^t$. This can be interpreted as a microstructured damage variable that however can be substituted by a specific number of subdomains n over all time-steps in order to simplify the numerical effort for describing the damage distribution inside Ω_{rep} . Finally, this results in the mentioned ERVE, see rightmost.

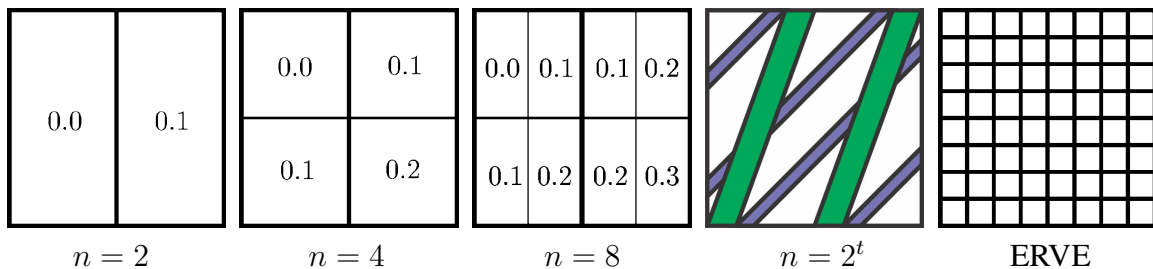


Figure 4.15: Model II [ERVE]: Development of ERVE starting from interpretation as microstructured damage variable leading to a fixed number of subdomains whereas the damage increase is always prescribed by $k\Delta t = 0.1$.

Figure 4.16 provides an exemplary application of the ERVE for a better understanding and a more detailed interpretation. A simplified case of the microstructured damage distribution

inside Ω_{rep} (left-hand side) and the corresponding ERVE (right-hand side) are presented by schematic illustrations and compared with each other. Hereby, the subdomains in the ERVE (right-hand side) emulate the damage structures (left-hand side) in such a way that the total amount of damage coincide in both illustrations. Therefore, the purple and green structures on the left-hand side are related to the purple and green subdomains constituting a corresponding damage distribution on the right-hand side. The prescribed increase of damage in this example is set to $k\Delta t = 0.1$ again.

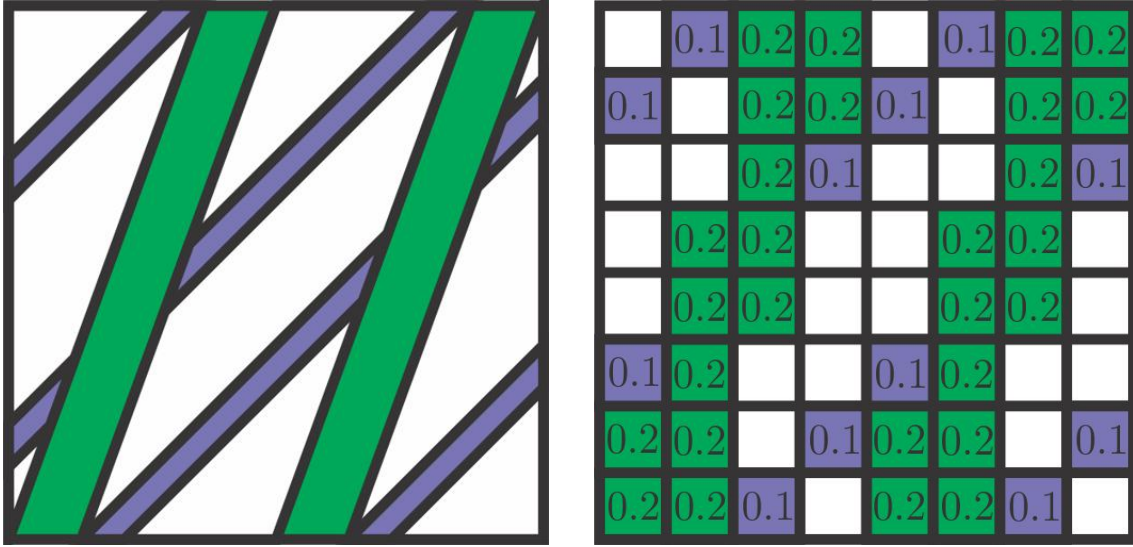


Figure 4.16: Model II [ERVE]: Exemplary application of ERVE by a simplified case of microstructured damage distribution (left-hand side) compared to corresponding interpretation of the ERVE (right-hand side) considering a prescribed damage increase of $k\Delta t = 0.1$.

A more precise description is following at this point. The volume Ω_{rep} is divided into n subdomains of equal volume, constant strain ϵ_i and constant damage d_i . The energy is no longer minimized with respect to \mathbf{u} but indeed with respect to all ϵ_i originating from the given overall strain ϵ . This results in

$$\Psi^{\text{rel}}(\epsilon, \{d_i\}) = \inf \left\{ \frac{1}{n} \sum_{i=1}^n f(d_i) \Psi_0(\epsilon_i) \mid \epsilon_i; \epsilon = \frac{1}{n} \sum_{i=1}^n \epsilon_i \right\}. \quad (4.81)$$

Minimization of the problem provides the strains of each subdomain

$$\epsilon_i = \frac{\bar{f}}{f(d_i)} \epsilon, \quad (4.82)$$

and the relaxed energy

$$\Psi^{\text{rel}}(\epsilon, \{d_i\}) = \bar{f} \Psi_0, \quad (4.83)$$

which is described with the effective damage function

$$\bar{f} = n \left(\sum_{i=1}^n \frac{1}{f(d_i)} \right)^{-1}, \quad (4.84)$$

capturing the damage states of all subdomains. The corresponding dissipation function reads

$$\mathcal{D}^{\text{rel}}(\{\dot{d}_i\}) = \frac{1}{n} \sum_{i=1}^n \mathcal{D}(d_i), \quad (4.85)$$

and evolution of \dot{d}_i can now be defined as

$$\{\dot{d}_i\} = \arg \min \left\{ \dot{\Psi}^{\text{rel}}(\boldsymbol{\varepsilon}, \{d_i\}) + \mathcal{D}^{\text{rel}}(\{\dot{d}_i\}) \mid \{\dot{d}_i\} \right\}. \quad (4.86)$$

Finally, a conclusive time-incremental setting is present with a dissipation distance provided by

$$\Delta \mathcal{D}^{\text{rel}}(\{d_{0i}\}, \{d_{1i}\}, \Delta t) = \frac{1}{n} \sum_{i=1}^n \Delta \mathcal{D}(d_{0i}, d_{1i}, \Delta t), \quad (4.87)$$

and is considered in the corresponding variational formulation

$$\{d_i\} = \arg \min \left\{ \Psi^{\text{rel}}(\boldsymbol{\varepsilon}, \{d_i\}) + \Delta \mathcal{D}^{\text{rel}}(\{d_{0i}\}, \{d_i\}, \Delta t) \mid \{d_i\} \right\}. \quad (4.88)$$

Derivating the energy yields the driving forces

$$p_i = -\frac{\partial \Psi^{\text{rel}}}{\partial d_i} = -\frac{\bar{f}^2 f'(d_i)}{n f(d_i)^2} \Psi_0 \quad (4.89)$$

regarding each subdomain. Investigating Equation (4.88) allows to determine

$$\begin{aligned} p_i < \frac{r_1}{n} &\Rightarrow d_i = d_{0i}, \\ d_{0i} < d_i < d_{0i} + k\Delta t &\Rightarrow p_i = \frac{r_1}{n}, \\ p_i > \frac{r_1}{n} &\Rightarrow d_i = d_{0i} + k\Delta t. \end{aligned} \quad (4.90)$$

Several numerical simulations led to the experience that the second case of Equation (4.90) is never realized. These values of d_i are related to linear mixture states of the energy plot and are vanishing during relaxation processes.

4.3.6 Elimination of Rate-Dependence

Due to the rate-dependent formulation of Model II [ERVE] the numerical results directly depend on the applied loading rate. This rate-dependence can be eliminated by relating the maximum damage rate \dot{d} , considered in Equation (4.74), to the power of external forces ℓ_{ext} given by

$$\ell_{\text{ext}}(\dot{\mathbf{u}}) = \int_{\Omega} \mathbf{f} \cdot \dot{\mathbf{u}} \, dV + \int_{\partial\Omega} \mathbf{t} \cdot \dot{\mathbf{u}} \, dV. \quad (4.91)$$

During elastic equilibrium, these external forces can directly be expressed in terms of material properties only. This provides

$$\dot{G} = \int_{\Omega} \dot{\Psi} + \mathcal{D} \, dV = \ell_{\text{ext}}(\dot{\mathbf{u}}). \quad (4.92)$$

The quantity G describes the total stored energy of the volume Ω and \dot{G} represents the well-known energy release rate. In context of finite element calculations the power of external forces ℓ_{ext} can easily be calculated as

$$\ell_{\text{ext}}(\dot{\mathbf{u}}) = \frac{\Delta \mathbf{u} \cdot \sum \mathbf{f}^*}{\Delta t}, \quad (4.93)$$

with the increment of applied displacements $\Delta \mathbf{u} = \mathbf{u}^{m+1} - \mathbf{u}^m$ and related sum over the resulting forces \mathbf{f}^* . The aforementioned maximum damage rate \dot{d} is then limited by the power of external forces in consideration of a factor α , consequently

$$0 \leq \dot{d} \leq \alpha \ell_{\text{ext}}. \quad (4.94)$$

In regard to the implementation in Equation (4.90), the prior quantity $k\Delta t$ is accordingly substituted by $\alpha \ell_{\text{ext}} \Delta t$. This procedure ensures same conditions for different loading rates by an adapting rate-limitation.

The achievement of rate-independent numerical results is proven in Subsection 5.3.1. Furthermore, the parameter α allows to adjust the rate-limitation and consequently the power of regularization. The influence of α is investigated in Subsection 5.3.3.

4.3.7 Determination of Stresses and Material Tangent

Based on Section 2.9 the determination of the stresses and the material tangent is presented in this Section. The stresses of the current model are given by

$$\tilde{\boldsymbol{\sigma}} = \tilde{\boldsymbol{\sigma}}(\tilde{\boldsymbol{\varepsilon}}, \mathbf{d}) = \bar{f}(\mathbf{d}) \tilde{\mathbb{E}}_0 \cdot \tilde{\boldsymbol{\varepsilon}}, \quad (4.95)$$

containing the damage variable \mathbf{d} as a vector of length n corresponding to the number of sub-domains of each material point. The linearized stresses are given by Taylor's theorem, thus

$$\tilde{\boldsymbol{\sigma}}^{m+1} = \tilde{\boldsymbol{\sigma}}^m + \left. \frac{\partial \tilde{\boldsymbol{\sigma}}}{\partial \tilde{\boldsymbol{\varepsilon}}} \right|^m \cdot \Delta \tilde{\boldsymbol{\varepsilon}} + \left. \frac{\partial \tilde{\boldsymbol{\sigma}}}{\partial \mathbf{d}} \right|^m \cdot \Delta \mathbf{d}. \quad (4.96)$$

Thereby, the increment of the stains $\Delta \tilde{\boldsymbol{\varepsilon}} = \tilde{\boldsymbol{\varepsilon}}^{m+1} - \tilde{\boldsymbol{\varepsilon}}^m$ and the increment of the damage variable $\Delta \mathbf{d} = \mathbf{d}^{m+1} - \mathbf{d}^m$ functioning as the internal variable are included. Straightforwardly, the stresses from the previous time-step $\tilde{\boldsymbol{\sigma}}^n$ and the appearing derivatives are calculated as follows

$$\tilde{\boldsymbol{\sigma}}^m = \bar{f}(\mathbf{d}^m) \tilde{\mathbb{E}}_0 \cdot \tilde{\boldsymbol{\varepsilon}}^m, \quad (4.97)$$

$$\left. \frac{\partial \tilde{\boldsymbol{\sigma}}}{\partial \tilde{\boldsymbol{\varepsilon}}} \right|^m = \bar{f}(\mathbf{d}^m) \tilde{\mathbb{E}}_0, \quad (4.98)$$

$$\left. \frac{\partial \tilde{\boldsymbol{\sigma}}}{\partial \mathbf{d}} \right|^m = \left(\tilde{\mathbb{E}}_0 \cdot \tilde{\boldsymbol{\varepsilon}}^m \right) \otimes \sum_{j=1}^n \left(\frac{f'(d_j^m)}{n f(d_j^m)^2} \bar{f}(\mathbf{d}^m) \mathbf{e}_j \right), \quad (4.99)$$

wherewith the stresses are resulting in

$$\tilde{\boldsymbol{\sigma}}^{m+1} = \bar{f}(\mathbf{d}^m) \tilde{\mathbb{E}}_0 \cdot \tilde{\boldsymbol{\varepsilon}}^{m+1} + \left(\tilde{\mathbb{E}}_0 \cdot \tilde{\boldsymbol{\varepsilon}}^m \right) \otimes \sum_{j=1}^n \left(\frac{f'(d_j^m)}{n f(d_j^m)^2} \bar{f}(\mathbf{d}^m) \mathbf{e}_j \right) \cdot \Delta \mathbf{d}. \quad (4.100)$$

The material tangent can be derived as

$$\left. \frac{d\tilde{\boldsymbol{\sigma}}}{d\tilde{\boldsymbol{\varepsilon}}} \right|^{m+1} = \left. \frac{\partial \tilde{\boldsymbol{\sigma}}}{\partial \tilde{\boldsymbol{\varepsilon}}} \right|^m + \left. \frac{\partial \tilde{\boldsymbol{\sigma}}}{\partial \mathbf{d}} \right|^m \cdot \left. \frac{\partial \mathbf{d}}{\partial \tilde{\boldsymbol{\varepsilon}}} \right|^{m+1}, \quad (4.101)$$

where the first two terms on the right-hand side are already determined in contrast to the third one. The derivative of the damage variable $(\partial \mathbf{d} / \partial \tilde{\boldsymbol{\varepsilon}}) |^{m+1}$ requires more investigations.

Since every material point includes a predefined number of subdomains with a separate damage evolution given by

$$d_i^{m+1} = d_i^m + \alpha \ell_{\text{ext}} \Delta t, \quad (4.102)$$

and this separate damage evolution is surrounded by a loop including a continually changing driving force, see Section 4.3.8 for more details, it is quite complicated to derive the wanted derivative of the vectorial quantity \mathbf{d} . For that reason, the energy Ψ_0 is taken into account as

$$\left. \frac{\partial \mathbf{d}}{\partial \tilde{\boldsymbol{\varepsilon}}} \right|^{m+1} = \left. \frac{\partial \mathbf{d}}{\partial \Psi_0} \right|^{m+1} \otimes \left. \frac{\partial \Psi_0}{\partial \tilde{\boldsymbol{\varepsilon}}} \right|^{m+1} = \left. \frac{\partial \mathbf{d}}{\partial \Psi_0} \right|^{m+1} \otimes (\tilde{\mathbb{E}}_0 \cdot \tilde{\boldsymbol{\varepsilon}}^{m+1}), \quad (4.103)$$

which allows to perform a numerical derivation of the damage derivative by applying the tolerance $tol = 10^{-8}$ to Ψ_0 , see Hermann (2011) more information, consequently

$$\left. \frac{\partial \mathbf{d}}{\partial \Psi_0} \right|^{m+1} = \frac{\mathbf{d}_{tol}^{m+1}(\Psi_0^{m+1} + tol) - \mathbf{d}^{m+1}(\Psi_0^{m+1})}{tol}. \quad (4.104)$$

Incidentally, this numerical procedure is not very expensive, since only a scalar quantity is affected by the numerical fluctuation due to the application of the tolerance. The result can then be considered for the derivative of the damage variable \mathbf{d} according to

$$\left. \frac{\partial \mathbf{d}}{\partial \tilde{\boldsymbol{\varepsilon}}} \right|^{m+1} = \frac{\mathbf{d}_{tol}^{m+1}(\Psi_0^{m+1} + tol) - \mathbf{d}^{m+1}(\Psi_0^{m+1})}{tol} \otimes (\tilde{\mathbb{E}}_0 \cdot \tilde{\boldsymbol{\varepsilon}}^{m+1}). \quad (4.105)$$

Finally, all components can be inserted into Equation (4.101) providing the material tangent

$$\begin{aligned} \left. \frac{d\tilde{\boldsymbol{\sigma}}}{d\tilde{\boldsymbol{\varepsilon}}} \right|^{m+1} &= \bar{f}(\mathbf{d}^m) \tilde{\mathbb{E}}_0 + (\tilde{\mathbb{E}}_0 \cdot \tilde{\boldsymbol{\varepsilon}}^m) \otimes \sum_{j=1}^n \left(\frac{f'(d_j^m)}{n f(d_j^m)^2} \bar{f}(\mathbf{d}^m) \mathbf{e}_j \right) \\ &\quad \cdot \frac{\mathbf{d}_{tol}^{m+1}(\Psi_0^{m+1} + tol) - \mathbf{d}^{m+1}(\Psi_0^{m+1})}{tol} \otimes (\tilde{\mathbb{E}}_0 \cdot \tilde{\boldsymbol{\varepsilon}}^{m+1}). \end{aligned} \quad (4.106)$$

In case of no evolving damage the material tangent reads

$$\left. \frac{d\tilde{\boldsymbol{\sigma}}}{d\tilde{\boldsymbol{\varepsilon}}} \right|^{m+1} = f(\mathbf{d}^m) \tilde{\mathbb{E}}_0. \quad (4.107)$$

4.3.8 Algorithm on Material Point and Finite Element Level

The Algorithms 2 and 3 presented in this subsection describe the numerical implementation of Model II [ERVE] in Section 4.3. Obviously, the algorithms are fairly simple and short. The first one, Algorithm 2, does not include the modification for rate-independence from Subsection

4.3.6 and is therefore rate-dependent. However, this model variant can completely be described on the material point level in contrast to the other algorithm 3 which involves external forces. For that reason 2 is also used for the calculations on material point level presented in the following Subsection 4.3.9. As already mentioned, the rate-independent model variant described by Algorithm 3 considers the power of external forces ℓ_{ext} which is related to the last time-step of the finite element calculation, and can therefore not be limited to the material point level.

Algorithm 2: Model II [ERVE]: Rate-dependent material point algorithm.

input: $\boldsymbol{\varepsilon}^{m+1}, \mathbf{d}^m$

set: $\mathbf{d}^{m+1} = \mathbf{d}^m$

for $i = 1, \dots, n$ **do**

- calc:** $q_i(\boldsymbol{\varepsilon}^{m+1}, \mathbf{d}^{m+1})$
- if** $q_i > \frac{r_1}{n}$ **then**
 - \lfloor $d_i^{m+1} = d_i^{m+1} + k\Delta t$
- if** $d_i^{m+1} > 0.999$ **then**
 - \lfloor **set:** $d_i^{m+1} = 0.999$
- \lfloor **set:** $\mathbf{d}^{m+1}(d_i^{m+1})$

Algorithm 3: Model II [ERVE]: Rate-independent finite element algorithm.

input: $\boldsymbol{\varepsilon}^{m+1}, \mathbf{d}^m, \ell_{\text{ext}}$

set: $\mathbf{d}^{m+1} = \mathbf{d}^m$

for $i = 1, \dots, n$ **do**

- calc:** $q_i(\boldsymbol{\varepsilon}^{m+1}, \mathbf{d}^{m+1})$
- if** $q_i > \frac{r_1}{n}$ **then**
 - \lfloor $d_i^{m+1} = d_i^{m+1} + \alpha \ell_{\text{ext}} \Delta t$
- if** $d_i^{m+1} > 0.999$ **then**
 - \lfloor **set:** $d_i^{m+1} = 0.999$
- \lfloor **set:** $\mathbf{d}^{m+1}(d_i^{m+1})$

calc: $\tilde{\boldsymbol{\sigma}}^{m+1} = \tilde{\boldsymbol{\sigma}}(\tilde{\boldsymbol{\varepsilon}}^m, \tilde{\boldsymbol{\varepsilon}}^{m+1}, \mathbf{d}^m, \mathbf{d}^{m+1})$

calc: $\frac{d\tilde{\boldsymbol{\sigma}}^{m+1}}{d\tilde{\boldsymbol{\varepsilon}}^{m+1}} = \frac{d\tilde{\boldsymbol{\sigma}}}{d\tilde{\boldsymbol{\varepsilon}}}(\tilde{\boldsymbol{\varepsilon}}^m, \tilde{\boldsymbol{\varepsilon}}^{m+1}, \mathbf{d}^m, \mathbf{d}^{m+1})$

4.3.9 Numerical Results on Material Point Level

In this subsection some numerical results on material point level based on Algorithm 2 from the previous Subsection are provided because the microstructural description of the present model by means of the ERVE includes interesting events and calculations and these results are expected to allow a better understanding of the functioning and behavior of the model. The presented calculations are strain-controlled, three-dimensional and the used material parameters are given by Table 4.1. In contrast to the finite element results provided later in Chapters 5 and 6, the present case of material point calculations was based on a damage function with exponential behavior $f(d) = e^{-d}$. The maximum strain $\boldsymbol{\varepsilon}_{\max} = (0.01 \quad -0.0033 \quad -0.0033 \quad 0 \quad 0 \quad 0)^T$ was applied in 100 loading steps and the according results are given by Figures 4.17 to 4.21.

E	ν	r_1	n	k	Δt
200 GPa	0.33 [-]	0.1 MPa	20 [-]	0.11 1/s	1 s

Table 4.1: Model II [ERVE]: Parameters for material point simulations.

Figure 4.17 presents the damage variable d_i of each subdomain i plotted for the last time-step. The number of subdomains was set to $n = 20$ and they are mirrored for presentation purposes in order to pretend a crack-like appearance in the microstructure of the ERVE.

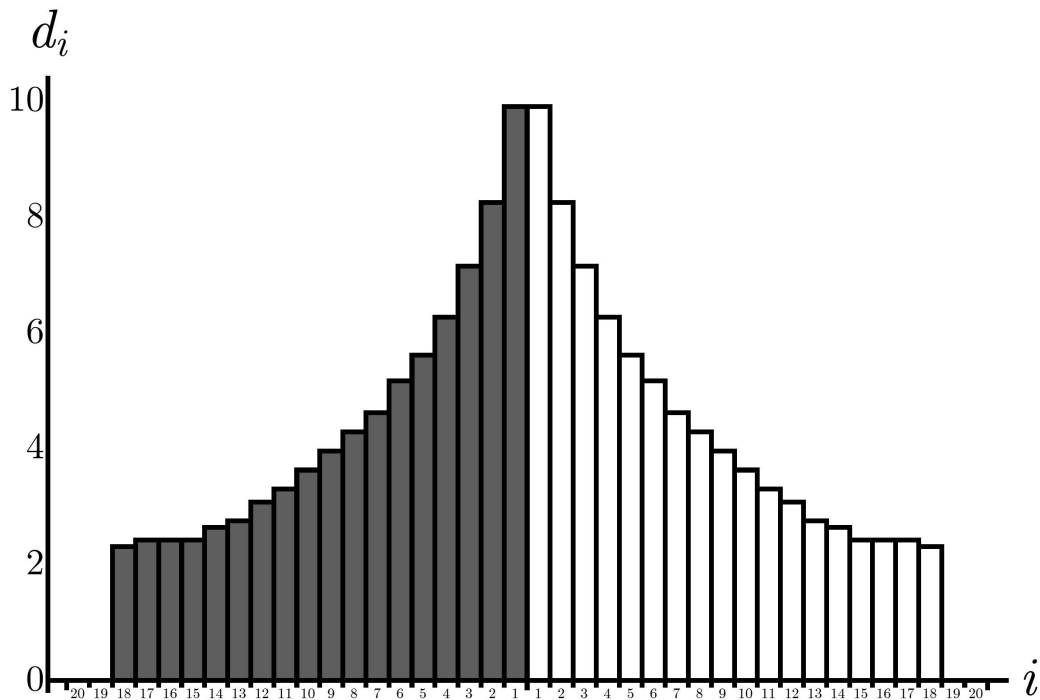


Figure 4.17: Model II [ERVE]: Damage variable d_i over mirrored subdomains i of number $n = 20$ on material point level in last time-step

This interpretation of a crack is not only given due to the mirroring of the subdomains but also by the behavior of the damage evolution in the subdomains by itself: the damage starts to evolve always in the first subdomain due to the order of access to the subdomains as presented

in Algorithm 3, and afterwards further subdomains are filled successively until the energetic equilibrium described by Equations (4.89) and (4.90) is achieved by the total amount of damage over all subdomains. In this way and due to the mirroring, the crack-like appearance with an amplitude in the middle of the mirrored x -axis is resulting.

Then, Figure 4.18 no longer presents the damage variable d_i for the last time-step only but instead the evolution of the damage variable d_i over all time-steps and therefore over the increase of the strains ε . This is again done for each subdomain i separately. In the beginning approximately until $\varepsilon = 0.001$, the material behaves purely elastic and accordingly no damage is evolving. Afterwards, obviously the driving forces of several subdomains exceed their energetic threshold limits r since damage is initiating and evolving. This continues until energetic equilibrium can be achieved for each time-step again. As described for the last Figure 4.17, subdomains are successively filled and by this separately evolving damage the branching structure of Figure 4.18 is resulting. The final damage structure at maximum strain complies with the damage distribution of Figure 4.17, of course. Interestingly, in both figures the subdomains are filled successively starting with $i = 1$, ending with $i = 18$ and due to energetic conditions the subdomains $i = 19$ and $i = 20$ remain unaffected by damage evolution.

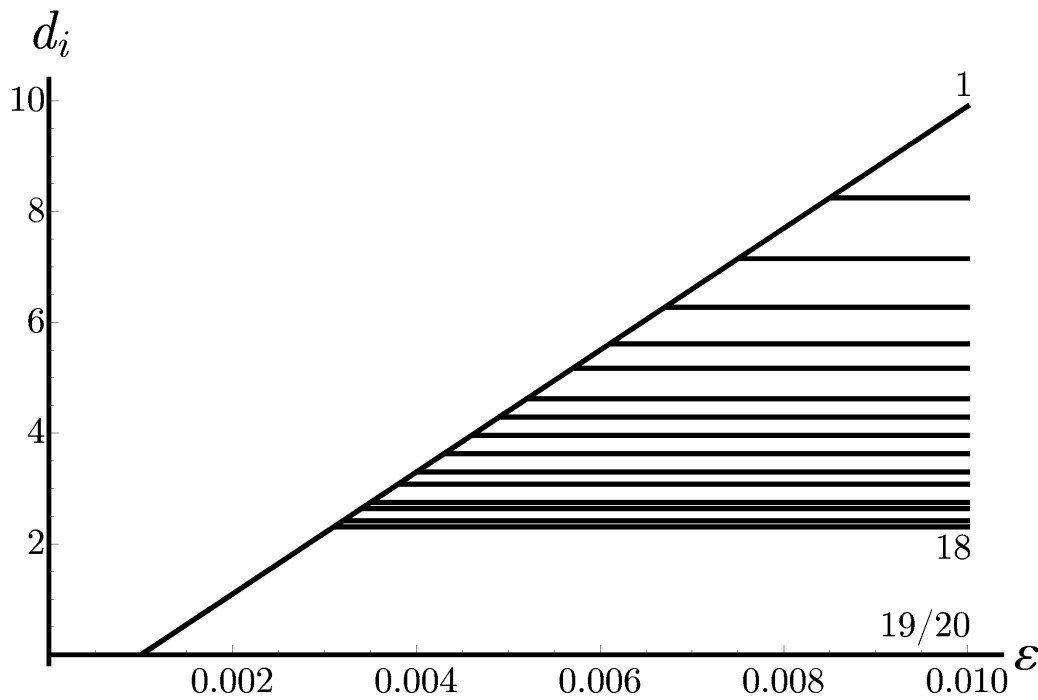


Figure 4.18: Model II [ERVE]: Evolution of damage variable d_i in subdomains i of number $n = 20$ over increase of strains ε on material point level.

Then, considering the mentioned damage function $f(d) = e^{-d}$ for each subdomain i provides the plot in Figure 4.19, in which the evolution of these damage functions f_i are presented over the increasing strains ε . Therefore, this plot is directly related to Figure 4.18, which is why the same elastic and damage parts can be identified. Since the damage function describes the material stiffness here for each subdomain separately, it is decreasing from 1 to 0, representing completely intact or damaged subdomains respectively.

For the material behavior in a global sense it is much more interesting and meaningful to observe the material stiffness over all subdomains. This is done in Figure 4.20 by plotting

the evolution of the effective damage function \bar{f} over the increasing strains ε . Herewith, the subdomains and therefore the microstructure is no longer considered but the global behavior of the macrostructure instead. It is also more interesting to consider this effective damage function since it is also used for the calculation of stresses.

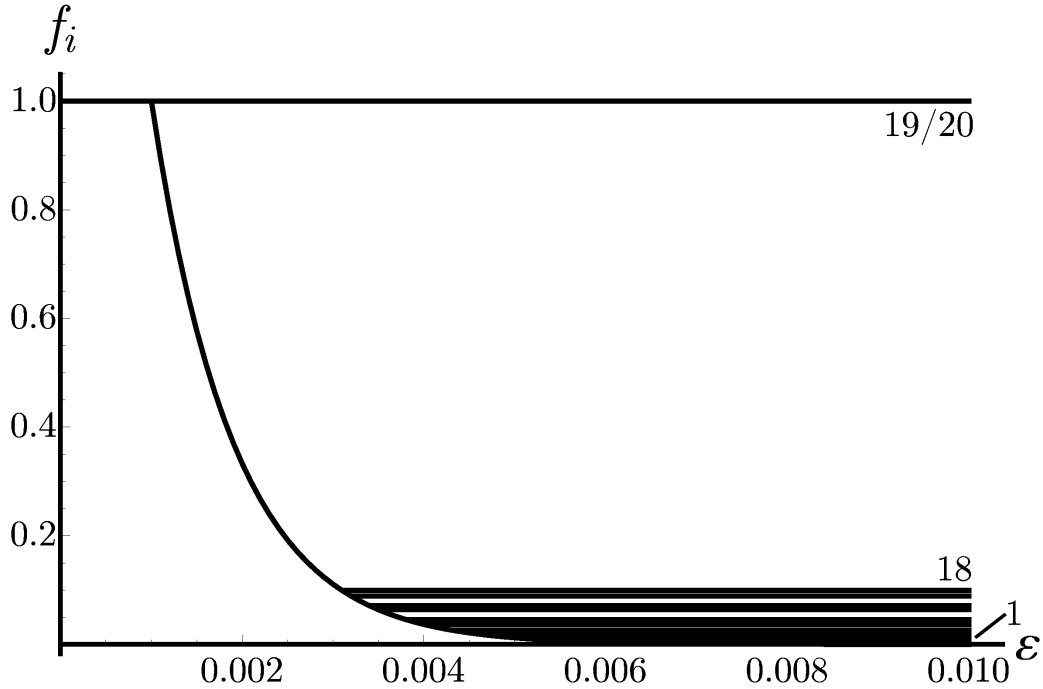


Figure 4.19: Model II [ERVE]: Evolution of damage function f_i in subdomains i of number $n = 20$ over strains ε on material point level.

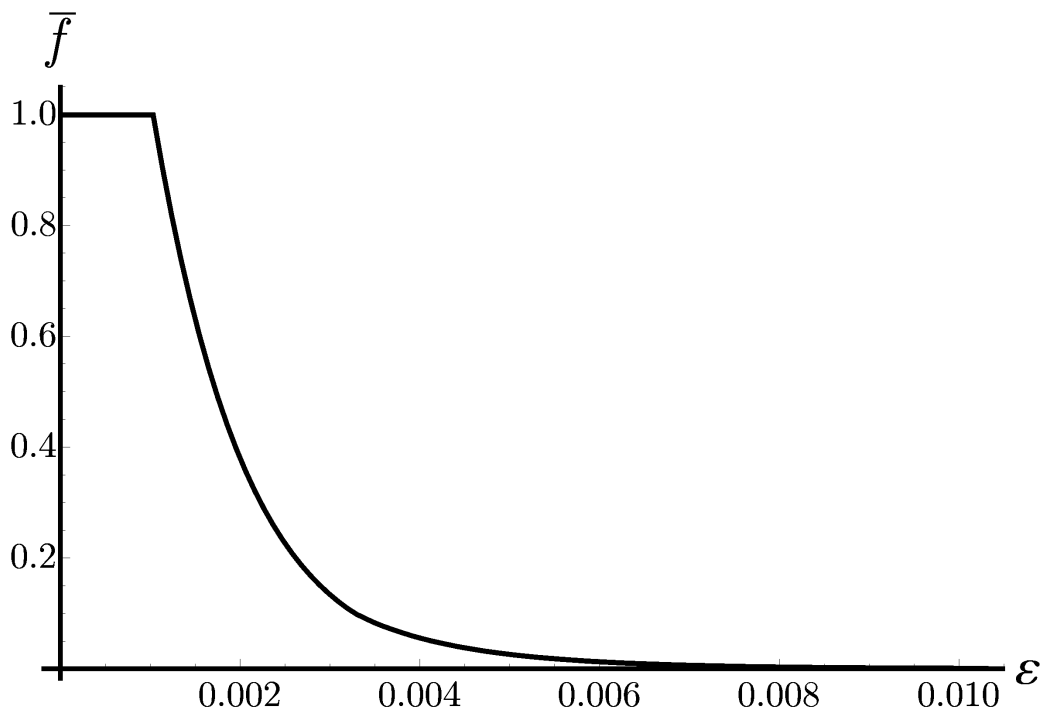


Figure 4.20: Model II [ERVE]: Effective damage function \bar{f} over strains ε on material point level.

These stresses σ are also plotted over the strains ε as presented in Figure 4.21 and possess a typical behavior for damage models including an initial elastic part as well as the significant drop due to the damage evolution afterwards. This drop is, as already described before, the result of the decreasing damage functions f_i of each subdomain i which, in turn, are resulting from the respective damage evolution d_i in each subdomain i . It should be noticed at this point, that the presented model is able to describe a global answer approaching zero stresses.

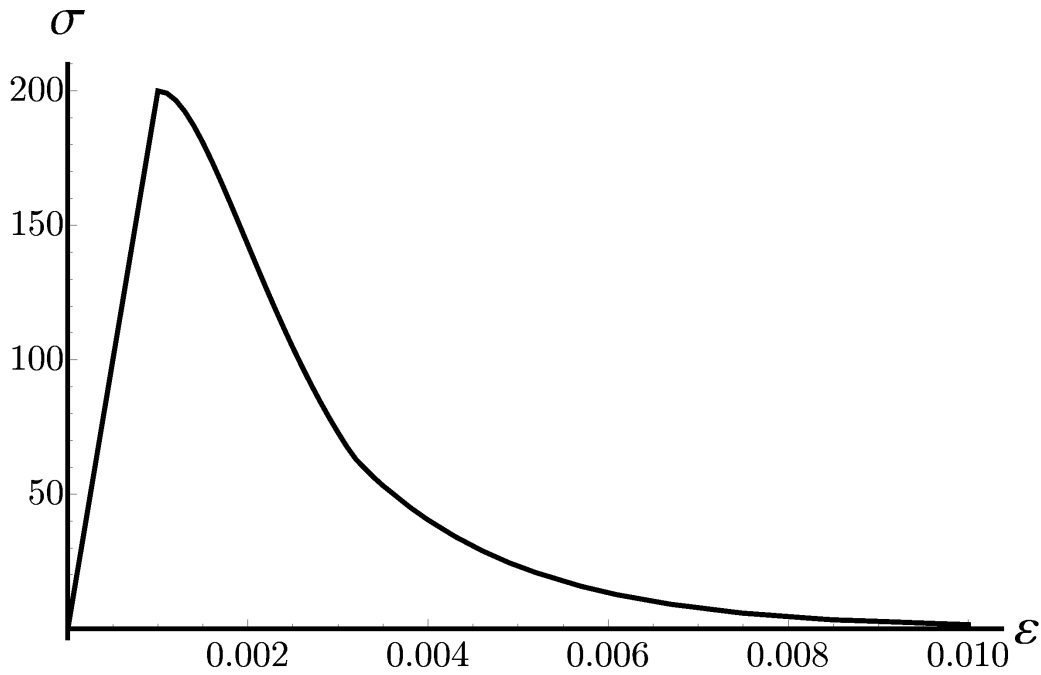


Figure 4.21: Model II [ERVE]: Stresses σ over strains ε on material point level.

4.4 Model III: Gradient-Enhanced Regularization with Efficient Laplacian

In this chapter a gradient-enhanced model with an efficient evaluation of the Laplace operator is presented. This is directly based on the works of Junker et al. (2018), Jantos et al. (2018) and Schwarz et al. (2019a) and is denoted as Model III [LAP] in this thesis.

The variational damage modeling is introduced in Subsection 4.4.1. Then, Subsection 4.4.2 presents the numerical treatment of the displacement field, whereas Subsection 4.4.3 presents the same for the damage function initially limiting to the one-dimensional case. More-dimensional cases are afterwards considered for structured meshes in Subsection 4.4.4 and for unstructured meshes in Subsection 4.4.5. Subsection 4.4.6 describes the allocation of the neighborhood relations. Finally, the algorithm on the finite element level is derived in Subsection 4.4.7.

4.4.1 Variational Damage Modeling

This model is described by the total Helmholtz free-energy function

$$\Psi = \Psi_m + \Psi_r \quad (4.108)$$

consisting of two parts: the mechanical energy Ψ_m and the regularization energy Ψ_r .

The first part, the mechanical energy Ψ_m , is based on the elastic energy Ψ_0 and extended by the isotropic damage function $f(d)$. See Section 4.1 for more details. The following applies

$$\Psi_m = \Psi_m(\boldsymbol{\varepsilon}, d) = f(d)\Psi_0, \quad (4.109)$$

with

$$\Psi_0 = \frac{1}{2} \boldsymbol{\varepsilon} : \mathbb{E}_0 : \boldsymbol{\varepsilon}. \quad (4.110)$$

For the current model the damage function $f(d) = \exp(-d)$ with the internal damage variable $d \in [0, \infty)$ is chosen. The special property that its derivative is corresponding to its own negative function, thus $f'(d) = -f(d)$, will be used later.

The second part, the regularization energy Ψ_r , is a quite common gradient-enhanced approach. The gradient is directly applied on the damage function though and not on the damage variable or an according field function as often done in the literature, see for example work of Dimitrijevic and Hackl (2008), consequently

$$\Psi_r = \frac{1}{2}\beta|\nabla f|^2. \quad (4.111)$$

The parameter β allows to adjust the power of the gradient and thus the power of regularization. This formulation, which is directly based on the damage function, leads to numerical advantages and allows a better and more natural understanding of the material failure.

In order to obtain the stationarity conditions, the Hamilton's principle based on Subsection 2.6.3 is applied as follows

$$\delta_{\mathbf{u}}\mathcal{G} + \delta_d\mathcal{G} + \int_{\Omega} \frac{\partial \mathcal{D}}{\partial \dot{d}} \delta d \, dV = 0 \quad \forall \delta \mathbf{u}, \delta d. \quad (4.112)$$

The variations of the two unknown quantities $\delta \mathbf{u}$ and δd , which are related to the displacement field and the internal damage variable, are independent from each other and have to be considered individually. In regard to Equation (4.112), the Gibbs energy

$$\mathcal{G} := \int_{\Omega} \Psi(\boldsymbol{\varepsilon}, d) \, dV - \int_{\Omega} \mathbf{f} \cdot \mathbf{u} \, dV - \int_{\partial\Omega} \mathbf{t} \cdot \mathbf{u} \, dA \quad (4.113)$$

and the dissipation function

$$\mathcal{D} = r_1 |\dot{d}| \quad (4.114)$$

have to be defined. For the dissipation function a rate-independent approach is chosen in order to prevent viscous effects. This assumption leads to a model preferred for a rather brittle damage behavior. The parameter r_1 in the dissipation function serves as an energetic threshold quantity that has to be overcome to start the damage evolution. The individual treatment of the variations $\delta \mathbf{u}$ and δd results in the stationarity conditions

$$\delta_{\mathbf{u}}\mathcal{G} = 0 \quad \forall \delta \mathbf{u} \quad \text{and} \quad \delta_d\mathcal{G} + \int_{\Omega} \frac{\partial \mathcal{D}}{\partial \dot{d}} \delta d \, dV = 0 \quad \forall \delta d. \quad (4.115)$$

A closer look at the first stationarity condition with respect to the displacement field \mathbf{u} provides the following formulation for $\delta_{\mathbf{u}}\mathcal{G}$

$$\delta_{\mathbf{u}}\mathcal{G} = \int_{\Omega} \frac{\partial \Psi_m}{\partial \boldsymbol{\varepsilon}} : \delta \boldsymbol{\varepsilon} \, dV - \int_{\Omega} \mathbf{f} \cdot \delta \mathbf{u} \, dV - \int_{\partial \Omega} \mathbf{t} \cdot \delta \mathbf{u} \, dA = 0 \quad \forall \delta \mathbf{u}. \quad (4.116)$$

Taking into account the mechanical stresses $\boldsymbol{\sigma} = \partial \Psi_m / \partial \boldsymbol{\varepsilon} = f \mathbb{E} : \boldsymbol{\varepsilon}$ leads to the formulation

$$\int_{\Omega} \boldsymbol{\sigma} : \delta \boldsymbol{\varepsilon} \, dV - \int_{\Omega} \mathbf{f} \cdot \delta \mathbf{u} \, dV - \int_{\partial \Omega} \mathbf{t} \cdot \delta \mathbf{u} \, dA = 0 \quad \forall \delta \mathbf{u}, \quad (4.117)$$

which can be solved by the finite element method considering the Dirichlet boundary conditions $\mathbf{u} = \mathbf{u}^*$, on $\partial \Omega_u$. The second stationarity condition for the internal variable d corresponds to

$$\int_{\Omega} \Psi_0 f' \delta d \, dV + \int_{\Omega} \beta \nabla f \cdot \nabla (f' \delta d) \, dV + \int_{\Omega} \partial \mathcal{D} \delta d \, dV = 0 \quad \forall \delta d, \quad (4.118)$$

since $\delta f = f' \delta d$. The three included terms can be identified as the mechanical and regularization parts of the Helmholtz energy as well as the dissipation function. Due to the non-differentiability of the dissipation function \mathcal{D} at $\dot{d} = 0$, a sub-differential $\partial \mathcal{D}$ has to be introduced. Hereby, the non-differentiable case is circumvented by substituting the derivative by prescribed quantities as

$$\partial \mathcal{D} := \begin{cases} r_1 \frac{\dot{d}}{|\dot{d}|} & \text{for } \dot{d} \neq 0 \\ [-r_1, r_1] & \text{else} \end{cases}. \quad (4.119)$$

Unfortunately, the stationarity condition for δd is complicated to solve in connection with the finite element method due to the sub-differential. Therefore, an integration by parts of the second term of Equation (4.118) is performed

$$\int_{\Omega} \beta \nabla f \cdot \nabla (f' \delta d) \, dV = \int_{\partial \Omega} \beta \mathbf{n} \cdot \nabla f f' \delta d \, dA - \int_{\Omega} \beta \nabla^2 f f' \delta d \, dV. \quad (4.120)$$

Two terms are resulting, the first one refers to the boundary by introducing the normal vector \mathbf{n} while the second one introduces the Laplace operator ∇^2 for the first time. Here, the Laplacian is applied on the damage variable and corresponds to the sum of all unmixed second derivatives with respect to all spatial directions, thus

$$\nabla^2 f := \nabla \cdot \nabla f = \sum_{i=1}^3 \frac{\partial^2 f}{\partial x_i^2}. \quad (4.121)$$

Inserting the outcome of the integration by parts in Equation (4.120) into the stationarity condition for δd in Equation (4.118) leads to its strong form

$$f' \Psi_0 - \beta f' \nabla^2 f + \partial \mathcal{D} \ni 0 \quad \mathbf{x} \in \Omega \quad (4.122)$$

$$\nabla f \cdot \mathbf{n} = 0 \quad \mathbf{x} \in \partial \Omega. \quad (4.123)$$

Hereby, the first term serves as the basis for the calculation of the damage evolution and the second term serves as the Neumann boundary condition for first equation. In order to determine an indicator function, which distinguishes between damage or no damage evolution, the

Legendre-Fenchel transformation of the dissipation function \mathcal{D}^* is performed

$$\begin{aligned}\mathcal{D}^* &= \sup_{\dot{d}} \left\{ p\dot{d} - \mathcal{D} \right\} \\ &= \sup_{\dot{d}} \left\{ |\dot{d}|(p \operatorname{sgn}(\dot{d}) - r_1) \right\} .\end{aligned}\quad (4.124)$$

The outcome basically consists of two parts: the expression $|\dot{d}|$ describes the amount of increasing damage while the expression $p \operatorname{sgn}(\dot{d}) - r_1$ constitutes the indicator function, which can be simplified later. First, the driving force p is defined as

$$p := -f'\Psi_0 + \beta f'\nabla^2 f \quad (4.125)$$

$$= f\Psi_0 - \beta f\nabla^2 f, \quad (4.126)$$

whereby the special property of the damage function $f' = -f$ was used. In general, the driving force competes against the threshold energy value r and therefore initiates the damage evolution. Since healing is not allowed in this model according to physical expectations, it can be assumed that $\operatorname{sgn}(\dot{d}) = \{0, 1\}$. Therefore, the indicator function can be defined from Equation (4.124) as

$$\Phi := p - r_1 \leq 0, \quad (4.127)$$

which distinguishes between two cases: either the driving force achieves the energetic threshold value r_1 and damage evolution occurs $\dot{d} > 0$ or the driving force stays under this limit case and there is no evolution of damage $\dot{d} = 0$, see

$$\begin{aligned}p &\in \partial\mathcal{D} \\ \Leftrightarrow \begin{cases} \dot{d} > 0 : & p = r_1 \\ \dot{d} = 0 : & p \leq r_1 \end{cases} .\end{aligned}\quad (4.128)$$

The governing equations can be summarized as

$$\int_{\Omega} \boldsymbol{\sigma} : \delta\boldsymbol{\varepsilon} \, dV - \int_{\Omega} \mathbf{f} \cdot \delta\mathbf{u} \, dV - \int_{\partial\Omega} \mathbf{t} \cdot \delta\mathbf{u} \, dA = 0 \quad \forall \delta\mathbf{u}, \quad \mathbf{u} = \mathbf{u}^* \quad \forall \mathbf{x} \in \partial\Omega_u, \quad (4.129)$$

$$\dot{d} \geq 0, \quad \Phi := f\Psi_0 - \beta f\nabla^2 f - r_1 \leq 0, \quad \dot{d}\Phi = 0. \quad (4.130)$$

Herewith, the calculation of the displacement field \mathbf{u} as well as the damage function f is completely described. However, the detailed numerical treatment is presented afterwards.

4.4.2 Numerical Treatment of the Displacement Field

According to typical procedures, the displacement field \mathbf{u} is determined by the finite element method. Analogously to Subsections 2.8.2 and 2.8.3 and by taking into account the Voigt notation, the shape functions \mathbf{N} and the operator matrix \mathbf{B} are considered. The stationarity con-

dition for the displacements \mathbf{u} , based on Equation (2.136), can be written in terms of the finite element method as the residual \mathbf{R}_u

$$\mathbf{R}_u = \sum_{e=1}^{N_e} \int_{\Omega_e} \mathbf{B}^T \cdot \tilde{\boldsymbol{\sigma}} \, dV - \sum_{e=1}^{N_e} \int_{\Omega_e} \mathbf{N}^T \cdot \mathbf{f} \, dV - \sum_{e=1}^{N_e} \int_{\partial\Omega_e} \mathbf{N}^T \cdot \mathbf{t} \, dA \stackrel{!}{=} \mathbf{0}. \quad (4.131)$$

This residual is in a common shape. Nevertheless, due to the differential inequality for f presented in Equation (4.130), the damage function is directly depending on the elastic energy and is therefore coupled to local strains. This relation increases the effort for calculating the current displacement field of the current time-step $\tilde{\boldsymbol{\varepsilon}}^{m+1}$ and for that reason a first operator split is introduced at this point: it is assumed that the damage function f is always considered from the last time-step f^m , therefore the stresses are calculated by

$$\tilde{\boldsymbol{\sigma}}^{m+1} = f^m \tilde{\mathbb{E}}_0 \cdot \tilde{\boldsymbol{\varepsilon}}^{m+1}. \quad (4.132)$$

This first operator-split separates the damage function and the strains (or displacements) for the computation of the current displacement field. As a consequence, the non-linearity of the stationarity condition converts into a linear algebraic equation and the tangent matrix in Equation (2.140) becomes constant for each time-step including the following material tangent

$$\left. \frac{d\tilde{\boldsymbol{\sigma}}}{d\tilde{\boldsymbol{\varepsilon}}} \right|^{m+1} = f^m \tilde{\mathbb{E}}_0. \quad (4.133)$$

This first operator split accompanies with the requirement of small loading increments in order to not obtain viscous-related effects. This effect will be analyzed in Subsection 5.3.1.

4.4.3 Numerical Treatment of the Damage Function for One-Dimensionality

In order to introduce the numerical treatment of the damage evolution, the problem is applied to the simplest case by restricting to one-dimensionality first. Hereto, the Laplace operator ∇^2 corresponds to the second derivative of the damage function with respect to the one-dimensional spatial coordinate x . This second derivative can easily be described with the finite difference method, which directly takes into account the related neighbors, see 4.22, even without introducing any additional (computation) time-consuming quantities at the nodes.

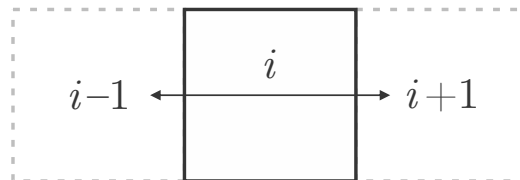


Figure 4.22: Model III [LAP]: Neighborhood relations of central element i for the one-dimensional case with two selected neighbors.

The distance to the neighboring elements is described by the spatial quantity Δx , which is here assumed to be constant for simplicity, as shown in Figure 4.23.

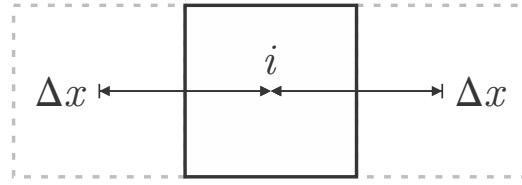


Figure 4.23: Model III [LAP]: Spatial quantity regarding central element i for the one-dimensional case with two selected neighbors.

First, the damage function is evaluated at the center of mass of each element i and therefore the indicator function is defined element-wise, such as

$$\Phi_i := f_i \bar{\Psi}_{0,i} - \beta f_i \nabla^2 f_i - r_1 \leq 0 . \quad (4.134)$$

Consequently, all Gauß points within one element basically have the same damage function f_i and it should be noted that even the formulation of element-wise damage allows for considerably sharp damage zones or cracks, as shown later. Then, the second derivative of the damage function or rather the Laplace operator is replaced by the finite differences discretization. The term transfers to

$$\Phi_i := f_i \bar{\Psi}_{0,i} - \beta f_i \frac{f_{i-1} - 2f_i + f_{i+1}}{\Delta x^2} - r_1 \leq 0 . \quad (4.135)$$

Hereby, the discretization is based on the direct left ($i - 1$) and right ($i + 1$) neighbor of the central element i . For the Neumann boundary conditions, ghost elements are introduced mirroring the damage function of the first and last element. Hereto, some investigations were done by Stacey (1994) for example. The indicator function also considers the averaged elastic energy

$$\bar{\Psi}_{0,i} = \frac{1}{\Omega_i} \int_{\Omega_i} \Psi_0 \, dV , \quad (4.136)$$

which can be computed for each element i with volume Ω_i by capturing the accumulated numerical volumes of the Gauß points. The indicator function Φ_i in Equation (4.135) is defined for each element i and due to the Laplace operator in addition to the damage function f_i also the direct neighbors f_{i-1} and f_{i+1} are included. For that reason, the equations are coupled with each other leading to a system of equations with a coefficient matrix of the dimension $n_e \times n_e$ with n_e as the number of finite elements. This is quite expensive to solve. Consequently, a second operator split is introduced at this point: it is assumed that the damage function f is always considered from the last iteration-step f^k , therefore the indicator function converts to

$$\Phi_i^k = f_i^k \bar{\Psi}_{0,i}^{m+1} - \beta f_i^k \frac{f_{i-1}^k - 2f_i^k + f_{i+1}^k}{\Delta x^2} - r_1 \leq 0 , \quad (4.137)$$

with iteration step k . This second operator-split prevents the coupling between the neighbors and thus between the equations because all entries are known from the last time-step. As a consequence, the system of coupled inequalities of the dimension $n_e \times n_e$ converts into a system of uncoupled inequalities of dimension n_e . Besides, the second operator-split circumvent using neighbored damage functions and considers the neighboring damage functions f_{i-1} and f_{i+1} to be fixed for each iteration step. As a result, the damage functions are calculated for each element separately while the indicator function is violated, according to $\Phi_i^k > 0$. As soon as the indicator function has converged to zero again, thus $\Phi_i^k = 0$, the damage functions are updated

by the Newton method, such as $f_i^k \rightarrow f_i^{k+1}$. Hereby, the Newton-Raphson method, see works of Schäfer (1999), Zienkiewicz et al. (2005), Fish and Belytschko (2007), and Hermann (2011) for example, is applied to the computation of the damage functions that looks as follows

$$f_i^{k+1} = f_i^k - \frac{\Phi_i^k}{\partial \Phi_i^k / \partial f_i^k}, \quad (4.138)$$

with the derivative of the indicator function with respect to the damage function

$$\frac{\partial \Phi_i^k}{\partial f_i^k} = \bar{\Psi}_{0,i}^{m+1} - \beta \frac{f_{i-1}^k - 2f_i^k + f_{i+1}^k}{\Delta x^2} + \beta f_i^k \frac{2}{\Delta x^2}. \quad (4.139)$$

4.4.4 Numerical Treatment of the Damage Function for Structured Meshes

After considering the one-dimensional case, the two- (2D) or three-dimensional (3D) cases for structured meshes, inspired by the work of Jantos et al. (2018), are presented here. The work of Abu Al-Rub and Voyiadjis (2005) can be mentioned as a similar approach. Previously, only two direct neighbors were present, the left and right neighbor, for a multi-dimensional treatment the number of elements is increased: there are four direct neighbors for the two-dimensional and six direct neighbors for the three-dimensional case.

This is illustrated by Figure 4.24: on the left-hand side the two-dimensional case with four direct neighbors (*north*, *east*, *south* and *west*) and on the right-hand side the three-dimensional case with two additional direct neighbors (*front* and *back*) is presented.

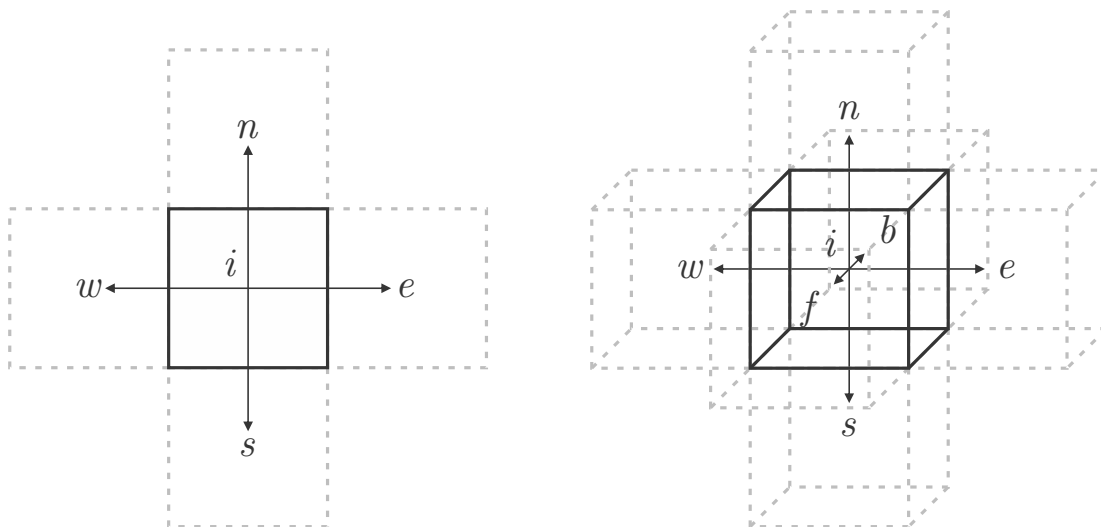


Figure 4.24: Model III [LAP]: Neighborhood relations of central element i for 2D with four selected neighbors (left) and for 3D with six selected neighbors (right).

For further procedure, the distances between the mid-point of the central element i and the mid-points of the neighboring elements have to be involved, hereto the spatial increments denoted by Δx_n , Δx_s , Δx_e , Δx_w , Δx_f , and Δx_b are considered as presented in Figure 4.25.

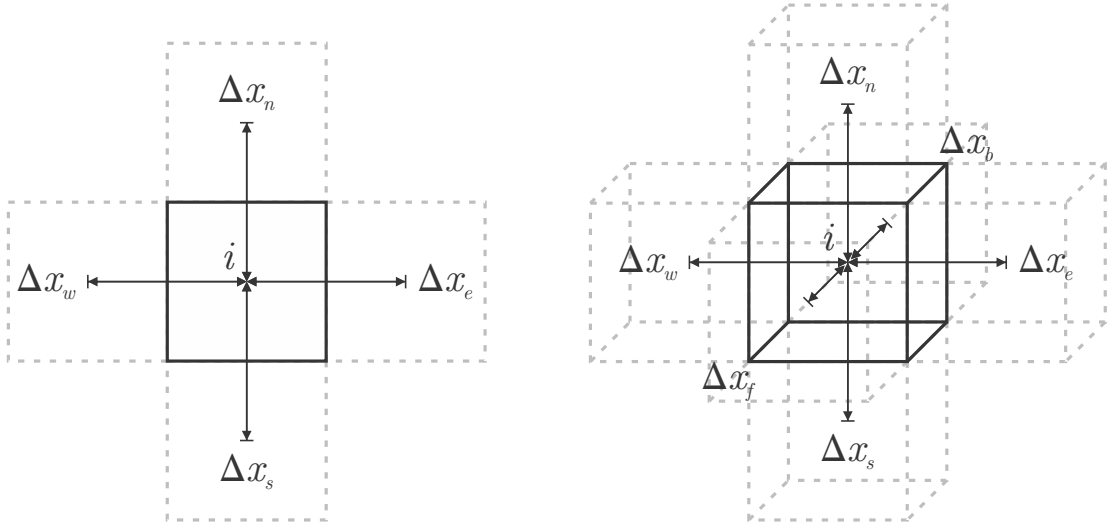


Figure 4.25: Model III [LAP]: Spatial increments regarding central element i for 2D with four selected neighbors (left) and for 3D with six selected neighbors (right).

The allocation of neighbors to respective elements and the determination of the spatial increments is done once before the main finite element calculation starts. In Subsection 4.4.6 more information about the neighborhood relations and dealing with the Neumann boundary conditions is provided. In accordance with Equation (4.121) and related to Figure 4.25, the second derivatives of f_i in all three spatial directions for the three-dimensional case are defined as

$$\frac{\partial^2 f_i}{\partial x_1^2} \approx \frac{2(f_w - f_i)}{\Delta x_w(\Delta x_w + \Delta x_e)} + \frac{2(f_e - f_i)}{\Delta x_e(\Delta x_w + \Delta x_e)}, \quad (4.140)$$

$$\frac{\partial^2 f_i}{\partial x_2^2} \approx \frac{2(f_n - f_i)}{\Delta x_n(\Delta x_n + \Delta x_s)} + \frac{2(f_s - f_i)}{\Delta x_s(\Delta x_n + \Delta x_s)}, \quad (4.141)$$

$$\frac{\partial^2 f_i}{\partial x_3^2} \approx \frac{2(f_f - f_i)}{\Delta x_f(\Delta x_f + \Delta x_b)} + \frac{2(f_b - f_i)}{\Delta x_b(\Delta x_f + \Delta x_b)}, \quad (4.142)$$

with f_n , f_s , f_e , f_w , f_f , and f_b indicating the damage functions of the neighboring elements. In case of a two-dimensional consideration, the third spatial direction as well as the front and back relations are neglected. Combining the second derivatives in the vector Λ_f finally yields the Laplace operator for the three-dimensional case as follows

$$\Lambda_f = (\Lambda_f)_i \mathbf{e}_i := \sum_{j=1}^3 \frac{\partial^2 f_i}{\partial x_j^2} \mathbf{e}_i \quad i = 1, \dots, n_e. \quad (4.143)$$

The length of the vector accordingly depends on the number of elements n_e . It should be emphasized here that, due to the formulation by means of the finite differences scheme and the direct relations to the neighboring elements, this numerical treatment is not applicable for unstructured meshes. This is because the neighboring elements are not located in line with the respective considered central element. However, this problem can be solved by the subsequent numerical treatment for unstructured meshes that is based on the idea of meshless methods by means of the inverted Taylor series expansion.

4.4.5 Numerical Treatment of the Damage Function for Unstructured Meshes

In order to extend the scope of application, the numerical treatment must be able to consider unstructured meshes as well. Subsequently, the derivation originating from the Taylor series expansion is presented for the two- and particularly the three-dimensional case. The procedure is inspired by the work of Jantos et al. (2018).

Instead of applying the finite differences scheme as before, meshless methods accounting for a more general procedure have to be used, see for example works of Prax et al. (1996) and Basic et al. (2018). Therefore, the Taylor series expansion is adjusted by inverting the idea of the Taylor series: usually the derivatives and spatial increments are known and the functions are the wanted objective, whereas in the present case the derivatives are the wanted objectives and the spatial increments and functions are known. More details about the Taylor's theorem are provided for example by Hermann (2011).

Initially, the Taylor series expansion for the damage function f_i around a central element \mathbf{x}_i up to degree two can be written as

$$\Delta f_{i,j} := f_j - f_i = \sum_{k=1}^3 \left(\frac{\partial f_i}{\partial x_k} \Delta x_{j,k} + \frac{1}{2} \sum_{p=1}^3 \frac{\partial^2 f_i}{\partial x_k \partial x_p} \Delta x_{j,k} \Delta x_{j,p} \right). \quad (4.144)$$

Hereby, the spatial increments, or more precisely the distances between the neighboring element \mathbf{x}_j and the central element \mathbf{x}_i in all three spatial directions, are captured by the vector

$$\Delta \mathbf{x}_j := \mathbf{x}_i - \mathbf{x}_j = \begin{pmatrix} x_{i,1} - x_{j,1} \\ x_{i,2} - x_{j,2} \\ x_{i,3} - x_{j,3} \end{pmatrix}, \quad (4.145)$$

whereby the index j runs over all neighboring elements. A deeper look at the Taylor series expansion for $f(d)$ leads to the following findings: there are nine unknown derivatives (five in 2D) and therefore, in order to be able to solve this system of equations, nine neighboring elements (five in 2D) are needed. Up to now, only the six direct neighbors $n, s, e, w, f,$ and b were considered in 3D (four direct neighbors $n, s, e,$ and w in 2D). For that reason, the three additional neighbors o, p, q have to be taken into account for the three-dimensional case (2D only requires one additional neighbor o). There are specific requirements for the additional neighbors, particularly the additional neighbors have to be selected once for a spatial plane and preferably close to the central element.

In general, the allocation of neighbors to the respective elements and the determination of the spatial increments is here again done once before the main calculation starts. More information about the neighborhood relations (also about the newly introduced additional neighbors) and dealing with the Neumann boundary conditions is provided in Subsection 4.4.6.

In the next step, the Taylor series expansion from Equation (4.144) can be combined in a linear system of equations appearing as

$$\Delta \mathbf{f}_i = \mathbf{D} \cdot \partial \mathbf{f}_i. \quad (4.146)$$

This system of equations consists of the following, which is now described in more detail:

On the left-hand side of Equation (4.146), the known increments of the damage function captured by the vector $\Delta \mathbf{f}_i$ of length 9 (5 in 2D) is provided, thus

$$\Delta \mathbf{f}_i = (\Delta f_{i,j}) \mathbf{e}_j, \quad j \in \{n, s, e, w, f, b, o, p, q\} \quad (4.147)$$

The first place on the right-hand side of Equation (4.146) provides the known spatial increments collected by the coefficient matrix \mathbf{D} of size 9×9 (5×5 in 2D). The entries

$$\begin{aligned} D_{j,1} &= \Delta x_{j,1}, & D_{j,4} &= \Delta x_{j,1} \Delta x_{j,2}, & D_{j,7} &= \frac{(\Delta x_{j,1})^2}{2}, \\ D_{j,2} &= \Delta x_{j,2}, & D_{j,5} &= \Delta x_{j,1} \Delta x_{j,3}, & D_{j,8} &= \frac{(\Delta x_{j,2})^2}{2}, \\ D_{j,3} &= \Delta x_{j,3}, & D_{j,6} &= \Delta x_{j,2} \Delta x_{j,3}, & D_{j,9} &= \frac{(\Delta x_{j,3})^2}{2} \end{aligned} \quad (4.148)$$

have to be applied for each neighbor j describing only one line of the whole coefficient matrix.

Finally, at second place on the right-hand side of Equation (4.146), the unknown partial derivatives captured by the vector $\partial \mathbf{f}_i$ of length 9 (5 in 2D) is provided. The transposed form reads as follows

$$\partial \mathbf{f}_i := \left(\frac{\partial f_i}{\partial x_1} \quad \frac{\partial f_i}{\partial x_2} \quad \frac{\partial f_i}{\partial x_3} \quad \frac{\partial^2 f_i}{\partial x_1 \partial x_2} \quad \frac{\partial^2 f_i}{\partial x_1 \partial x_3} \quad \frac{\partial^2 f_i}{\partial x_2 \partial x_3} \quad \frac{\partial^2 f_i}{\partial x_1^2} \quad \frac{\partial^2 f_i}{\partial x_2^2} \quad \frac{\partial^2 f_i}{\partial x_3^2} \right)^T. \quad (4.149)$$

At this point, the system of equations is solved for the unknown quantity, the partial derivatives $\partial \mathbf{f}_i$, therefore

$$\partial \mathbf{f}_i = \mathbf{D}^{-1} \cdot \Delta \mathbf{f}_i. \quad (4.150)$$

According to Equation (4.121), for the calculation of the laplace operator ∇^2 only the unmixed second derivatives of the damage function f are necessary: the first six entries of $\partial \mathbf{f}_i$ can be neglected (first three in 2D) and only the last three entries have to be considered (last two in 2D). Hereto, the matrix \mathbf{B}^{∇^2} of size 3×9 (2×5 in 2D) is introduced. This matrix replaces the inverted coefficient matrix \mathbf{D}^{-1} but only collects the last three lines (last two in 2D). This results in neglecting the unneeded partial derivatives. Consequently, \mathbf{B}^{∇^2} is defined as

$$\mathbf{B}_{l,j}^{\nabla^2} := \mathbf{D}_{l+6,j}^{-1}, \quad l \in \{1, 2, 3\}, \quad j \in \{1, \dots, 9\}, \quad (4.151)$$

such that only the unmixed second derivatives remain

$$\mathbf{B}^{\nabla^2} \cdot \Delta \mathbf{f}_i = \frac{\partial^2 f_i}{\partial x_l^2} \mathbf{e}_l, \quad l \in \{1, 2, 3\}. \quad (4.152)$$

Since \mathbf{B}^{∇^2} is only depending on mesh topology analogously to the coefficient matrix \mathbf{D} , it can be calculated together with the allocation of neighbors and determination of spatial increments once before the main finite element calculation starts.

Finally, the Laplace operator by Equation (4.121) for each element i is calculated as

$$(\Lambda_f)_i = \sum_{l=1}^3 \left(\mathbf{B}^{\nabla^2} \cdot \Delta \mathbf{f}_i \right)_l. \quad (4.153)$$

Moreover, the Laplace operator's derivative with respect to damage function is given by

$$(\mathbb{D}\Lambda_f)_i := \frac{\partial(\Lambda_f)_i}{\partial f_i} = \sum_{l=1}^3 \left(\mathbf{B}^{\nabla^2} \cdot \frac{\partial \Delta \mathbf{f}_i}{\partial f_i} \right)_l = - \sum_{l=1}^3 \left(\mathbf{B}^{\nabla^2} \cdot \mathbf{1} \right)_l, \quad (4.154)$$

with the identity vector $\mathbf{1}$ of length 9 (5 in 2D). All things considered, the yield function for an unstructured mesh can be written as

$$\Phi_i^k = f_i^k \bar{\Psi}_{0,i}^{m+1} - \beta f_i^k (\Lambda_f)_i - r_1 \leq 0 \quad (4.155)$$

with

$$f_i^{k+1} = \begin{cases} f_i^k - \frac{\Phi_i^k}{\bar{\Psi}_{0,i}^{m+1} - \beta (\Lambda_f)_i - \beta f_i^k (\mathbb{D}\Lambda_f)_i} & \text{if } \Phi_i^k > 0 \\ f_i^k & \text{else .} \end{cases} \quad (4.156)$$

4.4.6 Allocation of the Neighborhood Relations

At this point the allocation of neighborhood relations is presented. The neighborhood relations are accompanied with handling the Neumann boundary conditions. Both are inspired by the work of Jantos et al. (2018). There are three different cases: the one-dimensional (Section 4.4.3) as well as the more-dimensional consideration with structured (Section 4.4.4) or unstructured (Section 4.4.5) mesh. For all cases, the distances between the elements are always related to the center of mass. The numerical treatment of a one-dimensional consideration, based on Section 4.4.3, is quite easy: the neighborhood relations directly correspond to the numbering of the mesh or rather finite differences discretization. At the beginning and end of the one-dimensional specimen the Neumann boundary conditions are acting: no gradient is allowed and therefore additional pseudo-nodes are mirroring the damage function.

In case of a structured mesh for a two- or three-dimensional consideration, presented in Section 4.4.4, the neighborhood relations are not directly given by the discretization numbering. Since the geometry of the mesh is assumed to be constant during the whole finite element calculation following the assumption of small deformations, the relations of neighboring elements only have to be determined once before the main calculation starts. This is basically done by searching for a common edge that is corresponding to two common global nodes for the two-dimensional case or a common plane that is corresponding to four common global nodes for the three-dimensional case. Subsequently, a classification of the local numbering of the common nodes within the central element is done in order to assign the neighboring element to a direction n , s , e , w , and, if applicable, f and b . For simplicity, this is illustrated only for the two-dimensional case by Figure 4.26: in accordance with the schematic figure, the local numbers 1 and 4 of the common global nodes always correspond to the neighbor n , 2 and 3 to the neighbor s , 3 and 4 to the neighbor e , and 1 and 2 to the neighbor w . This is analogously done for the three-dimensional case: the local numbers of four common global nodes have to be assigned and the neighbors f and b have to be considered in addition. The Neumann boundary conditions, which prevent a gradient at the boundaries, are similarly considered as before in the one-dimensional case: pseudo-nodes are introduced at the boundary by mirroring the damage function of the outer elements. Some investigations on that are given by Stacey (1994).

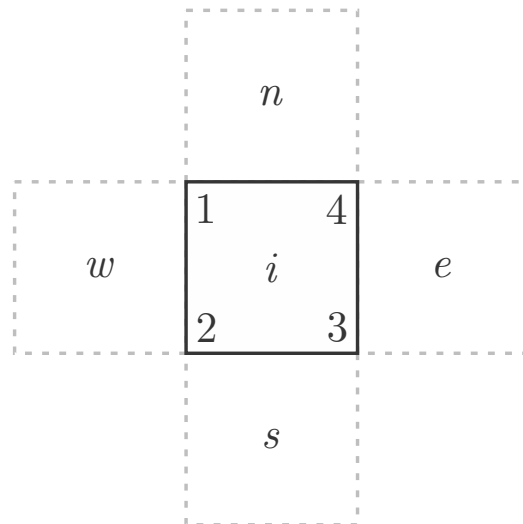


Figure 4.26: Model III [LAP]: Local numbering of central element i for structured mesh under two-dimensional consideration with four selected neighbors.

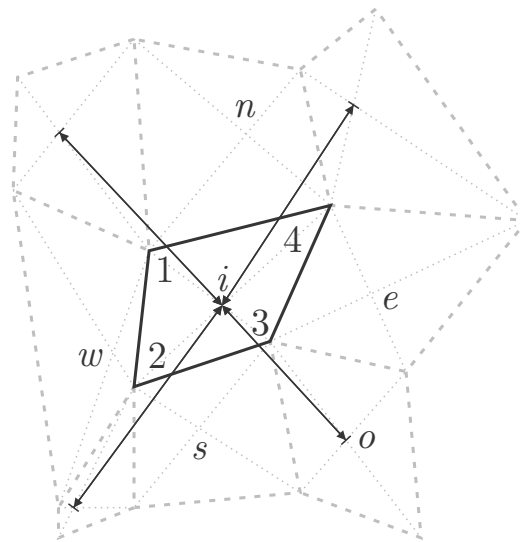


Figure 4.27: Model III [LAP]: Diagonal elements with respective distances and local numbering of central element i for unstructured mesh under two-dimensional consideration with five selected neighbors.

The most complicated case is an unstructured mesh for a two- or three-dimensional consideration, see Section 4.4.5. In principle, the same procedure as for the structured mesh is applied (see previous paragraph), but additionally the elements o (2D) and if applicable p and q (3D) have to be taken into account in order to allow for solving the system of equations in Equation (4.146). The requirements of these three additional elements are that they have to be selected once for each spatial plane and preferably close to the central element. Usually, these additional elements are the closest ones located in diagonal direction as illustrated in Figure 4.27. Again, only the two-dimensional case is presented for reasons of simplicity. The diagonal neighbors are basically assigned by searching for a common global node for the two-dimensional case or for a common edge that is corresponding to two common global nodes for the three-dimensional case. In case that there is no diagonal neighbor the closest element in the relevant plane is being

searched. Related to Figure 4.27 the closest diagonal element is o . Comparably to the structured mesh, the Neumann boundary conditions prohibiting a gradient at the boundaries are considered by pseudo-nodes mirroring the damage function of the outer elements.

4.4.7 Algorithm on Finite Element Level

This subsection provides the related Algorithm 4 for Model III [LAP] presented in Section 4.4. The implementation is based on the element level of the finite element calculations.

Algorithm 4: Model III [LAP]: Finite element algorithm on element level.

after convergence of the finite element routine for $\hat{\mathbf{u}}^{m+1}$:

input: $\tilde{\boldsymbol{\varepsilon}}^{m+1}, f^m$

calc: $\bar{\Psi}_{0,e}^{m+1}$

calc: $\tilde{\boldsymbol{\sigma}}^{m+1} = \tilde{\boldsymbol{\sigma}}(\tilde{\boldsymbol{\varepsilon}}^{m+1}, f^m)$

calc: $\frac{d\tilde{\boldsymbol{\sigma}}^{m+1}}{d\tilde{\boldsymbol{\varepsilon}}^{m+1}} = \frac{d\tilde{\boldsymbol{\sigma}}}{d\tilde{\boldsymbol{\varepsilon}}}(f^m)$

while $\sqrt{\Phi^k \cdot \Phi^k} > tol \times N_e$ **do**

calc: Laplace operator Λ_f and derivative $D\Lambda_f$

for $e \leq N_e$ **do**

set: $f_e^k = f_e^m$

calc: $\Phi_e^k = f_e^k \bar{\Psi}_{0,e}^{m+1} - \beta f_e^k (\Lambda_f)_e - r_1$

if $\Phi_e^k < tol$ **then**

$\Phi_e^k = 0$

$f_e^{k+1} = f_e^k$

else

$f_e^{k+1} = f_e^k - \frac{\Phi_e^k}{\bar{\Psi}_{0,e}^{m+1} - \beta(\Lambda_f)_i - \beta f_e^k (D\Lambda_f)_e}$

set: $f_e^{m+1} = f_e^{k+1}$

calc: Φ^k

5 Preparatory Work for Finite Element Results

The preparatory work for the finite element calculations is provided in this chapter starting with the presentation of the underlying boundary value problems in Section 5.1, followed by the parameter identification for the considered damage models. Hereby, Section 5.2 presents the investigations related to Model I [REL], Section 5.3 respectively to Model II [ERVE] and Section 5.4 to Model III [LAP].

Each parameter identification includes several parameter studies based on the double-notched plate with unstructured mesh and a final selected parameter set. The material parameters E and ν as well as the loading rate \dot{u} are anticipated in Table 5.1 since they are uniformly applied for all presented models and boundary value problems in this thesis.

E	ν	\dot{u}
210 GPa	0.33 [-]	15×10^{-6} mm/s

Table 5.1: Uniformly applied material parameters and loading rate for finite element results.

All finite element calculations in this thesis have been performed with the software FEAP (A Finite Element Analysis Program) developed by the University of California, Berkeley in the United States of America, further information to FEAP is provided for example by Taylor (2017a) and Taylor (2017b).

The previous creation of the geometries, accordingly the preprocessing, have been done with the software Gmsh developed by Geuzaine and Remacle (2009). The subsequent postprocessing of the finite element calculations have then been done with the software GiD developed by the International Center for Numerical Methods in Engineering (CIMNE) in Spain.

5.1 Boundary Value Problems for Investigations

In this section the underlying boundary value problems are presented which are applied for the numerical calculations in regard to the model comparison in Chapter 6 as well as for the parameter identification hereinafter. Hereby, the double-notched plate is included in Subsection 5.1.1, the plate with a centered hole in Subsection 5.1.2 and the cracked plate in Subsection 5.1.3. The three-dimensional specimens are fixed to all directions at the top and bottom and additionally a displacement is applied on the top. Therefore, plane stress conditions are prescribed. Details on the number of elements as well as indications of size are respectively provided.

5.1.1 Double-Notched Plate

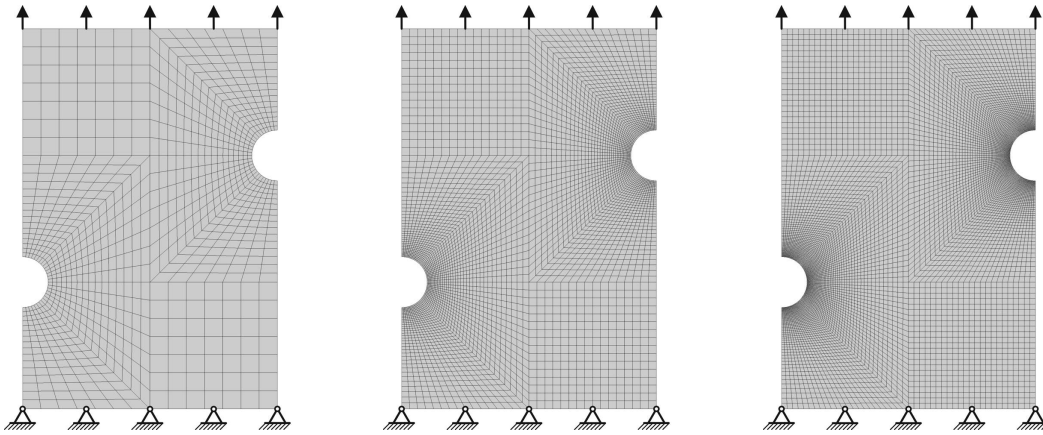


Figure 5.1: Structured finite element meshes with 994, 4992, and 10074 elements for the double-notched plate with dimensions $1.0 \times 1.5 \times 0.01$ mm (left to right).

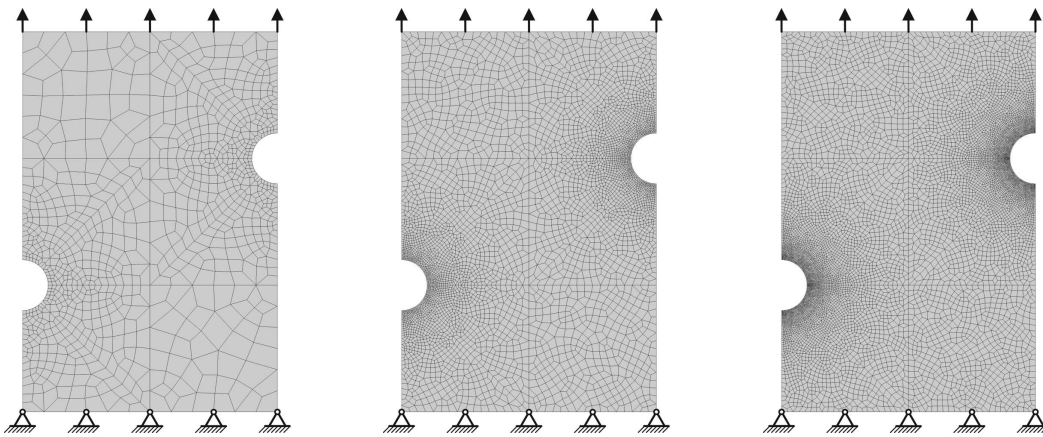


Figure 5.2: Unstructured finite element meshes with 986, 5064, and 10161 elements for the double-notched plate with dimensions $1.0 \times 1.5 \times 0.01$ mm (left to right).

5.1.2 Plate with a Centered Hole

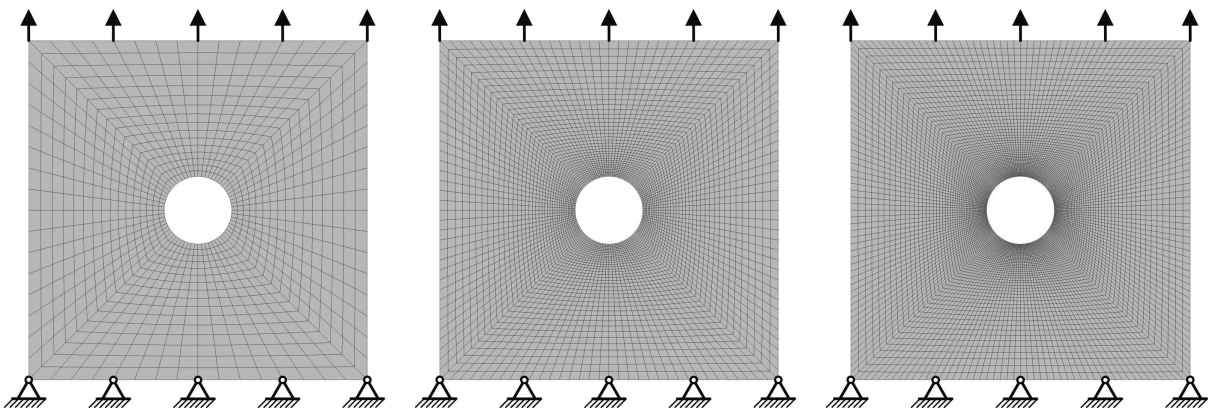


Figure 5.3: Structured finite element meshes with 1024, 5032, and 10000 elements for the plate with a centered hole with dimensions $1.0 \times 1.0 \times 0.01$ mm (left to right).

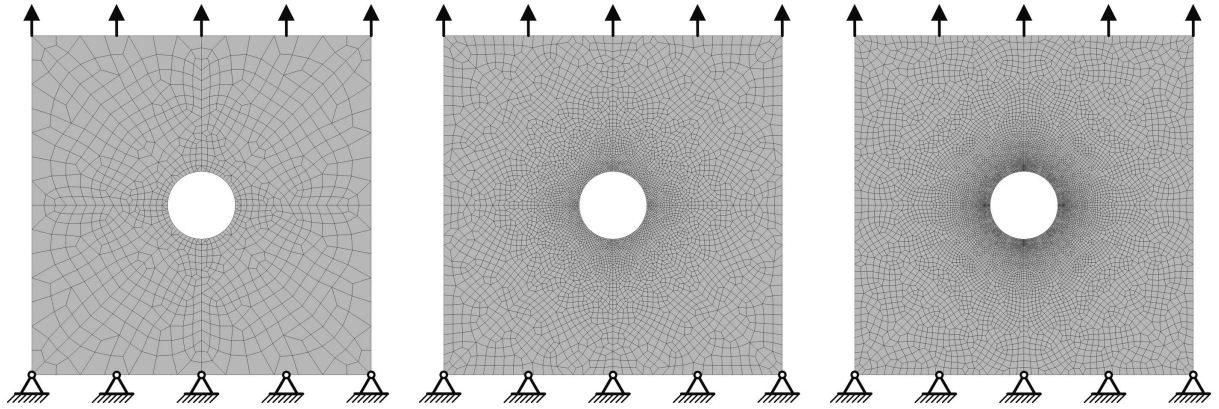


Figure 5.4: Unstructured finite element meshes with 996, 5090, and 10140 elements for the plate with a centered hole with dimensions $1.0 \times 1.0 \times 0.01$ mm (left to right).

5.1.3 Cracked Plate

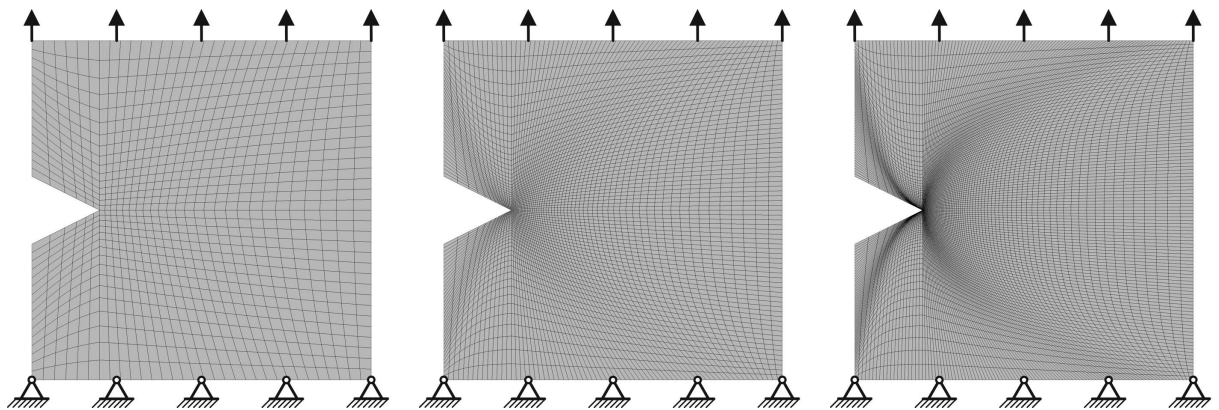


Figure 5.5: Structured finite element meshes with 1024, 4970, and 10000 elements for the cracked plate with dimensions $1.0 \times 1.0 \times 0.01$ mm (left to right).

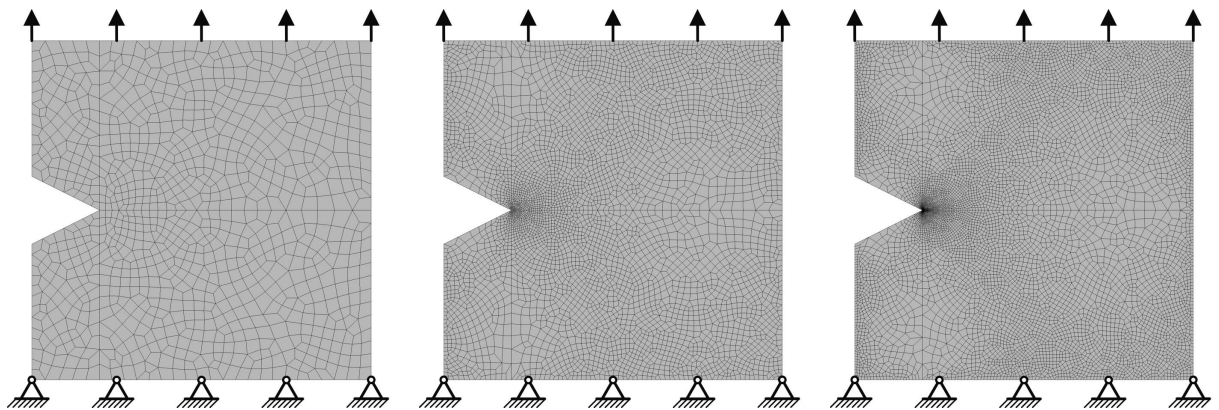


Figure 5.6: Unstructured finite element meshes with 1007, 5001, and 10040 elements for the cracked plate with dimensions $1.0 \times 1.0 \times 0.01$ mm (left to right).

5.2 Parameter Identification for Model I

Below, the rate-dependence is investigated in Subsection 5.2.1 and the homogenization parameter β in Subsection 5.2.2. Subsection 5.2.3 examines the viscosity r_2 and the final selected parameters are given in Subsection 5.2.4.

5.2.1 Investigation of Rate-Dependence

Since Model I [REL] is rate-dependent, the numerical results are rate-dependent as well. This is shown for five loading rates $\dot{u} = \{75.00, 37.50, 25.00, 18.75, 15.00\} \times 10^{-6}$ mm/s by the global structural response in Figure 5.7. Hereby, the localized (brittle-like) as well as the diffusive (ductile-like) case are distinguished with $r_2 = 0.20/1.00 \times 10^8$ MPa s and $\beta = 2.0$.

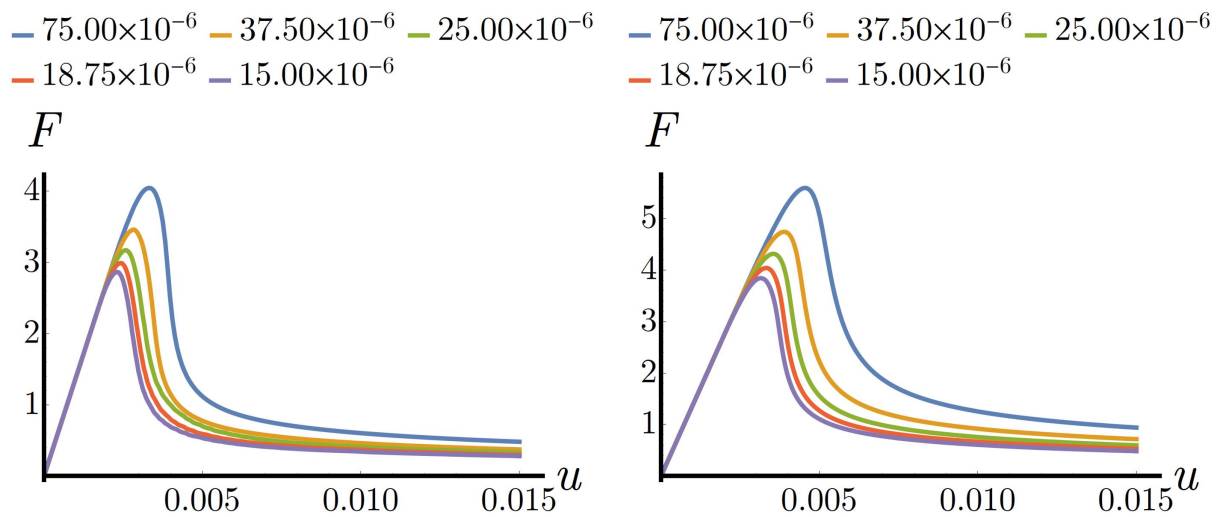


Figure 5.7: Model I [REL]: Study on loading rate $\dot{u} = [\text{mm/s}]$ by the double-notched plate with 986 unstructured elements for localized/diffusive cases with $r_2 = 0.20/1.00 \times 10^8$ MPa s (left/right) and $\beta = 2.0$.

The rate-dependence can further be observed by the contour plots in Figures 5.8 and 5.9 for the localized and diffusive cases. The selected loading rates $\dot{u} = \{75.00, 25.00, 15.00\} \times 10^{-6}$ mm/s underline the strongly rate-depending results. The higher the loading rate the stronger the regularization is acting. Thus, the damage distribution becomes more diffusive. This allows to transform the localized case on the right-hand side of Figure 5.8 into a diffusive case as shown on the left-hand side. Moreover, the diffusive case on the right-hand side of Figure 5.9 can be transformed into an extremely diffusive damage zone as shown on the left-hand side.

Due to the rate-dependence, the loading rates can be chosen in any manner and other parameters have to be adjusted, accordingly. However, in coordination with the other damage models in this thesis, the loading rate is set to $\dot{u} = 15.00 \times 10^{-6}$ mm/s for further investigations.

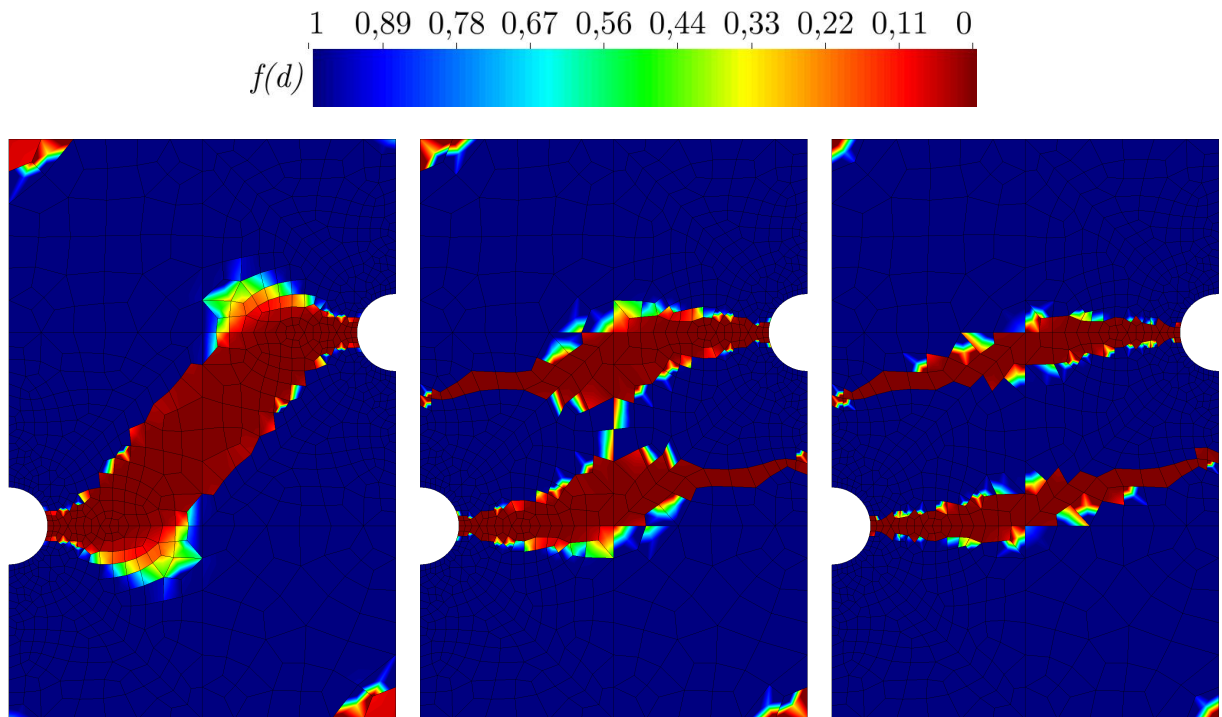


Figure 5.8: Model I [REL]: Distribution of $f(d)$ for the double-notched plate with 986 unstructured elements with $\dot{u} = \{75.00, 25.00, 15.00\} \times 10^{-6}$ mm/s (left to right) at the last loading step for the localized case with $r_2 = 0.20 \times 10^8$ MPa s and $\beta = 2.0$.

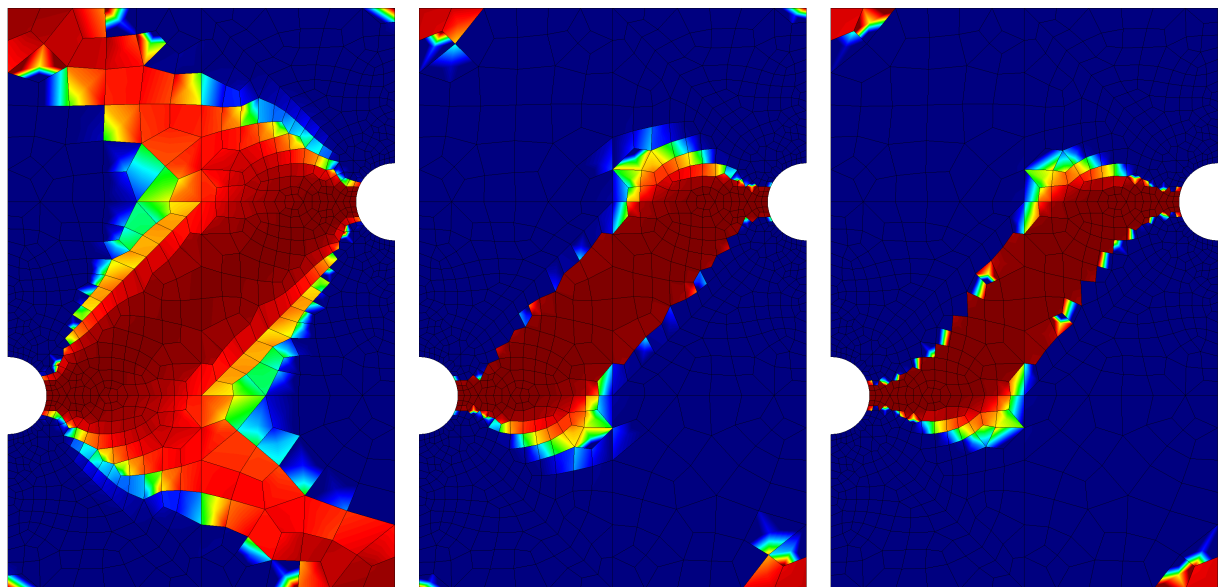


Figure 5.9: Model I [REL]: Distribution of $f(d)$ for the double-notched plate with 986 unstructured elements with $\dot{u} = \{75.00, 25.00, 15.00\} \times 10^{-6}$ mm/s (left to right) at the last loading step for the diffusive case with $r_2 = 1.00 \times 10^8$ MPa s and $\beta = 2.0$.

5.2.2 Investigation of Homogenization

Next, the influence of the homogenization parameter is investigated, which only allows for the drop in the force-displacements diagrams. The values $\beta = \{1.0, 1.2, 1.4, 1.6, 1.8, 2.0, 2.2, 2.4\}$

are selected for this purpose. For a better overview, the results are limited to the diffusive (ductile-like) results with $r_2 = 1.00 \times 10^8$ MPa s at a loading rate of $\dot{u} = 15.00 \times 10^{-6}$ mm/s.

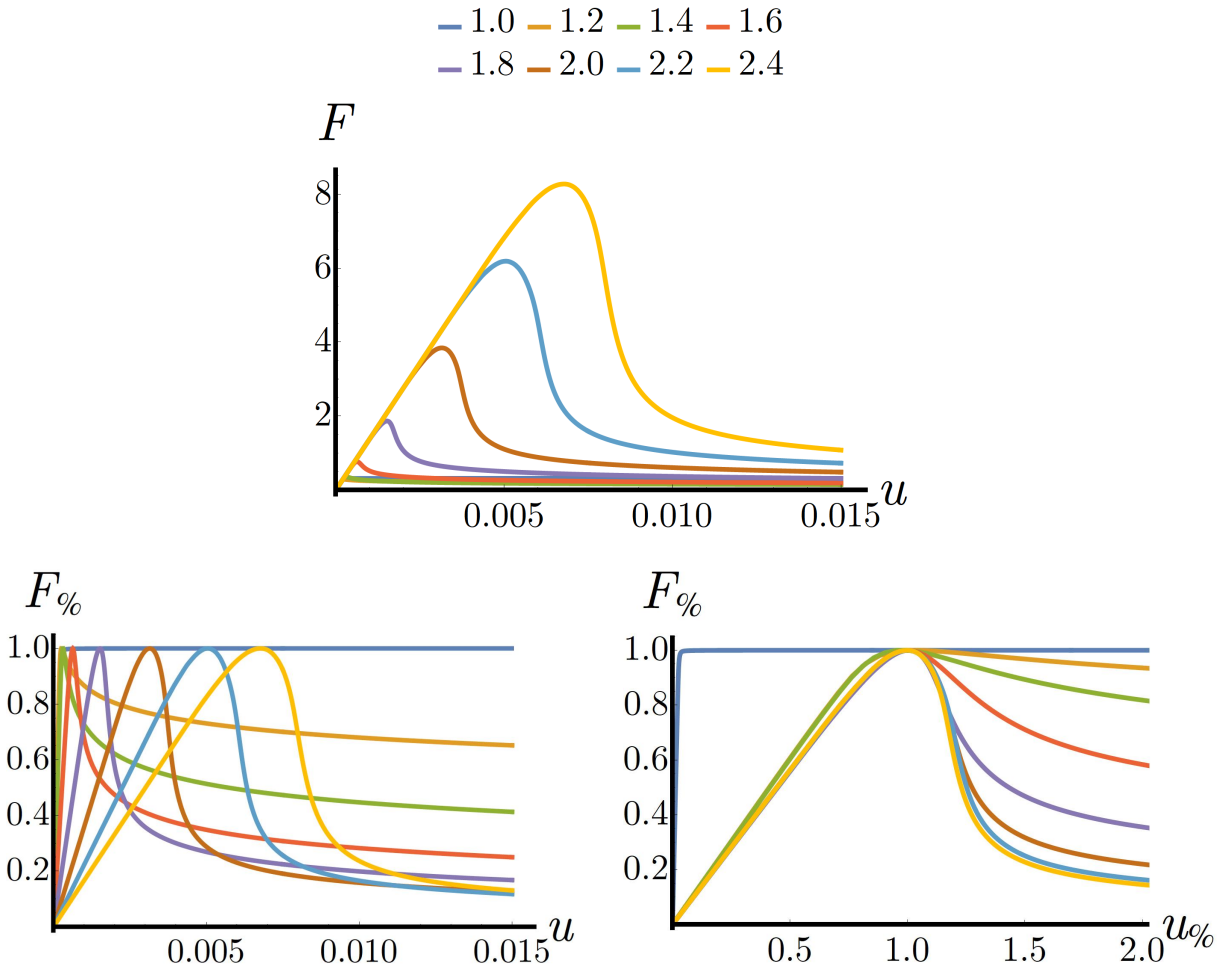


Figure 5.10: Model I [REL]: Study on homogenization parameter β by the original (top), single-normalized (left), and double-normalized (right) force-displacement diagram for the double-notched plate with 986 unstructured elements considering the diffusive case with $r_2 = 1.00 \times 10^8$ MPa s (left/right) and $\dot{u} = 15.00 \times 10^{-6}$ mm/s.

The top diagram in Figure 5.10 reveals that an increase of β leads to a strong increase of global forces. This is due to the impact on the driving forces resulting in a shifted damage evolution. In order to allow for a better comparison of the characteristics of β , the forces are normalized yielding the diagram on the left-hand side of Figure 5.10 and a further normalization of the displacements yields the diagram on the right-hand side. Both diagrams clearly show that an increasing β improves the physically expected behavior by reinforcing the drop of the forces up to a specific point. All values over $\beta = 2.0$ cause a quite similar global response with respect to their dropping behavior that seems to converge from $\beta = 2.2$ (see right diagram). However, higher values of β also delay the occurring drop in relation to the applied displacements and therefore require a higher maximum loading (see left diagram).

The influence of the homogenization parameter β is also investigated by the damage distribution as shown in Figure 5.11. The parameters $\beta = \{1.0, 1.2, 1.6, 1.8, 2.0, 2.4\}$ are considered here. Obviously, small values of β are not suitable since the damage is remarkably distributed

and far too diffusive in order to characterize cracks. On the other end of the range, the results for $\beta = 2.0$ and $\beta = 2.4$ are quite similar again.

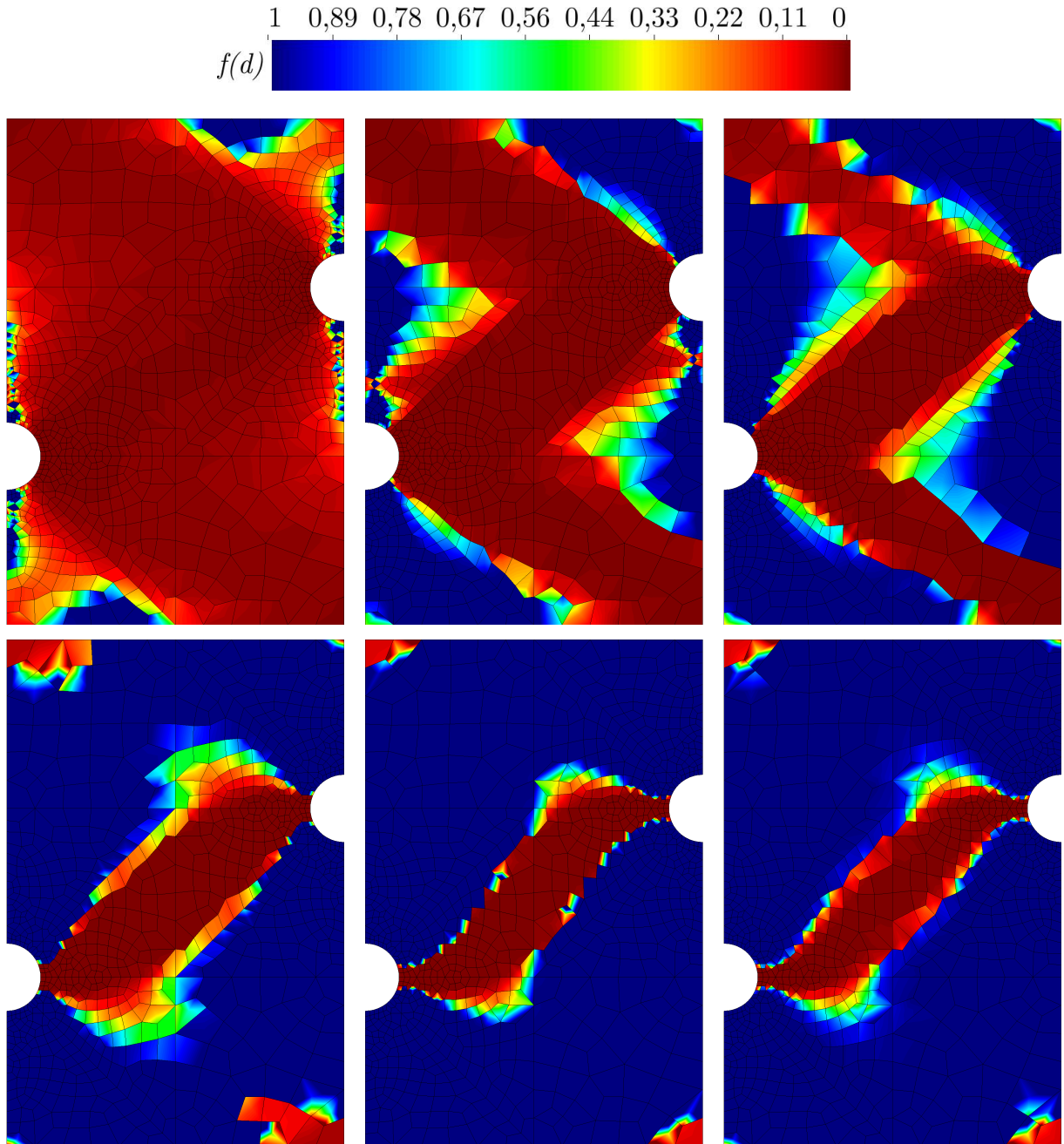


Figure 5.11: Model I [REL]: Distribution of $f(d)$ for the double-notched plate with 986 unstructured elements for $\beta = \{1.0, 1.2, 1.6, 1.8, 2.0, 2.4\}$ (top left to bottom right) at the last loading step for the diffusive case with $r_2 = 1.00 \times 10^8$ MPa s (left/right) and $\dot{u} = 15.00 \times 10^{-6}$ mm/s.

Summarizing, it was established by the force-displacement curves, especially by the double-normalized ones, that the dropping behavior converges for higher values of β . However, the drop of forces is delayed to increased displacements. With respect to the other damage models in this thesis and to comply with similar force-displacement conditions, the homogenization parameter is set to $\beta = 2.0$. The contour plots for the damage distribution support this choice by almost identical results compared to even higher values of β .

5.2.3 Investigation of Regularizing Viscosity

After defining the loading rate and the homogenization parameter, the regularization parameter by means of the viscosity is investigated. Hereby, it is focused on the impacts on the damage distribution and general model behavior and not on the actual regularization in regard to mesh-independent results, this is dedicated to Chapter 6 dealing with the model comparisons.

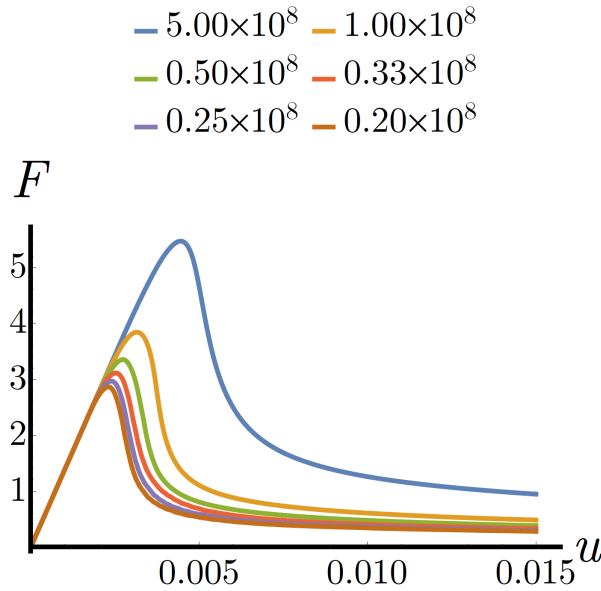


Figure 5.12: Model I [REL]: Study on viscosity parameter $r_2 = [\text{MPa s}]$ by the double-notched plate with 986 unstructured elements with $\beta = 2.0$ and $\dot{u} = 15.00 \times 10^{-6} \text{ mm/s}$.

The general model behavior is now examined by considering the global structural response for the parameters $r_2 = \{5.00, 1.00, 0.50, 0.33, 0.25, 0.20\} \times 10^8 \text{ MPa s}$ in Figure 5.12. At the same time, the parameters $\beta = 2.0$ and $\dot{u} = 15.00 \times 10^{-6} \text{ mm/s}$ stay constant. Obviously, the peaks of the curves in this diagram are increasing with an increasing viscosity parameter r_2 . This is expected since the viscosity parameter is included in the evolution equation as an inverted quantity, namely by $\Delta t/r_2$ with $\Delta t = 1 \text{ s}$, and the increase of viscosity therefore leads to a slower damage evolution resulting in a delayed drop. Besides that, the global response does not provide further information about the model behavior or damage distribution.

In order to achieve more information about the model behavior and damage distribution in relation to the viscosity, the contour plot in Figure 5.13 providing the distribution of $f(d)$ is taken into account. The same increments of the parameter are presented here and it is obvious that the viscosity has a huge impact on the results. Analogously to the force-displacement considerations, an increase of the viscosity parameter slows down the damage evolution. Therefore, more distributed and diffusive damage zones due to the stronger regularization effect are resulting. In contrast, smaller values of r_2 are leading to a higher damage evolution causing a smaller regularization effect that finally provides sharper and more localized zones or cracks.

Consequently, the extension and sharpness of the propagating damage can directly be adjusted by the viscosity. In accordance with the overall concept of the model comparisons, a localized (brittle-like) as well as a diffusive (ductile-like) parameter set is in demand. Therefore, the parameter $r_2 = 0.20 \times 10^8 \text{ MPa s}$, illustrated by the middle contour plot at the bottom of

Figure 5.13, is chosen for the localized case. The parameter $r_2 = 1.00 \times 10^8$ MPa s, illustrated by the middle contour plot at the top, is selected for the diffusive case.

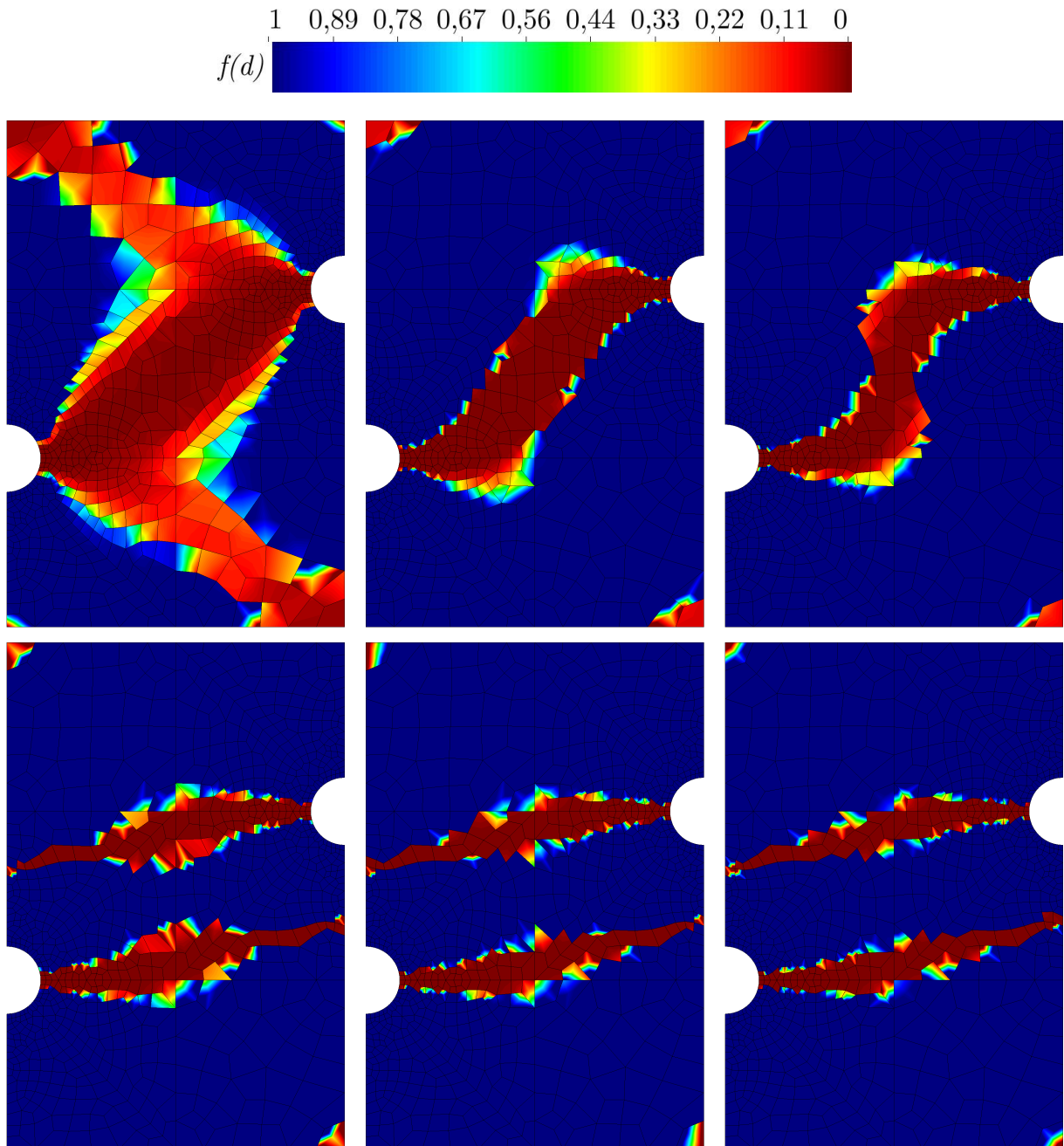


Figure 5.13: Model I [REL]: Distribution of $f(d)$ for the double-notched plate with 986 unstructured elements for $r_2 = \{5.00, 1.00, 0.50, 0.33, 0.25, 0.20\} \times 10^8$ MPa s (top left to bottom right) at the last loading step with $\beta = 2.0$ and $\dot{u} = 15.00 \times 10^{-6}$ mm/s.

5.2.4 Selected Parameter Set

Selected parameters from previous investigations regarding rate-dependence in Subsection 5.2.1, homogenization in Subsection 5.2.2, and viscosity in Subsection 5.2.3 are finally collected. Basically, two approaches are considered here. The rate-dependent approach from Subsection

4.2.3 is used for investigations in this chapter as well as for the regularized calculations for the comparisons in Chapter 6. Additionally, the rate-independent approach from Subsection 4.2.2 is used only for the non-regularized and therefore mesh-dependent calculations in Subsection 6.1. The latter approach is separately considered because the viscous-based regularization can only be deactivated by neglecting these viscous effects by a rate-independent formulation.

The damage and regularization parameters are provided in Table 5.2 in which the localized and diffusive parameter sets as well as the set without regularization is included. Generally, in order to obtain comparable conditions for all damage models in this thesis, the energetic threshold value for damage r_1 was initially set to $r_1 = 1$ MPa. However, due to the strong impact of the homogenization and the viscosity on the peaks of the force-displacement curves, this value had to be adjusted to $r_1 = 200$ MPa in order to achieve reasonable results. Only for the rate-independent case, at which a smaller value for β and naturally no viscosity was present, the initial value for r_1 could be applied. Besides, the numerical parameter α is always constant.

	r_1	α	β	r_2	Δt
no regularization	1 MPa	1×10^{-5} [-]	1.4 [-]	[-]	[-]
localized damage	200 MPa	1×10^{-5} [-]	2.0 [-]	0.20×10^8 MPa s	1 s
diffusive damage	200 MPa	1×10^{-5} [-]	2.0 [-]	1.00×10^8 MPa s	1 s

Table 5.2: Model I [REL]: Damage and regularization parameter for finite element results.

For the rate-independent approach, the parameters r_2 and Δt are not available, of course. Besides that, a relatively small value of β was chosen in order to underline that only little differences from the Reuß case at $\beta = 1.0$ leads to mesh-dependent results already.

5.3 Parameter Identification for Model II

This section provides the parameter identification for Model II [ERVE]. Initially, the rate-dependence is examined in Subsection 5.3.1. Afterwards in Subsection 5.3.2, the number of subdomains is investigated. The regularizing rate-limitation is inspected in Subsection 5.3.3 and conclusively Subsection 5.3.4 presents the final selected parameter set.

5.3.1 Investigation of Rate-Dependence

The rate-dependence of Model II [ERVE] is eliminated as presented in Subsection 4.3.6 and thus no influences by different loading rates \dot{u} , excepting small numerical fluctuations, are expected. To answer this expectation the global structural response in Figure 5.14 is taken into account.

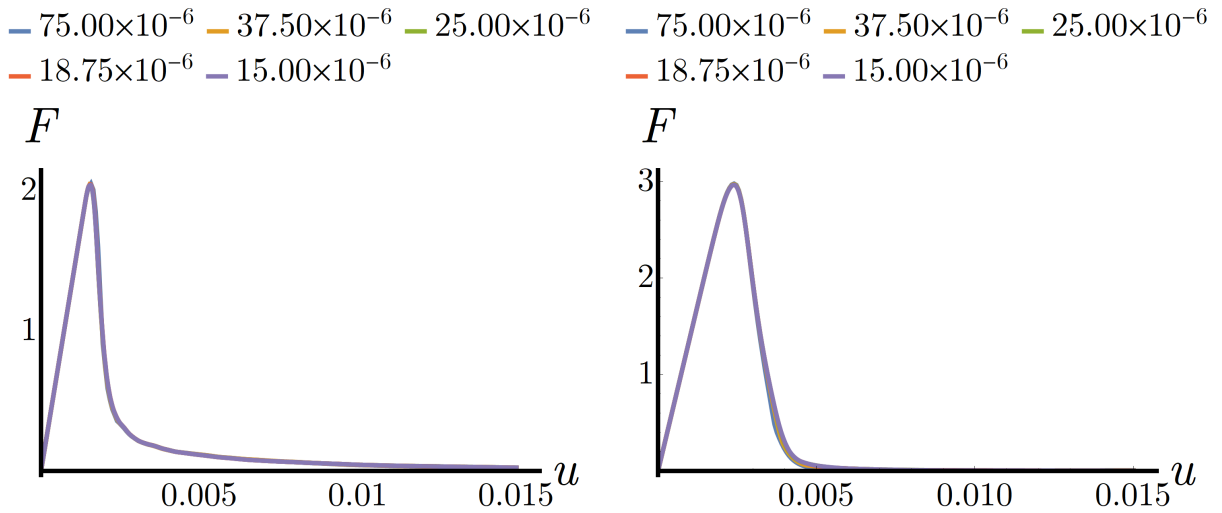


Figure 5.14: Model II [ERVE]: Study on loading rate $\dot{u} = [\text{mm/s}]$ by the double-notched plate with 986 unstructured elements for the localized/diffusive with $\alpha = 5000/500$ $1/(\text{N mm})$ cases (left/right) and $n = 20$.

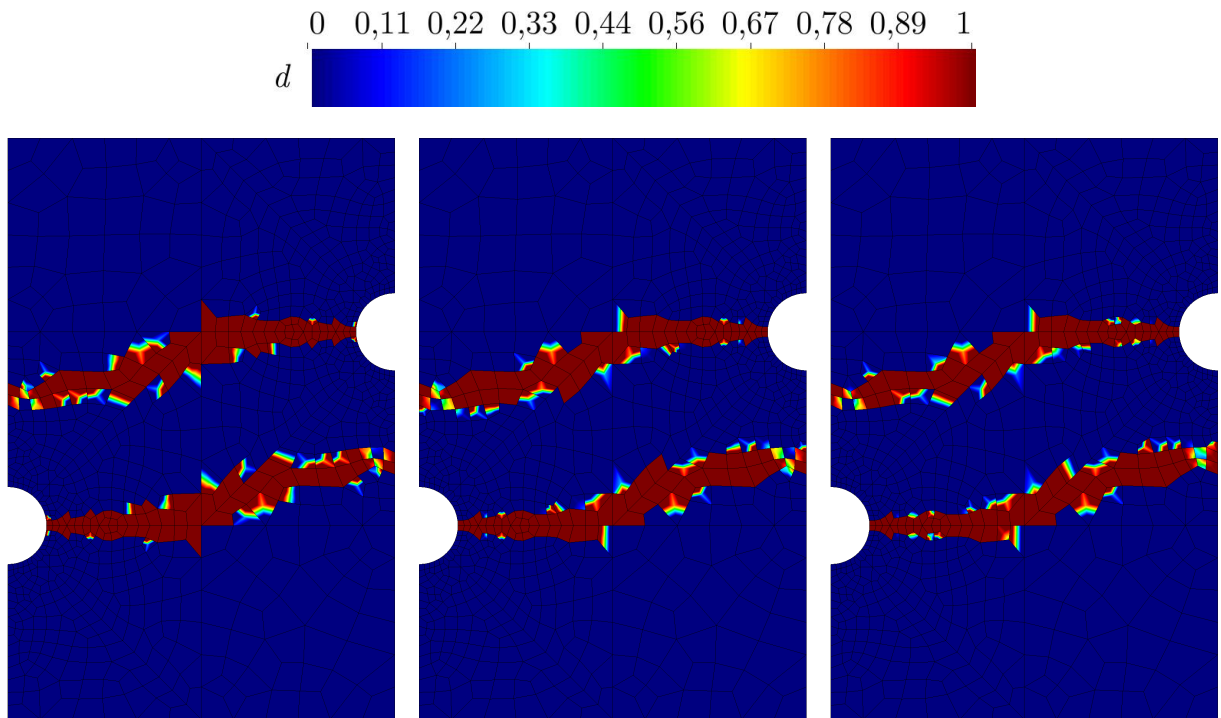


Figure 5.15: Model II [ERVE]: Distribution of $f(d)$ for the double-notched plate with 986 unstructured elements with $\dot{u} = \{75.00, 25.00, 15.00\} \times 10^{-6}$ mm/s (left to right) at the last loading step for the localized case with $\alpha = 5000$ $1/(\text{N mm})$ and $n = 20$.

While other parameters are set to $\alpha = 5000/500$ $1/(\text{N mm})$ and $n = 20$, the loading rates $\dot{u} = \{75.00, 37.50, 25.00, 18.75, 15.00\} \times 10^{-6}$ mm/s are considered. Obviously, all rates yield the same force-displacement curves and even small fluctuations can hardly be seen. Interestingly, the curves in the localized case on the left-hand side have an even better agreement than the curves for the diffusive case on the right-hand side. Obviously, the rate-independence is more stable for a slight regularization corresponding to the localized behavior.

The contour plots for the loading rates $\dot{u} = \{75.00, 25.00, 15.00\} \times 10^{-6}$ mm/s are given by Figure 5.15 for the localized (brittle-like) and Figure 5.16 for the diffusive (ductile-like) case. The results underline the previous observed behavior of rate-independence by quasi-identical damage distributions for the respective cases.

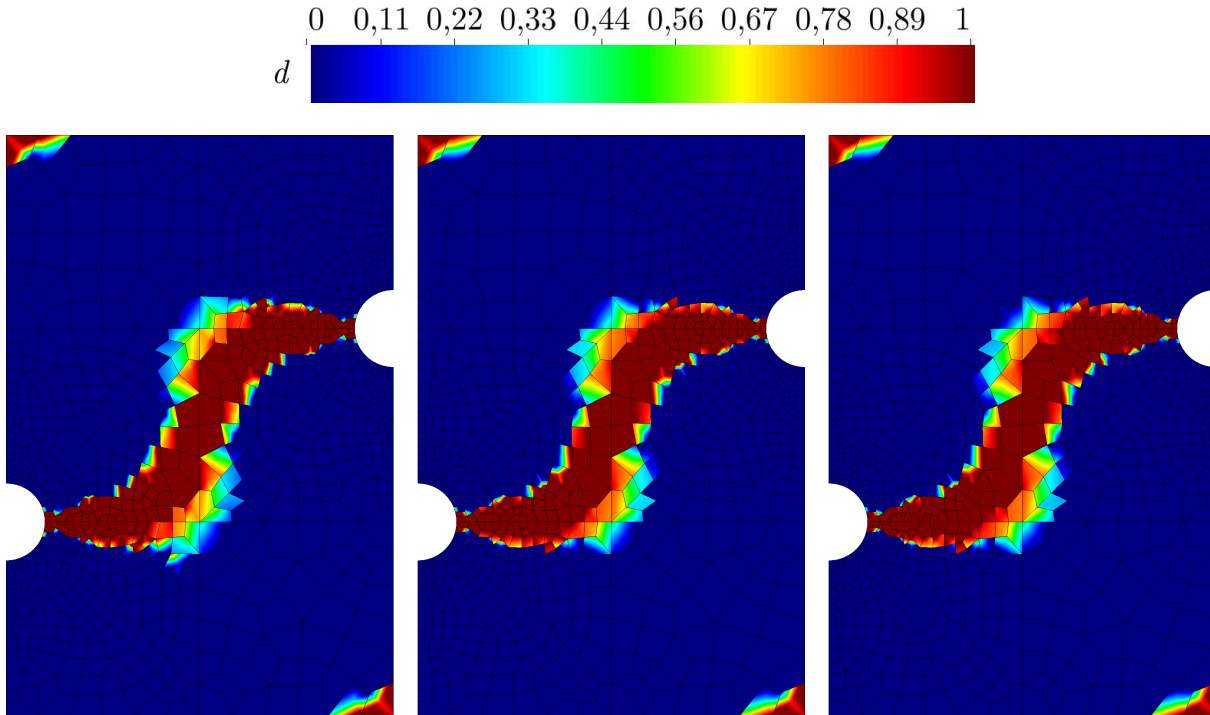


Figure 5.16: Model II [ERVE]: Distribution of $f(d)$ for the double-notched plate with 986 unstructured elements with $\dot{u} = \{75.00, 25.00, 15.00\} \times 10^{-6}$ mm/s (left to right) at the last loading step for the diffusive case with $\alpha = 500$ 1/(N mm) and $n = 20$.

For the mentioned reasons, an arbitrary choice for the loading rate can be made. However, in accordance with the other damage models presented in this thesis, a common loading rate of $\dot{u} = 15.00 \times 10^{-6}$ mm/s is selected.

5.3.2 Investigation of Regularizing Subdomains

It can be assumed that the subdomains do not directly affect the characteristics of the damage or regularization, but for numerical reasons a minimum number of subdomains n has to be ensured. This allows for the microstructural description in regard to the emulated representative volume element (ERVE). The minimum number of subdomains is determined in the following. In order to keep this investigation simple, this is done by means of the diffusive case only. Other parameters are fixed to $\alpha = 500$ 1/(N mm) and $\dot{u} = 15.00 \times 10^{-6}$ mm/s.

Initially, Figure 5.17 provides different numbers of subdomains with $n = \{1, 5, 10, 15, 20, 25\}$ for two different meshes: 986 elements are considered on the left-hand side as opposed to 5064 elements on the right-hand side. Both indicate that only five subdomains are enough to achieve convergence. In order to circumvent any potential exceptions, the number is set to $n = 20$.

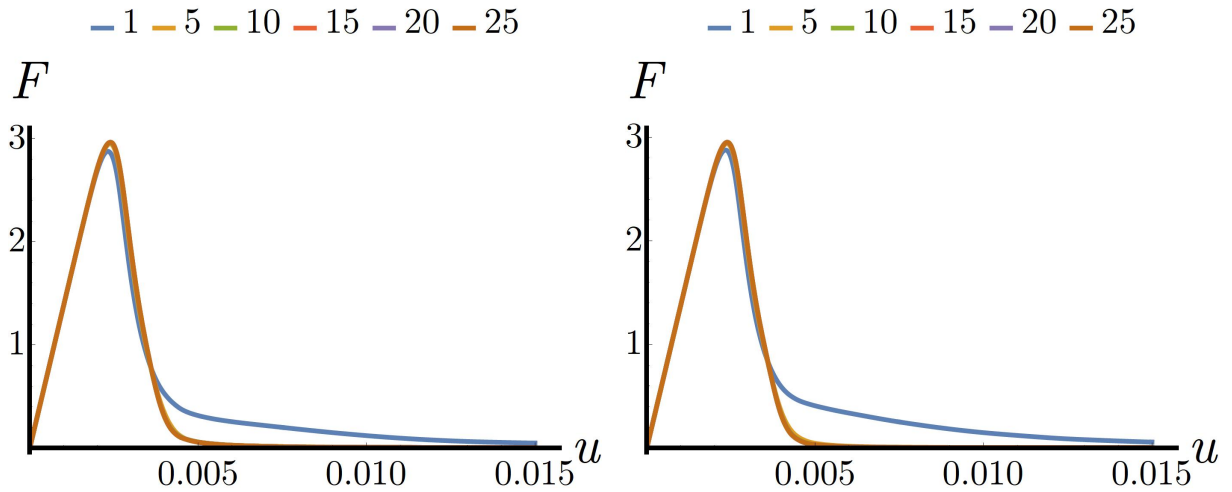


Figure 5.17: Model II [ERVE]: Study on subdomains n by the double-notched plate with 986 (left) and 5064 (right) unstructured elements for the diffusive case with $\alpha = 500$ $1/(\text{N mm})$ and $\dot{u} = 15.00 \times 10^{-6}$ mm/s.

Regarding this selection, Figure 5.18 confirms mesh-independence in contrast to only one subdomain. The latter case prevents the concept of the ERVE and thus regularization can not work properly. The comparison of the coarse and medium mesh with 986 and 5064 elements is sufficient since this is more problematic than a further comparison to a finer mesh.

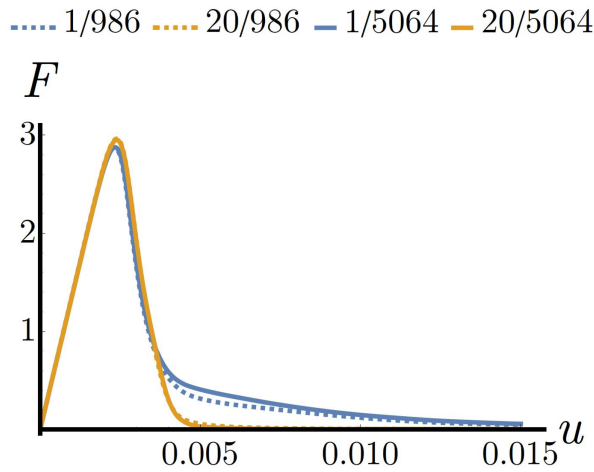


Figure 5.18: Model II [ERVE]: Comparing the number of subdomains $n = 1$ (blue lines) and $n = 20$ (dark yellow lines) by the double-notched plate with 986 (dashed lines) and 5064 (solid lines) unstructured elements for the diffusive case with $\alpha = 500$ $1/(\text{N mm})$ and $\dot{u} = 15.00 \times 10^{-6}$ mm/s.

Moreover, the distribution of the damage is also investigated. Hereto, the contour plots in Figure 5.19 considering the mesh with 986 elements and Figure 5.20 for 5064 elements are taken into account. Three different numbers of subdomains with $n = \{1, 10, 20\}$ are included. Thereby, the same observations can be made since only the case of a single subdomain leads to different and unexpected results. For $n = 10$ and $n = 20$ the distributions of $f(d)$ are apparently equal in case of both numbers of applied elements.

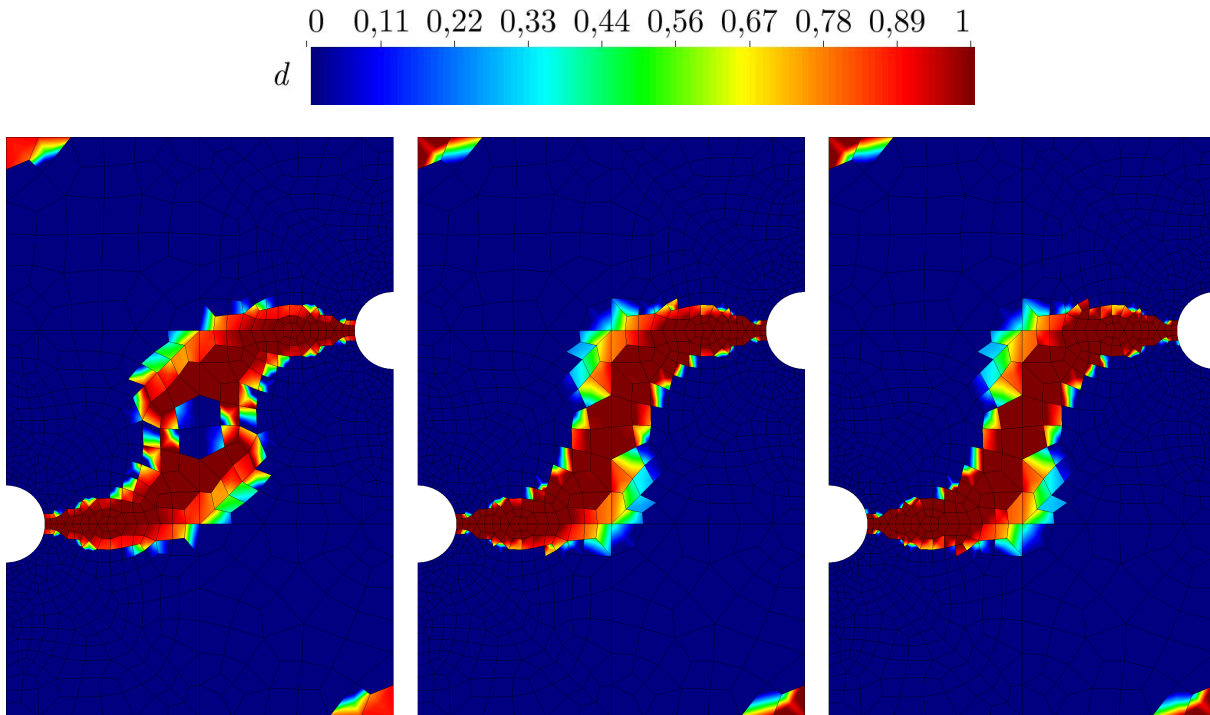


Figure 5.19: Model II [ERVE]: Distribution of $f(d)$ for the double-notched plate with 986 elements with $n = \{1, 10, 20\}$ (left to right) at the last loading step for the diffusive case with $\alpha = 500$ 1/(N mm) and $\dot{u} = 15.00 \times 10^{-6}$ mm/s.

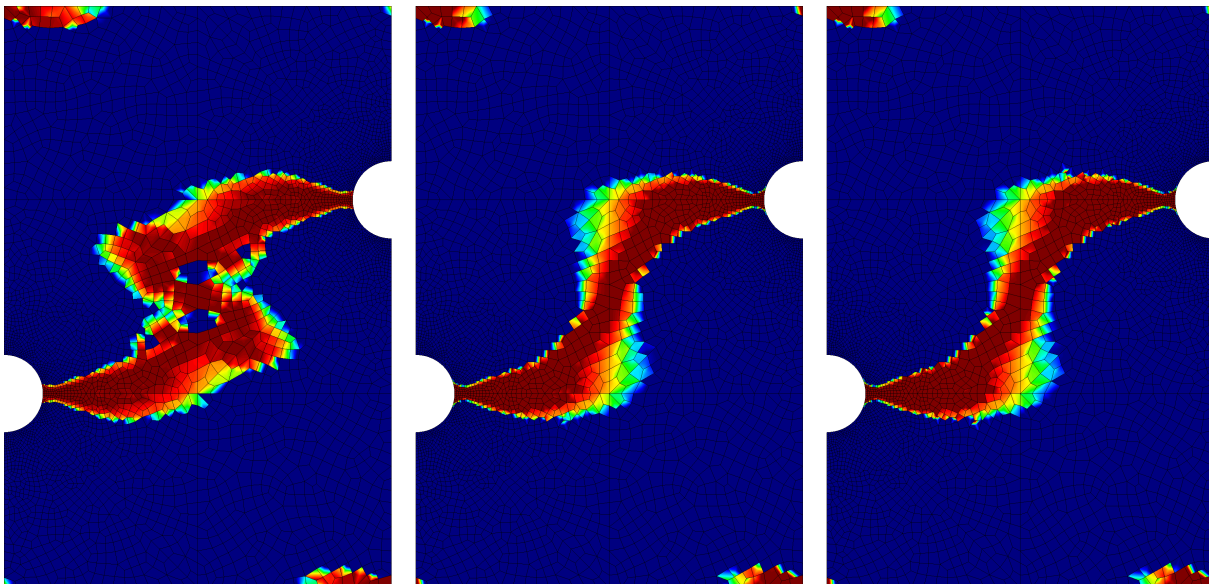


Figure 5.20: Model II [ERVE]: Distribution of $f(d)$ for the double-notched plate with 5064 elements with $n = \{1, 10, 20\}$ (left to right) at the last loading step for the diffusive case with $\alpha = 500$ 1/(N mm) and $\dot{u} = 15.00 \times 10^{-6}$ mm/s.

Concluding, the number of subdomains is obviously sufficient starting with $n = 5$. As a precaution, the subdomains are set to $n = 20$. Incidentally, this number of subdomains is also used for the numerical results on material point level in Subsection 4.3.9, in which interestingly almost all subdomains are affected by damage evolution during the calculation.

5.3.3 Investigation of Regularizing Rate-Limitation

The rate-limiting parameter α mainly influences the regularization in this damage model. Analogously to the previous model, the present investigation is not related to the mesh-independence of the calculations, this is dedicated to Chapter 6. At this point, the impacts of the rate-limitation on the damage distribution and general behavior of this damage model is examined. The parameters $n = 20$ and $\dot{u} = 15.00 \times 10^{-6}$ mm/s are fixed in this context.

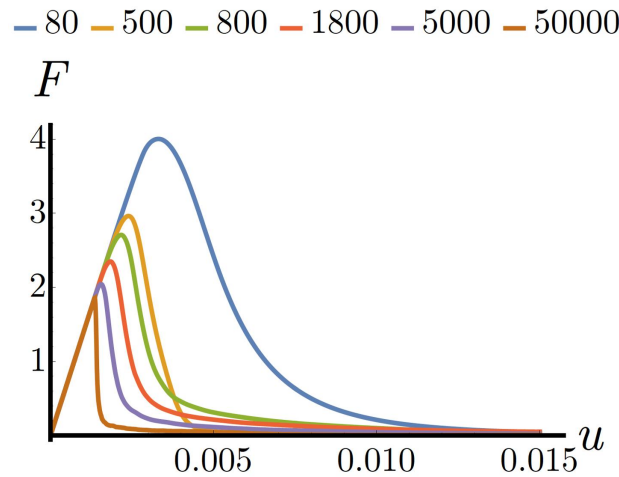


Figure 5.21: Model II [ERVE]: Study on rate-limiting factor $\alpha = [1/(N \text{ mm})]$ by the double-notched plate with 986 unstructured elements with $n = 20$ and $\dot{u} = 15.00 \times 10^{-6}$ mm/s.

The parameter α strongly influences the force-displacement curves in Figure 5.21 including the values $\alpha = \{80, 500, 800, 1800, 5000, 50000\} 1/(N \text{ mm})$. The arising global responses are delayed to higher peaks which results from the decreasing α . This leads to a stronger rate-limitation and regularization and can be matched to viscous regularization in general.

In order to obtain information about the damage distribution, the contour plot in Figure 5.22 is considered including the same range of values for the parameter α as before. Also these results, illustrating $f(d)$, show a strong influence of the rate-limitation as already detected for the global responses. Again, a decrease of the parameter α leads to a stronger rate-limitation accompanied by a stronger regularization that arises here by a strongly diffusive distribution of the damage zone. In contrast, a decreasing of α enlarges the damage evolution leading to a weaker regularization that results in more localized damage zones appearing like thin cracks.

Altogether, the crack behavior or rather the thickness of the propagating damage zone can be adjusted by the rate-limiting parameter α . Analogously to the previous model, two parameter sets are chosen in order to obtain a localized (brittle-like) as well as a diffusive (ductile-like) behavior for the comparisons to the other damage models. Hereto, the first case is enabled by $\alpha = 5000 1/(N \text{ mm})$, represented by the middle contour plot at the bottom of Figure 5.22, and the second one by $\alpha = 500 1/(N \text{ mm})$, represented by the middle contour plot at the top.

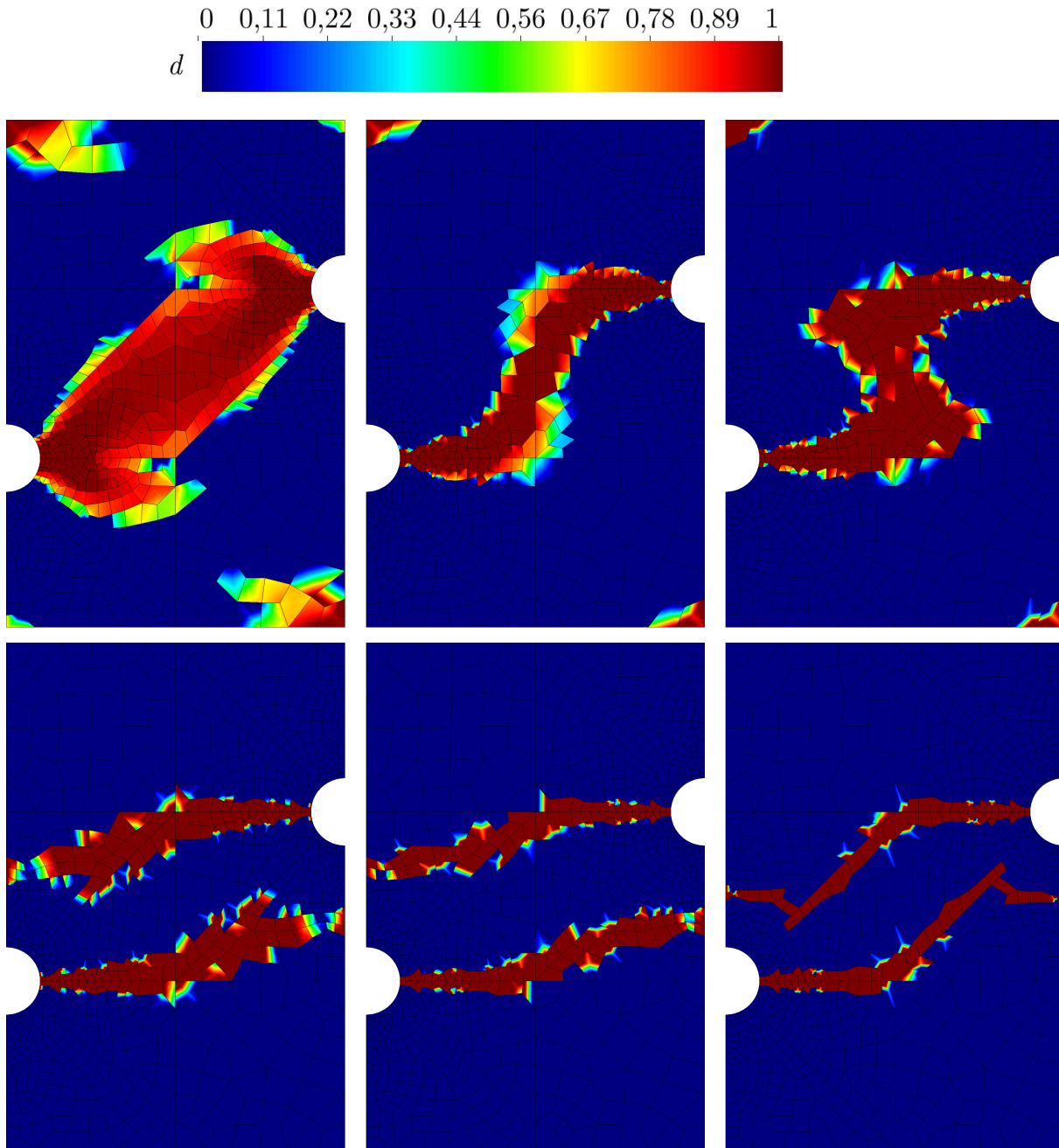


Figure 5.22: Model II [ERVE]: Distribution of $f(d)$ for the double-notched plate with 986 unstructured elements for $\alpha = \{80, 500, 800, 1800, 5000, 50000\} 1/(N \text{ mm})$ (top left to bottom right) at the last loading step with $n = 20$ and $\dot{u} = 15.00 \times 10^{-6} \text{ mm/s}$.

5.3.4 Selected Parameter Set

At this point, the selected parameters for Model II [ERVE] from the previous examinations in regard to rate-dependence in Subsection 5.3.1, regularizing subdomains in Subsection 5.3.2 and to the rate-limitation in Subsection 5.3.3 are conclusively collected. The damage and regularization parameters presented in Table 5.3 consider different cases: the first parameter set is related to calculations without any regularization, the second one for the localized and the third one for the diffusive case. The energetic threshold value r_1 is identically chosen for all cases and set to $r_1 = 1 \text{ MPa}$ in order to ensure equal conditions for all damage models (excepting

Model I [REL] in which another value had to be selected).

	r_1	n	α	Δt
no regularization	1 MPa	1 [-]	5000000 1/(N mm)	1 s
localized damage	1 MPa	20 [-]	5000 1/(N mm)	1 s
diffusive damage	1 MPa	20 [-]	500 1/(N mm)	1 s

Table 5.3: Model II [ERVE]: Damage and regularizing parameter for finite element results.

The case without regularization is restricted to one subdomain and has an quasi-unlimited damage rate with $\alpha = 5000000$ 1/(N mm), for which it has separately been proofed that no regularization effects are remaining. It should be mentioned that the increase of the damage has always been limited to $d_{\max} = 0.999$. In the present case, the applied damage function $f(d) = (1 - d)^2$ yields a lower limit of $f(d_{\max}) = 1 \times 10^{-6}$ for maximally destroyed material.

5.4 Parameter Identification for Model III

The parameter identification for Model III [LAP] is presented in this section. First, Subsection 5.4.1 investigates the rate-dependence. Subsequently, the regularizing gradient is examined in Subsection 5.4.2 and lastly the final selected parameter set is presented in Subsection 5.4.3.

5.4.1 Investigation of Rate-Dependence

Due to the rate-independent formulation of Model III [LAP] different loading rates \dot{u} should not have an impact on the results. However, the applied operator splits in the derivation cause rate-dependent effects. In order to overcome these influences the loading rate has to be decreased until a converged behavior can be observed.

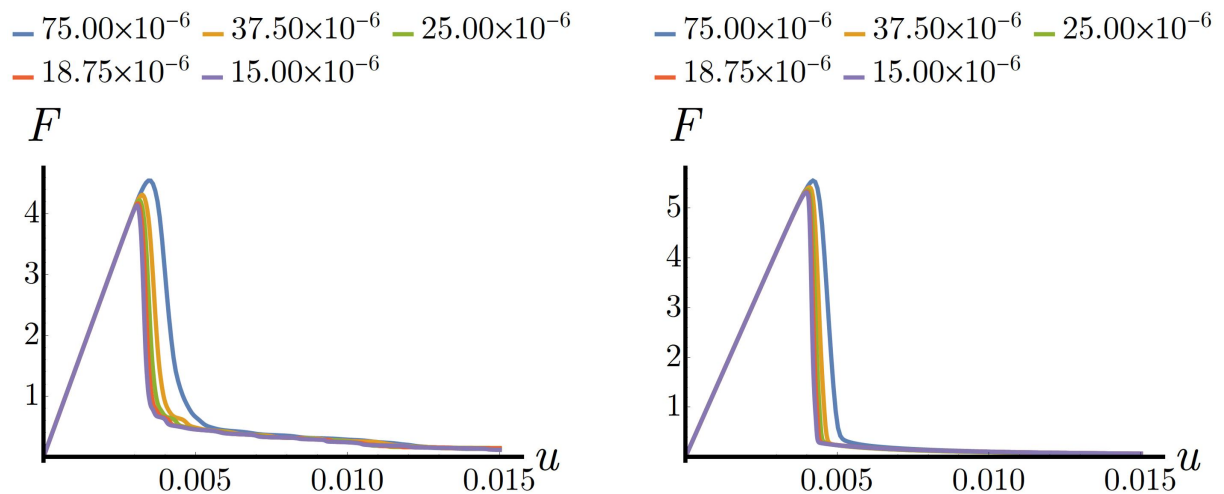


Figure 5.23: Model III [LAP]: Study on loading rate $\dot{u} = [\text{mm/s}]$ by the double-notched plate with 986 unstructured elements for localized/diffusive cases with $\beta = 0.002/0.015$ MPa mm² (left/right).

This is investigated by the force-displacement curves in Figure 5.23 by the loading rates $\dot{u} = \{75.00, 37.50, 25.00, 18.75, 15.00\} \times 10^{-6}$ mm/s for the localized and diffusive cases with $\beta = 0.002/0.015$ MPa mm². These curves are converging as assumed. Loading rates smaller than $\dot{u} = 25.00 \times 10^{-6}$ mm/s are considered to be close enough to the final converged result.

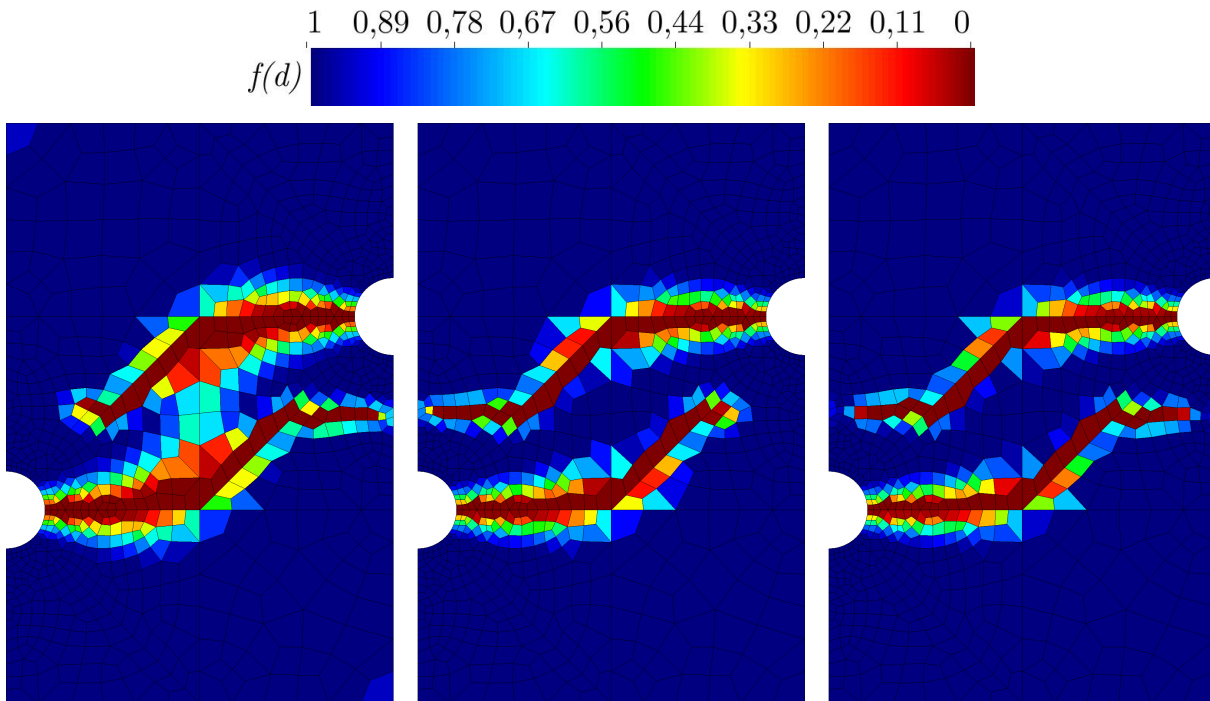


Figure 5.24: Model III [LAP]: Distribution of $f(d)$ for the double-notched plate with 986 unstructured elements with $\dot{u} = \{75.00, 25.00, 15.00\} \times 10^{-6}$ mm/s (left to right) at the last loading step for the localized case with $\beta = 0.002$ MPa mm².

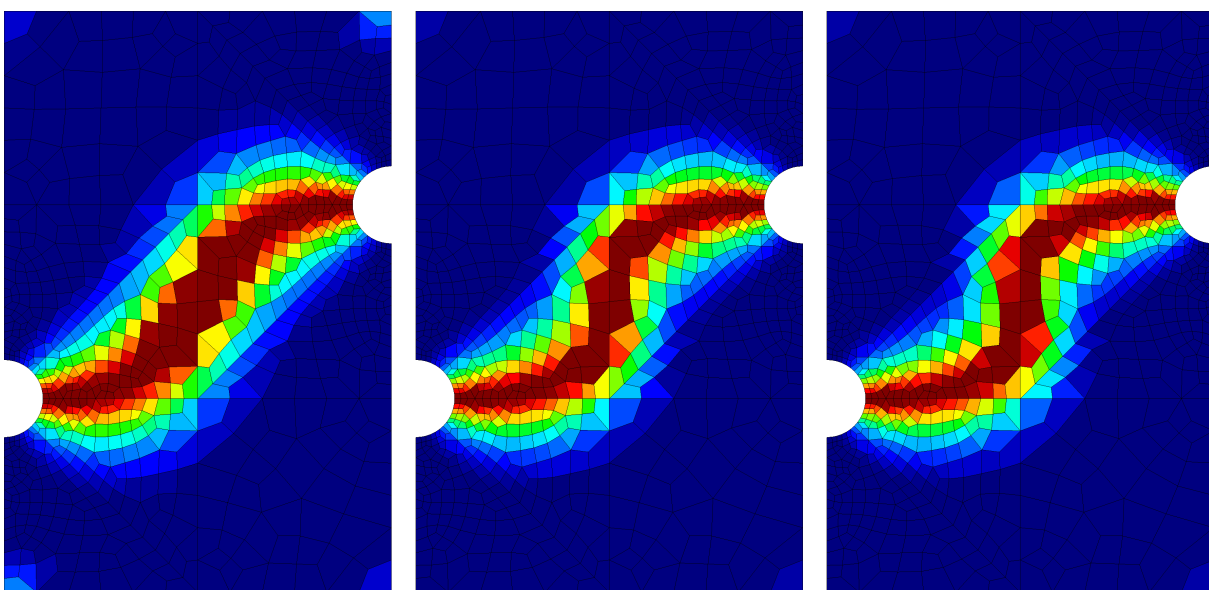


Figure 5.25: Model III [LAP]: Distribution of $f(d)$ for the double-notched plate with 986 unstructured elements with $\dot{u} = \{75.00, 25.00, 15.00\} \times 10^{-6}$ mm/s (left to right) at the last loading step for the diffusive case with $\beta = 0.015$ MPa mm².

The related contour plots are provided by Figure 5.24 for the localized case with $\beta = 0.002$ MPa mm² and by Figure 5.25 for the diffusive case with $\beta = 0.015$ MPa mm². Here, the loading rates are limited to $\dot{u} = \{75.00, 25.00, 15.00\} \times 10^{-6}$ mm/s. Both figures underline the previously described convergence for values smaller than $\dot{u} = 25.00 \times 10^{-6}$ mm/s with almost identical damage distributions for the respective two contour plots on the right-hand side of each case. In line with the other damage models in this thesis, the loading rate is prescribed by $\dot{u} = 15.00 \times 10^{-6}$ mm/s.

5.4.2 Investigation of Regularization Parameter

Besides the investigation of the loading rate, the only investigated further parameter is the regularization parameter β . As before, the mesh-independence is not subject of investigation here, this is part of the model comparison in Chapter 6. At this point, the impact of the gradient parameter on the damage distribution and general model behavior is examined for an prescribed loading rate of $\dot{u} = 15.00 \times 10^{-6}$ mm/s.

Hereto, it is started with the global structural response in Figure 5.26 including the parameters $\beta = \{0.000, 0.002, 0.010, 0.012, 0.015, 0.100\}$ MPa mm². The gradient parameter strongly influences the behavior of the curves. Obviously, an increasing of β leads to higher peaks and a delayed damage evolution. This is a result of the increasing regularization.

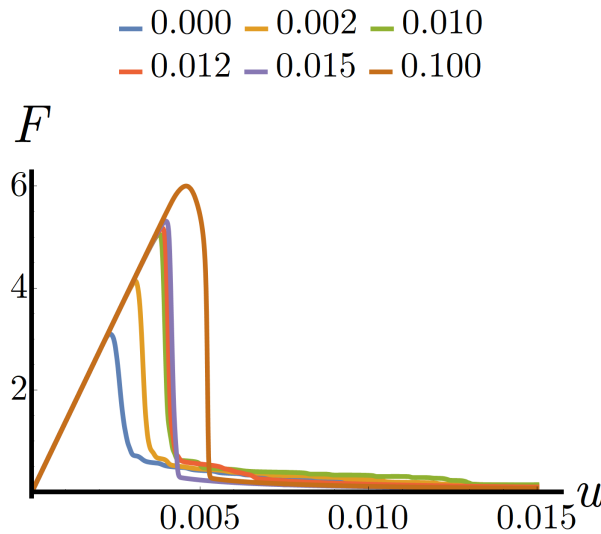


Figure 5.26: Model III [LAP]: Study on gradient parameter $\beta = [\text{MPa mm}^2]$ by the double-notched plate with 986 unstructured elements with $\dot{u} = 15.00 \times 10^{-6}$ mm/s.

The characteristics of the regularization parameter β can be observed by considering the contour plots in Figure 5.27 for the same parameter selection as before. These contour plots show the damage distribution by means of $f(d)$ and underline the previous observations: an increasing parameter β intensifies the regularization providing a more diffusive and distributed damage propagation. In contrast, a decrease results in very sharp and thin damage zones that are characteristic for cracks.

The final choice for the finite element simulations and model comparisons is done considering two sets of regularization again: analogously to the other damage models, a parameter

related to a localized damage distribution (brittle-like behavior) with $\beta = 0.002 \text{ MPa mm}^2$ and a parameter related to a diffusive damage distribution (ductile-like behavior) with $\beta = 0.015 \text{ MPa mm}^2$ are selected. The first case is illustrated by the middle contour plot at the bottom of Figure 5.27, the second case by the middle contour plot at the top.

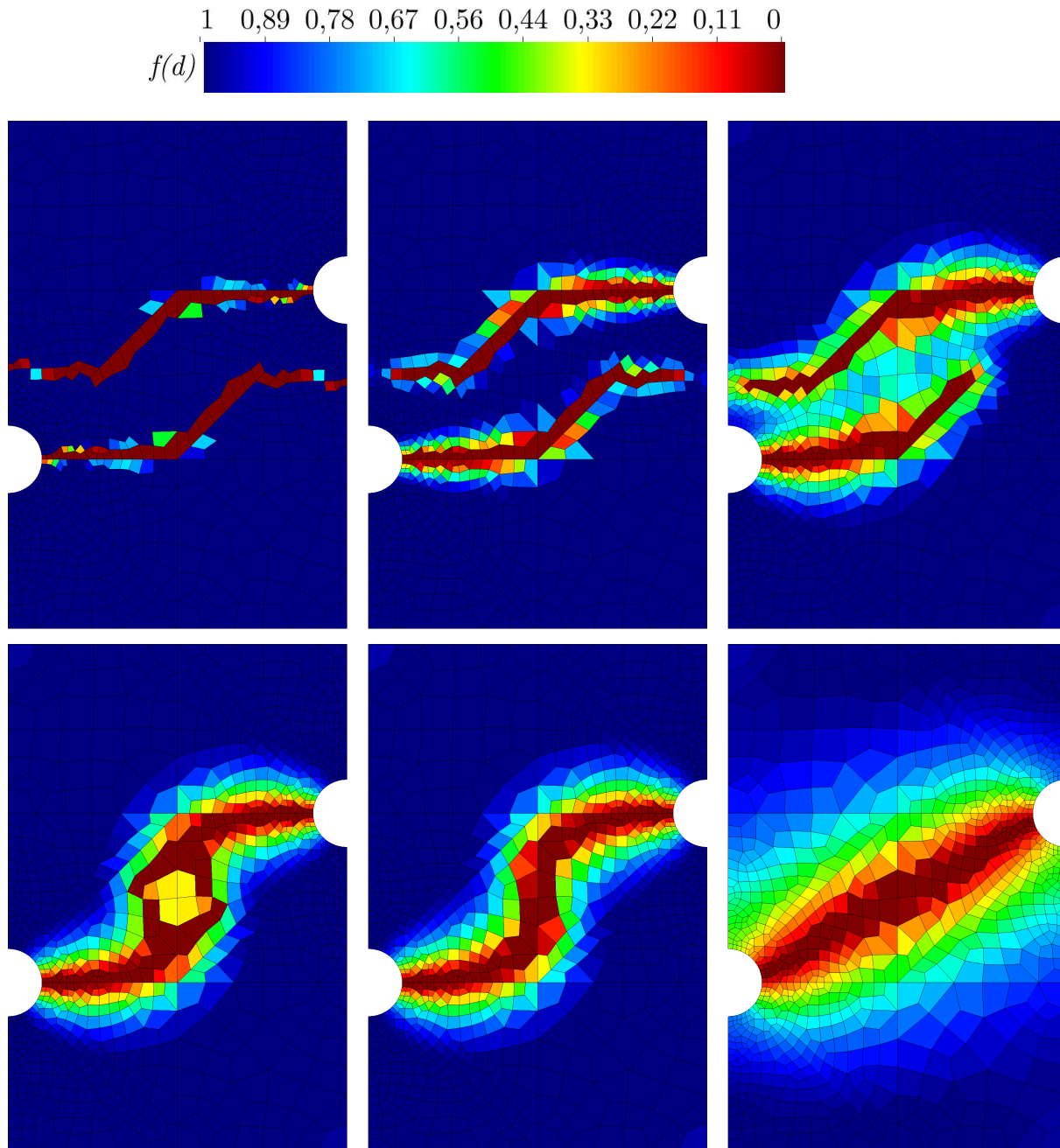


Figure 5.27: Model III [LAP]: Distribution of $f(d)$ for the double-notched plate with 986 unstructured elements with $\beta = \{0.000, 0.002, 0.010, 0.012, 0.015, 0.100\} \text{ MPa mm}^2$ (top left to bottom right) at the last loading step with $\dot{u} = 15.00 \times 10^{-6} \text{ mm/s}$.

5.4.3 Selected Parameter Set

Finally, the selected parameters from the previous investigations of the rate-dependence in Subsection 5.4.1 and the regularizing gradient in Subsection 5.4.2 are collected. The damage and

regularization parameters are provided by Table 5.4. In accordance with the other damage models in this thesis, the damage related energetic threshold value r_1 is chosen to be $r_1 = 1$ MPa for all calculations. On the contrary, the regularizing gradient parameter β is naturally depending on the respective application. A calculation without regularization and the already investigated cases of localized and diffusive damage are distinguished.

	r_1	β
no regularization	1 MPa	0.000 MPa mm ²
localized damage	1 MPa	0.002 MPa mm ²
diffusive damage	1 MPa	0.015 MPa mm ²

Table 5.4: Model III [LAP]: Damage and regularization parameter for finite element results.

6 Model Comparison with Finite Element Results

This chapter compares the three damage models introduced in Chapter 4. The underlying basis are the parameter studies and model validations described in Chapter 5. In the following, three different cases are distinguished: firstly, the initial situation of the damage models without any regularization is presented in Section 6.1. Secondly, the results of the localized damage behavior, which is related to a brittle-like characteristic, are given in Section 6.2. Thirdly, the diffusive damage behavior related to a ductile-like characteristic is considered in Section 6.3. Each case includes the three previously introduced boundary value problems. Three different mesh discretization levels are considered, where structured as well as unstructured meshes are utilized. Furthermore, the solution of each boundary value problem provides the damage distributions for Model I [REL], Model II [ERVE] and Model III [LAP], respectively. The contour plots are always related to the legend of the damage function $f(d)$ in Figure 6.1. Additionally, the overall structural response is discussed in terms of force-displacement diagrams. Subsequently, the computation times of the different models are taken into account in Section 6.4.

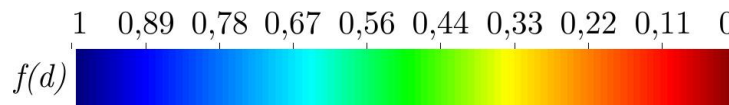


Figure 6.1: Legend representing the damage function $f(d)$ from 1 (undamaged) to 0 (damaged).

6.1 Damage Modeling without Regularization

As alluded in Chapter 3, the characteristic localization leads to numerical instabilities and mesh-dependent results. For illustration purposes and for enabling a direct comparison between non-regularized and regularized results, this section is related to non-regularized results.

The numerical examples in Subsections 6.1.1 to 6.1.9 provide expected results for all considered damage models: the damage is locally distributed and mainly limited to only one or a few element rows. Therefore, the width of the damage zones directly depends on the size of the element. Furthermore, in some cases different or splitting up crack paths are observed that have no physical reason but are only present due to numerical instabilities. The corresponding force-displacement curves in Subsections 6.1.3, 6.1.6, and 6.1.9 additionally underline this dependence on the size of the elements via different global responses. In case of Figures 6.9 and 6.18 the curves seem to be identical resulting from the abrupt and vertical drop. However, the peaks of the curves are different and the related contour plots are different anyway.

Obviously, the presented results are not suitable for the modeling of damage mechanisms. To this end, regularization strategies have to be applied such which are presented in Chapter 3. This has been done for the novel approaches from Chapter 4. The numerical results are presented afterwards in Sections 6.2 and 6.3 for the localized and diffusive characteristics.

6.1.1 Damage Distributions for the Double-Notched Plate (Stru. Mesh)

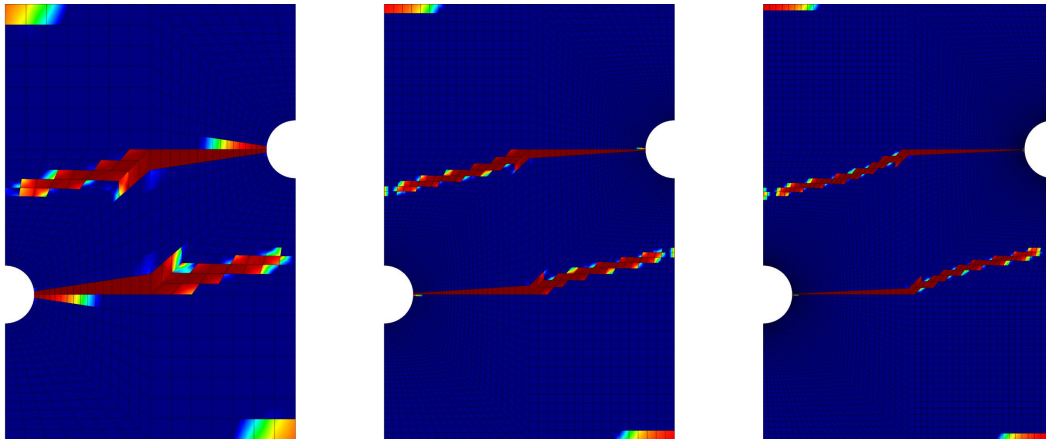


Figure 6.2: Model I [REL]: Distribution of $f(d)$ for the double-notched plate with 994, 4992, and 10074 structured elements (left to right) at the last loading step with $\dot{u} = 75.00 \times 10^{-9}$ mm/s, $r_1 = 1$ MPa and $\beta = 1.4$ (rate-independent).

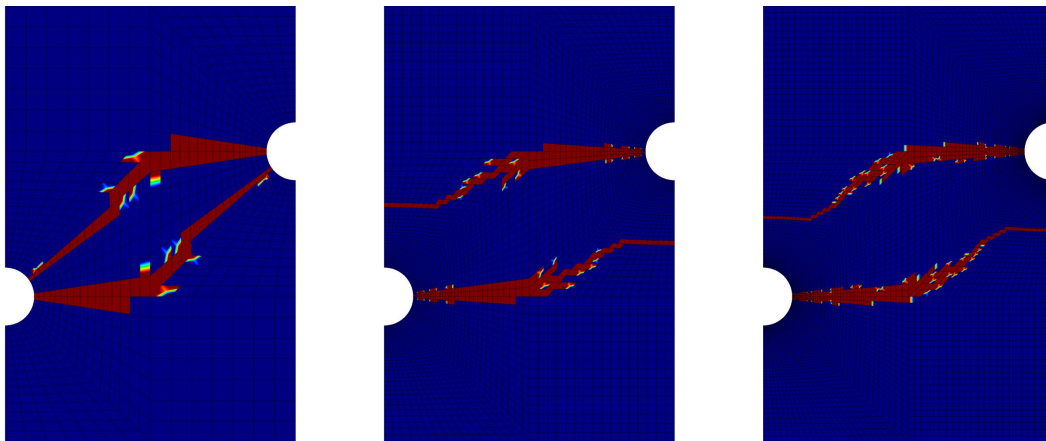


Figure 6.3: Model II [ERVE]: Distribution of $f(d)$ for the double-notched plate with 994, 4992, and 10074 structured elements (left to right) at the last loading step with $\dot{u} = 15.00 \times 10^{-6}$ mm/s, $r_1 = 1$ MPa, $n = 1$ and $\alpha = 5000000$ 1/(N mm).

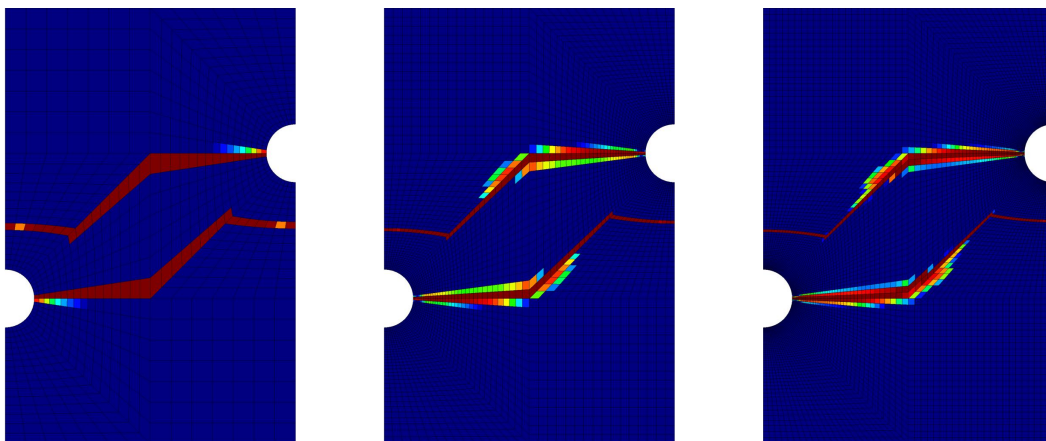


Figure 6.4: Model III [LAP]: Distribution of $f(d)$ for the double-notched plate with 994, 4992, and 10074 structured elements (left to right) at the last loading step with $\dot{u} = 15.00 \times 10^{-6}$ mm/s, $r_1 = 1$ MPa and $\beta = 0.000$ MPa mm².

6.1.2 Damage Distributions for the Double-Notched Plate (Unstru. Mesh)

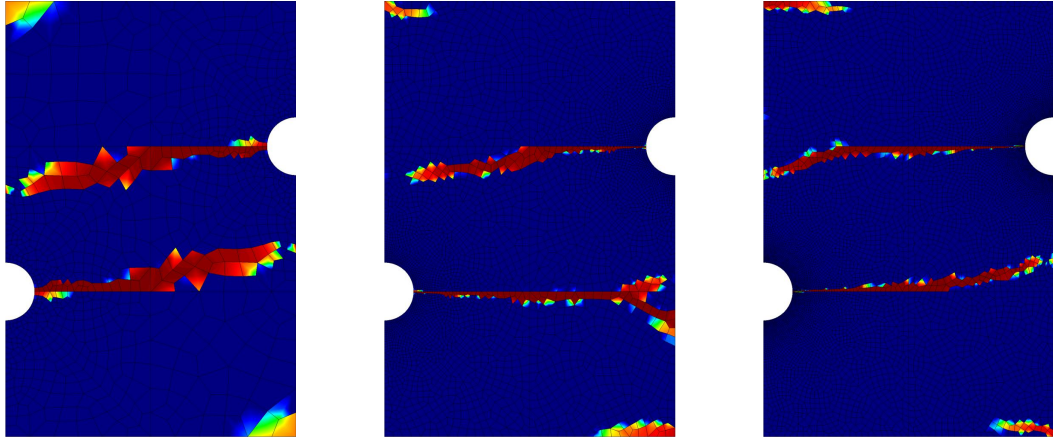


Figure 6.5: Model I [REL]: Distribution of $f(d)$ for the double-notched plate with 986, 5064, and 10161 unstructured elements (left to right) at the last loading step with $\dot{u} = 75.00 \times 10^{-9}$ mm/s, $r_1 = 1$ MPa and $\beta = 1.4$ (rate-independent).

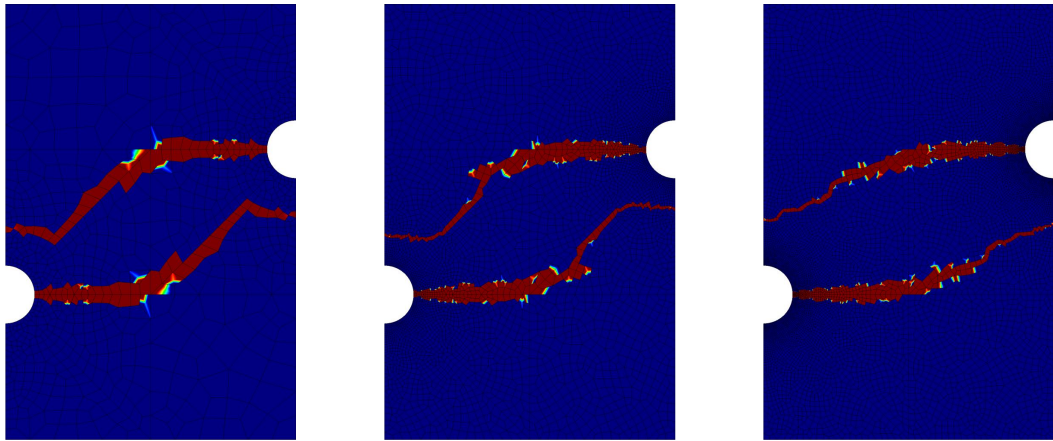


Figure 6.6: Model II [ERVE]: Distribution of $f(d)$ for the double-notched plate with 986, 5064, and 10161 unstructured elements (left to right) at the last loading step with $\dot{u} = 15.00 \times 10^{-6}$ mm/s, $r_1 = 1$ MPa, $n = 1$ and $\alpha = 5000000$ 1/(N mm).

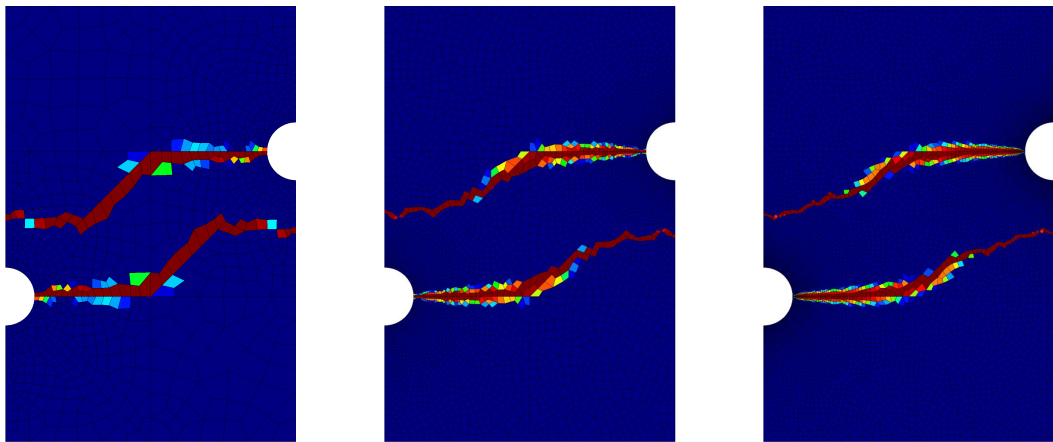


Figure 6.7: Model III [LAP]: Distribution of $f(d)$ for the double-notched plate with 986, 5064, and 10161 unstructured elements (left to right) at the last loading step with $\dot{u} = 15.00 \times 10^{-6}$ mm/s, $r_1 = 1$ MPa and $\beta = 0.000$ MPa mm².

6.1.3 Force-Displacement Diagrams for the Double-Notched Plate

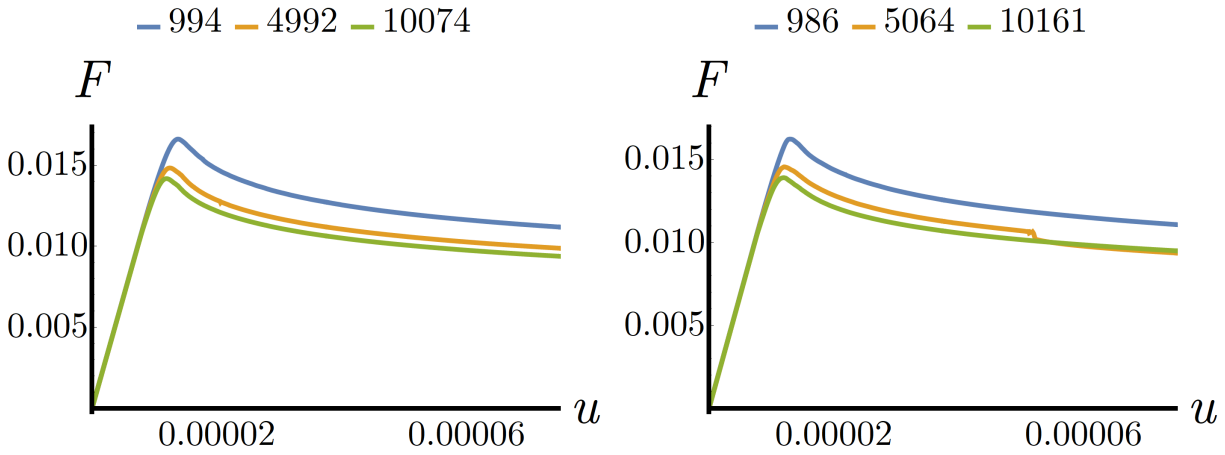


Figure 6.8: Model I [REL]: Structured/unstructured (left/right) elements of stated number.

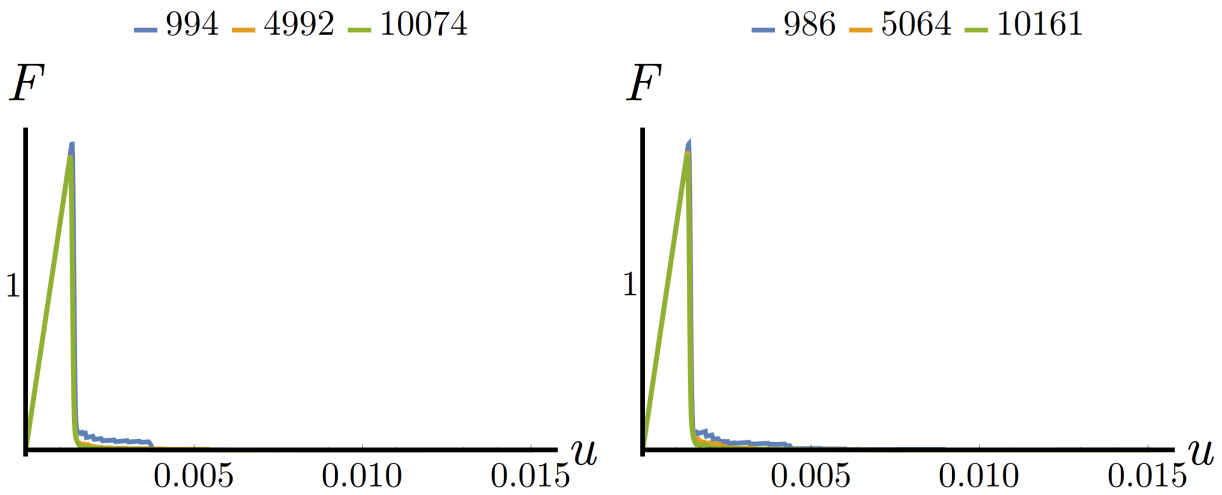


Figure 6.9: Model II [ERVE]: Structured/unstructured (left/right) elements of stated number.

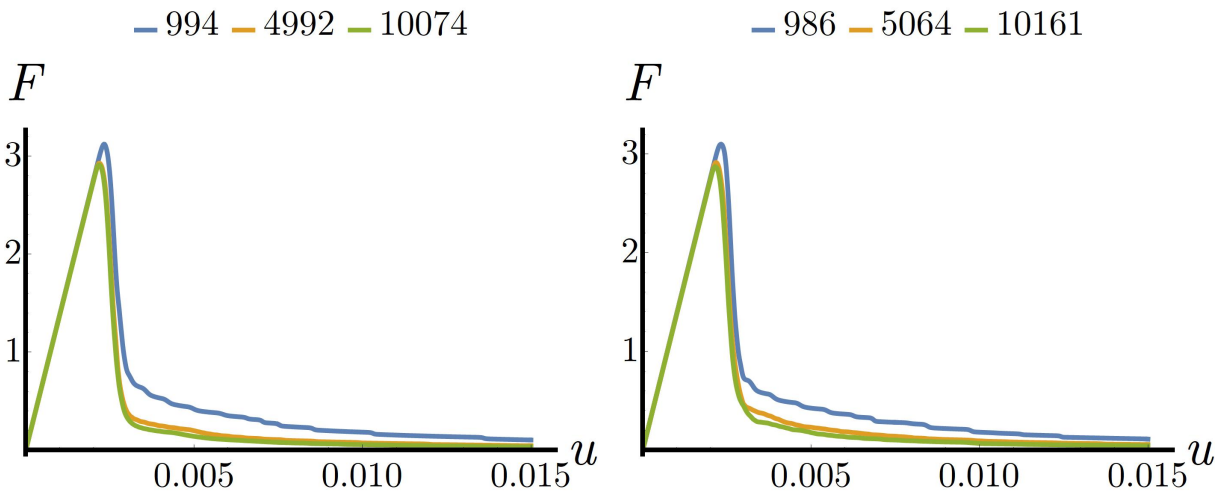


Figure 6.10: Model III [LAP]: Structured/unstructured (left/right) elements of stated number.

6.1.4 Damage Distributions for the Plate with a Centered Hole (Stru. Mesh)

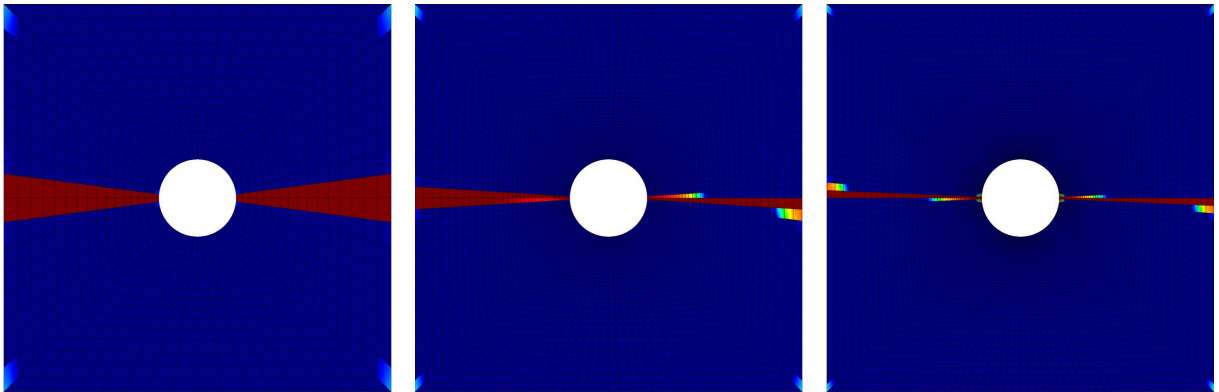


Figure 6.11: Model I [REL]: Distribution of $f(d)$ for the plate with a centered hole with 1024, 5032, and 10000 structured elements (left to right) at the last loading step with $\dot{u} = 50.00 \times 10^{-9}$ mm/s, $r_1 = 1$ MPa and $\beta = 1.4$ (rate-independent).

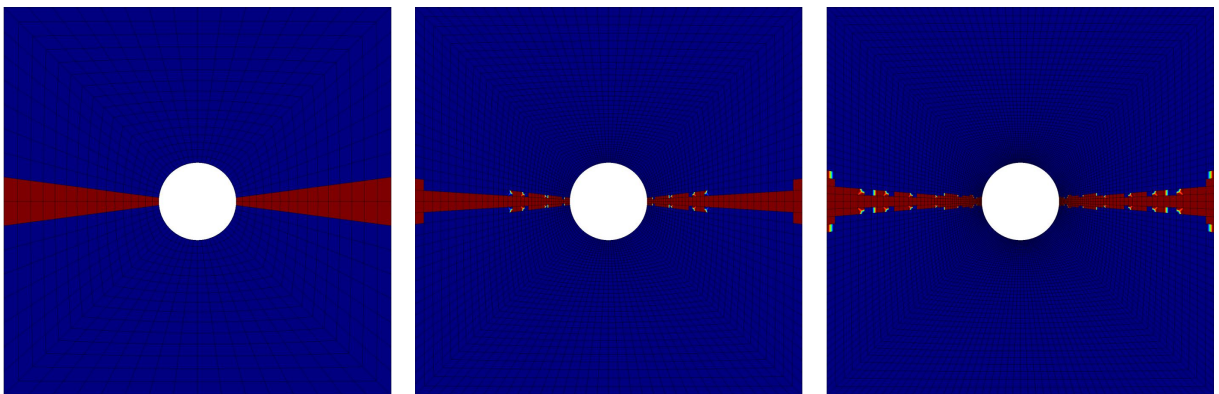


Figure 6.12: Model II [ERVE]: Distribution of $f(d)$ for the plate with a centered hole with 1024, 5032, and 10000 structured elements (left to right) at the last loading step with $\dot{u} = 15.00 \times 10^{-6}$ mm/s, $r_1 = 1$ MPa, $n = 1$ and $\alpha = 5000000$ 1/(N mm).

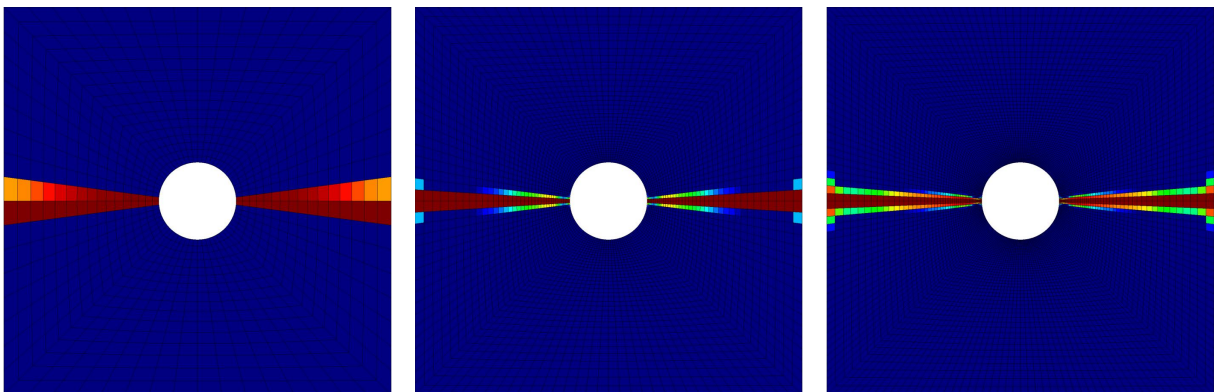


Figure 6.13: Model III [LAP]: Distribution of $f(d)$ for the plate with a centered hole with 1024, 5032, and 10000 structured elements (left to right) at the last loading step with $\dot{u} = 15.00 \times 10^{-6}$ mm/s, $r_1 = 1$ MPa and $\beta = 0.000$ MPa mm².

6.1.5 Damage Distributions for the Plate with a Centered Hole (Unstru. Mesh)

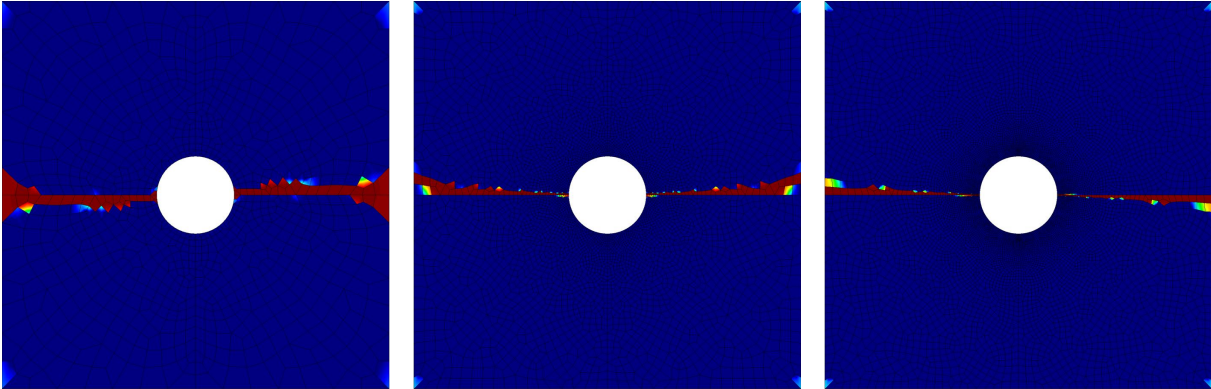


Figure 6.14: Model I [REL]: Distribution of $f(d)$ for the plate with a centered hole with 996, 5090, and 10140 unstructured elements (left to right) at the last loading step with $\dot{u} = 50.00 \times 10^{-9}$ mm/s, $r_1 = 1$ MPa and $\beta = 1.4$ (rate-independent).

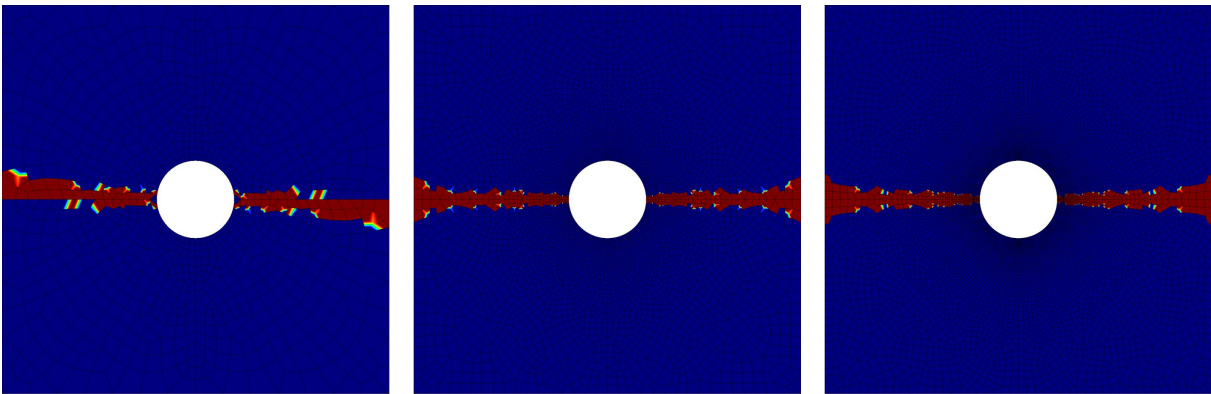


Figure 6.15: Model II [ERVE]: Distribution of $f(d)$ for the plate with a centered hole with 996, 5090, and 10140 unstructured elements (left to right) at the last loading step with $\dot{u} = 15.00 \times 10^{-6}$ mm/s, $r_1 = 1$ MPa, $n = 1$ and $\alpha = 5000000$ 1/(N mm).

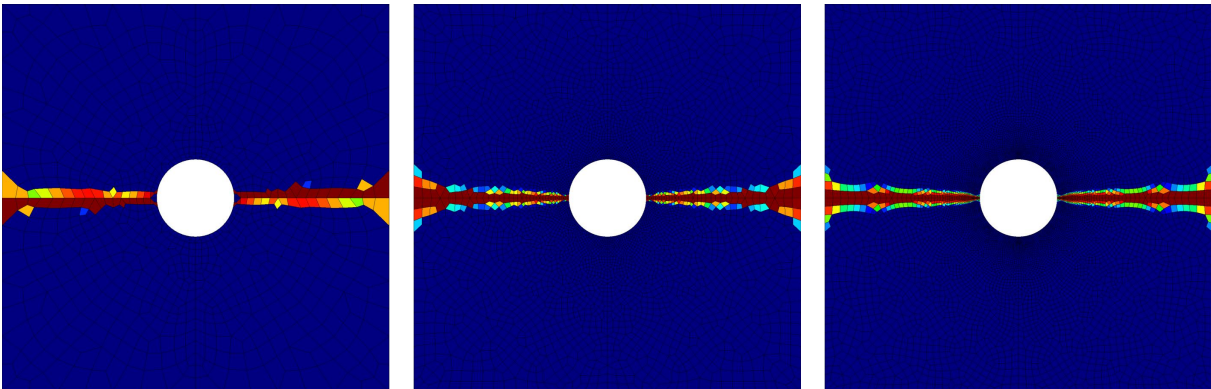


Figure 6.16: Model III [LAP]: Distribution of $f(d)$ for the plate with a centered hole with 996, 5090, and 10140 unstructured elements (left to right) at the last loading step with $\dot{u} = 15.00 \times 10^{-6}$ mm/s, $r_1 = 1$ MPa and $\beta = 0.000$ MPa mm².

6.1.6 Force-Displacement Diagrams for the Plate with a Centered Hole

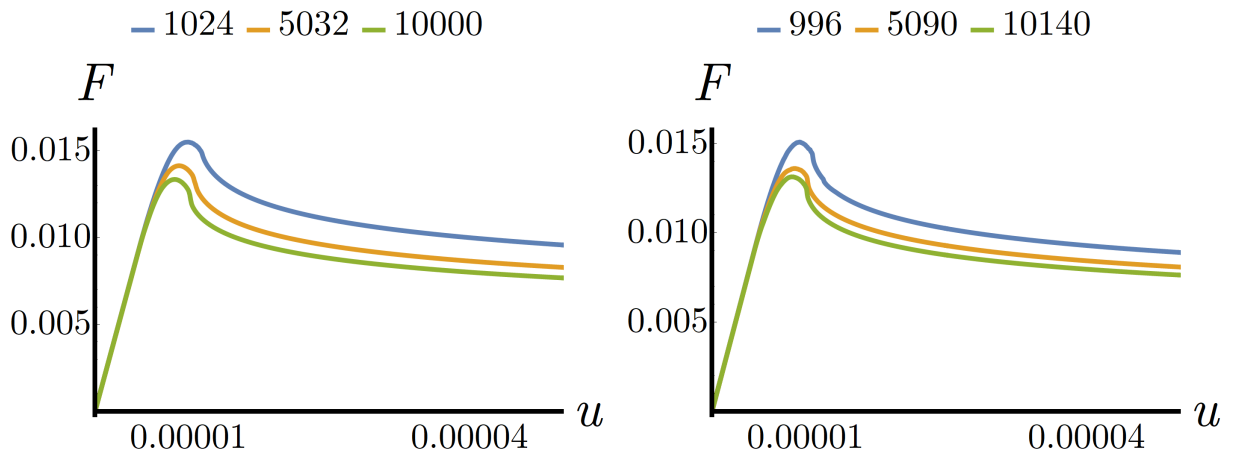


Figure 6.17: Model I [REL]: Structured/unstructured (left/right) elements of stated number.

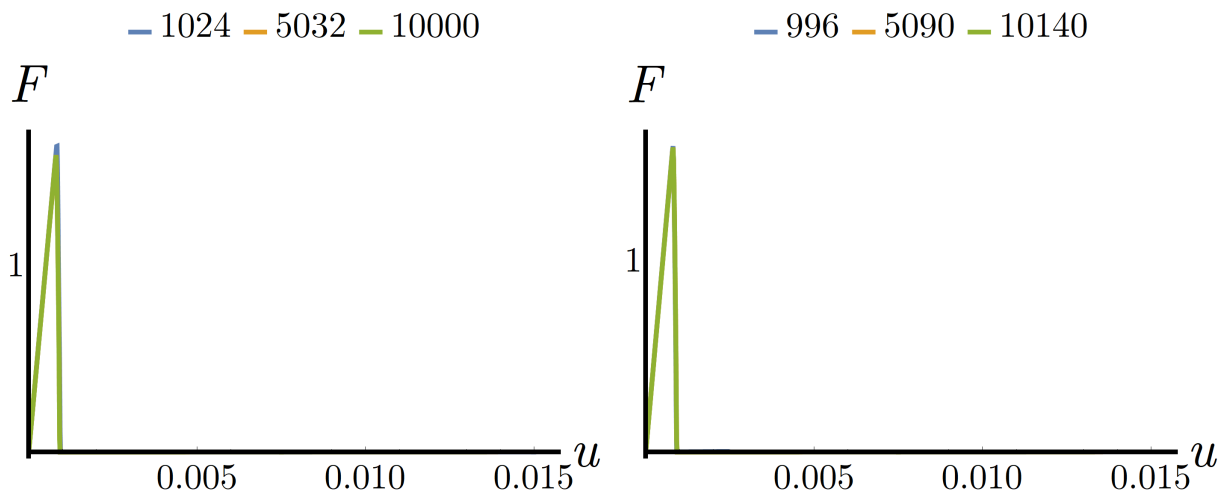


Figure 6.18: Model II [ERVE]: Structured/unstructured (left/right) elements of stated number.

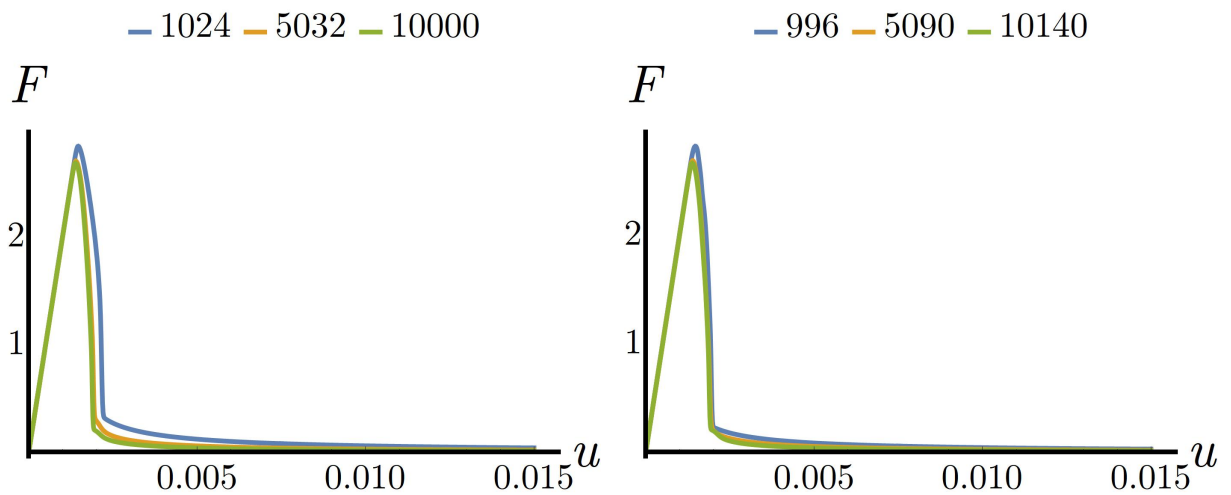


Figure 6.19: Model III [LAP]: Structured/unstructured (left/right) elements of stated number.

6.1.7 Damage Distributions for the Cracked Plate (Stru. Mesh)

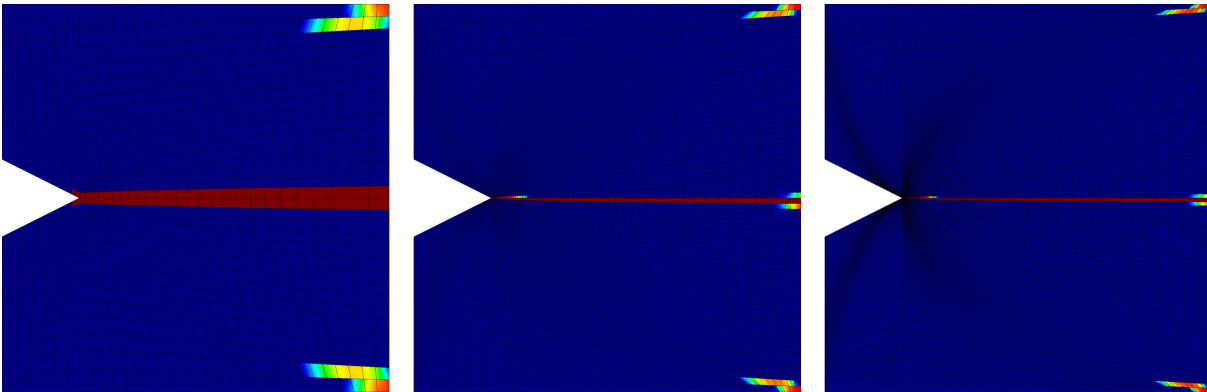


Figure 6.20: Model I [REL]: Distribution of $f(d)$ for the cracked plate with 1024, 4970, and 10000 structured elements (left to right) at the last loading step with $\dot{u} = 50.00 \times 10^{-9}$ mm/s, $r_1 = 1$ MPa and $\beta = 1.4$ (rate-independent).

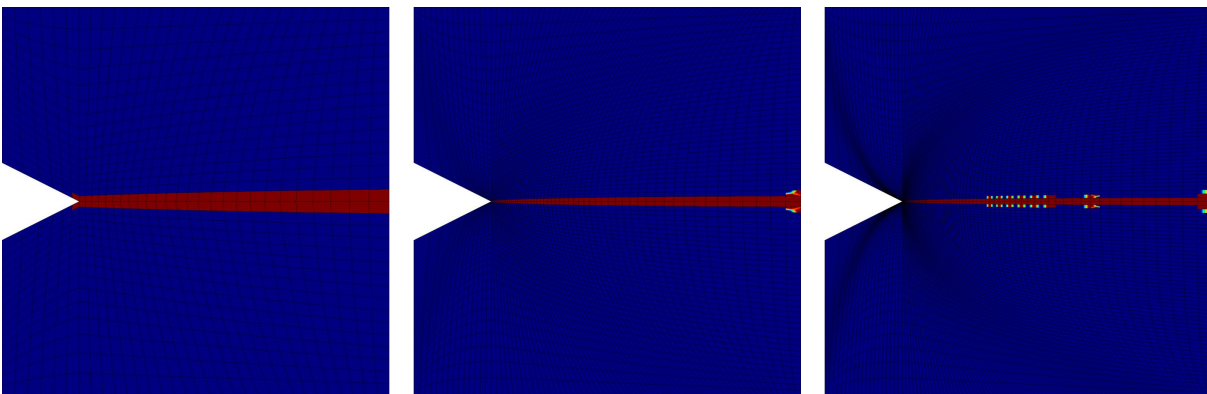


Figure 6.21: Model II [ERVE]: Distribution of $f(d)$ for the cracked plate with 1024, 4970, and 10000 structured elements (left to right) at the last loading step with $\dot{u} = 15.00 \times 10^{-6}$ mm/s, $r_1 = 1$ MPa, $n = 1$ and $\alpha = 5000000$ 1/(N mm).

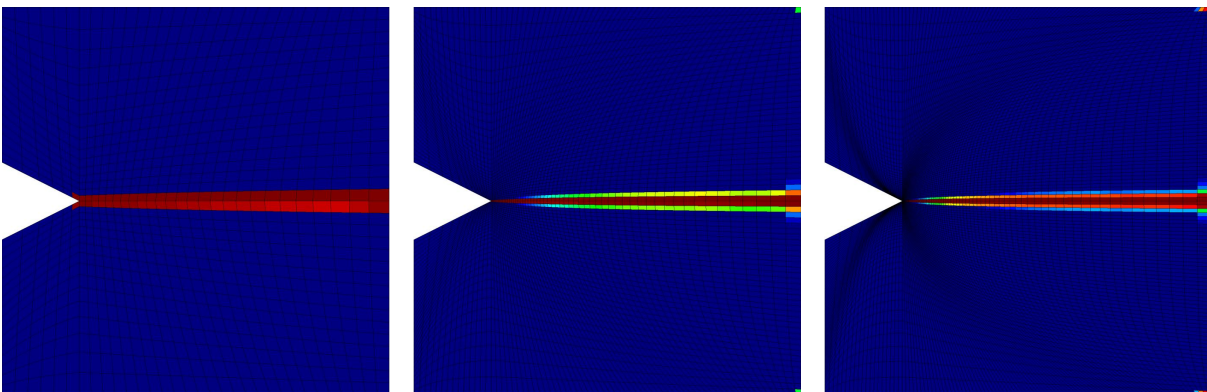


Figure 6.22: Model III [LAP]: Distribution of $f(d)$ for the cracked plate with 1024, 4970, and 10000 structured elements (left to right) at the last loading step with $\dot{u} = 15.00 \times 10^{-6}$ mm/s, $r_1 = 1$ MPa and $\beta = 0.000$ MPa mm².

6.1.8 Damage Distributions for the Cracked Plate (Unstru. Mesh)

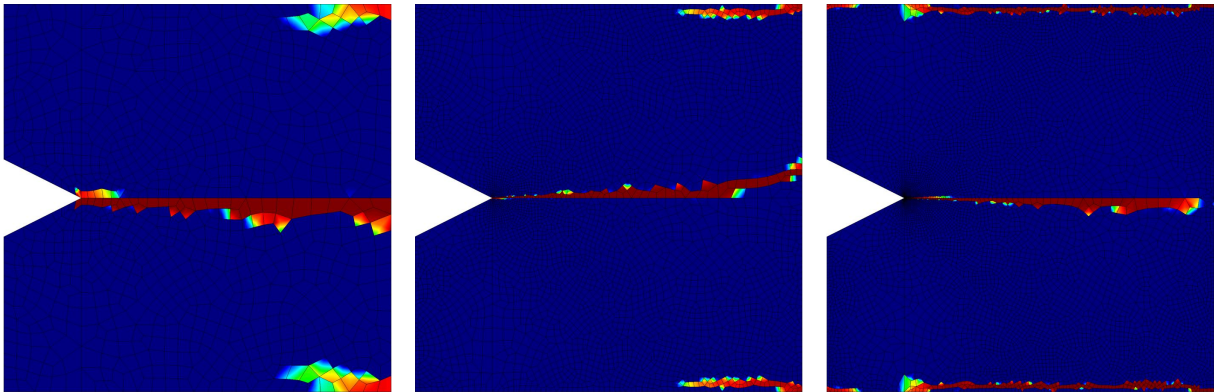


Figure 6.23: Model I [REL]: Distribution of $f(d)$ for the cracked plate with 1007, 5001, and 10040 unstructured elements (left to right) at the last loading step with $\dot{u} = 50.00 \times 10^{-9}$ mm/s, $r_1 = 1$ MPa and $\beta = 1.4$ (rate-independent).

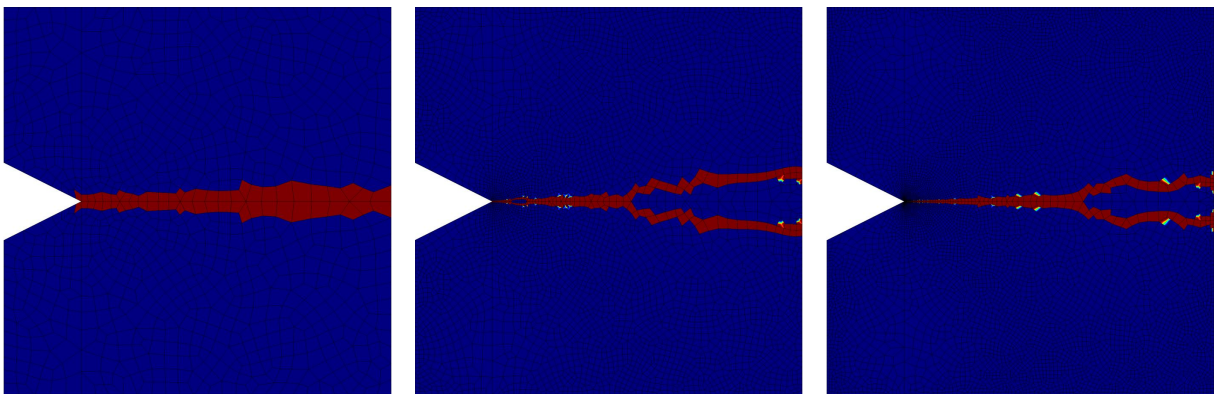


Figure 6.24: Model II [ERVE]: Distribution of $f(d)$ for the cracked plate with 1007, 5001, and 10040 unstructured elements (left to right) at the last loading step with $\dot{u} = 15.00 \times 10^{-6}$ mm/s, $r_1 = 1$ MPa, $n = 1$ and $\alpha = 5000000$ 1/(N mm).

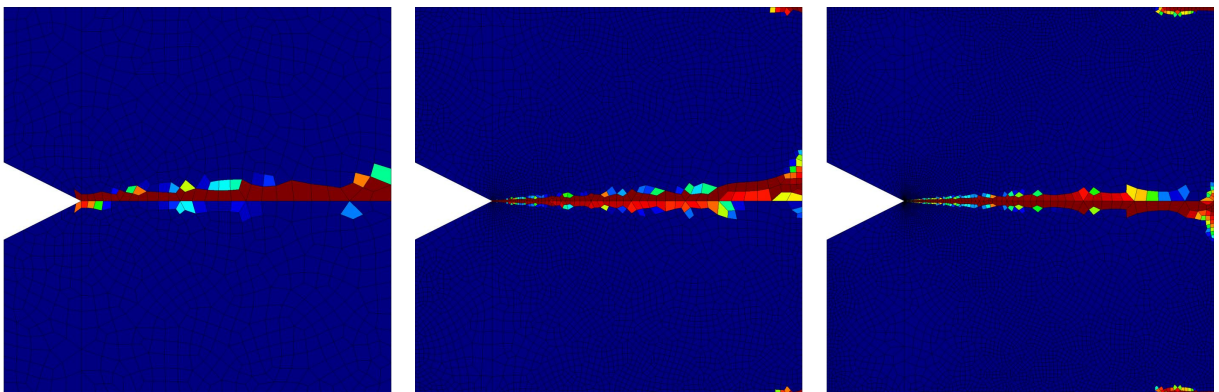


Figure 6.25: Model III [LAP]: Distribution of $f(d)$ for the cracked plate with 1007, 5001, and 10040 unstructured elements (left to right) at the last loading step with $\dot{u} = 15.00 \times 10^{-6}$ mm/s, $r_1 = 1$ MPa and $\beta = 0.000$ MPa mm².

6.1.9 Force-Displacement Diagrams for the Cracked Plate

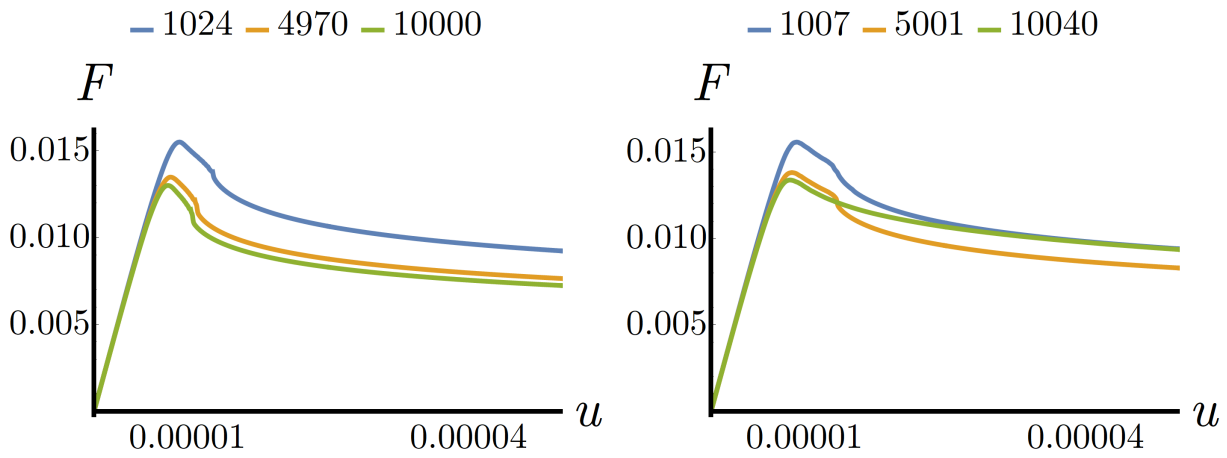


Figure 6.26: Model I [REL]: Structured/unstructured (left/right) elements of stated number.

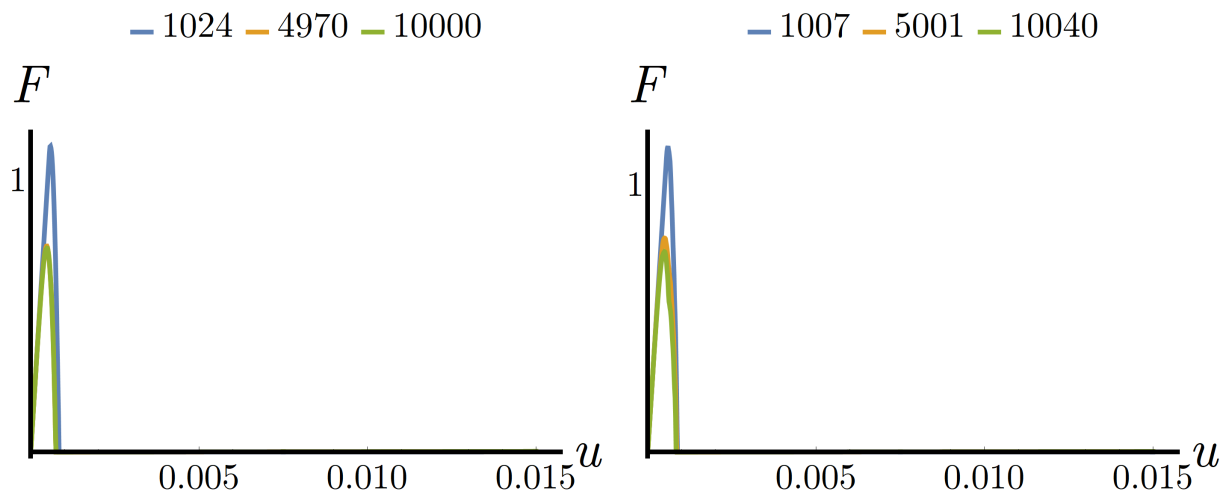


Figure 6.27: Model II [ERVE]: Structured/unstructured (left/right) elements of stated number.

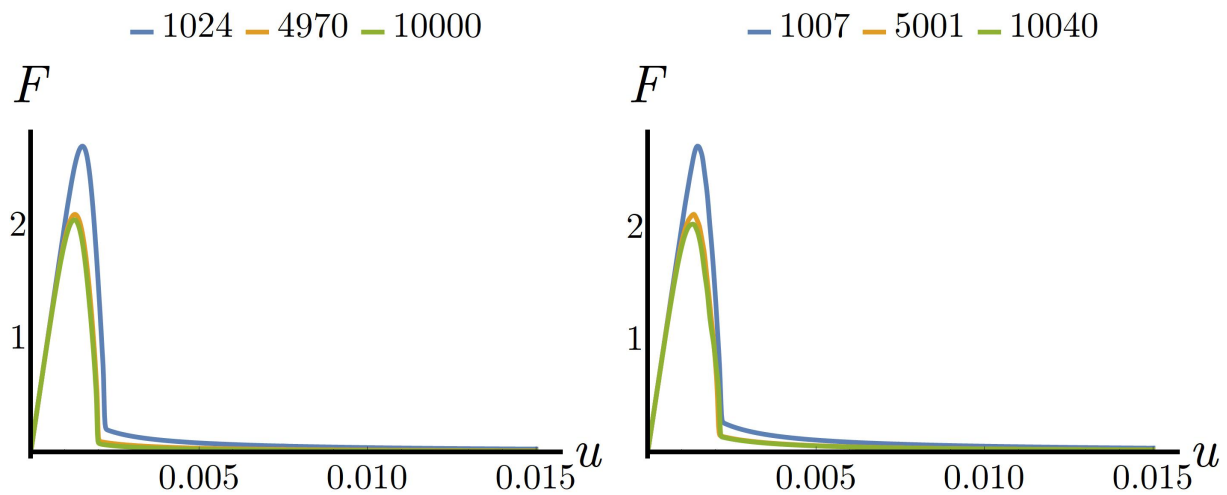


Figure 6.28: Model III [LAP]: Structured/unstructured (left/right) elements of stated number.

6.2 Localized Damage Characteristics

At this point, the finite element results are presented for the localized damage characteristics corresponding to a brittle-like behavior. More information about damage characteristics are given in Chapter 3 including the distinction between localized and diffusive damage. The latter is described in Section 6.3. In the present case of localized damage, only a slight regularization is applied in order to keep the damage distribution local. This allows for a thin and more crack-like characteristic. Hereby, it is desired to ensure an internal length scale corresponding to a crack width which is not much larger than the coarsest considered element. Usually, brittle damage is accompanied by abruptly decreasing global structural responses due to a sudden crack initiation and propagation. This is also part of the investigation.

Initially, the double-notched plate is examined of which the damage distribution is given in Subsections 6.2.1 and 6.2.2 and the global structural response in Subsection 6.2.3. The main characteristic of the damage models is similar: two relatively thin cracks initiate at the notches of the beam and independently propagate through the material to the opposite edges. Due to influences of the boundary conditions, the cracks slightly tend towards the opposite notches.

All damage models apparently provide mesh-independent damage distributions. There are two small particularities in the contour plots. The first one is that the damage distribution in the structured coarse mesh in case of Model I [REL] slightly appears thicker than in the other respective meshes. The second one is that the structured coarse mesh reveals a numerical fluctuation leading to a different damage distribution. This fluctuation should not be given too much attention here, because a slight modification of the mesh discretization or the regularization parameter might solve this issue. However, the mesh discretization as well as the regularization parameters were unchanged due to comparison aspects. Of course, due to the specific model formulation, the characteristics of the damage zones are different. Model I [REL] provides slightly thicker cracks with very sharp transition zones between the undamaged and damaged material. Model II [ERVE] also has these sharp transition zones but the cracks are slightly thinner and have a more regular width. In contrast to that, Model III [LAP] has very smooth transition zones and hereby the cracks additionally appear even thinner which reinforces towards the crack tips.

Taking into account the global structural responses underlines that the results are mesh-independent for all models. However, some differences are noticed. Model II [ERVE] and Model III [LAP] have a perfect agreement in terms of the force-displacement curves, whereas Model I [REL] shows minimal differences. Nevertheless, the agreement is still good for application. It should be mentioned that the curves of Model III [LAP] start to split up when approaching the lower end of the drop. However, since the material is assumed to be destroyed already, this part of the global structural response is not of interest. Further differences between the models can be found in the characteristic of the drops of the forces. Model I [REL] shows the steepest drop in the force-displacement curve. The less steepest drop is observed for Model III [LAP]. Model II [ERVE] is positioned in between. The curves of the last mentioned two models approach zero forces with increasing displacements. The first model approaches some non-zero value instead. From a physical point of view, the curves should directly drop to zero.

Considering the plate with a centered hole in Subsections 6.2.4 to 6.2.6 basically provides similar observations. In this case, the cracks initiate at the centered hole and propagate independently and in opposite directions to the edges of the plate.

The damage distributions for this case again show mesh-independent results for all models. The only exception is the structured coarse mesh of Model III [LAP], in which the crack appears thicker compared to the very thin cracks in the other meshes. Obviously, the developing crack in the structured coarse mesh is actually thinner than the mesh is able to illustrate. Therefore, this is a problem of a too coarse mesh or a too small internal length scale. Both drawbacks could easily be solved. However, the assumed conditions are further on applied in order to call attention to these kinds of problems. The characteristics are basically the same as for the double-notched plate. Whereas Model I [REL] and Model II [ERVE] have very sharp transition zones, Model III [LAP] provides smooth transitions instead. Moreover, the cracks of the last mentioned two models are significantly thinner than the cracks of the first model. The widths of the cracks increase towards the edges resulting in a slight triangular shape. Although this behavior is strengthened by the shape of the elements, the finer meshes demonstrate that this triangular is rather a result of the model's sensitivity regarding the boundary's impact. These effects can also be seen in case of Model II [ERVE] but less pronounced. In case of Model III [LAP], these effects are negligibly small.

The mesh-independence is emphasized by interpreting the force-displacement curves of the calculations. These curves coincide for all three model results. Obviously, the plate with a centered hole is less problematic in regard to mesh-independence. The general characteristics are the same as before, also in regard to the drops of forces.

The last boundary value problem in context of localized damage is the cracked plate discussed in Subsections 6.2.7 to 6.2.9. Especially the relaxation-based damage models, Model I [REL] and Model II [ERVE], are strongly influenced by the boundary conditions. This influence can basically be reduced by assuming larger modeling domains or different boundary conditions. However, the modeling domains as well as the boundary conditions are uniformly set once. The cracks, which are forming at the boundaries due to the aforementioned boundary effects, are only side effects and thus are not considered in what follows.

At first glance, the distribution of damage apparently provides mesh-independent results, although the crack tips of the coarse meshes already seem to be problematic because the elements are quite big. Moreover, the general characteristics for all damage models are basically the same as before. Model I [ERVE] has thicker cracks than the other models and Model III [LAP] has much smoother transition zones. What certainly can be noticed is that the triangular shape of damage is almost vanished and substituted by a more straight pronounced damage zone. The exceptional case is Model I [REL] with a bump-like area in the middle, and that again the structured coarse mesh of Model III [LAP] is hardly able to illustrate the thin crack.

The largest difference to the previous boundary value problems becomes obvious when considering the global structural response. The force-displacement curves have significant discrepancies for the coarse meshes for all damage models. Obviously, this is not a problem of the respective regularization strategy but rather a general problem of describing the sharp crack tip of the geometry. The coarse mesh apparently has too large elements in this area which was already assumed to be problematic. A refinement could be a possible solution. Alternatively, a strong increase of the regularization resulting in a much bigger internal length scale might also solve this problem or improve the mesh convergence. However, these large elements constitute an example for illustrating the limits of the regularization. Nevertheless, the medium and fine mesh have good agreements as expected.

Further discussions are following in Chapter 7.

6.2.1 Damage Distributions for the Double-Notched Plate (Stru. Mesh)

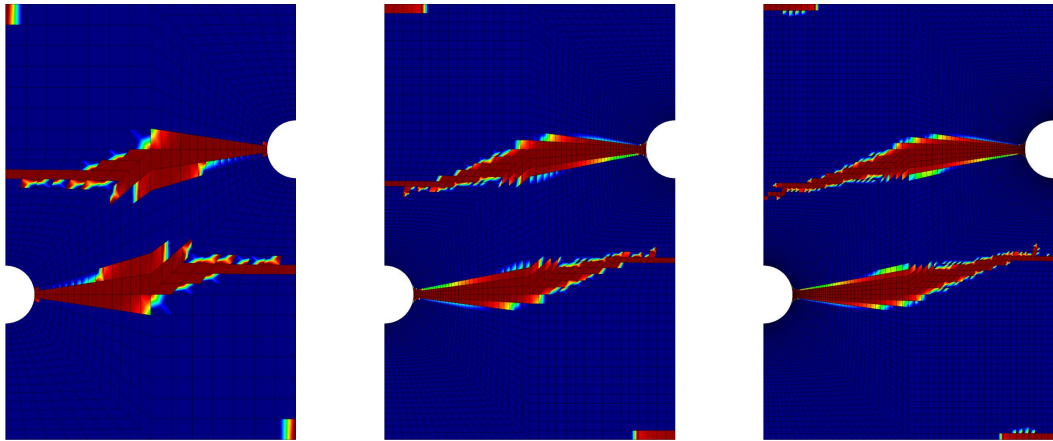


Figure 6.29: Model I [REL]: Distribution of $f(d)$ for the double-notched plate with 994, 4992, and 10074 structured elements (left to right) at the last loading step with $\dot{u} = 15.00 \times 10^{-6}$ mm/s, $r_1 = 200$ MPa, $\beta = 2.0$ and $r_2 = 0.20 \times 10^8$ MPa s.

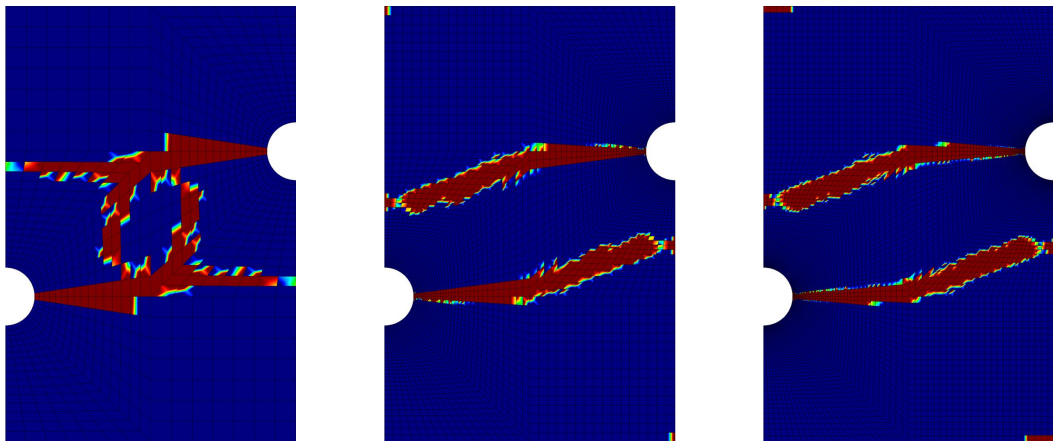


Figure 6.30: Model II [ERVE]: Distribution of $f(d)$ for the double-notched plate with 994, 4992, and 10074 structured elements (left to right) at the last loading step with $\dot{u} = 15.00 \times 10^{-6}$ mm/s, $r_1 = 1$ MPa, $n = 20$ and $\alpha = 5000$ 1/(N mm).

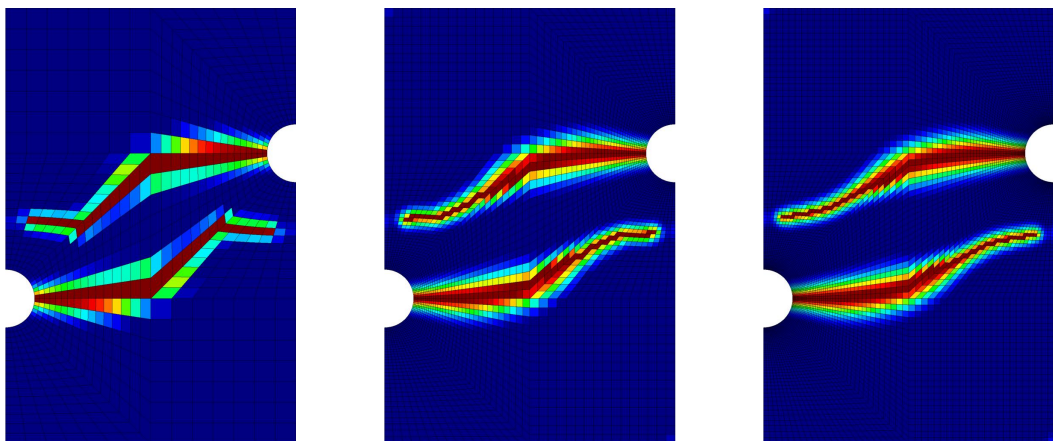


Figure 6.31: Model III [LAP]: Distribution of $f(d)$ for the double-notched plate with 994, 4992, and 10074 structured elements (left to right) at the last loading step with $\dot{u} = 15.00 \times 10^{-6}$ mm/s, $r_1 = 1$ MPa and $\beta = 0.002$ MPa mm².

6.2.2 Damage Distributions for the Double-Notched Plate (Unstru. Mesh)

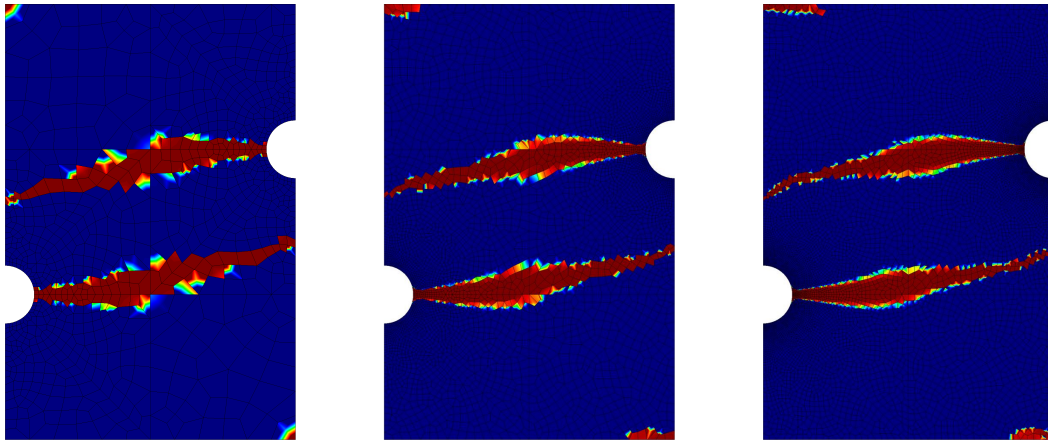


Figure 6.32: Model I [REL]: Distribution of $f(d)$ for the double-notched plate with 986, 5064, and 10161 unstructured elements (left to right) at the last loading step with $\dot{u} = 15.00 \times 10^{-6}$ mm/s, $r_1 = 200$ MPa, $\beta = 2.0$ and $r_2 = 0.20 \times 10^8$ MPa s.

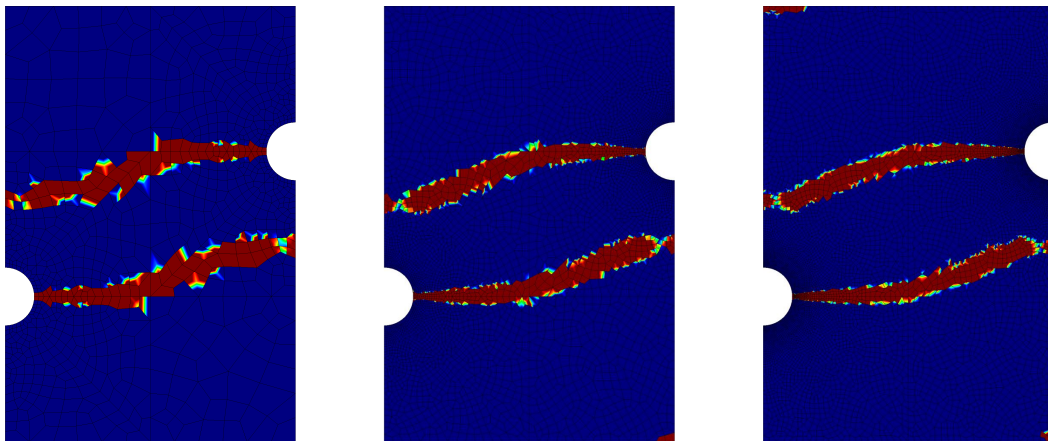


Figure 6.33: Model II [ERVE]: Distribution of $f(d)$ for the double-notched plate with 986, 5064, and 10161 unstructured elements (left to right) at the last loading step with $\dot{u} = 15.00 \times 10^{-6}$ mm/s, $r_1 = 1$ MPa, $n = 20$ and $\alpha = 5000$ 1/(N mm).

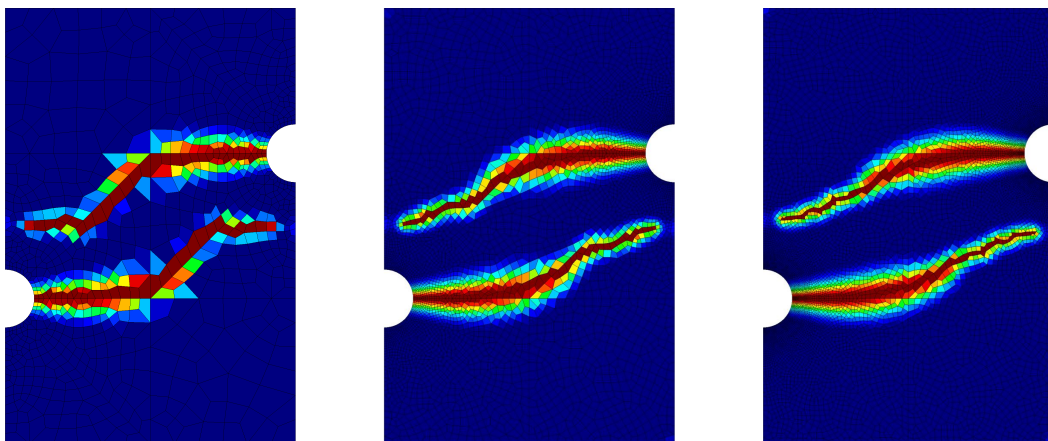


Figure 6.34: Model III [LAP]: Distribution of $f(d)$ for the double-notched plate with 986, 5064, and 10161 unstructured elements (left to right) at the last loading step with $\dot{u} = 15.00 \times 10^{-6}$ mm/s, $r_1 = 1$ MPa and $\beta = 0.002$ MPa mm².

6.2.3 Force-Displacement Diagrams for the Double-Notched Plate

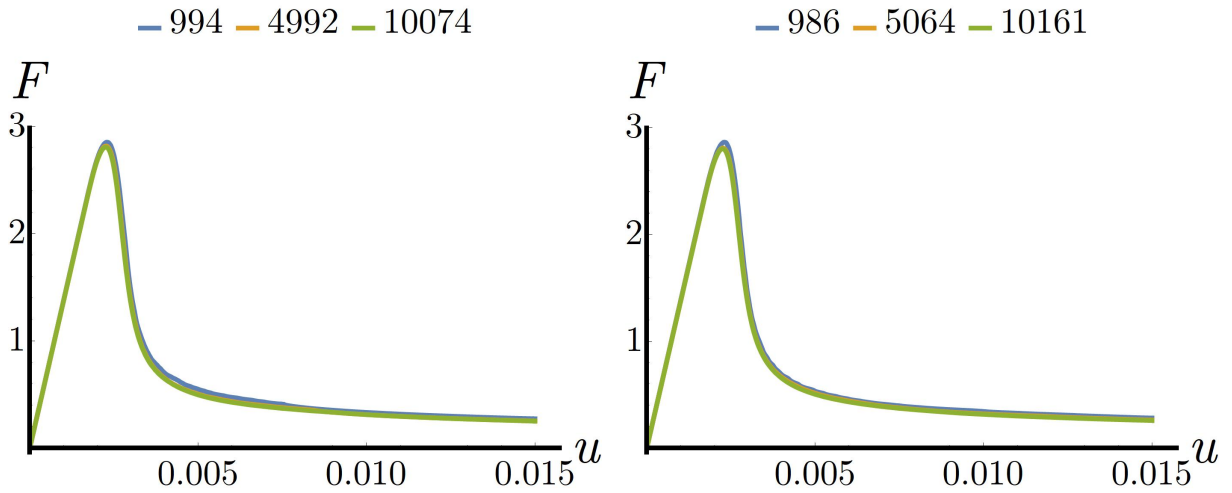


Figure 6.35: Model I [REL]: Structured/unstructured (left/right) elements of stated number.

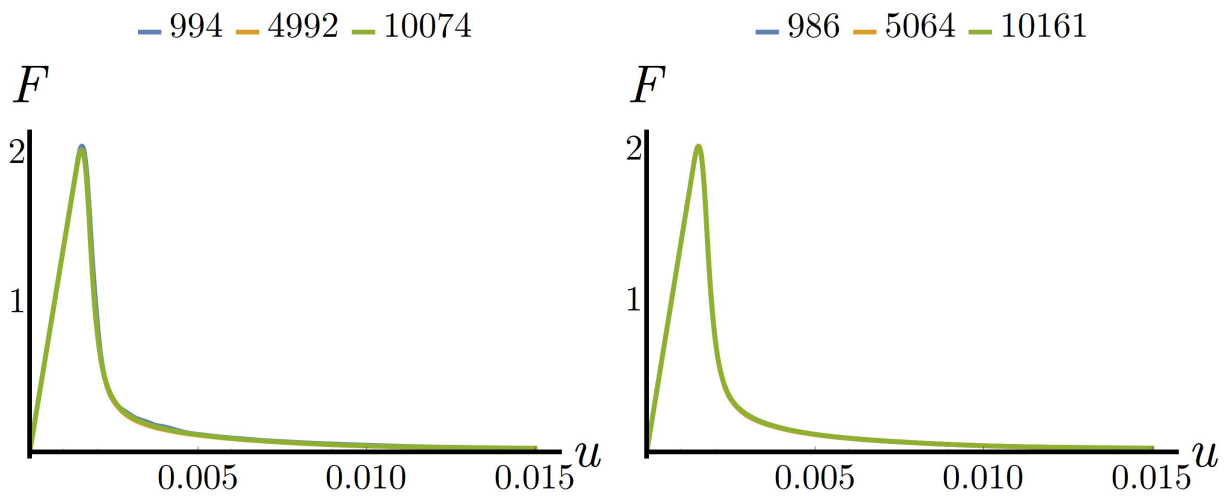


Figure 6.36: Model II [ERVE]: Structured/unstructured (left/right) elements of stated number.

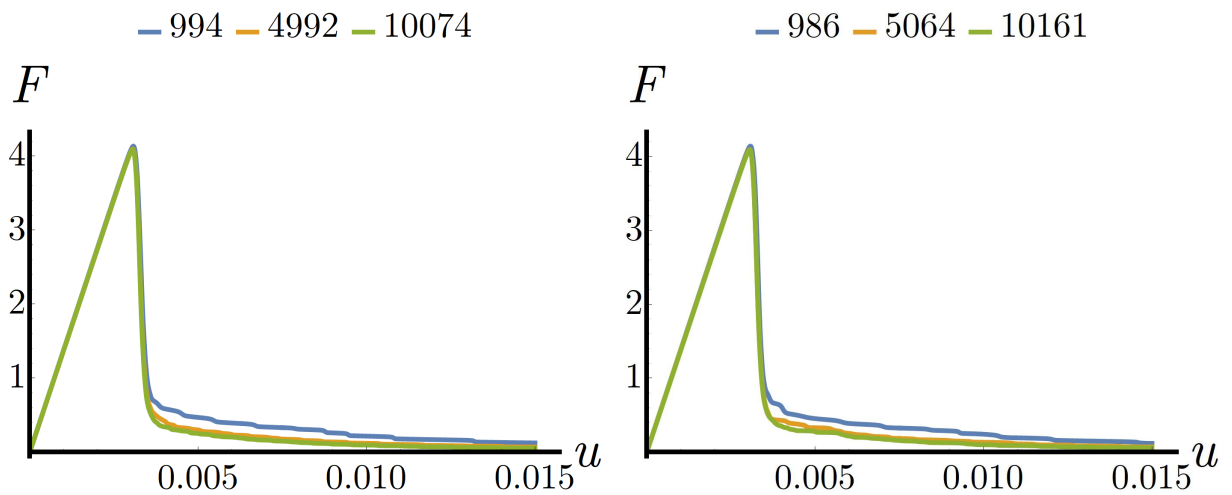


Figure 6.37: Model III [LAP]: Structured/unstructured (left/right) elements of stated number.

6.2.4 Damage Distributions for the Plate with a Centered Hole (Stru. Mesh)

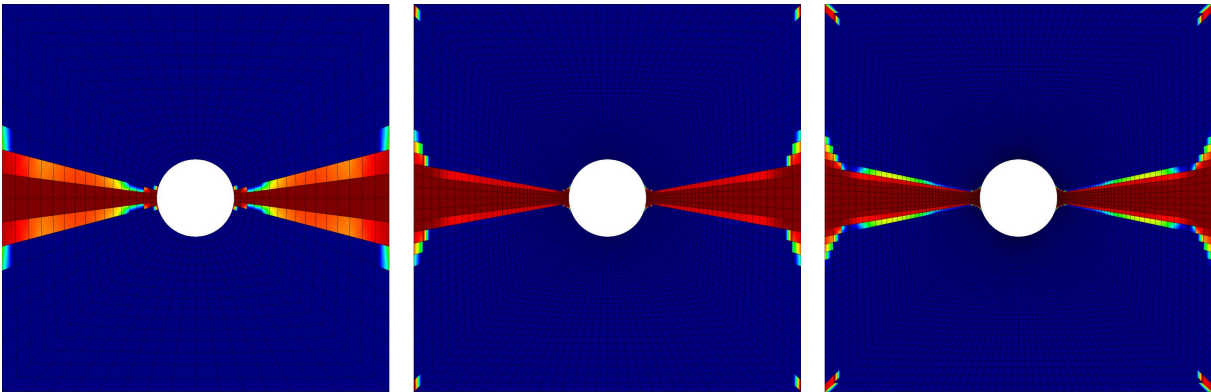


Figure 6.38: Model I [REL]: Distribution of $f(d)$ for the plate with a centered hole with 1024, 5032, and 10000 structured elements (left to right) at the last loading step with $\dot{u} = 15.00 \times 10^{-6}$ mm/s, $r_1 = 200$ MPa, $\beta = 2.0$ and $r_2 = 0.20 \times 10^8$ MPa s.

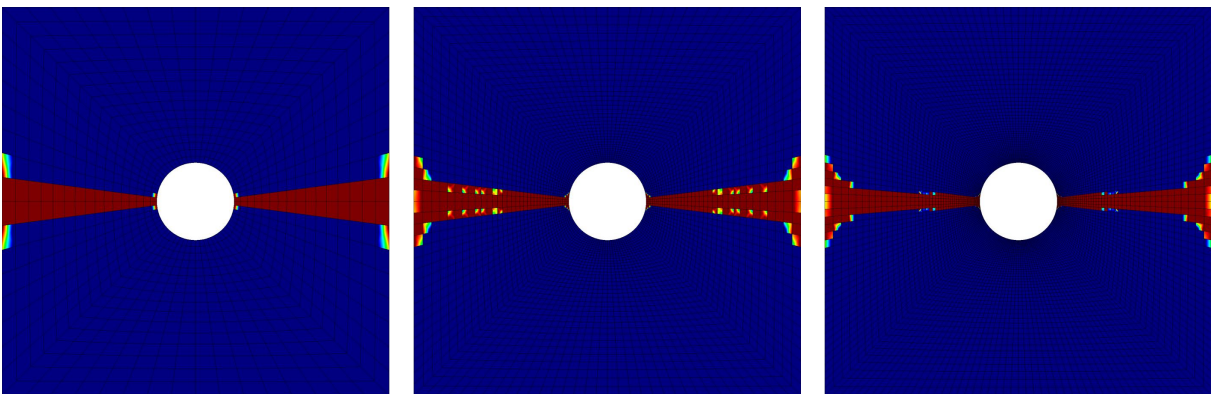


Figure 6.39: Model II [ERVE]: Distribution of $f(d)$ for the plate with a centered hole with 1024, 5032, and 10000 structured elements (left to right) at the last loading step with $\dot{u} = 15.00 \times 10^{-6}$ mm/s, $r_1 = 1$ MPa, $n = 20$ and $\alpha = 5000$ 1/(N mm).

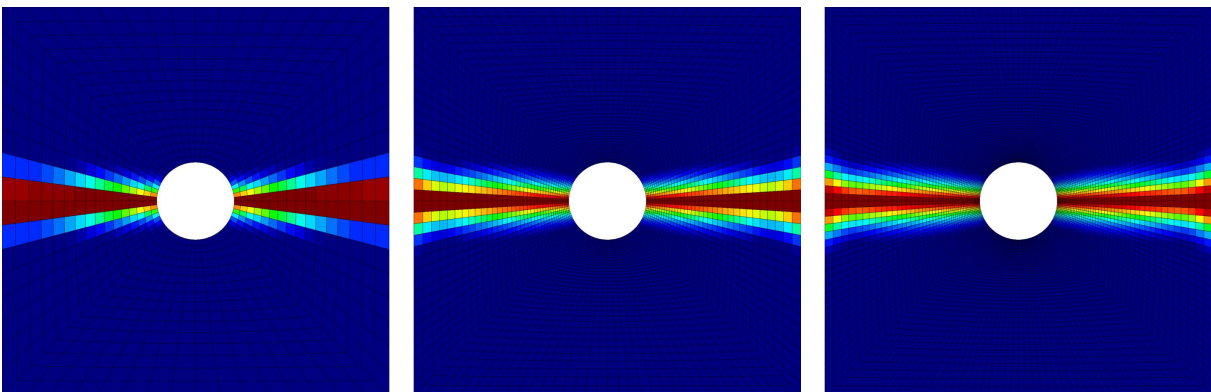


Figure 6.40: Model III [LAP]: Distribution of $f(d)$ for the plate with a centered hole with 1024, 5032, and 10000 structured elements (left to right) at the last loading step with $\dot{u} = 15.00 \times 10^{-6}$ mm/s, $r_1 = 1$ MPa and $\beta = 0.002$ MPa mm².

6.2.5 Damage Distributions for the Plate with a Centered Hole (Unstru. Mesh)

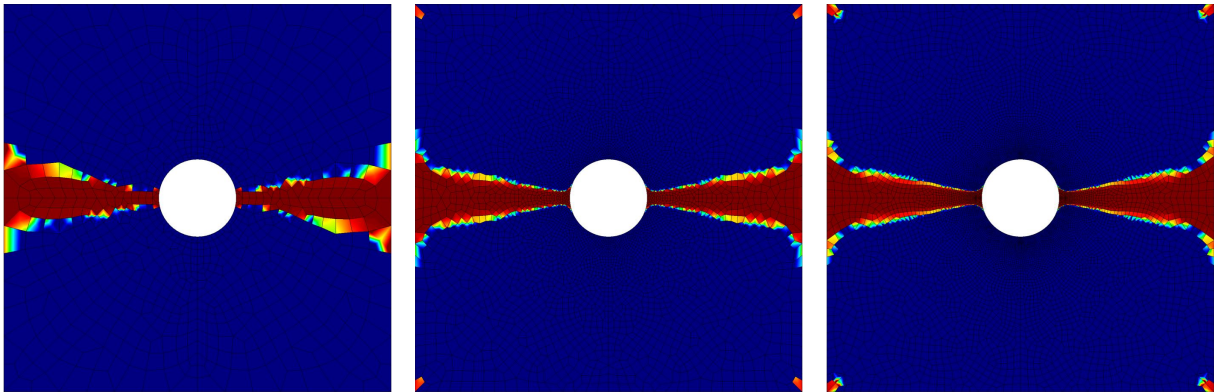


Figure 6.41: Model I [REL]: Distribution of $f(d)$ for the plate with a centered hole with 996, 5090, and 10140 unstructured elements (left to right) at the last loading step with $\dot{u} = 15.00 \times 10^{-6}$ mm/s, $r_1 = 200$ MPa, $\beta = 2.0$ and $r_2 = 0.20 \times 10^8$ MPa s.

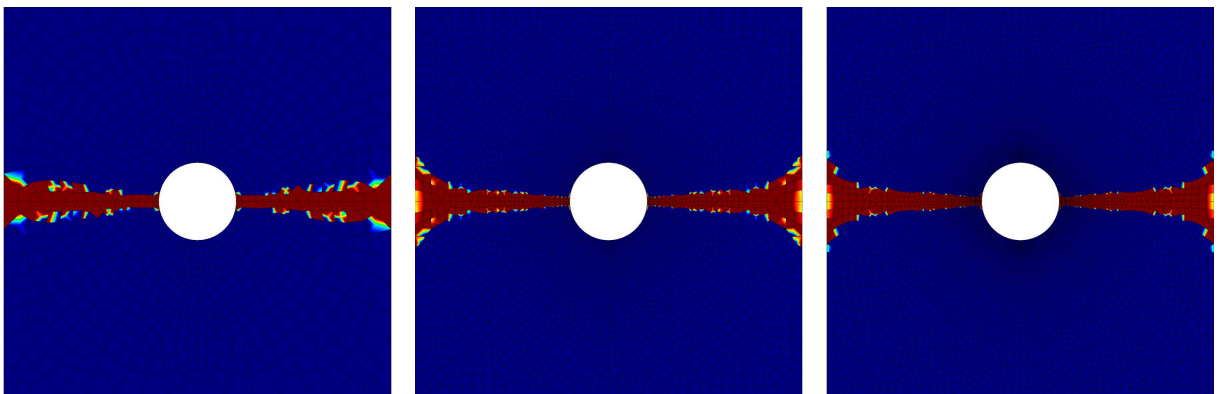


Figure 6.42: Model II [ERVE]: Distribution of $f(d)$ for the plate with a centered hole with 996, 5090, and 10140 unstructured elements (left to right) at the last loading step with $\dot{u} = 15.00 \times 10^{-6}$ mm/s, $r_1 = 1$ MPa, $n = 20$ and $\alpha = 5000$ 1/(N mm).

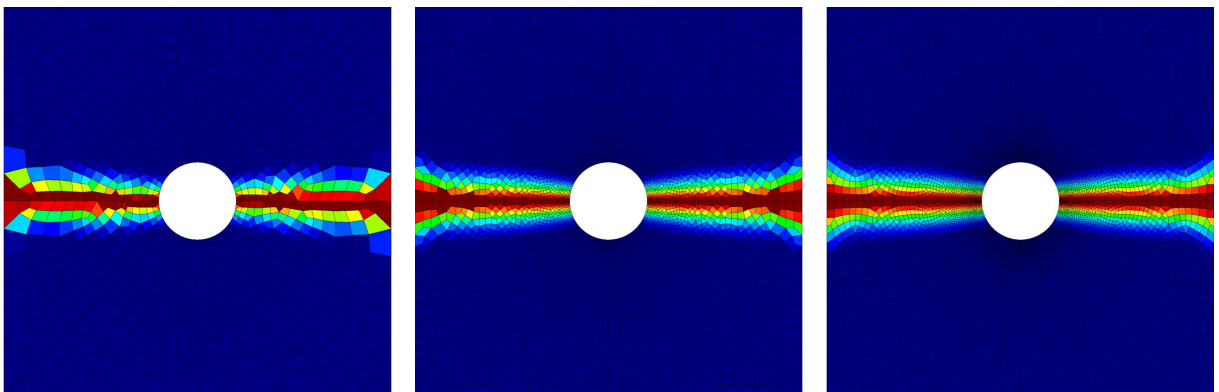


Figure 6.43: Model III [LAP]: Distribution of $f(d)$ for the plate with a centered hole with 996, 5090, and 10140 unstructured elements (left to right) at the last loading step with $\dot{u} = 15.00 \times 10^{-6}$ mm/s, $r_1 = 1$ MPa and $\beta = 0.002$ MPa mm².

6.2.6 Force-Displacement Diagrams for the Plate with a Centered Hole

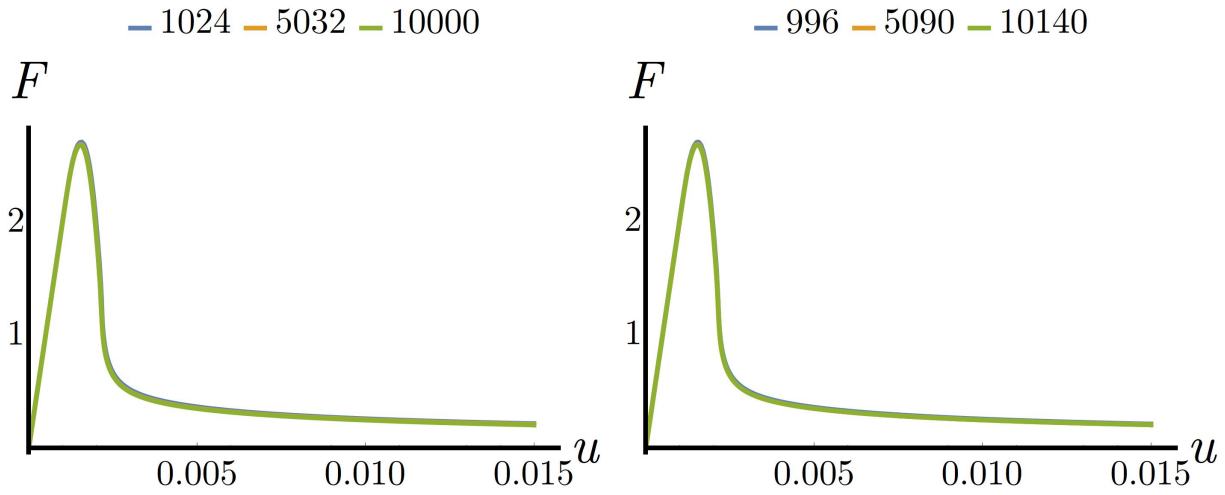


Figure 6.44: Model I [REL]: Structured/unstructured (left/right) elements of stated number.

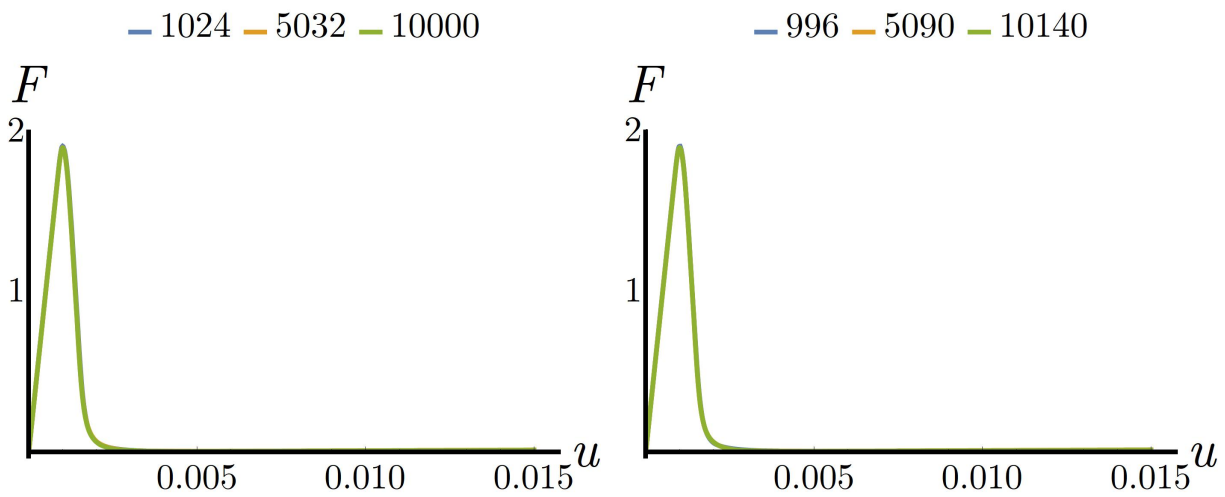


Figure 6.45: Model II [ERVE]: Structured/unstructured (left/right) elements of stated number.

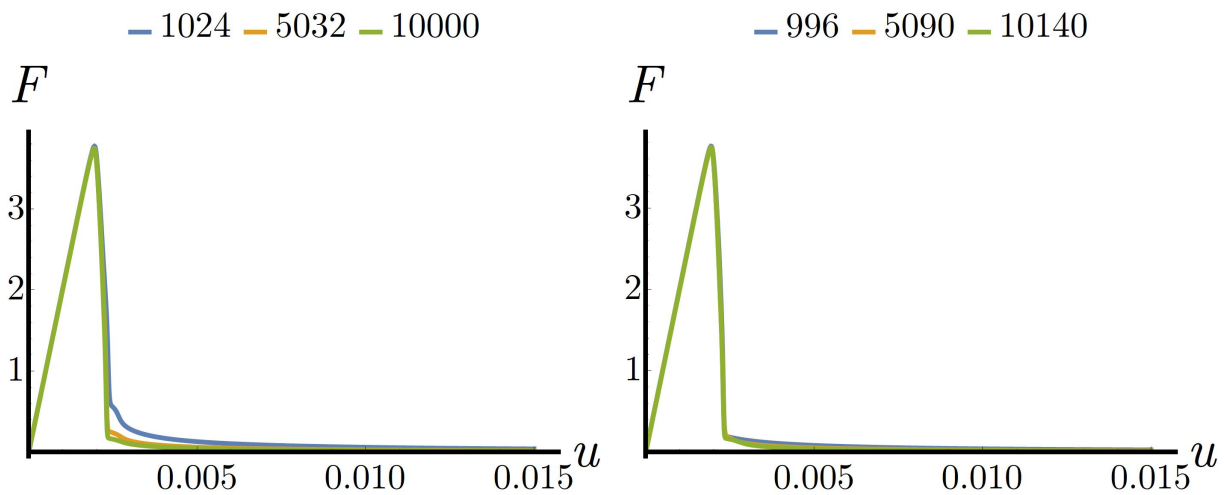


Figure 6.46: Model III [LAP]: Structured/unstructured (left/right) elements of stated number.

6.2.7 Damage Distributions for the Cracked Plate (Stru. Mesh)

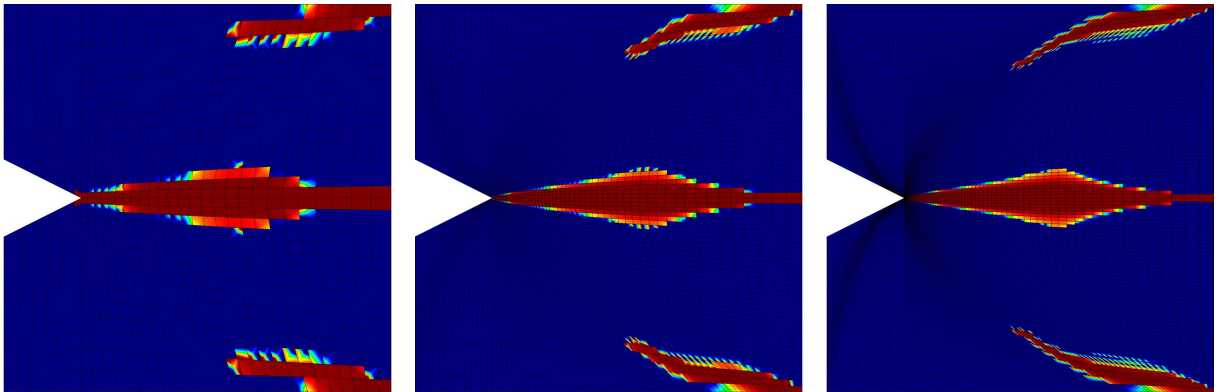


Figure 6.47: Model I [REL]: Distribution of $f(d)$ for the cracked plate with 1024, 4970, and 10000 structured elements (left to right) at the last loading step with $\dot{u} = 15.00 \times 10^{-6}$ mm/s, $r_1 = 200$ MPa, $\beta = 2.0$ and $r_2 = 0.20 \times 10^8$ MPa s.

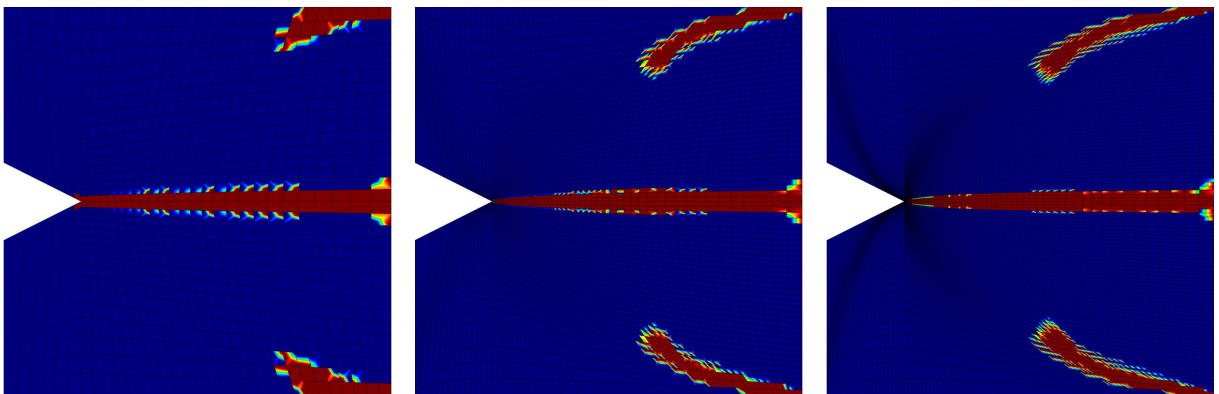


Figure 6.48: Model II [ERVE]: Distribution of $f(d)$ for the cracked plate with 1024, 4970, and 10000 structured elements (left to right) at the last loading step with $\dot{u} = 15.00 \times 10^{-6}$ mm/s, $r_1 = 1$ MPa, $n = 20$ and $\alpha = 5000$ 1/(N mm).

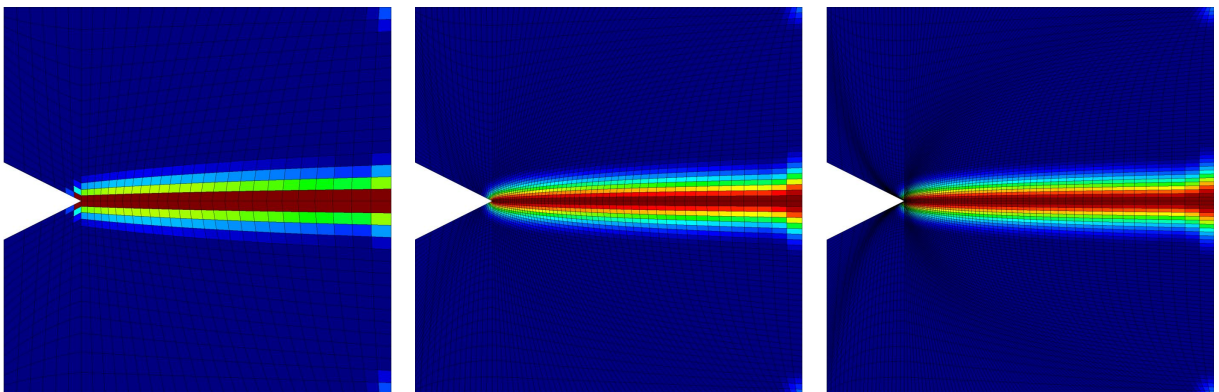


Figure 6.49: Model III [LAP]: Distribution of $f(d)$ for the cracked plate with 1024, 4900, and 10000 structured elements (left to right) at the last loading step with $\dot{u} = 15.00 \times 10^{-6}$ mm/s, $r_1 = 1$ MPa and $\beta = 0.002$ MPa mm².

6.2.8 Damage Distributions for the Cracked Plate (Unstru. Mesh)

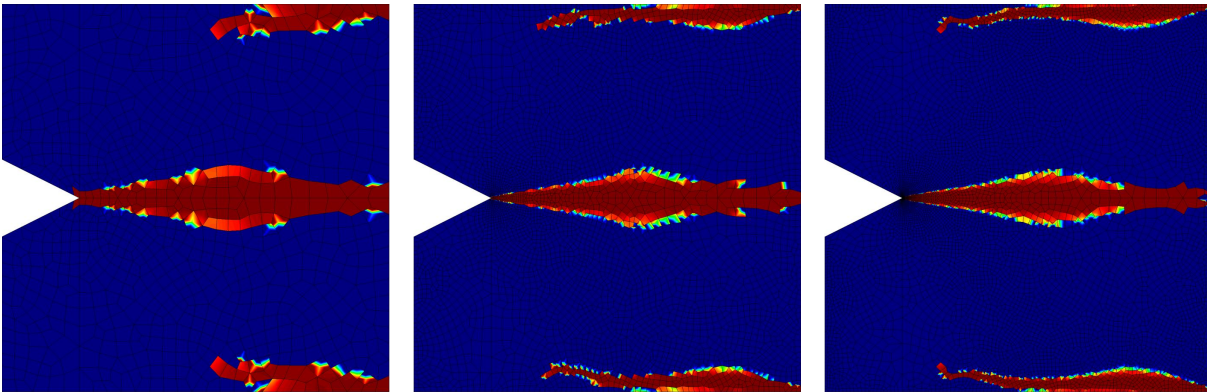


Figure 6.50: Model I [REL]: Distribution of $f(d)$ for the cracked plate with 1007, 5001, and 10040 unstructured elements (left to right) at the last loading step with $\dot{u} = 15.00 \times 10^{-6}$ mm/s, $r_1 = 200$ MPa, $\beta = 2.0$ and $r_2 = 0.20 \times 10^8$ MPa s.

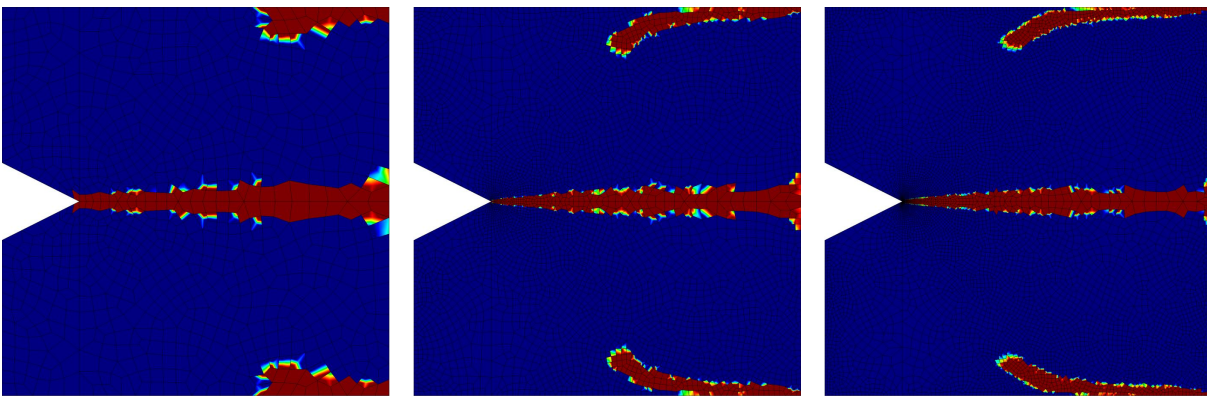


Figure 6.51: Model II [ERVE]: Distribution of $f(d)$ for the cracked plate with 1007, 5001, and 10040 unstructured elements (left to right) at the last loading step with $\dot{u} = 15.00 \times 10^{-6}$ mm/s, $r_1 = 1$ MPa, $n = 20$ and $\alpha = 5000$ 1/(N mm).

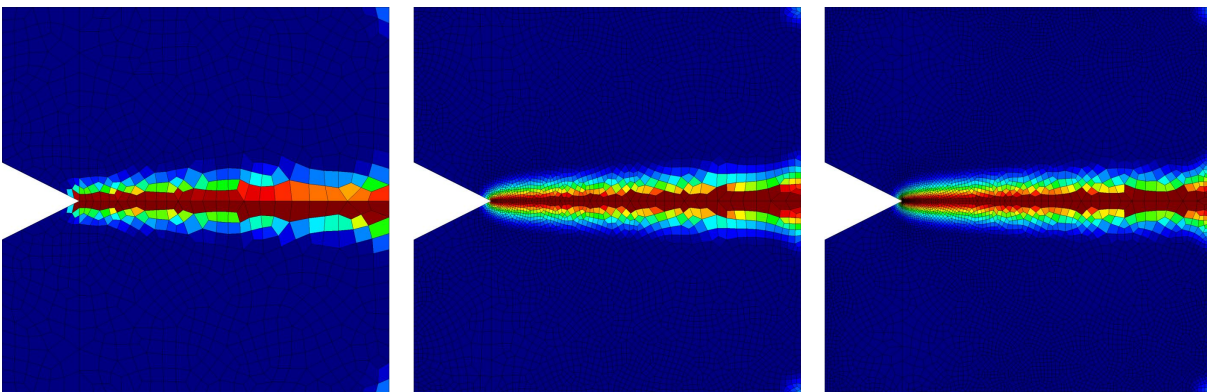


Figure 6.52: Model III [LAP]: Distribution of $f(d)$ for the cracked plate with 1007, 5001, and 10040 unstructured elements (left to right) at the last loading step with $\dot{u} = 15.00 \times 10^{-6}$ mm/s, $r_1 = 1$ MPa and $\beta = 0.002$ MPa mm².

6.2.9 Force-Displacement Diagrams for the Cracked Plate

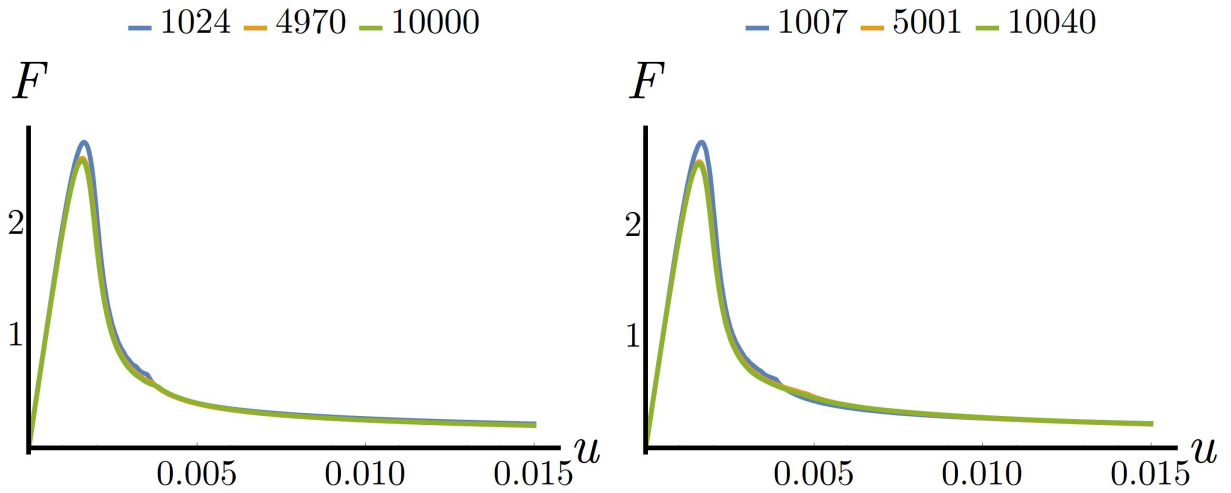


Figure 6.53: Model I [REL]: Structured/unstructured (left/right) elements of stated number.

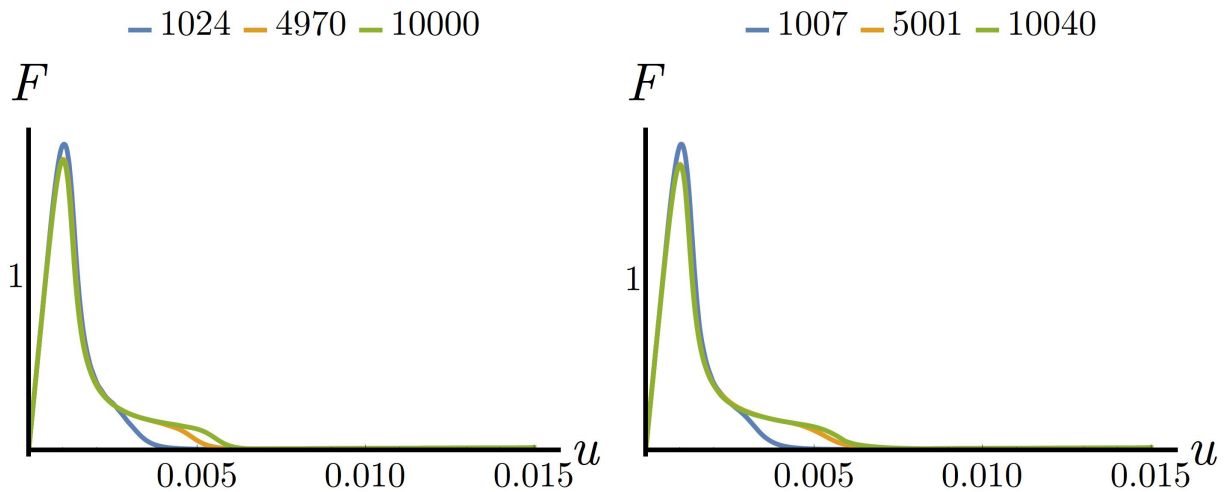


Figure 6.54: Model II [ERVE]: Structured/unstructured (left/right) elements of stated number.

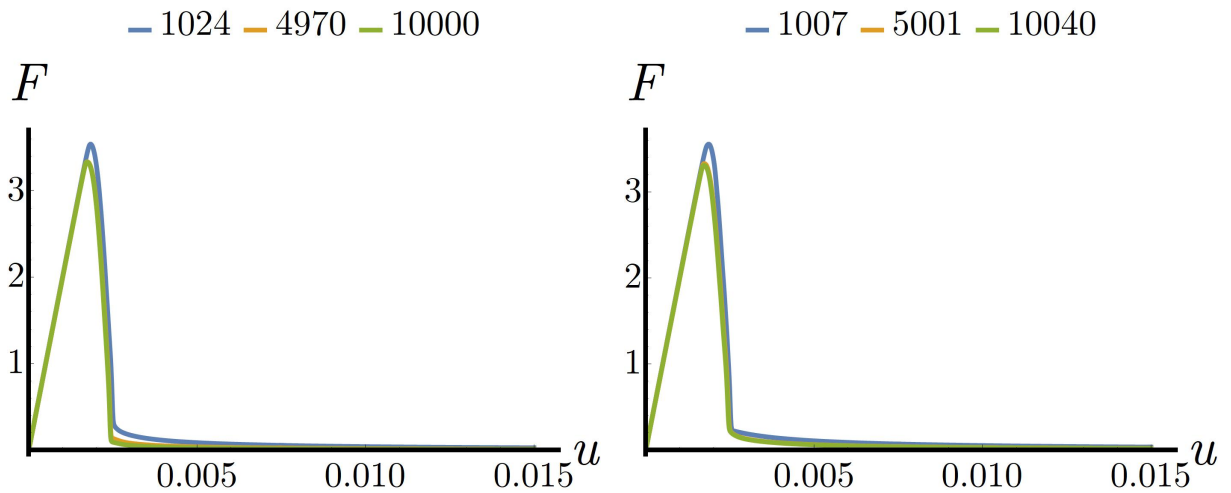


Figure 6.55: Model III [LAP]: Structured/unstructured (left/right) elements of stated number.

6.3 Diffusive Damage Characteristics

This section is dedicated to diffusive damage characteristics for a ductile-like behavior and finite element results are presented, in what follows. Again, Chapter 3 provides more information about damage characteristics such as the distinction between the previously considered localized damage, see Section 6.2, and the diffusive damage to be discussed below. For this diffusive damage a stronger regularization is applied in order to expand the damage distribution to a certain level. This corresponds to a plastic zone that usually evolves in case of ductile damage but is not considered here. This stronger regularization also results in an increase of the area of influence. Based on that, the present parameters are fitted such that the cracks in regard to the double-notched plate are propagating towards each other and consequently connect.

The first boundary value problem investigated is the double-notched plate. The related damage distribution is given in Subsections 6.3.1 and 6.3.2 and the related global structural response in Subsection 6.3.3. As already mentioned, the propagating cracks connect to one single crack. The characteristic of this single crack is depending on the respective damage model and the specific choice of parameters, merging between an I-shape and S-shape.

Taking into account the damage distributions obviously exhibits that the results are mesh-independent. Only the unstructured coarse mesh provides thicker cracks than the other respective meshes in case of all damage models. The centered elements, through which the cracks propagate, are probably too large. However, this is an interesting point to be investigated. Moreover, the characteristic of the damage distribution corresponds to the I-shape in case of Model I [REL], to the S-shape for Model III [LAP], and something inbetween for Model II [ERVE]. The overall transition zones are now slightly smoother than for the localized case. However, Model III [LAP] still provides significantly smoother results than the other models. In accordance with previous observations, the crack of the first model is thicker in turn. On the contrary, the other models have a comparable thickness compared to the localized results.

The corresponding force-displacement curves confirm the mesh-independence which is represented by very good agreements. The latter are even better than for the localized case which actually is expected due to the stronger regularization. This leads to almost identical global structural responses in terms of Model I [REL] even for the coarse mesh and Model III [LAP] provides very similar results after approaching the lower end of the drop. However, more interesting is the general characteristic of the curves when comparing the present diffusive case with the previous localized case. As expected, the peak in the curves of Model I [REL] and Model II [ERVE] which represents the beginning drop, is now smoother and has a more distinct range of decreasing forces. Model III [LAP] in turn does not show any differences. Only the remaining forces after the drop are now faster approaching zero, which also applies for Model II [ERVE]. In general, the steepness of the dropping curves are hardly influenced by the stronger regularization in case of all damage models.

Next, the plate with a centered hole is considered for further investigations by Subsections 6.3.4 to 6.3.6. The cracks propagate from the hole to the edges as expected. However, the boundary conditions obviously have a significant impact on the relaxation based models, Model I [REL] and Model II [ERVE], with respect to the width and shape of the cracks.

In principle, the distribution of damage appears to be mesh-independent for all models and the stronger regularization also improves the previous problems regarding the structured coarse mesh in context of Model III [LAP]. However, even though the cracks are assumed to be thicker

due to the stronger regularization, the damage distribution for the mentioned relaxation-based models is questionable from the physical point of view. Large triangular damage zones evolve. In case of Model I [REL] these zones are even thicker. Obviously and as already observed for the localized results, the relaxation-based models are sensitive with respect to boundary conditions especially for the diffusive damage characteristic. Either, applications of these models should be limited to cases of localized damage or the influence of boundary effects be decreased by exemplarily considering a larger domain.

The aforementioned problem does not have any effect on the structural response. Perfectly mesh-independent force-displacement curves are given for all models, since the plate with a centered hole is less problematic, as already figured out for the localized results. Analogously to the double-notched plate, the drops are smoother and have a more distinct range. Furthermore, the curves partially approach zero forces quicker than for the localized case.

The cracked plate is the last boundary value problem considered in this context as presented in Subsections 6.3.7 to 6.3.9. Again, the influences of the boundary conditions are strong.

Initially, despite the mentioned influences and besides some small fluctuations, the damage distributions are in good agreement for all damage models. Only a detailed view on the crack tips of the coarse meshes reveals accuracy problems analogously to the localized case. However, the characteristic of the distributed damage is completely different for each model. Model I [REL] provides a splitting crack inducing a V-shape that tends to grow towards the opposite corners. The crack in Model II [ERVE] is also strongly affected by the boundary conditions and therefore damage zones are evolving in the corners, as well. However, in contrast to the previous model, the crack is in turn not connected to these parts but developing to a triangular shaped or almost drop shaped damage zone. A completely different characteristic is given by Model III [LAP] that is still not affected by any boundary effects and provides thin and straight on propagating cracks. Actually, these are the only physically reasonable results.

Nevertheless, a better agreement of the force-displacement curves is provided than for the localized case due to the stronger regularization. From that point of view, the influences of boundary effects do not have a negative effect on the mesh-independence. The results show that the stronger regularization better captured the critical crack tip. Therefore, Model II [ERVE] has a good agreement, Model III [LAP] has a still better agreement, and in turn the curves of Model I [REL] are only slightly better and still are not agreeing for the coarse meshes.

Further discussions are following in Chapter 7.

6.3.1 Damage Distributions for the Double-Notched Plate (Stru. Mesh)

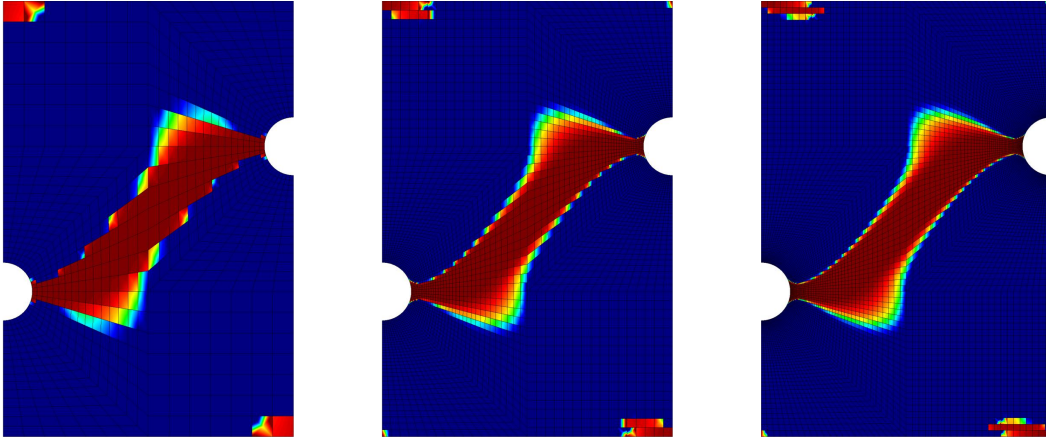


Figure 6.56: Model I [REL]: Distribution of $f(d)$ for the double-notched plate with 994, 4992, and 10074 structured elements (left to right) at the last loading step with $\dot{u} = 15.00 \times 10^{-6}$ mm/s, $r_1 = 200$ MPa, $\beta = 2.0$ and $r_2 = 1.00 \times 10^8$ MPa s.

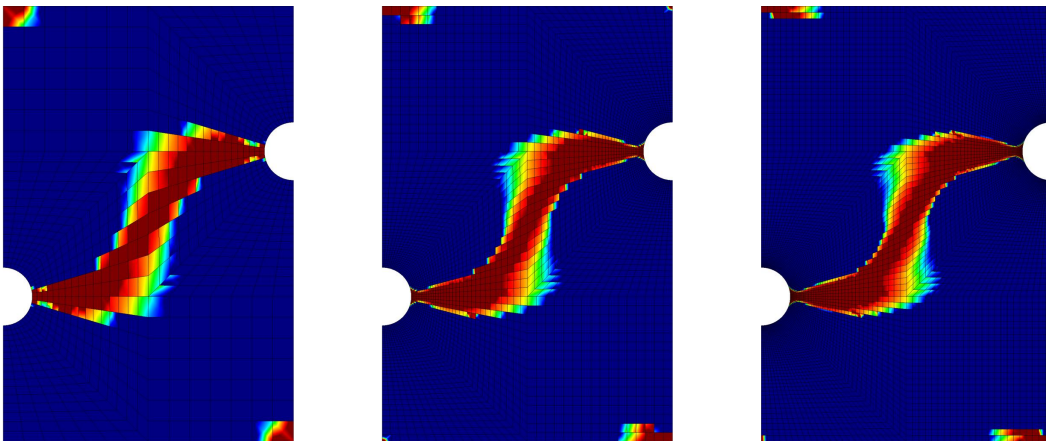


Figure 6.57: Model II [ERVE]: Distribution of $f(d)$ for the double-notched plate with 994, 4992, and 10074 structured elements (left to right) at the last loading step with $\dot{u} = 15.00 \times 10^{-6}$ mm/s, $r_1 = 1$ MPa, $n = 20$ and $\alpha = 500$ 1/(N mm).

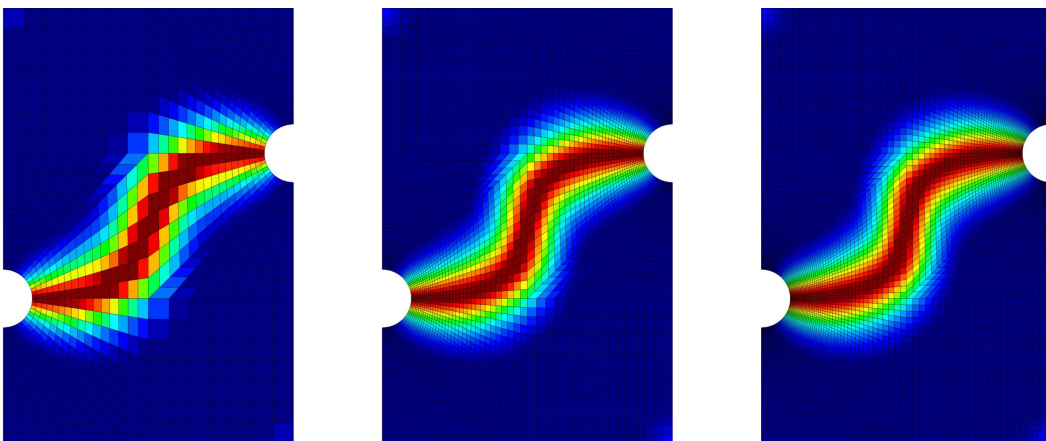


Figure 6.58: Model III [LAP]: Distribution of $f(d)$ for the double-notched plate with 994, 4992, and 10074 structured elements (left to right) at the last loading step with $\dot{u} = 15.00 \times 10^{-6}$ mm/s, $r_1 = 1$ MPa and $\beta = 0.015$ MPa mm².

6.3.2 Damage Distributions for the Double-Notched Plate (Unstru. Mesh)

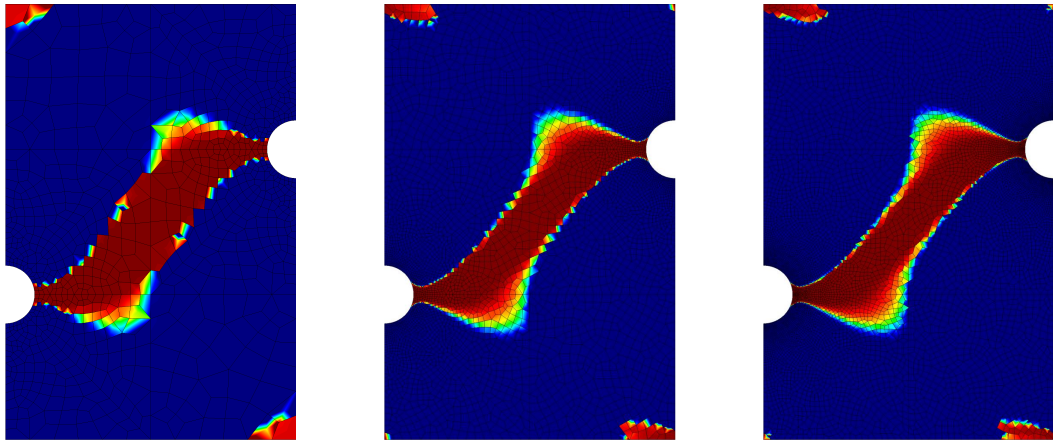


Figure 6.59: Model I [REL]: Distribution of $f(d)$ for the double-notched plate with 986, 5064, and 10161 unstructured elements (left to right) at the last loading step with $\dot{u} = 15.00 \times 10^{-6}$ mm/s, $r_1 = 200$ MPa, $\beta = 2.0$ and $r_2 = 1.00 \times 10^8$ MPa s.

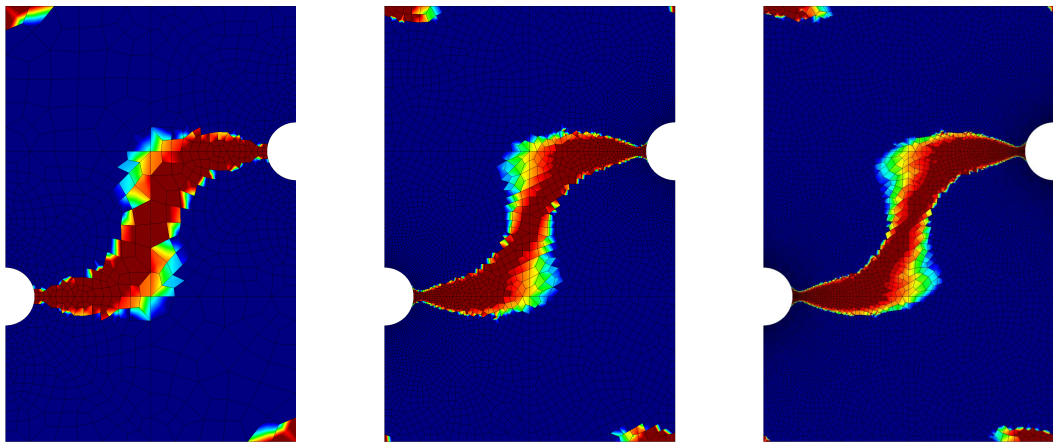


Figure 6.60: Model II [ERVE]: Distribution of $f(d)$ for the double-notched plate with 986, 5064, and 10161 unstructured elements (left to right) at the last loading step with $\dot{u} = 15.00 \times 10^{-6}$ mm/s, $r_1 = 1$ MPa, $n = 20$ and $\alpha = 500$ 1/(N mm).

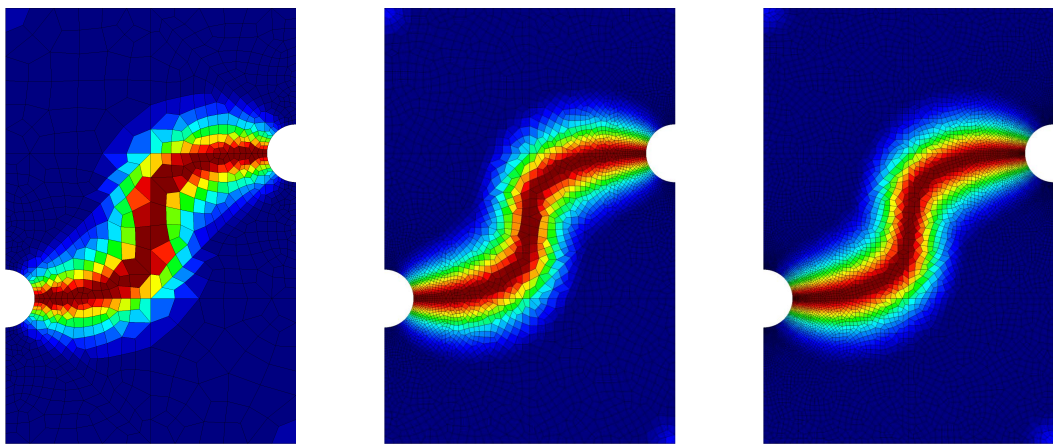


Figure 6.61: Model III [LAP]: Distribution of $f(d)$ for the double-notched plate with 986, 5064, and 10161 unstructured elements (left to right) at the last loading step with $\dot{u} = 15.00 \times 10^{-6}$ mm/s, $r_1 = 1$ MPa and $\beta = 0.015$ MPa mm².

6.3.3 Force-Displacement Diagrams for the Double-Notched Plate

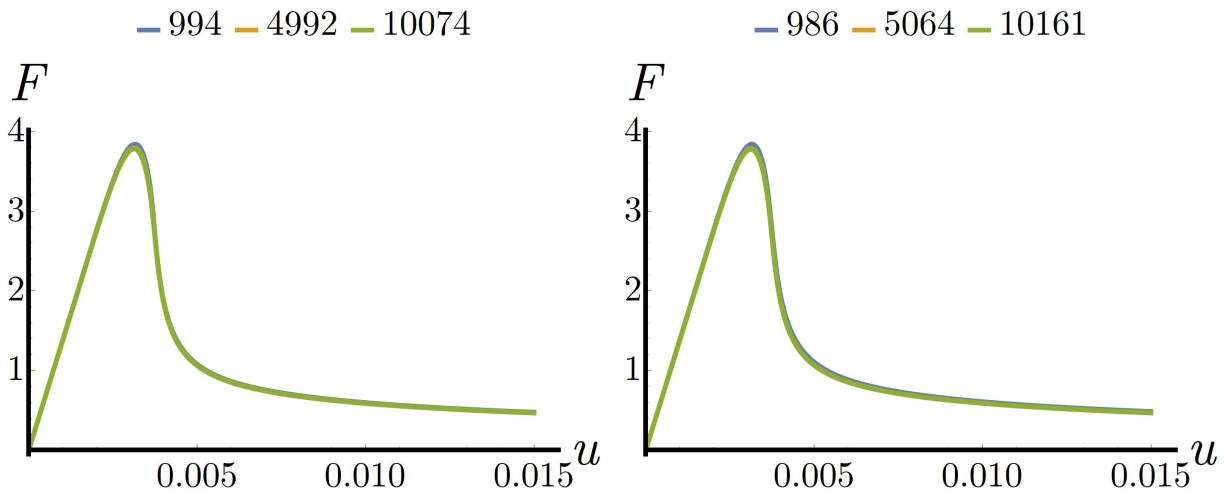


Figure 6.62: Model I [REL]: Structured/unstructured (left/right) elements of stated number.

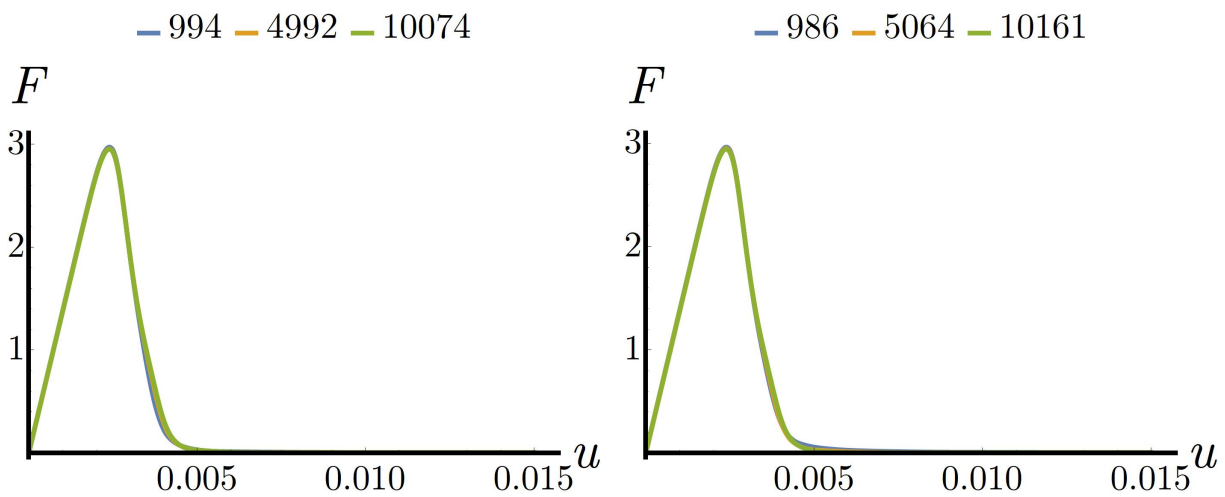


Figure 6.63: Model II [ERVE]: Structured/unstructured (left/right) elements of stated number.

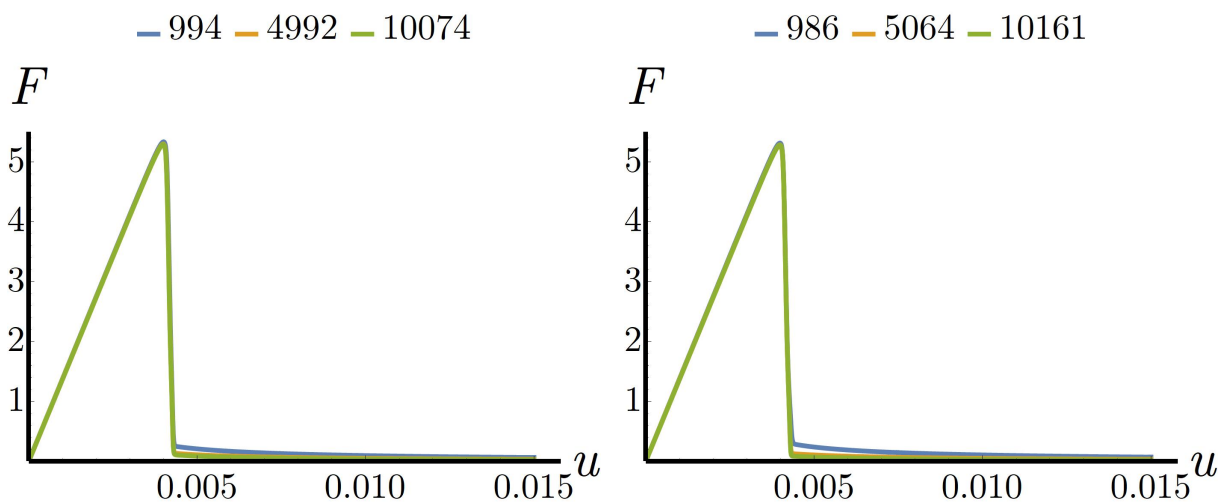


Figure 6.64: Model III [LAP]: Structured/unstructured (left/right) elements of stated number.

6.3.4 Damage Distributions for the Plate with a Centered Hole (Stru. Mesh)

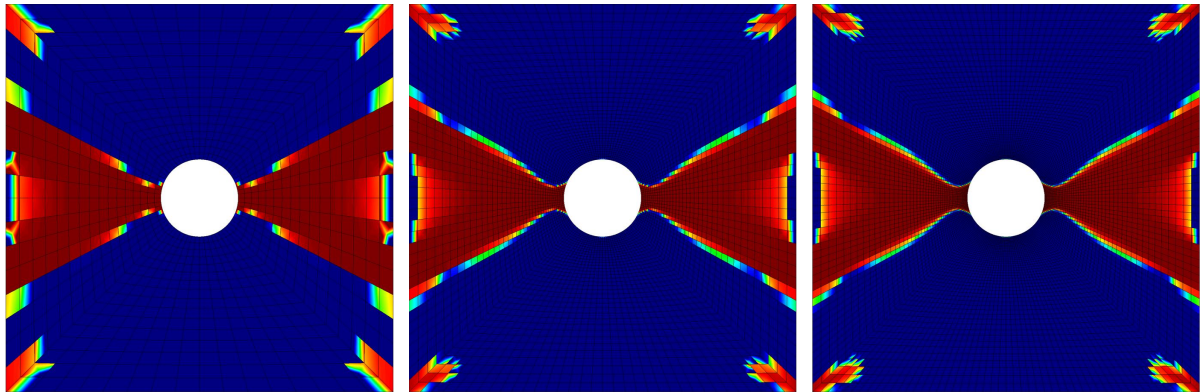


Figure 6.65: Model I [REL]: Distribution of $f(d)$ for the plate with a centered hole with 1024, 5032, and 10000 structured elements (left to right) at the last loading step with $\dot{u} = 15.00 \times 10^{-6}$ mm/s, $r_1 = 200$ MPa, $\beta = 2.0$ and $r_2 = 1.00 \times 10^8$ MPa s.

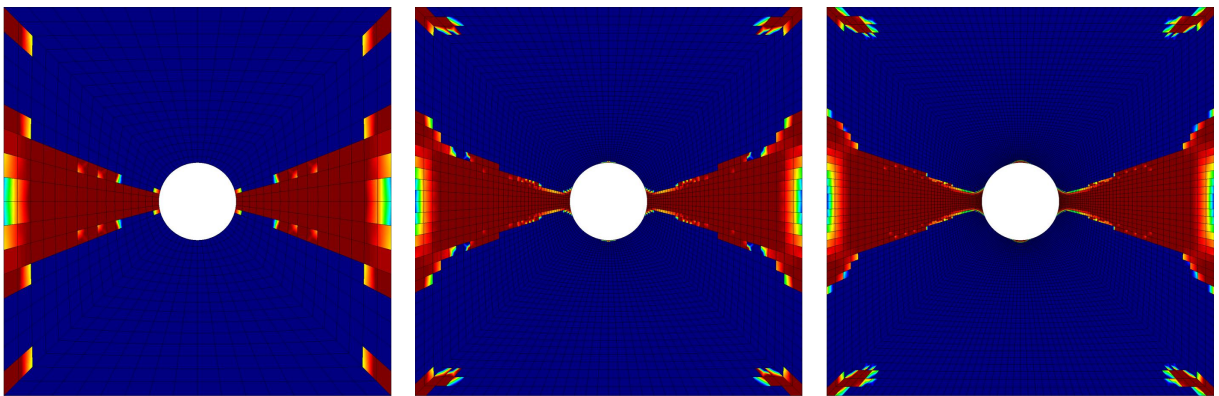


Figure 6.66: Model II [ERVE]: Distribution of $f(d)$ for the plate with a centered hole with 1024, 5032, and 10000 structured elements (left to right) at the last loading step with $\dot{u} = 15.00 \times 10^{-6}$ mm/s, $r_1 = 1$ MPa, $n = 20$ and $\alpha = 500$ 1/(N mm).

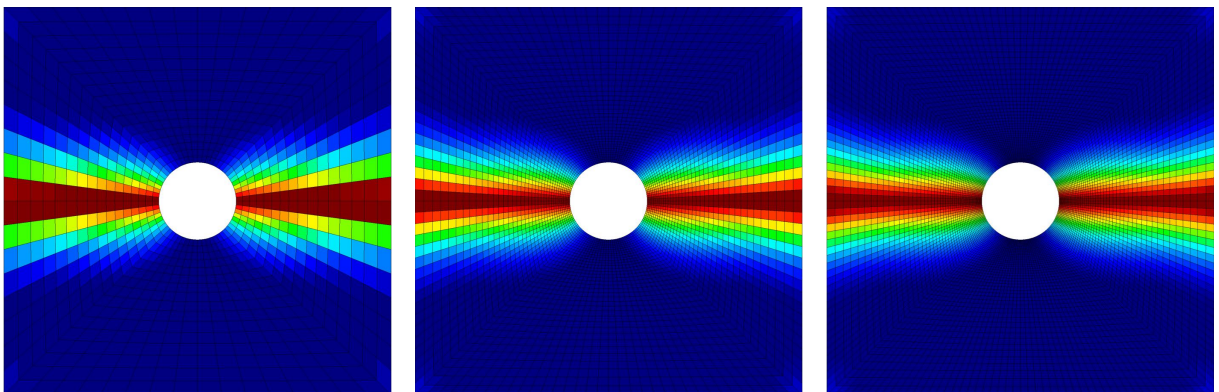


Figure 6.67: Model III [LAP]: Distribution of $f(d)$ for the plate with a centered hole with 1024, 5032, and 10000 structured elements (left to right) at the last loading step with $\dot{u} = 15.00 \times 10^{-6}$ mm/s, $r_1 = 1$ MPa and $\beta = 0.015$ MPa mm².

6.3.5 Damage Distributions for the Plate with a Centered Hole (Unstru. Mesh)

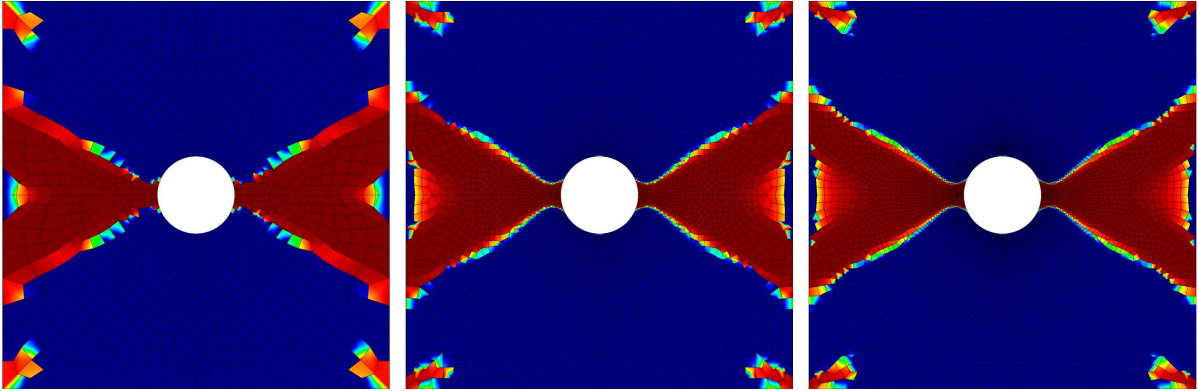


Figure 6.68: Model I [REL]: Distribution of $f(d)$ for the plate with a centered hole with 996, 5090, and 10140 unstructured elements (left to right) at the last loading step with $\dot{u} = 15.00 \times 10^{-6}$ mm/s, $r_1 = 200$ MPa, $\beta = 2.0$ and $r_2 = 1.00 \times 10^8$ MPa s.

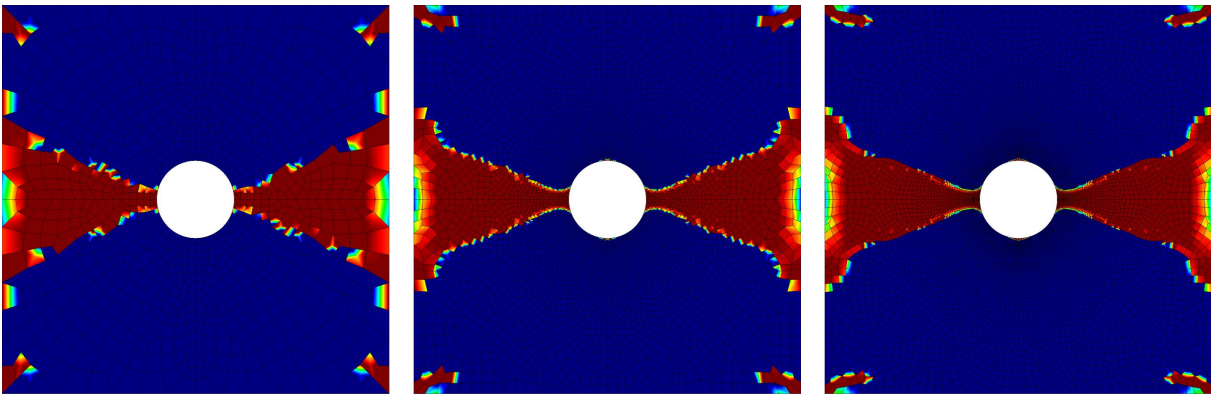


Figure 6.69: Model II [ERVE]: Distribution of $f(d)$ for the plate with a centered hole with 996, 5090, and 10140 unstructured elements (left to right) at the last loading step with $\dot{u} = 15.00 \times 10^{-6}$ mm/s, $r_1 = 1$ MPa, $n = 20$ and $\alpha = 500$ 1/(N mm).

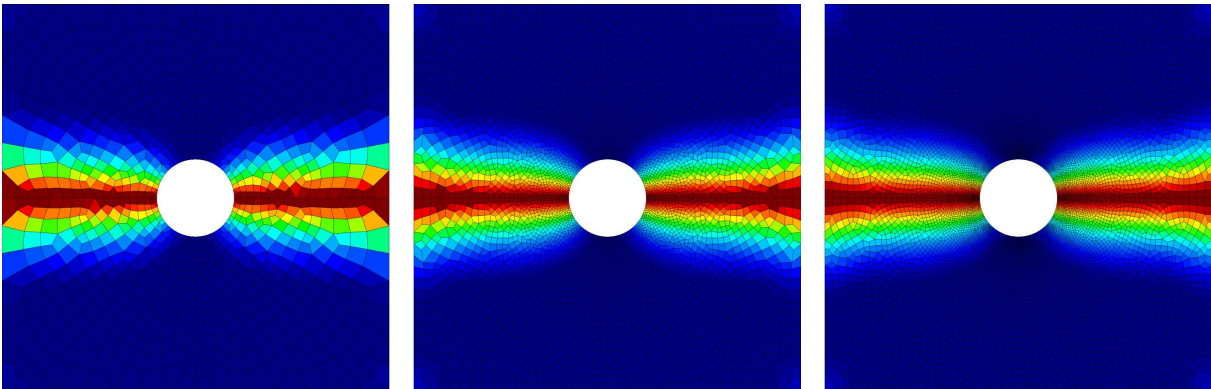


Figure 6.70: Model III [LAP]: Distribution of $f(d)$ for the plate with a centered hole with 996, 5090, and 10140 unstructured elements (left to right) at the last loading step with $\dot{u} = 15.00 \times 10^{-6}$ mm/s, $r_1 = 1$ MPa and $\beta = 0.015$ MPa mm².

6.3.6 Force-Displacement Diagrams for the Plate with a Centered Hole

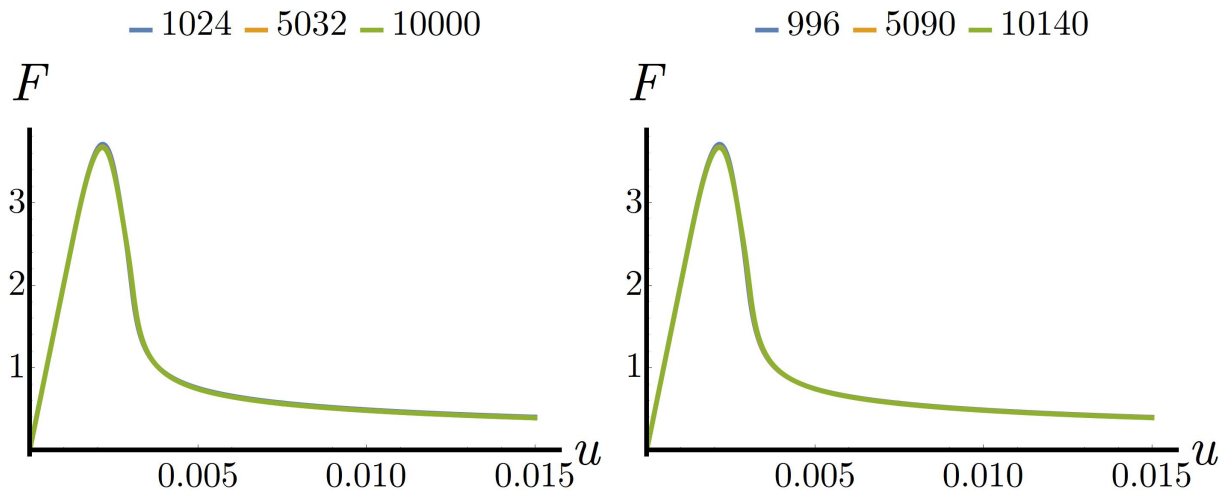


Figure 6.71: Model I [REL]: Structured/unstructured (left/right) elements of stated number.

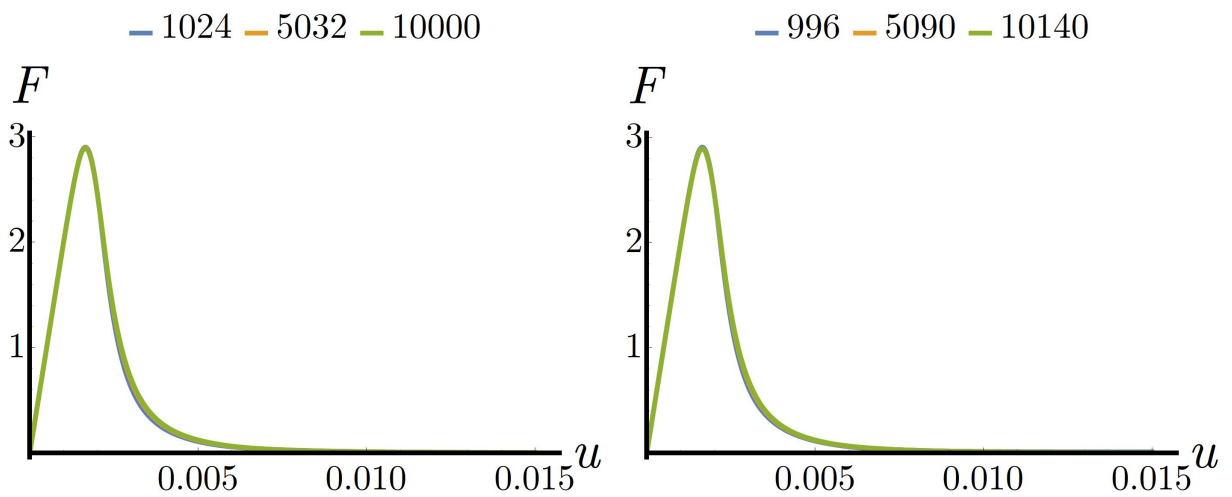


Figure 6.72: Model II [ERVE]: Structured/unstructured (left/right) elements of stated number.

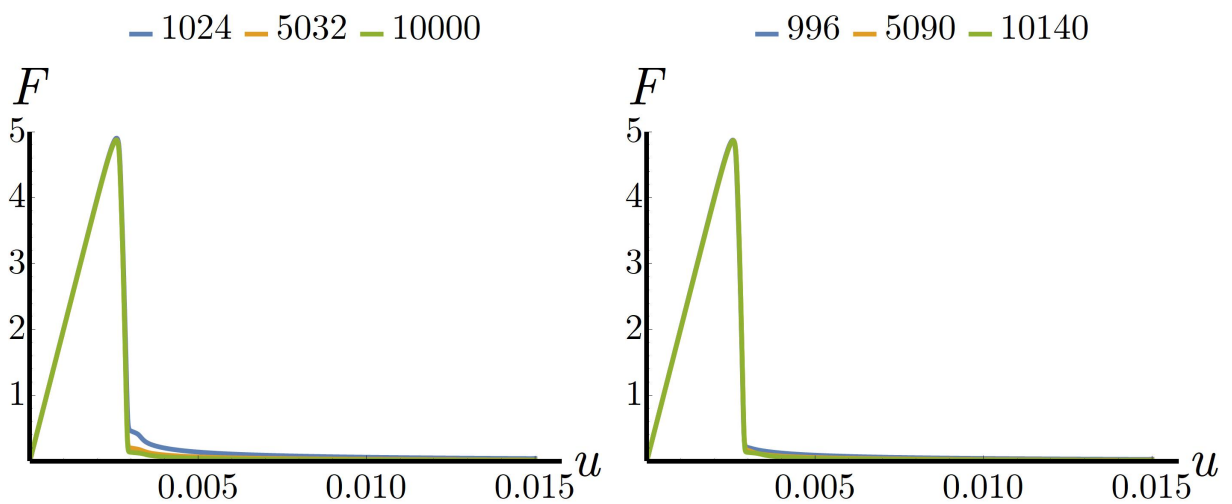


Figure 6.73: Model III [LAP]: Structured/unstructured (left/right) elements of stated number.

6.3.7 Damage Distributions for the Cracked Plate (Stru. Mesh)

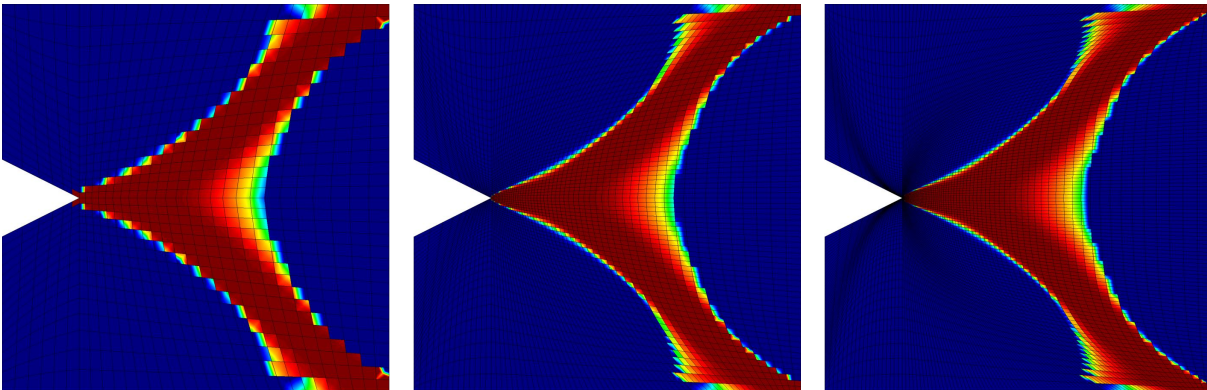


Figure 6.74: Model I [REL]: Distribution of $f(d)$ for the cracked plate with 1024, 4970, and 10000 structured elements (left to right) at the last loading step with $\dot{u} = 15.00 \times 10^{-6}$ mm/s, $r_1 = 200$ MPa, $\beta = 2.0$ and $r_2 = 1.00 \times 10^8$ MPa s.

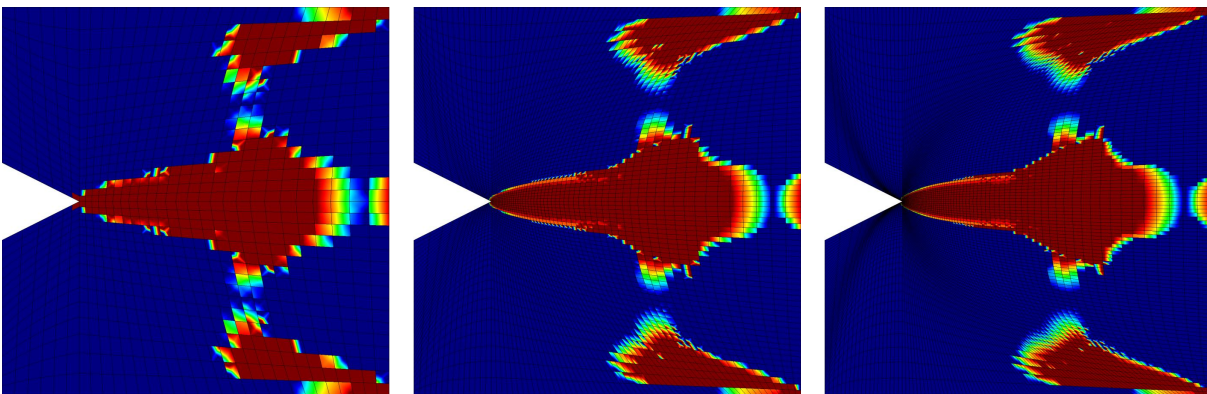


Figure 6.75: Model II [ERVE]: Distribution of $f(d)$ for the cracked plate with 1024, 4970, and 10000 structured elements (left to right) at the last loading step with $\dot{u} = 15.00 \times 10^{-6}$ mm/s, $r_1 = 1$ MPa, $n = 20$ and $\alpha = 500$ 1/(N mm).

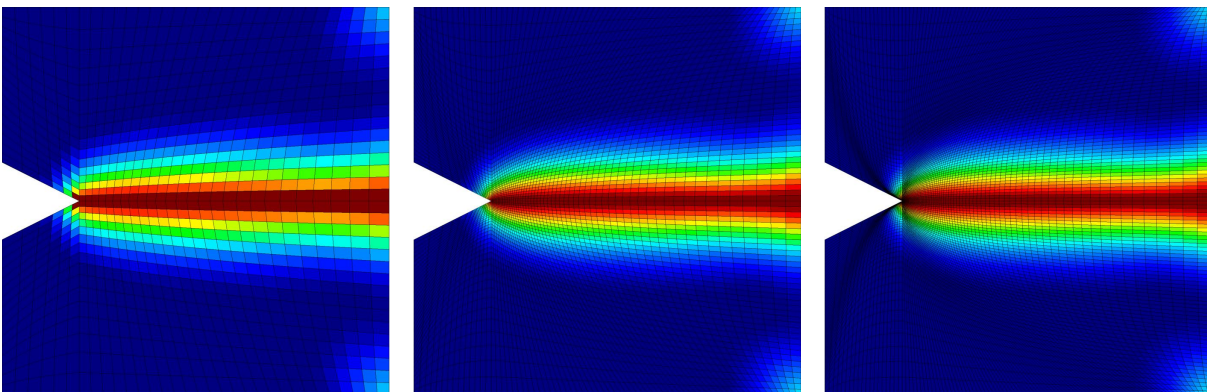


Figure 6.76: Model III [LAP]: Distribution of $f(d)$ for the cracked plate with 1024, 4900, and 10000 structured elements (left to right) at the last loading step with $\dot{u} = 15.00 \times 10^{-6}$ mm/s, $r_1 = 1$ MPa and $\beta = 0.015$ MPa mm².

6.3.8 Damage Distributions for the Cracked Plate (Unstru. Mesh)

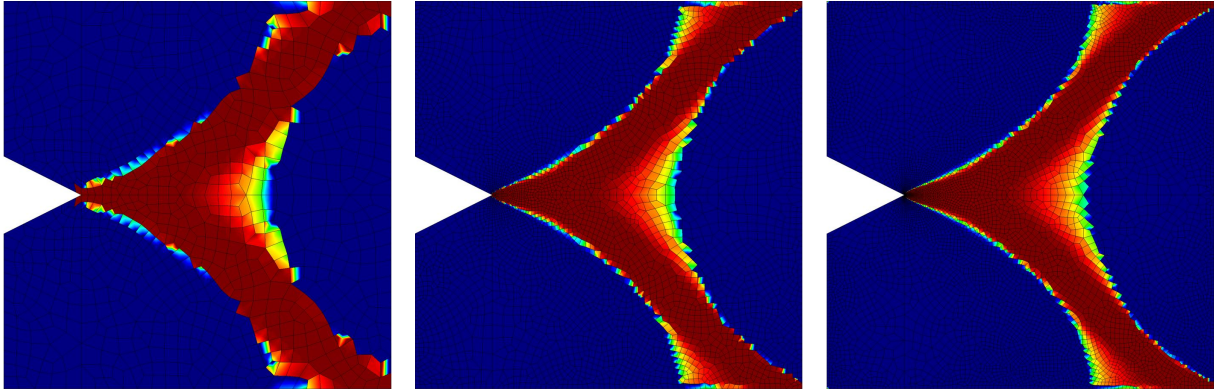


Figure 6.77: Model I [REL]: Distribution of $f(d)$ for the cracked plate with 1007, 5001, and 10040 unstructured elements (left to right) at the last loading step with $\dot{u} = 15.00 \times 10^{-6}$ mm/s, $r_1 = 200$ MPa, $\beta = 2.0$ and $r_2 = 1.00 \times 10^8$ MPa s.

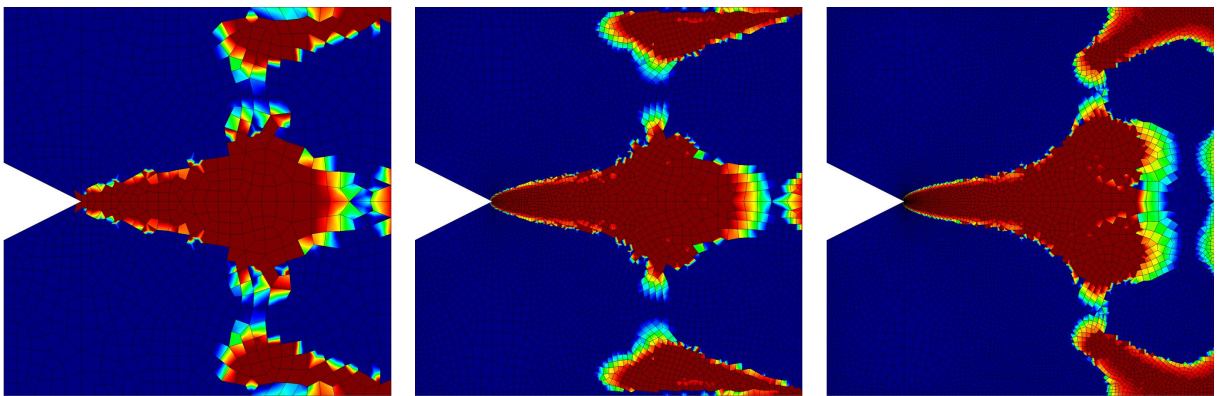


Figure 6.78: Model II [ERVE]: Distribution of $f(d)$ for the cracked plate with 1007, 5001, and 10040 unstructured elements (left to right) at the last loading step with $\dot{u} = 15.00 \times 10^{-6}$ mm/s, $r_1 = 1$ MPa, $n = 20$ and $\alpha = 500$ 1/(N mm).

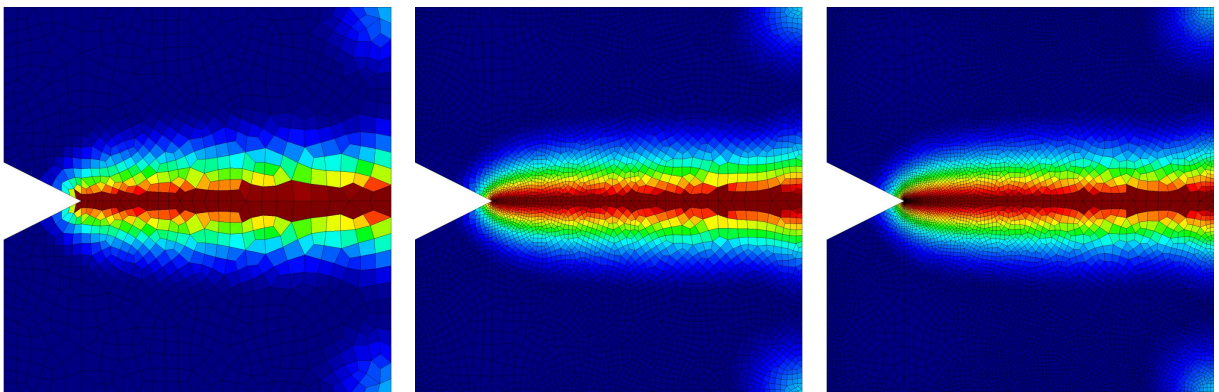


Figure 6.79: Model III [LAP]: Distribution of $f(d)$ for the cracked plate with 1007, 4896, and 10040 unstructured elements (left to right) at the last loading step with $\dot{u} = 15.00 \times 10^{-6}$ mm/s, $r_1 = 1$ MPa and $\beta = 0.015$ MPa mm².

6.3.9 Force-Displacement Diagrams for the Cracked Plate

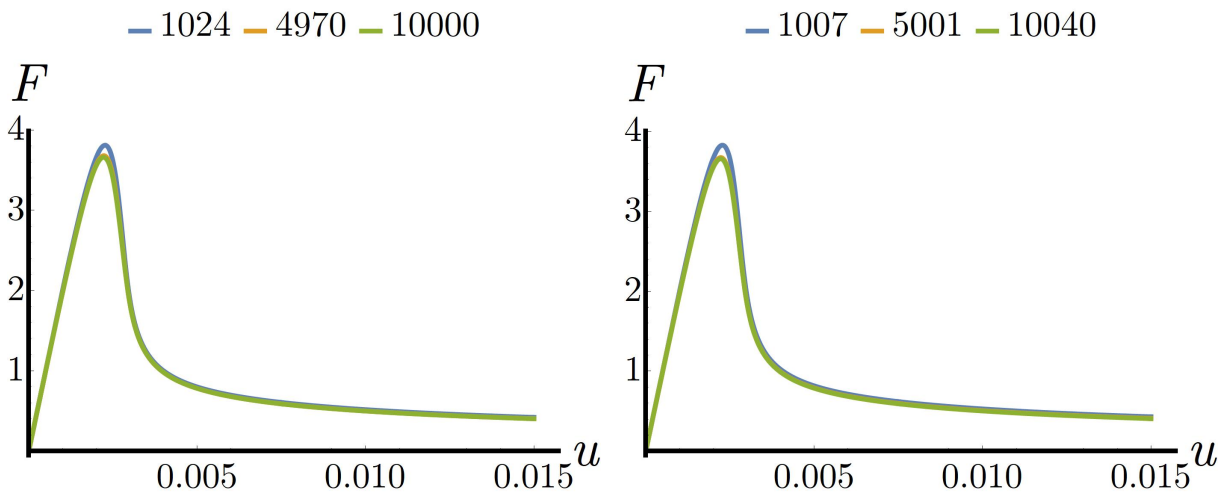


Figure 6.80: Model I [REL]: Structured/unstructured (left/right) elements of stated number.

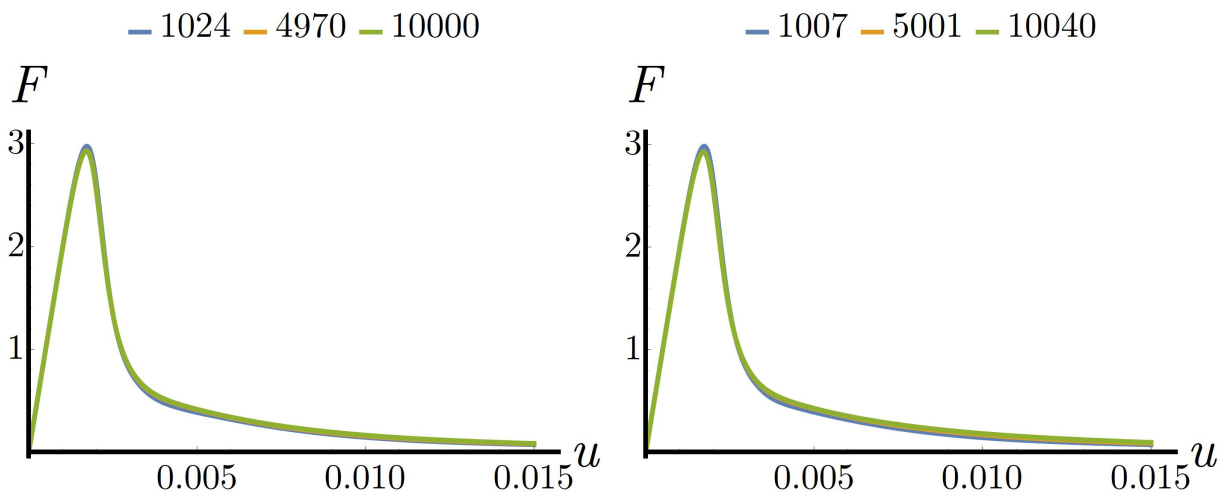


Figure 6.81: Model II [ERVE]: Structured/unstructured (left/right) elements of stated number.

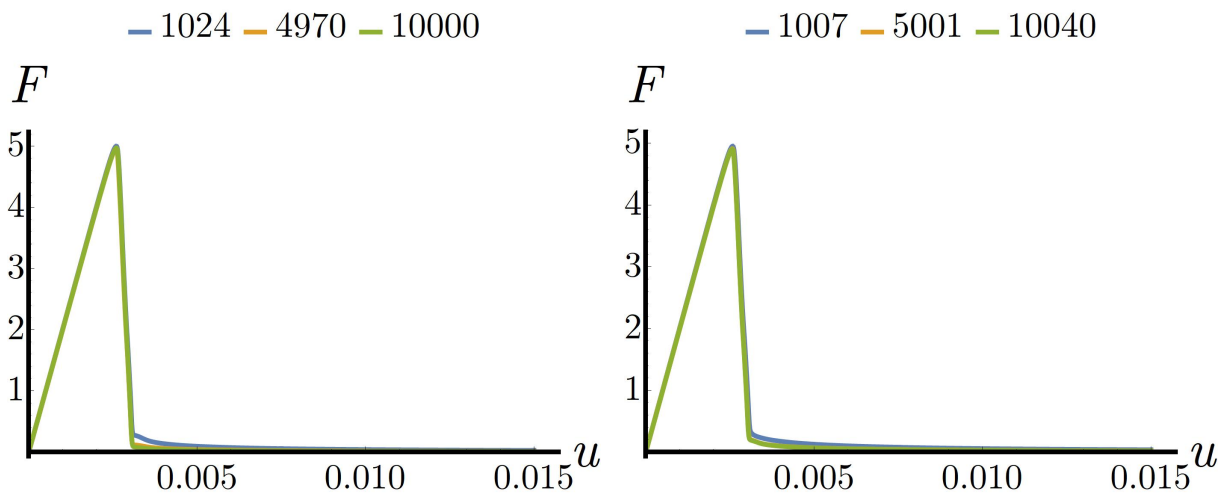


Figure 6.82: Model III [LAP]: Structured/unstructured (left/right) elements of stated number.

6.4 Investigation of Computation Times

This section is concerned with the computation times for the double-notched plate with unstructured elements. The three damage models introduced in Chapter 4 are compared including a comparison to purely elastic calculations. Hereby, Table 6.1 provides the absolute values of the measured computation times whereas Table 6.2 provides the values that are normalized with respect to the elastic case. All calculations were performed individually under same conditions on an overclocked Intel Core i7-2600K processor with 4430 MHz.

		purely elastic	localized damage	diffusive damage
Model I [REL]	986 elements	85 s	321 s	270 s
	10161 elements	5621 s	41240 s	13296 s
Model II [ERVE]	986 elements	85 s	394 s	349 s
	10161 elements	5621 s	23813 s	17793 s
Model III [LAP]	986 elements	85 s	85 s	87 s
	10161 elements	5621 s	5658 s	5708 s

Table 6.1: Absolute computation times for the double-notched plate with unstructured elements.

First of all, it should be mentioned that Model I [REL] and Model II [ERVE] are formulated at the material point level whereas Model III [LAP] is formulated at the element level without evaluating the material points for the main calculations. This reduction to the element-level is accordingly accompanied by numerical advantages at costs of a slightly decreasing accuracy. Finally comparing the computation times yields to interesting observations.

		purely elastic	localized damage	diffusive damage
Model I [REL]	986 elements	1.0	3.8	3.2
	10161 elements	1.0	7.6	2.5
Model II [ERVE]	986 elements	1.0	4.6	4.1
	10161 elements	1.0	4.4	3.3
Model III [LAP]	986 elements	1.0	1.0	1.0
	10161 elements	1.0	1.0	1.1

Table 6.2: Normalized computation times for the double-notched plate with unstructured elements.

Although Model III [LAP] is formulated at the element level only, the computation speed is an remarkable advantage. This speed of computations is almost equal to the purely elastic

calculations which is due to the fact that the main computational effort is done only once in the beginning of the calculation. Afterwards, the effort is almost comparable to the elastic case. In the context of the diffusive damage case, the computation times are slightly higher which results from the larger regularization parameter β causing more iteration steps at the element level. Since the material tangent is constant due to the operator split, the numbers of iterations for the finite element calculation are always the same (2000 in the present case of 1000 loading increments). Differences regarding the convergence can only be observed by means of the iterations at the element level for calculating the updated damage function (without displacements). In this regard, the following point was noticed: for the coarse mesh 3069 total iteration steps were required for the localized case in contrast to 7912 for the diffusive case, respectively 28317 to 143522 steps for the fine mesh. The increase from the coarse to the fine mesh has the same reason like the increase from localized to brittle damage: the range of the neighborhood consideration is limited to only one element around the considered central element and the influence can only be passed by iteration steps. Therefore, the number of iteration steps directly depends on the internal length scale defined by β and furthermore by the number of elements included within this defined area around the central element which is of course higher for finer meshes.

In comparison to that, Model I [REL] needs about 2.5 to 3.8 times more computation time than for the elastic case. In case of the localized damage and the fine mesh, the longer computation time with a factor of 7.6 should be considered separately, since a more robust and expensive solver, which is able to handle asymmetrical tangents as well, has been used in order to handle numerical instabilities. However, this is a further disadvantage of course. Generally, the localized calculations takes more time than the diffusive ones since more iterations for the finite element calculations were required: the coarse mesh needed 2828 total iteration steps for the localized case in contrast to 2290 for the diffusive case, and for the fine mesh the relation was 3390 to 2335. The increase of iteration steps with more localized results stems from a higher numerical effort since the localization is more critical due to less viscous effects which certainly are fundamental for the model.

The computation times for Model II [ERVE] are slightly higher than for the previous model with a factor of about 3.3 to 4.6 compared to the elastic case. In regard to the number of iteration steps basically the same observations can be made as before: the coarse mesh required 3517 total iteration steps for the localized case in contrast to 3026 for the diffusive case, the relation for the fine mesh was 4223 to 3123. Therefore, again more iterations are needed for the localized case than for the diffusive one due to the mentioned higher numerical effort.

Altogether, Model III [LAP] clearly is the fastest damage model and almost on the same level as purely elastic calculations. Localized results are even in advantage to the diffusive ones. Model I [REL] is slightly faster than Model II [ERVE]. However, both are about 4 times slower than Model III [LAP], which actually is still very fast. In the work of Junker et al. (2018), a comparison of Model III [LAP] to the well-established gradient-enhanced damage model by Dimitrijevic and Hackl (2008) was done by means of a comparable double-notched geometry with an equal number of loading increments of 1000. This investigation showed that the comparative gradient-enhanced model required about ten times more computation time than Model III [LAP]. Accordingly, Model I [REL] and Model II [ERVE] require less than half the time of this established model. Besides that, Model I [REL] occasionally struggles with numerical instabilities in context of the localized calculations. Therefore, it is partly necessary to use a more robust solver, which increases the computation times.

7 Discussion of Models and Comparison

In this chapter the finite element results and the model comparisons are discussed. Hereto, the localized damage characteristics from Section 6.2 as well as the diffusive case from Section 6.3 are considered. Moreover, the computation times provided in Section 6.4 are taken into account. Further information on the models based on Chapter 4 are provided as well.

7.1 Discussion of Model I

Model I [REL] is implemented at material point level and can thus easily be applied to conventional/commercial finite element software. Furthermore, the implementation of the underlying set of model equations as well as the material tangent is straightforward. The overall finite element results are mesh-independent for most cases.

Unfortunately, the formulation of the damage model is rate-dependent which restricts the model to specific materials or applications. Particularly, considering common materials such as steels or concretes can be difficult. Additionally, this formulation is sensitive in terms of boundary effects resulting in unexpected damage distributions for the diffusive damage characteristics. In contrast to that, the model predicts cracks that are relatively thick and a further decrease of the width of the cracks leads to numerical instabilities or less mesh-independent results. As stated earlier, the model requires a minimum amount of viscosity that obviously exceeds the possibility of illustrating thinner cracks for the present conditions. Besides, the drops in the force-displacement curves are not very steep and non-zero forces are observed after failure. These non-zero forces actually contradict the assumption of failed material, for the localized and diffusive case. The localized calculations are accompanied by numerical instabilities in some cases that require a more robust solver. This leads in turn to increasing numerical efforts, which is only moderate anyways. Altogether, this model seems to be more suitable for calculations somewhere inbetween the localized and the diffusive case maybe.

7.2 Discussion of Model II

Originally, a rate-dependent formulation was utilized for Model II [ERVE]. On this basis, it was extended to rate-independence. For this reason, this model is not restricted to specific materials or applications. If needed, the rate-dependence can be considered at any time, which of course also applies for Model III [LAP] by slightly modifying the dissipation function. Moreover, the implementation of Model II [ERVE] is done at material point level which allows for a simple implementation to conventional/commercial finite element software. The model is mainly suitable for localized damage characteristics due to its ability to provide very thin and also sharp cracks without considerable transition zones between undamaged and damaged material. Hereby, the global responses approach zero forces after the drops. This is in agreement with

physical expectations. Furthermore, the results show a mesh-independent behavior which is satisfactory also in extreme cases and the calculations are numerically stable.

However, the formulation of the model is quite sensitive with respect to boundary effects and therefore numerical results in context of diffusive damage characteristics provide unexpectedly shaped damage zones. This could be improved or prevented by assuming different boundary conditions or larger distances between the damaged area and the boundaries. For the localized damage characteristics, the drops of the force-displacement curves are not as steep as expected from a physical point of view. Besides that, the implementation of the material tangent is relatively complicated. Finally, the computation times are only moderate, but there is potential for further improvements such as considering less subdomains.

7.3 Discussion of Model III

Model III [LAP] has a rate-independent formulation and is therefore not restricted to specific materials or applications. The computation times are extremely fast and almost on the same level as purely elastic calculations. Furthermore, the model can be customized to versatile applications due to its ability to provide localized as well as diffusive damage characteristics. The model does not show any problems with respect to boundary effects or numerical instabilities. The presented finite element results exhibit perfect mesh-independence. Even extreme cases yield satisfactory results. Thereby, the damage distribution could be adjusted to very thin cracks, which satisfies physical expectations for brittle damage, but also to more diffusive damage distributions for ductile-like damage. For the latter case the smooth transition zones between undamaged and damaged material can be interpreted as plastic zones evolving in front or around the crack tip. This model provides an extremely steep force-displacement drop after the peak as expected in context of brittle damage. Thereby, the curves approach zero forces, which corresponds to a completely failed material. Moreover, the material tangent is very simple because it is constant.

On the contrary, the implementation is done at the element level and complex routines for the neighborhood relations and the Laplace operator are required. Therefore, the implementation into some finite element software could be complicated. However, this only has to be done once. The physical interpretation of the smooth transition zones is problematic in context of assuming brittle damage, for which the model is actually more suitable due to its steep displacement-curves and also due to the ability of providing very thin cracks. However, these transition zones are a typical property when involving gradient formulations and since they do not affect the global responses in any negative way, they probably can just be accepted.

7.4 Comparative Discussion and Final Remarks

Important advantages of Model I [REL] can unfortunately neither be found for the localized nor for the diffusive damage characteristics. The behavior of the model is always accompanied by several restrictions and/or disadvantages. Actually, the formulation of the model itself is a disadvantage compared to the other models due to its limitation to rate-dependence. Occasional numerical instabilities in the context of localized damage and unexpected damage distributions due to sensitivities with respect to the boundary effects further restrict the model. The simple

implementation and moderate computation times do not justify the application of the model, at least in its current form and compared to the other models investigated in this thesis. Several modifications would be required to improve the model, which would be desirable, since the simple implementation allows for an easy application and versatile enhancements, in general. Incidentally, some improvements have already been implemented by Langenfeld et al. (2018). Apart from that, the model might possibly be better suited to damage characteristics somewhere inbetween the localized and diffusive considered cases. Then, the occurring cracks are not expected to be very thin anymore and at the same time the boundary conditions do not have a considerable impact on the results. However, the question is whether another of the subsequent damage models would not be a better choice.

For the aforementioned reasons, the remaining interesting damage models in the present consideration are Model II [ERVE] and Model III [LAP]. Originating from completely different ideas and approaches, in the end both damage models are able to provide excellent mesh-independent finite element results. Moreover, both formulations are rate-independent and therefore unrestricted. Furthermore, they are numerically stable which allows for very thin cracks. The dropped force-displacement curves approach zero values as expected for failed material. However, besides some minor points, there are some main differences between both models. Due to unexpected damage zones in case of diffusive characteristics and also very sharp transition zones between undamaged and damaged material, Model II [ERVE] is basically limited in the present consideration to localized behavior, which is certainly the more interesting case for crack propagation. Furthermore, the model is characterized by moderate computation times only. The implementation is very simple and universally applicable due to its formulation at material point level. In contrast to that, Model III [LAP] requires a more demanding implementation due to its formulation at the element level and due to complex routines for the determination of the neighborhood relations and Laplacian. Furthermore, the smooth transition zones are questionable depending on the respective application. On the other hand, the computation times are paramount and the force-displacement drops are the steepest complying with expectations in regard to brittle damage.

In the end, the most suitable choice depends in the particular application. In many cases Model III [LAP] would be preferred particularly because of its enormous computation efficiency advantage. Thereby, the implementation is more complicated. However, this disadvantage is not of high importance. In case of restrictions due to the finite element software or when requesting sharp transitions between undamaged and damaged material, Model II [ERVE] would probably be the better choice. It should thereby be underlined, that the moderate computation times of Model II [ERVE] but also of Model I [REL] are still very fast in comparison to other established regularized damage models from the literature as explained in more detail in Section 6.4 comparing the computation times.

8 Conclusions

8.1 Summary

Throughout this thesis, three novel and efficient approaches for the regularization of thermodynamically consistent damage models have been introduced. Having established the theoretical and algorithmic framework, the characteristics of each damage model are explained in detail. Hereto, finite element calculations have been performed and the results been discussed in order to compare the different approaches.

First of all, a brief review over the applied models is provided. The first damage model, denoted by Model I [REL], is based on an energy relaxed formulation and on two-phase damage modeling. Viscous effects are required to obtain mesh-independence after introducing the non-linear homogenization between the undamaged and damaged states. This allows for the overall damage softening behavior. Moreover, the second damage model, denoted by Model II [ERVE], is also based on energy relaxation. However, in contrast to Model I [REL], the main idea is related to rate-limitation as well as describing the assumed microstructure by an emulated representative volume element, which is called ERVE. Finally, the third damage model, denoted by Model III [LAP], has a gradient-enhanced formulation, where the Laplace operator is efficiently involved by means of an inverted Taylor series. All damage models were derived based on the Hamilton's principle or the principle of the minimum of the dissipation potential, respectively. This ensures thermodynamical consistence. Furthermore, the related determinations of stresses and material tangents are provided as well as algorithms for implementation.

Afterwards, parameter identifications have been performed for the respective damage models including several parameter studies. Here, the influence and effects of the regularization or related parameters have been investigated as well as the behavior under varying loading rates. The final parameter sets determined have then been applied for the main finite element calculations. Hereby, the following three boundary value problems have been investigated: the double-notched beam, the plate with a centered hole, and the cracked plate. Besides that, the initial situation without any regularization as well as the localized and diffusive damage characteristics have also been involved for the investigations.

The numerical simulations revealed interesting findings in regard to the behavior of the models but also to their respective advantages and disadvantages. In regard to Model I [REL] the drawbacks obviously are paramount, since restrictions or disadvantages can be found for basically all intents and purposes. The formulation is rate-dependent and the model is consequently restricted to specific materials or applications only. Occasional instabilities occur as well as relatively thick damage distributions in context of localized damage characteristics. In contrast, diffusive damage characteristics are accompanied by influences due to boundary effects leading to unexpected damage distributions. Furthermore, the force-displacement curves do not drop to zero as expected for failed material and the computation times are only moderate in comparison to the considered damage models in this thesis. Nevertheless, these times are still lower in comparison to many existing regularized damage models which can be found in the literature.

For the aforementioned reasons, the other two regularized damage models are preferred. Interestingly, the initial concepts of Model II [ERVE] and Model III [LAP] completely differ. However, both rate-independent and thus unrestricted models provide perfect mesh-independent finite element results including force-displacement curves that drop to zero and very thin propagating cracks can be observed. Besides that, Model II [ERVE] was strongly influenced by the boundary conditions in case of diffusive damage characteristics leading to unexpected damage distributions. Moreover, the model is characterized by moderate calculations times and is a little less efficient than Model I [REL]. However, these moderate computation times are still lower than the computation times of other well-established damage models. On the contrary, the very sharp transitions zones between undamaged and damaged material complies with assumptions related to brittle damage behavior for which this model's application is obviously better suited. Additionally, the implementation of this model is straightforward and its application flexible due to the formulation at the material point level. In contrast to that, Model III [LAP] is much more efficient in terms of computation times. The latter are almost comparable to linear elastic finite element calculations. Furthermore, this model provides the steepest drops of the global structural responses which is desirable in context of brittle damage. Of course, there are drawbacks to be mentioned, as well: the implementation of the model is more difficult due to the formulation at the element level and the complex routines for the neighborhood relations and the Laplace operator. Moreover, the typical smooth transition zones in context of gradient-enhanced formulations are questionable in context of brittle damage characteristics.

Three novel damage models with different regularization strategies have been presented. Satisfactory mesh-independent behavior has been demonstrated and advantages compared to other existing models have been emphasized. The relaxation based two-phase Model I [REL] is accompanied by several restrictions and disadvantages in comparison to the other presented models. Thus, Model I [REL] is not preferred. The microstructure-emulating Model II [ERVE] was especially suitable for localized damage characteristics corresponding to brittle damage behavior due to sharp transition zones between undamaged and damaged material. Furthermore, it is easy to implement within the finite element framework. Model III [LAP], which very efficiently evaluates the Laplace operator by a more complex implementation, provides paramount computation times almost approaching the speed of purely elastic calculations.

8.2 Additional and Future Research

In this thesis different novel aspects related to regularized damage modeling in the context of localized and diffusive damage characteristics have been addressed. Based on the findings described in Chapters 6 and 7, several extensions might be done in future work. First, a parameter fitting to experimental data is crucial to examine the applicability and accuracy of the respective models. Furthermore, the extension to elasto-plasticity improves the capability to describe the evolving zones in front/around the crack tip, consequently the diffusive damage characteristics are superfluous. Recently, plasticity-enhanced versions have been published by Schwarz et al. (2018b) and Hoormazdi et al. (2019). Moreover, taking into account adaptivity of the mesh as well as the loading rates significantly improves the behavior of the model in terms of steep force-displacement drops and allow for an extremely sharp crack propagation. This has already been implemented for Model III [LAP] in cooperation with the working group High Performance Computing in the Engineering Sciences at the Ruhr-Universität Bochum providing promising first results, see work of Vogel and Junker (2019).

In regard to Model I [REL], further modifications are desirable in order to facilitate zero forces of the global responses describing completely failed material. Also, a decrease of the influences of the boundary conditions is an objective of future work. Furthermore, finding a possibility to come up with a rate-independent formulation while maintaining mesh-independence would be preferable. Incidentally, zero driving forces have already been achieved by a model enhancement in the work of Langenfeld et al. (2018). Moreover, also Model II [ERVE] could further be improved by faster computation times, for example. Hereto, more investigations might be dedicated to the number of subdomains providing a compromise between mesh-independence and speed. Improvements are also conceivable for Model III [LAP], for example the number of iterations at the element level could significantly be reduced accompanied by even faster computation times by considering more neighbored element at the same time. This is inspired by meshless methods and first investigations are currently in progress.

A Appendix - Additional Derivations to Model I

Material Tangent for Rate-Independent Case

The determination of the material tangent for the rate-independent case of Model I [REL], related to Subsections 4.2.1 and 4.2.2, is based on preceded derivations in Subsection 4.2.4. Thereby, Equation (4.53) provides the following general formulation for the material tangent

$$\left. \frac{d\tilde{\sigma}}{d\tilde{\epsilon}} \right|^{m+1} = \left. \frac{\partial\tilde{\sigma}}{\partial\tilde{\epsilon}} \right|^m + \left. \frac{\partial\tilde{\sigma}}{\partial d} \right|^m \otimes \left. \frac{\partial d}{\partial\tilde{\epsilon}} \right|^{m+1}, \quad (\text{A.1})$$

in which the derivative of the damage variable $(\partial d / \partial \tilde{\epsilon})|^{m+1}$ has to be determined depending on the respective case. For the present rate-independent case the evolution equation is given by

$$d^{m+1} = d^m + \Delta\rho p(\tilde{\epsilon}^{m+1}, d^m), \quad (\text{A.2})$$

including the consistency parameter $\Delta\rho$ that is depending on the current strains

$$\Delta\rho = \Delta\rho(\tilde{\epsilon}^{m+1}). \quad (\text{A.3})$$

The derivative of the evolution equation is provided by

$$\left. \frac{\partial d}{\partial\tilde{\epsilon}} \right|^{m+1} = \Delta\rho \frac{\partial p(\tilde{\epsilon}^{m+1}, d^m)}{\partial\tilde{\epsilon}^{m+1}} + \frac{\partial\Delta\rho}{\partial\tilde{\epsilon}^{m+1}} p(\tilde{\epsilon}^{m+1}, d^m), \quad (\text{A.4})$$

with

$$\frac{\partial p(\tilde{\epsilon}^{m+1}, d^m)}{\partial\tilde{\epsilon}^{m+1}} = -f'(d^m) \tilde{\mathbb{E}}_0 \cdot \tilde{\epsilon}^{m+1}. \quad (\text{A.5})$$

The derivative of $\Delta\rho$ can not directly be calculated but by taking into account the yield function

$$\Phi = \Phi(\tilde{\epsilon}^{m+1}, d^{m+1}) \quad (\text{A.6})$$

$$= |p(\tilde{\epsilon}^{m+1}, d^{m+1})| - r_1 \stackrel{!}{=} 0 \quad (\text{A.7})$$

$$= |p(\tilde{\epsilon}^{m+1}, d^m + \Delta\rho p(\tilde{\epsilon}^{m+1}, d^m))| - r_1 \stackrel{!}{=} 0, \quad (\text{A.8})$$

and taking the derivative of the yield function leads to

$$\frac{d\Phi}{d\tilde{\epsilon}^{m+1}} = \frac{\partial\Phi}{\partial\tilde{\epsilon}^{m+1}} + \frac{\partial\Phi}{\partial\Delta\rho} \frac{\partial\Delta\rho}{\partial\tilde{\epsilon}^{m+1}} \stackrel{!}{=} 0. \quad (\text{A.9})$$

Now, solving for the wanted derivative of $\Delta\rho$ yields

$$\frac{\partial\Delta\rho}{\partial\tilde{\epsilon}^{m+1}} = - \left(\frac{\partial\Phi}{\partial\Delta\rho} \right)^{-1} \frac{\partial\Phi}{\partial\tilde{\epsilon}^{m+1}}, \quad (\text{A.10})$$

including the straightforwardly determinable terms

$$\frac{\partial \Phi}{\partial \Delta \rho} = \frac{p(\tilde{\boldsymbol{\varepsilon}}^{m+1}, d^{m+1})}{|p(\tilde{\boldsymbol{\varepsilon}}^{m+1}, d^{m+1})|} \frac{\partial p(\tilde{\boldsymbol{\varepsilon}}^{m+1}, d^{m+1})}{\partial d^{m+1}} \frac{\partial d^{m+1}}{\partial \Delta \rho} \quad (\text{A.11})$$

$$= -\frac{p(\tilde{\boldsymbol{\varepsilon}}^{m+1}, d^{m+1})}{|p(\tilde{\boldsymbol{\varepsilon}}^{m+1}, d^{m+1})|} \frac{1}{2} f''(d^{m+1}) \tilde{\boldsymbol{\varepsilon}}^{m+1} \cdot \tilde{\mathbb{E}}_0 \cdot \tilde{\boldsymbol{\varepsilon}}^{m+1} p(\tilde{\boldsymbol{\varepsilon}}^{m+1}, d^m), \quad (\text{A.12})$$

and

$$\begin{aligned} \frac{\partial \Phi}{\partial \tilde{\boldsymbol{\varepsilon}}^{m+1}} &= \frac{p(\tilde{\boldsymbol{\varepsilon}}^{m+1}, d^{m+1})}{|p(\tilde{\boldsymbol{\varepsilon}}^{m+1}, d^{m+1})|} \left(\frac{\partial p(\tilde{\boldsymbol{\varepsilon}}^{m+1}, d^{m+1})}{\partial \tilde{\boldsymbol{\varepsilon}}^{m+1}} \right. \\ &\quad \left. + \frac{\partial p(\tilde{\boldsymbol{\varepsilon}}^{m+1}, d^{m+1})}{\partial d^{m+1}} \frac{\partial d^{m+1}}{\partial p(\tilde{\boldsymbol{\varepsilon}}^{m+1}, d^m)} \frac{\partial p(\tilde{\boldsymbol{\varepsilon}}^{m+1}, d^m)}{\partial \tilde{\boldsymbol{\varepsilon}}^{m+1}} \right) \end{aligned} \quad (\text{A.13})$$

$$\begin{aligned} &= \frac{p(\tilde{\boldsymbol{\varepsilon}}^{m+1}, d^{m+1})}{|p(\tilde{\boldsymbol{\varepsilon}}^{m+1}, d^{m+1})|} \tilde{\mathbb{E}}_0 \cdot \tilde{\boldsymbol{\varepsilon}}^{m+1} \left(-f'(d^{m+1}) \right. \\ &\quad \left. + \frac{1}{2} f''(d^{m+1}) \tilde{\boldsymbol{\varepsilon}}^{m+1} \cdot \tilde{\mathbb{E}}_0 \cdot \tilde{\boldsymbol{\varepsilon}}^{m+1} \Delta \rho f'(d^m) \right). \end{aligned} \quad (\text{A.14})$$

These two terms are inserted back into the derivative of $\Delta \rho$ as follows

$$\frac{\partial \Delta \rho}{\partial \tilde{\boldsymbol{\varepsilon}}^{m+1}} = \tilde{\mathbb{E}}_0 \cdot \tilde{\boldsymbol{\varepsilon}}^{m+1} \frac{-f'(d^{m+1}) + \frac{1}{2} f''(d^{m+1}) \tilde{\boldsymbol{\varepsilon}}^{m+1} \cdot \tilde{\mathbb{E}}_0 \cdot \tilde{\boldsymbol{\varepsilon}}^{m+1} \Delta \rho f'(d^m)}{\frac{1}{2} f''(d^{m+1}) \tilde{\boldsymbol{\varepsilon}}^{m+1} \cdot \tilde{\mathbb{E}}_0 \cdot \tilde{\boldsymbol{\varepsilon}}^{m+1} p(\tilde{\boldsymbol{\varepsilon}}^{m+1}, d^m)}, \quad (\text{A.15})$$

so that the derivative of the damage variable can be calculated by

$$\begin{aligned} \left. \frac{\partial d}{\partial \tilde{\boldsymbol{\varepsilon}}} \right|^{m+1} &= -\Delta \rho f'(d^m) \tilde{\mathbb{E}}_0 \cdot \tilde{\boldsymbol{\varepsilon}}^{m+1} \\ &\quad + \tilde{\mathbb{E}}_0 \cdot \tilde{\boldsymbol{\varepsilon}}^{m+1} \frac{-f'(d^{m+1}) + \frac{1}{2} f''(d^{m+1}) \tilde{\boldsymbol{\varepsilon}}^{m+1} \cdot \tilde{\mathbb{E}}_0 \cdot \tilde{\boldsymbol{\varepsilon}}^{m+1} \Delta \rho f'(d^m)}{\frac{1}{2} f''(d^{m+1}) \tilde{\boldsymbol{\varepsilon}}^{m+1} \cdot \tilde{\mathbb{E}}_0 \cdot \tilde{\boldsymbol{\varepsilon}}^{m+1}}, \end{aligned} \quad (\text{A.16})$$

and therewith finally the material tangent based on Equation (4.53)

$$\begin{aligned} \left. \frac{d \tilde{\boldsymbol{\sigma}}}{d \tilde{\boldsymbol{\varepsilon}}} \right|^{m+1} &= f(d^m) \tilde{\mathbb{E}}_0 - \left(\tilde{\mathbb{E}}_0 \cdot \tilde{\boldsymbol{\varepsilon}}^m \right) \otimes \left(\tilde{\mathbb{E}}_0 \cdot \tilde{\boldsymbol{\varepsilon}}^{m+1} \right) \times \left(\Delta \rho f'(d^m)^2 \right. \\ &\quad \left. - f'(d^m) \frac{-f'(d^{m+1}) + \frac{1}{2} f''(d^{m+1}) \tilde{\boldsymbol{\varepsilon}}^{m+1} \cdot \tilde{\mathbb{E}}_0 \cdot \tilde{\boldsymbol{\varepsilon}}^{m+1} \Delta \rho f'(d^m)}{\frac{1}{2} f''(d^{m+1}) \tilde{\boldsymbol{\varepsilon}}^{m+1} \cdot \tilde{\mathbb{E}}_0 \cdot \tilde{\boldsymbol{\varepsilon}}^{m+1}} \right). \end{aligned} \quad (\text{A.17})$$

In case of no evolving damage, the material tangent corresponds to

$$\left. \frac{d \tilde{\boldsymbol{\sigma}}}{d \tilde{\boldsymbol{\varepsilon}}} \right|^{m+1} = f(d^m) \tilde{\mathbb{E}}_0. \quad (\text{A.18})$$

Algorithm on Finite Element Level

The subsequent Algorithm 5 gives an overview of the finite element implementation of the rate-independent variants of Model I [REL] presented in the Subsections 4.2.1 and 4.2.2. The algorithm can be related to both rate-independent model variants, the two-phase model as well as the non-linearly homogenized model, since the algorithm is generally formulated and the equations can respectively be assigned for each case.

Algorithm 5: Model I [REL]: Algorithm for the rate-independent approaches.

input: $\tilde{\varepsilon}^m, \tilde{\varepsilon}^{m+1}, d^m$

calc: $p^{m+1} = p(\tilde{\varepsilon}^{m+1}, d^m)$

calc: $\Phi^{m+1} = \Phi(p(\tilde{\varepsilon}^{m+1}, d^m))$

set: $\Delta\rho = 0$

while $\Phi^{m+1} > 0$ **do**

$$d^{m+1} = d^m + \Delta\rho p^{m+1}$$

$$d_{tol}^{m+1} = d^m + (\Delta\rho + tol) p^{m+1}$$

calc: $p^{m+1} = p(\tilde{\varepsilon}^{m+1}, d^{m+1})$

calc: $p_{tol}^{m+1} = p_{tol}(\tilde{\varepsilon}^{m+1}, d_{tol}^{m+1})$

calc: $\Phi^{m+1} = \Phi(p(\tilde{\varepsilon}^{m+1}, d^{m+1}))$

calc: $\Phi_{tol}^{m+1} = \Phi_{tol}(p_{tol}(\tilde{\varepsilon}^{m+1}, d_{tol}^{m+1}))$

$$\frac{\partial\Phi}{\partial\Delta\rho} = \frac{\Phi_{tol}^{m+1} - \Phi^{m+1}}{tol}$$

$$\Delta\rho = \Delta\rho - \Phi^{m+1} \left(\frac{\partial\Phi}{\partial\Delta\rho} \right)^{-1}$$

if $\Delta\rho < 0$ **then**

└ abort

calc: $\tilde{\sigma}^{m+1} = \tilde{\sigma}(\tilde{\varepsilon}^m, \tilde{\varepsilon}^{m+1}, d^m, d^{m+1})$

calc: $\frac{d\tilde{\sigma}^{m+1}}{d\tilde{\varepsilon}^{m+1}} = \frac{d\tilde{\sigma}}{d\tilde{\varepsilon}}(\tilde{\varepsilon}^m, \tilde{\varepsilon}^{m+1}, d^m, d^{m+1})$

Bibliography

- [Abu Al-Rub and Voyiadjis 2005] ABU AL-RUB, Rashid K. ; VOYIADJIS, George Z.: A direct finite element implementation of the gradient-dependent theory. In: *International Journal for Numerical Methods in Engineering* 63 (2005), Nr. 4, S. 603–629
- [Achenbach 1975] ACHENBACH, Jan D.: *Wave propagation in elastic solids*. Bd. 16. 1. Amsterdam : North-Holland Publishing Company, 1975
- [Aifantis 1992] AIFANTIS, Elias C.: On the role of gradients in the localization of deformation and fracture. In: *International Journal for Engineering Science* 30 (1992), Nr. 10, S. 1279–1299
- [Allaire and Kohn 1993] ALLAIRE, Gregoire ; KOHN, Robert V.: Optimal bounds on the effective behavior of a mixture of two well-ordered elastic materials. In: *Quarterly of Applied Mechanics* 51 (1993), 12, Nr. 4, S. 643–674
- [Allaire and Lods 1999] ALLAIRE, Gregoire ; LODS, Veronique: Minimizers for a double-well problem with affine boundary conditions. In: *Proceedings of the Royal Society of Edinburgh Section A: Mathematics* 129 (1999), Nr. 3, S. 439–466
- [Allix 2012] ALLIX, Oliver: The bounded rate concept: A framework to deal with objective failure predictions in dynamic within a local constitutive model. In: *International Journal of Damage Mechanics* 22 (2012), Nr. 6, S. 808–828
- [Altenbach and Altenbach 1994] ALTENBACH, Johannes ; ALTENBACH, Holm: *Einführung in die Kontinuumsmechanik*. 1. Stuttgart : B. G. Teubner, 1994
- [Anderson 2005] ANDERSON, Ted L.: *Fracture mechanics: fundamentals and applications*. 3. Boca Raton : Taylor & Rancis Group, LLC, 2005
- [Bailey 2002] BAILEY, C. D.: The unifying laws of classical mechanics. In: *Foundations of Physics* 32 (2002), 01, Nr. 1, S. 159–176
- [Ball 1977] BALL, John M.: Constitutive inequalities and existence theorems in nonlinear elastostatics. In: *Nonlinear Analysis and Mechanics: Heriot-Watt Symposium, Pitman* 1 (1977), Nr. 1, S. 187–241
- [Bargmann and Steinmann 2005] BARGMANN, Swantje ; STEINMANN, Paul: Finite element approaches to non-classical heat conduction in solids. In: *Computer Modeling in Engineering and Sciences* 9 (2005), 08, Nr. 2, S. 133–150
- [Basic et al. 2018] BASIC, Josip ; DEGIULI, Nastia ; BAN, Dario: A class of renormalised meshless Laplacians for boundary value problems. In: *Journal of Computational Physics* 354 (2018), S. 269–287
- [Bathe 2002] BATHE, Klaus-Jürgen: *Finite-Elemente-Methoden, Aus dem Englischen übersetzt von Peter Zimmermann*. 2. Heidelberg : Springer-Verlag, 2002

- [Bažant and Jirásek 2002] BAŽANT, Zdeněk P. ; JIRÁSEK, M.: Nonlocal integral formulations of plasticity and damage: survey of progress. In: *Journal of Engineering Mechanics* 128 (2002), Nr. 11, S. 1119–1149
- [Bažant and Lin 1988] BAŽANT, Zdeněk P. ; LIN, Feng-Bao: Nonlocal smeared cracking model for concrete fracture. In: *Journal of Structural Engineering* 114 (1988), 11, Nr. 11
- [Bažant and Pijaudier-Cabot 1988] BAŽANT, Zdeněk P. ; PIJAUDIER-CABOT, Gilles: Nonlocal continuum damage, localization instability and convergence. In: *Journal of Applied Mechanics* 55 (1988), 06
- [Bedford 1985] BEDFORD, Anthony: Hamilton's principle in continuum mechanics. In: *Pitman Publishing* 1 (1985), 01, Nr. 1
- [Biot 1962] BIOT, Maurice A.: Mechanics of deformation and acoustic propagation in porous media. In: *Journal of Applied Physics* 33 (1962), 04, Nr. 4, S. 1482–1498
- [Bourdin 2001] BOURDIN, Blaise: Filters in topology optimization. In: *International Journal for Numerical Methods in Engineering* 50 (2001), 03, Nr. 9, S. 2143–2158
- [Brepols et al. 2017] BREPOLS, Tim ; WULFINGHOFF, Stephan ; REESE, Stefanie: Gradient-extended two-surface damage-plasticity: micromorphic formulation and numerical aspects. In: *International Journal of Plasticity* 97 (2017), S. 64–106
- [Carstensen et al. 2001] CARSTENSEN, Carsten ; HACKL, Klaus ; MIELKE, Alexander: Non-convex potentials and microstructures in finite-strain plasticity. In: *Proceedings of the Royal Society A: Mathematical, Physical and Engineering Sciences* 458 (2001), 12, Nr. 2018, S. 299–317
- [Chaboche 1981] CHABOCHE, Jean-Louis: Continuous damage mechanics - a tool to describe phenomena before crack initiation. In: *Nuclear Engineering and Design* 64 (1981), 04, Nr. 2, S. 233–247
- [Chaboche et al. 2001] CHABOCHE, Jean-Louis ; FEYEL, F. ; MONERIE, Y.: Interface debonding models: a viscous regularization with a limited rate dependency. In: *International Journal of Solids and Structures* 38 (2001), Nr. 18, S. 3127–3160
- [Ciarlet 1988] CIARLET, Philippe G.: *Mathematical elasticity, Volume I: Three-dimensional elasticity*. 1. Amsterdam : Elsevier Science Publishers B.V., 1988
- [Coleman and Gurtin 1967] COLEMAN, Bernhard D. ; GURTIN, Morton E.: Thermodynamics with internal state variables. In: *The Journal of Chemical Physics* 47 (1967), 02, Nr. 2, S. 597–613
- [Coleman and Noll 1963] COLEMAN, Bernhard D. ; NOLL, Walter: The thermodynamics of elastic material with heat conduction and viscosity. In: *Archive for Rational Mechanics and Analysis* 13 (1963), 12, Nr. 1, S. 167–178
- [Comi 2001] COMI, Claudia: A non-local model with tension and compression damage mechanisms. In: *European Journal of Mechanics-A/Solids* 20 (2001), Nr. 1, S. 1–22

- [Coulomb 1776] COULOMB, Charles-Augustin d.: Essai sur une application des règles des maximis et minimis à quelques problèmes de statique, relatifs à l'architecture. In: *Mémoires de Mathématique et de Physique, Présentés à l'Académie Royale des Sciences, par divers Savants, et lus dans ses Assemblées* 7 (1776), Nr. 1, S. 343–387
- [Dacorogna 1982a] DACOROGNA, Bernard: Quasiconvexity and relaxation of nonconvex problems in the calculus of variations. In: *Journal of Functional Analysis* 46 (1982), 03, Nr. 1, S. 102–118
- [Dacorogna 1982b] DACOROGNA, Bernard: *Weak continuity and weak lower semicontinuity of non-linear functionals*. 1. Berlin Heidelberg : Springer-Verlag, 1982
- [Dacorogna 1989] DACOROGNA, Bernard: *Direct Methods in the Calculus of Variations*. 78. New York : Springer-Verlag, 1989
- [De Borst and Mühlhaus 1992] DE BORST, René ; MÜHLHAUS, Hans-Bernd: Gradient-dependent plasticity: formulation and algorithmic aspects. In: *International Journal for Numerical Methods in Engineering* 35 (1992), 08, Nr. 3, S. 521–539
- [Demtröder 2017] DEMTRÖDER, Wolfgang: *Mechanics and thermodynamics*. 1. Cham : Springer-Verlag, 2017
- [Dimitrijevic et al. 2012] DIMITRIJEVIC, Bojan J. ; AIFANTIS, Katerina E. ; HACKL, Klaus: The influence of particle size and spacing on the fragmentation of nanocomposite anodes for Li batteries. In: *Journal of Power Sources* 206 (2012), S. 343–348
- [Dimitrijevic and Hackl 2008] DIMITRIJEVIC, Bojan J. ; HACKL, Klaus: A method for gradient enhancement of continuum damage models. In: *Technische Mechanik* 28 (2008), 09, Nr. 1, S. 43–52
- [Dimitrijevic and Hackl 2011] DIMITRIJEVIC, Bojan J. ; HACKL, Klaus: A regularization framework for damage–plasticity models via gradient enhancement of the free energy. In: *International Journal for Numerical Methods in Biomedical Engineering* 27 (2011), Nr. 8, S. 1199–1210
- [Dube et al. 1996] DUBE, Jean-Francois ; PIJAUDIER-CABOT, G. ; BORDERIE, Christian L.: Rate dependent damage model for concrete in dynamics. In: *Journal of Engineering Mechanics* 122 (1996), 10, Nr. 10, S. 939–947
- [Elsgolc 1961] ELSGOLC, Lev E.: *Calculus of variations*. 19. London : Pergamon Press, 1961
- [Faria et al. 1998] FARIA, R. ; OLIVER, J. ; CERVERA, M.: A strain-based plastic viscous-damage model for massive concrete structures. In: *International journal of solids and structures* 35 (1998), Nr. 14, S. 1533–1558
- [Fish and Belytschko 2007] FISH, Jacob ; BELYTSCHKO, Ted: *A first course in finite elements*. 1. Chichester : John Wiley & Sons, 2007
- [Forest and Lorentz 2004] FOREST, Samuel ; LORENTZ, Eric: *Local approach to fracture*. 1. Presse des Mines, 2004
- [Francfort and Garroni 2006] FRANCFORT, Gilles A. ; GARRONI, Adriana: A variational view of partial brittle damage evolution. In: *Archive for Rational Mechanics and Analysis* 182 (2006), 09, Nr. 1, S. 125–152

- [Francfort and Marigo 1993] FRANCFORT, Gilles A. ; MARIGO, Jean-Jacques: Stable damage evolution in a brittle continuous medium. In: *European Journal of Mechanics - A/Solids* 12 (1993), 01, Nr. 2, S. 149–189
- [Francfort and Mielke 2006] FRANCFORT, Gilles A. ; MIELKE, Alexander: Existence results for a class of rate-independent material models with nonconvex elastic energies. In: *Journal für die reine und angewandte Mathematik* 2006 (2006), 06, Nr. 595, S. 55–91
- [Gelfand and Fomin 2000] GELFAND, Izrail' M. ; FOMIN, Sergei V.: *Calculus of variations*. 1. New York : Dover Publications, 2000
- [Geuzaine and Remacle 2009] GEUZAINE, Christophe ; REMACLE, Jean-François: Gmsh: a 3-D finite element mesh generator with built-in pre- and post-processing facilities. In: *International Journal for Numerical Methods in Engineering* 79 (2009), 09, Nr. 11, S. 1309–1331
- [Gross and Seelig 2011] GROSS, Dietmar ; SEELIG, Thomas: *Bruchmechanik, Mit einer Einführung in die Mikromechanik*. 5. Berlin Heidelberg : Springer-Verlag, 2011
- [Gurson 1977] GURSON, A. L.: Continuum Theory of Ductile Rupture by Void Nucleation and Growth: Part I-Yield Criteria and Flow Rules for Porous Ductile Media. In: *Journal of Engineering Materials and Technology* 99 (1977), 01, Nr. 1, S. 2–15
- [Gurtin et al. 2010] GURTIN, Morton E. ; FRIED, Eliot ; ANAND, Lallit: *The mechanics and thermodynamics of continua*. 1. New York : Cambridge University Press, 2010
- [Hackl and Fischer 2008] HACKL, Klaus ; FISCHER, Franz D.: On the relation between the principle of maximum dissipation and inelastic evolution given by dissipation potentials. In: *Proceedings of the Royal Society A: Mathematical, Physical and Engineering Sciences* 464 (2008), 01, Nr. 2089, S. 117–132
- [Hackl et al. 2011] HACKL, Klaus ; FISCHER, Franz D. ; SVOBODA, Jiri: A study on the principle of maximum dissipation for coupled and non-coupled non-isothermal processes in materials. In: *Proceedings of the Royal Society A: Mathematical, Physical and Engineering Sciences* 467 (2011), 08, Nr. 2132, S. 2422–2426
- [Hägg and Wadbro 2017] HÄGG, Linus ; WADBRO, Eddie: Nonlinear filters in topology optimization: existence of solution and efficient implementation for minimum compliance problems. In: *Structural and Multidisciplinary Optimization* 55 (2017), 03, Nr. 3, S. 1017–1028
- [Hamilton 1834] HAMILTON, Willian R.: On a general method in dynamics; by which the study of the motions of all free systems of attracting or repelling points is reduced to the search and differentiation of one central relation, or characteristic function. In: *Philosophical Transactions of the Royal Society* 124 (1834), 04, Nr. 1, S. 247–308
- [Hamilton 1835] HAMILTON, Willian R.: Second essay on a general method in dynamics. In: *Philosophical Transactions of the Royal Society* 125 (1835), 01, Nr. 1, S. 95–144
- [Hermann 2011] HERMANN, Martin: *Numerische Mathematik*. 3. München : Oldenbourg Wissenschaftsverlag GmbH, 2011
- [Hertzberg et al. 2013] HERTZBERG, Richard W. ; VINCI, Richard P. ; HERTZBERG, Jason L.: *Deformation and fracture mechanics of engineering materials*. 5. Danvers : John Wiley & Sons, 2013

- [Holm 2018] HOLM, Altenbach: *Kontinuumsmechanik, Einführung in die materialunabhängigen und materialabhängigen Gleichungen*. 4. Berlin Heidelberg : Springer-Verlag, 2018
- [Holzapfel 2000] HOLZAPFEL, Gerhard A.: *Nonlinear solid mechanics, a continuum approach for engineering*. 1. Chichester : John Wiley & Sons, 2000
- [Hoormazdi et al. 2019] HOORMAZDI, Golnaz ; HACKL, Klaus ; JUNKER, Philipp: Numerical investigation of wear processes by a gradient-enhanced damage-plasticity model. In: *Proceedings in Applied Mathematics and Mechanics, submitted 19* (2019), Nr. 1
- [Hornbogen et al. 2008] HORNBOKEN, Erhard ; EGGELER, Gunther ; WERNER, Ewald: *Werkstoffe, Aufbau und Eigenschaften*. 9. Berlin Heidelberg : Springer-Verlag, 2008
- [Jantos et al. 2018] JANTOS, Dustin ; JUNKER, Philipp ; HACKL, Klaus: An accurate and fast regularization approach to thermodynamic topology optimization. In: *International Journal for Numerical Methods in Engineering* 117 (2018), 11, Nr. 9
- [Jirásek 1998] JIRÁSEK, Milan: Nonlocal models for damage and fracture: comparison of approaches. In: *International Journal of Solids and Structures* 35 (1998), 11, Nr. 31-32, S. 4133–4145
- [Junker 2011] JUNKER, Philipp: *Simulation of shape memory alloys: material modeling using the principle of maximum dissipation*. Bochum : Dissertation, Ruhr-Universität Bochum, 2011
- [Junker 2016] JUNKER, Philipp: *Variational modeling of martensitic phase transformations - Hamiltonian principles, experimental validation, numerical approaches*. Bochum : Habilitationsschrift, Ruhr-Universität Bochum, 2016
- [Junker and Hackl 2015] JUNKER, Philipp ; HACKL, Klaus: A variational growth approach to topology optimization. In: *Structural and Multidisciplinary Optimization* 52 (2015), 08, Nr. 2, S. 1–12
- [Junker and Hackl 2016] JUNKER, Philipp ; HACKL, Klaus: A discontinuous phase field approach to variational growth-based topology optimization. In: *Structural and Multidisciplinary Optimization* 54 (2016), 01, Nr. 1
- [Junker et al. 2014] JUNKER, Philipp ; MAKOWSKI, Jerzy ; HACKL, Klaus: The principle of the minimum of the dissipation potential for non-isothermal processes. In: *Continuum Mechanics and Thermodynamics* 29 (2014), 10, Nr. 1, S. 259–268
- [Junker et al. 2016] JUNKER, Philipp ; SCHWARZ, Stephan ; HACKL, Klaus: A relaxation-based approach to damage modeling. In: *Continuum Mechanics and Thermodynamics* 29 (2016), 10, Nr. 1, S. 291–310. – doi.org/10.1007/s00161-016-0528-8
- [Junker et al. 2018] JUNKER, Philipp ; SCHWARZ, Stephan ; JANTOS, Dustin ; HACKL, Klaus: A fast and robust numerical treatment of a gradient-enhanced model for brittle damage. In: *International Journal for Multiscale Computational Engineering* (2018), 01. – doi.org/10.1615/IntJMCompEng.2018027813
- [Kachanov 1958] KACHANOV, Lazar M.: Time of the rupture process under creep conditions. In: *Izvestia Akademii Nauk SSSR, Otdelenie tekhnicheskich nauk* 8 (1958), Nr. 1, S. 26–31

- [Kachanov 1999] KACHANOV, Lazar M.: Rupture time under creep conditions. In: *International Journal of Fracture* 97 (1999), 04, Nr. 1-4, S. 11–18
- [Kielhöfer 2010] KIELHÖFER, Hansjörg: *Variationsrechnung, Eine Einführung in die Theorie einer unabhängigen Variablen mit Beispielen und Aufgaben*. 1. Wiesbaden : Vieweg+Teubner, 2010
- [Krajcinovic 1996] KRAJGINOVIC, Dusan: *damage mechanics*. 1. Amsterdam : Elsevier Science, 1996
- [Lanczos 1970] LANCZOS, Cornelius: *The variational principles of mechanics*. 4. Toronto : University of Toronto Press, 1970
- [Langenfeld et al. 2018] LANGENFELD, Kai ; JUNKER, Philipp ; MOSLER, Jörn: Quasi-brittle damage modeling based on incremental energy relaxation combined with a viscous-type regularization. In: *Continuum Mechanics and Thermodynamics* 30 (2018), 09, Nr. 5, S. 1125–1144
- [Lemaitre 1971] LEMAITRE, Jean: Evaluation of dissipation and damage in metals submitted to dynamic loading. In: *Proceeding of the International Conference on the mechanical behavior of materials, Kyoto, Japan, August 15-20, 1971* 1 (1971), Nr. 1, S. 1–16
- [Lemaitre 1985] LEMAITRE, Jean: A Continuous Damage Mechanics Model for Ductile Fracture. In: *Journal of Engineering Materials and Technology* 107 (1985), Nr. 1, S. 83–89
- [Liu et al. 1999] LIU, W. K. ; HAO, S. ; BELYTSCHKO, T. ; LI, S. F. ; CHANG, C. T.: Multiple scale meshfree methods for damage fracture and localization. In: *Computational materials science* 16 (1999), Nr. 1, S. 197–205
- [Lokilech 2007] LOKILECH: *Pedalarm Bruch*. 2007. – converted to black and white, taken from https://commons.wikimedia.org/wiki/File:Pedalarm_Bruch.jpg, licensed by <https://creativecommons.org/licenses/by-sa/3.0/legalcode>
- [Lorentz and Andrieux 1999] LORENTZ, Eric ; ANDRIEUX, Stéphane: A variational formulation for nonlocal damage models. In: *International Journal of Plasticity* 15 (1999), 03, Nr. 2, S. 119–138
- [Lorentz and Andrieux 2003] LORENTZ, Eric ; ANDRIEUX, Stéphane: Analysis of non-local models through energetic formulations. In: *International Journal of Solids and Structures* 40 (2003), Nr. 12, S. 2905–2936
- [Lorentz and Benallal 2005] LORENTZ, Eric ; BENALLAL, A.: Gradient constitutive relations: numerical aspects and application to gradient damage. In: *Computer methods in applied mechanics and engineering* 194 (2005), Nr. 50, S. 5191–5220
- [Matzenmiller et al. 1995] MATZENMILLER, A. ; LUBLINER, J. ; TAYLOR, R. L.: A constitutive model for anisotropic damage in fiber-composits. In: *Mechanics of Materials* 20 (1995), 04, Nr. 2, S. 125–152
- [Menzel et al. 2005] MENZEL, Andreas ; EKH, Magnus ; RUNESSON, Kenneth ; STEINMANN, Paul: A framework for multiplicative elastoplasticity with kinematic hardening coupled to anisotropic damage. In: *International Journal of Plasticity* 21 (2005), 03, Nr. 3, S. 397–434

- [Miehe et al. 2010a] MIEHE, Christian ; HOFACKER, Martina ; WELSCHINGER, Fabian: A phase field model for rate-independent crack propagation: Robust algorithmic implementation based on operator splits. In: *Computer Methods in Applied Mechanics and Engineering* 199 (2010), Nr. 45-48, S. 2765–2778
- [Miehe et al. 2010b] MIEHE, Christian ; WELSCHINGER, Fabian ; HOFACKER, Martina: Thermodynamically consistent phase-field models of fracture: Variational principles and multi-field FE implementations. In: *International Journal for Numerical Methods in Engineering* 83 (2010), Nr. 10, S. 1273–1311
- [Mohr 1906] MOHR, Otto: *Abhandlungen aus dem Gebiet der technischen Mechanik*. 1. Berlin : Ernst & Sohn, 1906
- [Müller 2016] MÜLLER, Rainer: *Thermodynamik, Vom Tautropfen zum Solarkraftwerk*. 2. Berlin Boston : Walter de Gruyter GmbH, 2016
- [Needleman 1988] NEEDLEMAN, Alan: Material rate dependence and mesh sensitivity in localization problems. In: *Computer Methods in Applied Mechanics and Engineering* 67 (1988), Nr. 1, S. 69–85
- [Nguyen et al. 2015] NGUYEN, Giang D. ; KORSUNSKY, Alexander M. ; BELNOUE, Joanthan P.-H.: A nonlocal coupled damage-plasticity model for the analysis of ductile failure. In: *International Journal of Plasticity* 64 (2015), 01, S. 56–75
- [Niazi et al. 2013] NIAZI, Muhammad S. ; WISSELINK, H. H. ; MEINDERS, Vincent T.: Viscoplastic regularization of local damage models: revisited. In: *Computational Mechanics* 51 (2013), Nr. 2, S. 203–216
- [Onsager 1931] ONSAGER, Lars: Reciprocal relations in irreversible processes. I. In: *American Physical Society* 37 (1931), 02, Nr. 4, S. 405–426
- [Ortiz and Repetto 1999] ORTIZ, Michael ; REPETTO, Eduardo A.: Nonconvex energy minimization and dislocation structures in ductile single crystals. In: *Journal of the Mechanics and Physics of Solids* 47 (1999), 02, Nr. 2, S. 397–462
- [Ortiz and Stainier 1999] ORTIZ, Michael ; STAINIER, Laurent: The variational formulation of viscoplastic constitutive updates. In: *Computer methods in applied mechanics and engineering* 171 (1999), Nr. 3, S. 419–444
- [Pandolfi and Ortiz 2012] PANDOLFI, Anna ; ORTIZ, Michael: An eigenerosion approach to brittle fracture. In: *International Journal for Numerical Methods in Engineering* 92 (2012), Nr. 8, S. 694–714
- [Peerlings et al. 1995] PEERLINGS, Ron H. J. ; DE BORST, René ; BREKELMANS, W. A. M. ; DE VREE, J. H. P.: Computational modelling of gradient-enhanced damage for fracture and fatigue problems. In: *Computational Plasticity, Fundamentals and Applications: Proceedings of the 4th International Conference* Pineridge Press: Swansea, 1995, S. 975–986
- [Peerlings et al. 2001] PEERLINGS, Ron H. J. ; GEERS, Marc G. D. ; DE BORST, René ; BREKELMANS, W. A. M.: A critical comparison of nonlocal and gradient-enhanced softening continua. In: *International Journal of Solids and Structures* 38 (2001), Nr. 44, S. 7723–7746

- [Peters and Hackl 2005] PETERS, Markus ; HACKL, Klaus: Numerical aspects of the eXtended Finite Element Method. In: *Proceedings in Applied Mathematics and Mechanics* 5 (2005), 12, Nr. 1
- [Pezeshki et al. 2018] PEZESHKI, Mahmoud ; LOEHNERT, Stefan ; WRIGGERS, Peter ; GUIDAULT, Pierre-Alain ; BARANGER, Emmanuel: 3D Dynamic Crack Propagation by the Extended Finite Element Method and a Gradient-Enhanced Damage Model. In: *Multiscale Modeling of Heterogeneous Structures*. Springer, 2018, S. 277–299
- [Pijaudier-Cabot and Bažant 1987] PIJAUDIER-CABOT, Gilles ; BAŽANT, Zdeněk P.: Nonlocal damage theory. In: *Journal of Engineering Mechanics* 113 (1987), 10, Nr. 10
- [Pijaudier-Cabot et al. 1988] PIJAUDIER-CABOT, Gilles ; BAŽANT, Zdeněk P. ; TABBARA, Mazen: Comparison of various models for strain-softening. In: *Engineering Computations* 5 (1988), 12, Nr. 2, S. 141–150
- [Prax et al. 1996] PRAX, Christian ; SADAT, Hamou ; SALAGNAC, Patrick: Diffuse approximation method for solving natural convection in porous media. In: *Transport in Porous Media* 22 (1996), Nr. 2, S. 215–223
- [Rabotnov 1959] RABOTNOV, Yu. N.: On the mechanism of delayed fracture. In: *Strength of Materials and Structures (Izd. Akad. Nauk SSSR, Moscow, in Russian)* 1 (1959), Nr. 1, S. 5–7
- [Rankine 1857] RANKINE, William John M.: On the stability of loose earth. In: *Philosophical Transactions of the Royal Society of London* 147 (1857), 01, Nr. 1, S. 9–27
- [Riley et al. 2006] RILEY, Ken F. ; HOBSON, Michael P. ; BENCE, Stephen J.: *Mathematical methods for physics and engineering*. 3. New York : Cambridge University Press, 2006
- [Rockafellar and Wets 1998] ROCKAFELLAR, R. T. ; WETS, Roger J-B.: *Variational analysis*. 317. Berlin Heidelberg : Springer-Verlag, 1998
- [Saint-Venant 1856] SAINT-VENANT, Adhémar-Jean-Claude Barré de: *Mémoire sur la torsion des prismes*. 1. Paris : Journal de Mathématiques Pures et Appliquées de Liouville, 1856. – 234–560 S.
- [Schäfer 1999] SCHÄFER, Michael: *Numerik im Maschinenbau*. 1. Berlin Heidelberg : Springer-Verlag, 1999
- [Schmidt et al. 2009] SCHMIDT, Bernd ; FRATERNALI, Fernando ; ORTIZ, Michael: Eigenfracture: an eigendeformation approach to variational fracture. In: *Multiscale Modeling & Simulation* 7 (2009), Nr. 3, S. 1237–1266
- [Schwarz et al. 2018a] SCHWARZ, Stephan ; HACKL, Klaus ; JUNKER, Philipp: On a relaxation-based and time-incremental approach to damage modeling. In: *Proceedings in Applied Mathematics and Mechanics* 18 (2018), 12, Nr. 1, S. 1–2. – doi.org/10.1002/pamm.201800131
- [Schwarz et al. 2019a] SCHWARZ, Stephan ; HACKL, Klaus ; JUNKER, Philipp: An Efficient Treatment of the Laplacian in a Gradient-Enhanced Damage Model. In: *Proceedings in Applied Mathematics and Mechanics, Minisymposia, accepted* 19 (2019), Nr. 1, S. 1–4

- [Schwarz et al. 2016] SCHWARZ, Stephan ; JUNKER, Philipp ; HACKL, Klaus: A relaxation-based approach to damage modeling. In: *Proceedings in Applied Mathematics and Mechanics* 16 (2016), 10, Nr. 1, S. 173–174. – doi.org/10.1002/pamm.201610075
- [Schwarz et al. 2017] SCHWARZ, Stephan ; JUNKER, Philipp ; HACKL, Klaus: The coupling of plasticity with a relaxation-based approach to damage modeling. In: *Proceedings in Applied Mathematics and Mechanics* 17 (2017), Nr. 1, S. 275–576. – doi.org/10.1002/pamm.201710107
- [Schwarz et al. 2018b] SCHWARZ, Stephan ; JUNKER, Philipp ; HACKL, Klaus: The effect of plasticity on damage evolution using a relaxation-based material model. In: *Journal of the Mechanical Behavior of Materials* 27 (2018), 12, Nr. 5-6. – doi.org/10.1515/jmbm-2018-2001
- [Schwarz et al. 2019b] SCHWARZ, Stephan ; JUNKER, Philipp ; HACKL, Klaus: Variational regularization of damage models based on the emulated RVE. In: *under review* (2019)
- [Simo and Hughes 2000] SIMO, Juan C. ; HUGHES, Thomas J. R.: *Computational inelasticity*. 7. New York : Springer-Verlag, 2000
- [Simo and Ju 1987] SIMO, Juan C. ; JU, Jiannwen W.: Strain- and stress-based continuum damage models - I. formulation. In: *International Journal of Solids and Structures, Mathematical and Computer Modelling Reports* 23 (1987), 12, Nr. 7, S. 821–840
- [Simo and Ju 1989] SIMO, Juan C. ; JU, Jiannwen W.: Strain- and stress-based continuum damage models - II. computational aspects. In: *International Journal of Solids and Structures, Mathematical and Computer Modelling Reports* 12 (1989), Nr. 3, S. 378
- [Simo et al. 1993] SIMO, Juan C. ; OLIVER, Javier ; ARMERO, Francisco: An analysis of strong discontinuities induced by strain softening in rate-independent inelastic solids. In: *Computational Mechanics* 12 (1993), S. 277–296
- [Skrzypek and Ganczarski 1999] SKRZYPEK, Jacek J. ; GANCZARSKI, Artur: *Modeling of material damage and failure of structures, theory and applications*. 1. Berlin Heidelberg : Springer-Verlag, 1999
- [Sluys and De Borst 1992] SLUYS, Lambertus J. ; DE BORST, René: Wave propagation and localization in a rate-dependent cracked medium - model formulation and one-dimensional examples. In: *International Journal of Solids and Structures* 29 (1992), Nr. 23, S. 2945–2958
- [Stacey 1994] STACEY, Richard: New finite-difference methods for free surfaces with a stability analysis. In: *Bulletin of the Seismological Society of America* 84 (1994), Nr. 1, S. 171–184
- [Strobl and Seelig 2015] STROBL, Michael ; SEELIG, Thomas: A novel treatment of crack boundary conditions in phase field models of fracture. In: *PAMM* 15 (2015), Nr. 1, S. 155–156
- [Strobl and Seelig 2016] STROBL, Michael ; SEELIG, Thomas: On constitutive assumptions in phase field approaches to brittle fracture. In: *Procedia Structural Integrity* 2 (2016), S. 3705–3712

- [Suffis et al. 2003] SUFFIS, Arnaud ; LUBRECHT, Ton A. A. ; COMBESURE, Alain: Damage model with delay effect: Analytical and numerical studies of the evolution of the characteristic damage length. In: *International Journal of Solids and Structures* 40 (2003), Nr. 13-14, S. 3463–3476
- [Taylor 2017a] TAYLOR, Robert L.: *FEAP - - a finite element analysis program, Version 8.5 theory manual*. 1. Berkeley : University of California at Berkeley, 2017
- [Taylor 2017b] TAYLOR, Robert L.: *FEAP - - a finite element analysis program, Version 8.5 user manual*. 1. Berkeley : University of California at Berkeley, 2017
- [Tresca 1864] TRESCA, Henri-Édouard: *Mémoire sur l'écoulement des corps solides soumis à de fortes pressions*. 1. Paris : Gauthier-Villars, 1864
- [Tvergaard 1981] TVERGAARD, Viggo: Influence of voids on shear band instabilities under plane strain conditions. In: *International Journal of Fracture* 17 (1981), 08, Nr. 4, S. 389–407
- [Tvergaard and Needleman 1984] TVERGAARD, Viggo ; NEEDLEMAN, Alan: Analysis of the cup-cone fracture in a round tensile bar. In: *Acta Metallurgica* 32 (1984), 01, Nr. 1, S. 157–169
- [Vogel and Junker 2019] VOGEL, Andreas ; JUNKER, Philipp: Adaptive and highly-accurate numerical treatment for a gradient-enhanced brittle damage model. In: *submitted* (2019)
- [Voigt 1910] VOIGT, Woldemar: *Lehrbuch der Kristallphysik (mit Ausschluss der Kristallographik)*. 34. Leipzig Berlin : B. G. Teubner, 1910
- [Šilhavý 1997] ŠILHAVÝ, Miroslav: *The mechanics and thermodynamics of continuous media*. 1. Berlin Heidelberg : Springer-Verlag, 1997
- [Waimann 2018] WAIMANN, Johanna: *Variationelle Modellierung irreversibler Effekte in polykristallinen Formgedächtnislegierungen*. Bochum : Dissertation, Ruhr-Universität Bochum, 2018
- [Wang et al. 1996] WANG, W. M. ; SLUYS, Lambertus J. ; DE BORST, René: Interaction between material length scale and imperfection size for localisation phenomena in viscoplastic media. In: *European Journal of Mechanics. A* 15 (1996), Nr. 3, S. 447–464
- [Willner 2003] WILLNER, Kai: *Kontinuums- und Kontaktmechanik, Synthetische und analytische Darstellung*. 1. Berlin Heidelberg : Springer-Verlag, 2003
- [Wriggers 2001] WRIGGERS, Peter: *Nichtlineare Finite-Element-Methoden*. 1. Berlin Heidelberg New York : Springer-Verlag, 2001
- [Wriggers and Moftah 2006] WRIGGERS, Peter ; MOFTAH, S. O.: Mesoscale models for concrete: homogenization and damage behavior. In: *Finite Elements in Analysis and Design* 42 (2006), 04, Nr. 7, S. 623–636
- [Yang and Misra 2012] YANG, Yang ; MISRA, Anil: Micromechanics based second gradient continuum theory for shear band modeling in cohesive granular materials following damage elasticity. In: *International Journal of Solids and Structures* 49 (2012), Nr. 18, S. 2500–2514

[Zienkiewicz and Taylor 2005] ZIENKIEWICZ, Olgierd C. ; TAYLOR, Robert L.: *The finite element method, for solid and structural mechanics*. 6. Oxford : Elsevier, 2005

[Zienkiewicz et al. 2005] ZIENKIEWICZ, Olgierd C. ; TAYLOR, Robert L. ; ZHU, J. Z.: *The finite element method, its basis & fundamentals*. 6. Oxford : Elsevier, 2005

Reference to Pre-Publications

In accordance with §7(1) parts of this dissertation have been published in international scientific journals and conference proceedings in consultation with the supervisors, PD Dr.-Ing. Philipp Junker and Prof. Dr. rer. nat. Klaus Hackl. Where appropriate, references in this thesis note the following pre-publications:

- Schwarz, S., Hackl, K. and Junker, P. (2019), *An efficient treatment of the Laplacian in a gradient-enhanced damage model*, Proceedings in Applied Mathematics and Mechanics, Minisymposia, *accepted*
- Schwarz, S., Junker, P. and Hackl, K., (2018), *Variational regularization of damage models based on the emulated RVE*, Continuum Mechanics and Thermodynamics, *under review*
- Schwarz, S., Hackl, K. and Junker, P. (2018), *On a relaxation-based and time-incremental approach to damage modeling*, Proceedings in Applied Mathematics and Mechanics, 18(1): 1–2. doi.org/10.1002/pamm.201800131
- Schwarz, S., Hackl, K. and Junker, P. (2018), *The effect of plasticity on damage evolution using a relaxation-based material model*, Journal of the Mechanical Behavior of Materials, 27(5-6): doi.org/10.1515/jmbm-2018-2001
- Junker, P., Schwarz, S., D.R. Jantos and Hackl, K. (2018), *A fast and robust numerical treatment of a gradient-enhanced model for brittle damage*, International Journal for Multiscale Computational Engineering, doi.org/10.1615/IntJMCompEng.2018027813
- Schwarz, S., Junker, P. and Hackl, K. (2017), *The coupling of plasticity with a relaxation-based approach to damage modeling*, Proceedings in Applied Mathematics and Mechanics, 17(1): 275–276. doi.org/10.1002/pamm.201710107
- Junker, P., Schwarz, S. and Hackl, K. (2016), *A relaxation-based approach to damage modeling*, Continuum Mechanics and Thermodynamics, 29(1): 291–310. doi.org/10.1007/s00161-016-0528-8
- Schwarz, S., Junker, P. and Hackl, K. (2016), *A relaxation-based approach to damage modeling*, Proceedings in Applied Mathematics and Mechanics, 16(1): 173–174. doi.org/10.1002/pamm.201610075
- Schwarz, S., Junker, P. and Hackl, K. (2015), *A regularization approach for damage models based on a displacement gradient*, Proceedings in Applied Mathematics and Mechanics, 15(1): 151–152. doi.org/10.1002/pamm.201510066
- Pöhl, F., Schwarz, S., Junker, P., Hackl, K. and Theisen, W. (2015), *Indentation and scratch testing - experiment and simulation*, International Conference on Stone and Concrete Machining, 3. doi.org/10.13154/icscm.3.2015.292-308
- Schwarz, S., Junker, P. and Hackl, K. (2014), *Modeling and simulation of damage processes based on a gradient-enhanced free energy function*, Proceedings in Applied Mathematics and Mechanics, 14(1): 151–152. doi.org/10.1002/pamm.201410063

Curriculum Vitae

Personal Data

Name	Stephan Schwarz
Place of Residence	Recklinghausen, NRW, Germany
Date of Birth	November 11th, 1987
Place of Birth	Neumünster, SH, Germany
Nationality	German

Employment

11/2013 – present	Research associate, Institute of Mechanics of Materials, Department of Civil and Environmental Engineering, Ruhr-Universität Bochum, NRW, Germany
05/2012 – 04/2013	Student assistant, Institute of Mechanics of Materials, Department of Civil and Environmental Engineering, Ruhr-Universität Bochum, NRW, Germany
09/2011 – 12/2011	Specialized internship, ThyssenKrupp GfT Gleistechnik, Bochum, NRW, Germany

University Education

11/2013 – present	Doctoral student, Institute of Mechanics of Materials, Ruhr-Universität Bochum, NRW, Germany
07/2014	Research stay (Prof. Sanjay Govindjee), University of California, Berkeley, CA, USA
04/2012 – 10/2013	Master of Science, Mechanical Engineering, applied mechanics, Ruhr-Universität Bochum, NRW, Germany, Scholarship by Rhestahl Stiftung
05/2013 – 08/2013	Research visiting student / master thesis (Prof. Sanjay Govindjee), University of California, Berkeley, CA, USA, PROMOS Scholarship, German Academic Exchange Service (DAAD)
10/2008 – 03/2012	Bachelor of Science, Mechanical Engineering, applied mechanics, Ruhr-Universität Bochum, NRW, Germany

Community Service

09/2007 – 05/2008	Prosper-Hospital, technical department, approved as basic internship, Recklinghausen, NRW, Germany
-------------------	---

School Education

08/1998 – 07/2007	Hittorf-Gymnasium, majors: math and physics, Recklinghausen, NRW, Germany
08/1994 – 07/1998	Evangelische Grundschule im Reitwinkel, Recklinghausen, NRW, Germany

**Mitteilungen aus dem Institut für Mechanik
RUHR-UNIVERSITÄT BOCHUM
Nr. 182**

ISBN 978-3-935892-60-5